A computational study of the effects of non-invasive neurostimulation on the neurons of the cerebellar cortex

Eleonora Bernasconi

Supervisors: Prof. Volker Steuber

Dr. Nada Yousif

School of Physics, Engineering and Computer Science
University of Hertfordshire

Submitted to the University of Hertfordshire in partial fulfilment of the requirement of the degree of PhD

March 2026

Acknowledgments

This has been a long, rewarding journey which I could not have done alone.

First and foremost, I want to thank my supervisors, prof. Volker Steuber and Dr Nada Yousif, for their guidance along the way. I want to thank my friends and colleagues from my lab, the Biocomputation group, and from my school, SPECS. I will miss our chats and informative discussions. I want to thank everyone who attended the Robotics and AI cafe', it has been refreshing to share struggles and successes with fellow PhD candidates. Doing a PhD can be a lonely, isolating journey. The presence of all of you gave me a sense of belonging.

I want to thank my friends, near and far, who have kept me company throughout these years and had to endure my frequent complaints about the struggles of research. I want to thank the lovely Brewhouse Babes and their horses for welcoming me into their barn. If I survived the gloomy, cold and wet English winters it is thanks to you.

I want to thank my parents, for always supporting my academic career as well as me as a person. I want to thank my husband for grounding me when things got too overwhelming for me to handle alone. Finally, I want to thank myself, for following the nudge I felt to start this PhD, and for bringing it to completion.

A deep, sincere thank you, to all of you who were part of my journey.

Abstract

Non-invasive neurostimulation techniques, in particular transcranial magnetic stimulation (TMS), have attracted increasing attention as potential treatments for neurological disorders associated with cerebellar dysfunction. However, treatment outcomes are variable across individuals and protocols. A deeper understanding of how TMS interacts with cerebellar circuits is therefore necessary to improve its therapeutic effectiveness and reliability.

Current research has produced computational models of both the cerebellum and TMS. Multi-scale approaches that combine TMS electric-field simulations with neuronal models represent the current state of the art. However, several gaps remain in the literature. In particular, there is still a lack of multi-scale models that explicitly include synaptic connectivity within neuronal networks while simultaneously accounting for the electric fields generated by TMS. Another major limitation is the lack of validation methods for models of TMS.

The objective of this research is to expand the current knowledge regarding the feasibility of TMS for cerebellar pathologies through the development of a computational framework integrating a biologically realistic cerebellar cortex model, a multi-scale TMS model, and a validation method for the latter. The central research questions addressed in this work are whether neurons in the cerebellar vermis are affected by TMS, how a continuous theta-burst stimulation protocol influences neuronal activity, and whether a model of eye movements can serve as a validation tool for stimulation models targeting the cerebellum.

To address these questions, I developed a detailed model of the cerebellar cortex including granule cells, Golgi cells, and Purkinje cells connected through synaptic interactions. I then coupled this network to a TMS model based on the estimation of the electric field induced in a realistic head model. As a validation approach, I employed a vertical oculomotor system model capable of predicting eye movements

based on cerebellar activity. By comparing predicted eye movements in baseline and in stimulated conditions with experimental observations, I assessed the validity of the stimulation model.

My results indicate that the examined stimulation magnitude used in experimental settings is insufficient to influence the firing rate of neurons in the cerebellar cortex, but that it produces sub-threshold effects. The vertical oculomotor system model can detect stimulation-induced differences in predicted eye movements, supporting its use as a validation framework for cerebellar TMS models.

The computational framework presented in this dissertation provides a foundation for future studies aimed at improving our understanding of non-invasive neurostimulation and optimising stimulation protocols for clinical applications targeting cerebellar disorders.

Table of Contents

List of figures XI
List of tables XVII
List of abbreviations XIX
Chapter 1
Introduction 1
1.1 Scope 1
1.1.1 Research questions 2
1.1.2 Contributions to knowledge 2
1.1.3 Research outputs 2
1.1.4 Code availability 3
1.1.5 Dissertation structure 3
1.2 The cerebellum 4
1.2.1 Anatomy of the cerebellum 4
1.2.2 Cerebellar cortex 5
1.2.3 Functional roles of the cerebellum 7
1.3 Non-invasive neurostimulation 9
1.3.1 Transcranial magnetic stimulation 9
1.4 Conclusion 12
Chapter 2
Literature Review 13
2.1 Models of the cerebellum 13
2.2 TMS targeting the cerebellum 22
2.2.1 TMS targeting the cerebellar vermis 29
2.3 Models of non-invasive stimulation 30
2.3.1 Neuron-field models 31
2.3.2 Head models 32
2.3.3 Multi-scale models 34

2.4 Conclusion 36

Chapter 3

Tools and techniques 37

3.1 Modelling neurons 37

3.1.1 Neuron electrophysiology 37

3.1.2 The Hodgkin-Huxley model 41

3.1.3 Beyond the Hodgkin-Huxley neuron 43

3.1.4 Markov multistate transition models 44

3.1.5 Neural synapses 45

3.2 Physics of transcranial magnetic stimulation 47

3.2.1 Magnetic field generated by the TMS coil 48

3.2.2 Electric field induced in the head 49

3.3 Modelling transcranial magnetic stimulation using SimNIBS 50

3.3.1 Generating head models from MR images 50

3.3.2 Electric field calculation 51

3.4 Conclusion 52

Chapter 4

Model of the cerebellar cortex 53

4.1 Cerebellar model by Katakura et al. 53

4.1.1 Granular layer network model 54

4.1.2 Purkinje cell model 56

4.1.3 Synaptic connections 57

4.1.3.1 Synaptic model 57

4.1.3.2 Mossy fibre to Golgi cells connections 58

4.1.3.3 Golgi cells to granule cells connections 58

4.1.3.4 Granule cells to Golgi cells connections 58

4.1.3.5 Golgi cells to Golgi cells connections 59

4.1.3.6 Purkinje cell connections 60

4.1.3.7 Mossy fibre to granule cell connections 60
4.2 Updated cerebellar cortex model 63
4.2.1 Ionic current notation 64
4.2.2 Granule cell model 65
4.2.3 Golgi cell model 69
4.2.4 Purkinje cell model 73
4.2.4.1 Spine model 75
4.2.4.2 Ionic currents 75
4.2.4.3 Calcium dynamics 80
4.2.4.4 Temperature correction 82
4.2.5 Connectivity 83
4.2.6 Analysis 84
4.3 Results 86
4.4 Discussion 89
4.5 Conclusion 91
Chapter 5
Model of transcranial magnetic stimulation 93
5.1 Reproduced experimental setup 94
5.2 Methods 95
5.2.1 Estimation of the spatial electric field 97
5.2.2 Generation of the time-varying electric field 99
5.2.3 Generation and coupling of the extracellular voltage to the cerebellar model 99
5.2.4 Analysis 102
5.3 Results 103
5.3.1 Coil orientation 104
5.3.2 Electric field in ROI 106
5.3.3 Azimuth angle 107

5.3.4 Stimulation effect at network level 114
5.4 Discussion 117
5.5 Conclusion 120
Chapter 6
Validation method for the model of transcranial magnetic stimulation 121
6.1 Eye movements 121
6.1.1 Saccades 122
6.1.2 Gaze holding 122
6.1.3 Role of the cerebellum 123
6.2 Vertical oculomotor system model 123
6.2.1 Model equations 125
6.2.2 Purkinje cell activation function 126
6.3 Methods 127
6.3.1 Generation of the population response 128
6.3.2 Generation of the activation function 129
6.3.3 Simulation of the vertical oculomotor system model 130
6.4 Results 130
6.5 Discussion 134
6.6 Conclusion 136
Chapter 7
Conclusion 137
7.1 Answers to my research questions 138
7.2 Addressed gaps in the literature 138
7.3 Future work 139
Bibliography 141
Appendix
Research output 163
A.1 CNS*2023, Leipzig 164

A.2 CNS*2024, Natal 167
A.3 CNS*2025, Florence 171
A.4 CNS*2026, Halifax 174
Bibliography 177

List of figures

Figure 1.1 Location of the cerebellum in the brain, with the primary fissure highlighted in red. Image taken from "Primary fissure of cerebellum -- 01" [15], "Primary fissure of cerebellum -- 04" [16] and "Primary fissure of cerebellum -- 05" [17] by BodyParts3D generated by DBCLS and licensed under CC BY-SA 2.1..... 4
Figure 1.2 Subdivision of the cerebellum in its main anatomical regions: anterior (purple), posterior (green) and flocculonodular (orange) lobes. Image taken from “Major Regions of the Cerebellum” [18] by OpenStax College and licensed under CC BY 3.0. 5
Figure 1.3 Circuitry of the cerebellar cortex. Taken from “Cerebellar Circuit.svg” by Tom282f3 [19] and licensed under CC BY-SA 3.0. 7
Figure 1.4 General mechanism of TMS. An electric field is induced in the brain by placing an electromagnetic coil near the scalp. Taken from “Transcranial_magnetic_stimulation_(TMS).png” [32] by Ilovestarbies and licensed under CC BY-SA 4.0. 10
Figure 1.5 Geometry of a double-cone coil. Taken from “Double_cone_coil.jpg” [33] by Baburov and licensed under CC BY-SA 4.0. 11
Figure 2.1 Three layer spherical head model. 32
Figure 2.2 Schematic representation of simple neurons in a cortical sulcus. Figure taken from [232]. 35
Figure 2.3 Model neurons located in the crown of the pre-central gyrus between the grey matter and white matter surfaces. Figure taken from [215]. 35
Figure 3.1 Typical structure of a neuron. Image taken from "Neuron typical structure" [235] by Ajimonthomas and licensed under CC BY-SA 4.0. 38
Figure 3.2 The stages of an action potential:
At rest, sodium (green circles) and potassium (purple triangles) ions are unable to cross the neuron’s membrane.
The neuron depolarises. Sodium ions enter the cell through the sodium ion channels (in green).
The sodium channels close, the potassium channels open (in purple), and potassium ions flow outside the neuron. The neuron repolarises.

Potassium channels close. Potassium and sodium ions are actively transported through the cell membrane via sodium-potassium pumps (in red), restoring the resting potential.
Image taken from "Membrane Permeability of a Neuron During an Action Potential" [240] by CThompson02 and licensed under CC BY-SA 4.0. 39
Figure 3.3 Transition states of voltage-gated sodium channels. At resting potential, the activation gate is closed, so no ions may flow through the channel. When the cell is depolarized, the channel switches to the activated state. In this configuration, sodium ions may flow through the channel. Finally, the channel stops conducting ions since the inactivation gate blocks it. Image taken from "Open and closed conformations of ion channels" [241] by Efazzari and licensed under CC BY-SA 4.0. Modified to add the inactivated state. 41
Figure 3.4 Neuron electrical circuit as proposed by Hodgkin and Huxley. R_{leak} is considered constant, while R_{Na} and R_K vary with the membrane potential and time. Reproduced from [235]. 42
Figure 3.5 Chemical synapse. Image taken from "1225 Chemical Synapse" [246] by Young, KA., Wise, JA., DeSaix, P., Kruse, DH., Poe, B., Johnson, E., Johnson, JE., Korol, O., Betts, JG., & Womble, M. licensed under CC BY 4.0. 46
Figure 3.6 Segmentation and meshing results for “Ernie”, an exemplary subject whose pre-built head model is available on SimNIBS. A: View of the surfaces of the final meshes, including skin, skull, cerebrospinal fluid, grey matter and white matter. B: Coronal and axial slices of the T1-weighted image with the segmented tissue boundaries in red. Image taken from [250]. 51
Figure 4.1 Network architecture of the cerebellar model. Light green dots represent the mossy fibre locations, dark green dots represent Golgi cells soma, dark red dots represent granule cells soma, transparent red dots represent the T-junction and the parallel fibre terminals of each granule cell and blue triangles represent the location of the spines of the Purkinje cell. 54
Figure 4.2 Golgi cell morphology. Soma in black, basolateral dendrites in blue, apical dendrites in green and axon in red. The angles formed by the straight line parallel to the vertical axis passing through the soma and the apical dendrites, $\theta a1$ and $\theta a2$, and the basolateral dendrites, $\theta b1$ and $\theta b2$, are shown. 56
Figure 4.3 Granule cell morphology 66
Figure 4.4 Rotated Purkinje cell morphology 74

Figure 4.5 F-I curve of the Purkinje cell model (blue triangles). Taken from the original modelling study where this Purkinje cell model was proposed [6]. 85
Figure 4.6 Population response of granule (red stars) and Golgi (blue dots) cells obtained simulating the granular layer network with single compartment granule cells. 86
Figure 4.7 Population response of granule (red stars) and Golgi (blue dots) cells obtained simulating the granular layer network with multi-compartment granule cells. 87
Figure 4.8 Passive behaviour of the Purkinje cell when injecting a step current in a spiny dendrite or, when present, into the spine head located at the centre of that dendrite. Voltage traces of the soma (blue), a main dendrite, parent of the clamped spiny dendrite (red), and the current clamped spiny dendrite (green) are shown..... 88
Figure 4.9 F-I curve of the Purkinje cell with one spine per spiny dendrite modelled explicitly (in blue) and F-I curve of the Purkinje cell with all spines modelled explicitly (in red). 89
Figure 5.1 Schematics of TMS model.
A: Left - Estimated electric field in a realistic head model. Right - Location of the region of interest (in red) in the grey matter. Caudal view of the grey matter rotated 10° around the vertical axis and 10° around the horizontal axis for a clearer view of the ROI.
B: Time-varying electric field, showing 1 s of a continuous theta burst pulse.
C: Extracellular potential across a simple neuron model including a soma, an axon and three dendrites. A dipole is generated by coupling the extracellular voltage to the neuron. 96
Figure 5.2 Representation of polar, ϑ, and azimuth, Φ, angles. The blue vector represents the mean electric field in the ROI. The x, y and z axes are the cerebellar network axes, with the z-axis being parallel to the neurons' axons. The polar angle, ϑ, is the angle between the electric field and the z-axis; the azimuth angle, Φ, is the angle between the electric field and the x-axis. 98
Figure 5.3 Placement and orientation of the axes of the cerebellar network in the head model. The white and grey matter surface elements in proximity to the ROI are shown in grey and in pink. The axes of the cerebellar network are placed with the origin in the stimulation target (red dot). The z-axis is aligned with the weighted mean

of the grey and white matter unit normal vectors. The x- and y-axes are oriented arbitrarily. 101
Figure 5.4 Cerebellar network architecture oriented according to the brain structure in the ROI in the head model. The z-axis is parallel to the ascending axons. The x and y-axes are arbitrarily set. 103
Figure 5.5 Coil starting position. The coil handle is pointing downwards. The coil is rotated around its z-axis, in blue in the figure. 104
Figure 5.6 Polar angle (top) and mean electric field magnitude (bottom) for the tested coil orientations. The selected coil orientation is highlighted in red. 105
Figure 5.7 Mean electric field in the ROI. In black the axes of the cerebellar network, in blue the mean electric field unit vector. The network centre, black dot, is located at the stimulation target, [7, −60, −40] in the stereotaxic Talairach coordinate system. ……...106
Figure 5.8 Sagittal section of the grey matter showing the electric field magnitude, in V/m, on the left and the ROI location highlighted with a red dot on the right. 107
Figure 5.9 Instantaneous firing rate of the isolated Purkinje cell, in blue, stimulated by a uniform electric field with magnitude 6.08 V/m. In orange the stimulation pulse, the pulse amplitude is not to scale. The results shown are obtained with an azimuth angle, ϕ, of 30°. ……..…108
Figure 5.10 Instantaneous firing rate, in blue, of the isolated Purkinje cell stimulated with mean electric field magnitude of 6.08 V/m and an azimuth angle, ϕ, of 30°. Best linear fit in red. ……109
Figure 5.11 Coefficient of determination, R2, (top) and root mean square error, RMSE, (bottom) of the best linear fit for the instantaneous firing rate of the isolated Purkinje cell. The cell is stimulated with a uniform electric field of mean magnitude 6.08 V/m. The azimuth angle, ϕ, is varied between 0° and 360° in 10° steps. 110
Figure 5.12 Instantaneous firing rate of the isolated Purkinje cell, in blue, stimulated by a uniform electric field with magnitude 30.4 V/m. In orange the stimulation pulse, the pulse amplitude is not to scale. The results shown are obtained with an azimuth angle, ϕ, of 30°, 200° and 150° from top to bottom. 112
Figure 5.13 Coefficient of determination, R2, (top) and root mean square error, RMSE, (bottom) of the best linear fit for the instantaneous firing rate of the isolated Purkinje cell. The cell is stimulated with a uniform electric field of mean magnitude

30.4 V/m. The azimuth angle, ϕ, is varied between 0° and 360° in 10° steps. The chosen azimuth angle, 30°, is highlighted in red. 113
Figure 5.14 Golgi cell voltage trace at a spike following a stimulation burst. In blue the voltage trace of the Golgi cell stimulated with the low-amplitude condition. In red the voltage trace of the Golgi cell stimulated with the high-amplitude condition. The spikelets present at 600, 620 and 640 ms are caused by the stimulation pulses. .. 115
Figure 5.15 Granule cell voltage trace at a spike following a stimulation burst. In blue the voltage trace of the granule cell stimulated with the low-amplitude condition. In red the voltage trace of the granule cell stimulated with the high-amplitude condition. 115
Figure 5.16 Isolated Purkinje cell voltage trace at a spike following a stimulation burst. In blue the voltage trace of the Purkinje cell stimulated with the low-amplitude condition. In red the voltage trace of the Purkinje cell stimulated with the high-amplitude condition. The spikelets present at 1600, 1620 and 1640 ms are caused by the stimulation pulses. 116
Figure 5.17 Purkinje cell voltage trace at a spike following a stimulation burst. In blue the voltage trace of the Purkinje cell stimulated with the low-amplitude condition. In red the voltage trace of the Purkinje cell stimulated with the high-amplitude condition. The spikelet present at 800 ms is caused by a stimulation pulse..... 117
Figure 6.1 Outline of the vertical oculomotor system model. The model of the cerebellum is highlighted in light grey. Figure taken from [1]..... 124
Figure 6.2 Response of a population of Purkinje cells fitted with a logistic function. In blue, mean firing rate of each Purkinje cell simulation. In red, best logistic fit.
Top (A): Simulations obtained without stimulating the network with the TMS model (baseline condition).
Middle (B): Simulations obtained stimulating the network with the TMS model with an electric field magnitude of 6.08 V/m (low-amplitude stimulation condition).
Bottom (C): Simulations obtained stimulating the network with the TMS model with an electric field magnitude of 30.4 V/m (high-amplitude stimulation condition). 133
Figure 6.3 Activation functions to be used in the vertical oculomotor system model, generated by normalising the best logistic fits (see Figure 6.2). Baseline, low-amplitude stimulation and high-amplitude stimulation conditions are shown in green, blue and red. 133

Figure 6.4 Position and slow phase velocity of predicted eye movements. On the left, target position (dashed line) and predicted eye position (solid line). On the right, predicted slow phase velocity of the eye (solid line) and target position (dashed line, not to scale). In green, predicted eye movements obtained employing the activation function generated without stimulating the network with the TMS model (baseline condition). In blue, predicted eye movements employing the activation function generated stimulating the network with the TMS model with an electric field magnitude of 6.08 V/m (low-amplitude stimulation condition). In red, predicted eye movements employing the activation function generated stimulating the network with the TMS model with an electric field magnitude of 30.4 V/m (high-amplitude stimulation condition). Note that the solid green line is not visible as it is overlayed by the solid blue line. 134

List of tables

Table 2.1 Summary of the reviewed cerebellar models published on ModelDB [43]. 21
Table 2.2 Summary of clinical applications of TMS targeting the cerebellum. The table includes the considered pathology, the TMS intervention protocol, the coil used and the observed effects of the stimulation. 28
Table 4.1 Summary of the modelled cells. Granule, Golgi and Purkinje cells are explicitly modelled. Mossy fibres, stellate cells and basket cells are modelled as Poisson spike trains. 64
Table 4.2 Passive properties of the granule cell for each compartment type. The specific membrane capacitance is expressed in μF/cm^2, the specific membrane conductance is expressed in S/cm^2 and the specific axial resistance is expressed in Ωcm. 66
Table 4.3 Maximum conductance of the ionic currents of the granule cell expressed in μS/cm^2. If the channel is not present in a section, no value for the conductance is given. 67
Table 4.4 Rate constants of the ionic channels of the granule cell. Gating variable dynamics follow equations 4.16 and 4.17. If the steady state of the time constant of the gating variable does not follow equation 4.17, their equation is provided below the rate constants for the corresponding channel. m denotes activating gating variables, h denotes inactivating gating variables. The exponents denote the number of activation and inactivation channels (a and b in equation 4.15). 68
Table 4.5 Temperature at which the ionic currents were recorded. 69
Table 4.6 Maximum conductance of the ionic currents of the Golgi cells expressed in μS/cm^2. 70
Table 4.7 Rate constants of the ionic currents of the Golgi cell. Gating variable dynamics follow equations 4.16 and 4.17. If the steady state of the time constant of the gating variable does not follow equation 4.17, their equation is provided below the rate constants for the corresponding channel. m denotes activating gating variables, h denotes inactivating gating variables. The exponents denote the number of activation and inactivation channels (a and b in equation 4.15). 72

Table 4.8 Passive properties of the Purkinje cell for each compartment type. The specific membrane capacitance is expressed in μF/cm^2, the specific membrane resistance is expressed in Ωcm^2 and the specific axial resistance is expressed in Ωcm. The compensation factors 1.2 and Fd account for the fact that not all spines are explicitly modelled. 74
Table 4.9 Maximum conductance of the ionic currents of the Purkinje cell expressed in μS/cm^2. If the channel is not present in a section, no value for the conductance is given..... 76
Table 4.10 Gating variable dynamics and rate constants of the ionic channels of the Purkinje cell. m denotes activating gating variables, h denotes inactivating gating variables. The exponents denote the number of activation and inactivation channels (a and b in equation 4.15). 79
Table 4.11 Reaction parameters describing the calcium dynamics in relation to the two buffers, calbindin and paravalbumin. 82
Table 4.12 $Q10$ factor and temperature at which the ionic channels were recorded. 83
Table 4.13 Total cell capacitance, in pF, of the Purkinje cell model in the three analysed configurations: without spines, with one spine per spiny dendrite, and with all spines explicitly modelled. 87
Table 5.1 Mean firing rate of Golgi, granule and Purkinje cells in three conditions: the network is not stimulated (no stimulation), the network is stimulated with and electric field magnitude of 6.08 V/m (low-amplitude) and an electric field magnitude of 30.4 V/m (high-amplitude). The mean firing rate of the Purkinje cell is shown both without receiving any synaptic inputs (isolated Purkinje cell) and when receiving the granular layer inputs (Purkinje cell). 114
Table 6.1 Parameters of the best logistic fit of the population response of the Purkinje cells in the three tested conditions, along with the root mean square error (RMSE) and coefficient of determination (R2) of the fit. 131

List of abbreviations

- cTBS: continuous theta burst stimulation
- DTI: diffusion tensor imaging
- F-I: frequency-current
- FEM: finite element method
- MFR: mean firing rate
- R2: coefficient of determination
- RMSE: root mean square error
- ROI: region of interest
- rTMS: repetitive transcranial magnetic stimulation
- TMS: transcranial magnetic stimulation

Chapter 1

Introduction

The objective of this research is to expand the current knowledge on the feasibility of non-invasive neurostimulation to treat neurological disorders linked to cerebellar pathologies via a computational approach. I focused on developing a computational framework that integrates a model of the cerebellar cortex, a model of transcranial magnetic stimulation (TMS) and a validation method for the latter.

1.1 Scope

Transcranial magnetic stimulation (TMS) is a promising technique to alleviate symptoms related to cerebellar pathologies. Being able to obtain therapeutic outcomes without invasive methods is revolutionary. However, the outcomes of the stimulation are variable and it is not understood how neurons are affected by it. Many models, at different scales, have been developed to try to address the many open questions on the functioning of TMS. In this work I focus on continuous theta burst stimulation (cTBS) targeting the cerebellar cortex in the vermis. In particular, I focus on how the stimulation affects Golgi, granule and Purkinje cells.

I developed a detailed, biologically plausible model of the cerebellar cortex, which includes Golgi, granule and Purkinje cells. I analysed its baseline activity to ensure it reproduces key behaviours seen in experimental data.

I stimulated the cerebellar network with a TMS model. I estimated the electric field induced in a realistic head model by a TMS pulse. I simulated a cTBS protocol by multiplying the estimated electric field with a cTBS pulse. I calculated the extracellular voltage generated by the stimulation and coupled it to the cerebellar network.

I developed a validation method for the transcranial stimulation model, by linking the output of the cerebellar cortex to a measurable behaviour - eye movements. I validated the transcranial stimulation model by comparing predicted eye movements in baseline conditions versus eye movements in stimulated conditions with experimental measures.

1.1.1 Research questions

The following three research questions are addressed in this work:

1. Are the neurons in the cerebellar vermis, lobules VI–VII, affected by TMS?
2. How does a cTBS protocol affect the neurons in terms of mean firing rate, instantaneous firing rate and spike timing?
3. Is a vertical oculomotor system model [1] suitable as a validation method for transcranial stimulation models targeting the cerebellum?

The term neurons in research questions 1 and 2, refers to granule, Golgi and Purkinje cells. Research questions 1 and 2 will be discussed in Chapter 5, research question 3 will be discussed in Chapter 6.

1.1.2 Contributions to knowledge

I addressed the following gaps in the field:

1. **The lack of a biologically realistic model of the cerebellar cortex.** To tackle this, I further developed Katakura et al.'s cerebellar model [2]. It is made up of the granular layer model by Sudhakar et al. [3] connected to the De Schutter & Bower Purkinje cell [4], [5]. I have updated it by employing a more recent Purkinje cell model by Zang et al. [6] and by switching the single compartment granule cells in the granular layer model to multi-compartment neurons [7]. This is discussed in Chapter 4.
2. **The lack of a multi-scale non-invasive stimulation model including synaptic connections.** To tackle this, I excited my cerebellar model with an electric field estimated by an MRI-generated head model. This is discussed in Chapter 5.
3. **The lack of validation methods for non-invasive stimulation models.** To tackle this, I linked the output of the cerebellar model to a measurable behaviour - slow phase velocity eye movements. This step serves as a validation method for the non-invasive stimulation model, ensuring its accuracy and reliability. This is discussed in Chapter 6.

1.1.3 Research outputs

During my PhD I have presented posters at the following conferences:

- 32nd Annual Computational Neuroscience Meeting (CNS*2023 Leipzig) [8], describing the model of the cerebellar cortex;

- 33th Annual Computational Neuroscience Meeting (CNS*2024 Natal) [9], describing the model of slow phase velocity eye movements;
- 34th Annual Computational Neuroscience Meeting (CNS*2025 Florence) [10], describing the preliminary model of transcranial stimulation;
- 35th Annual Computational Neuroscience Meeting (CNS*2026 Halifax), describing the model of transcranial stimulation and its validation. At the time of writing this dissertation, this abstract is under review;
- Italian Network for Computational and Theoretical Neuroscience Conference in 2024 and 2025.

The abstracts submitted to the Annual Computational Neuroscience Meetings are included in the appendix.

1.1.4 Code availability

Code for the cerebellar model, the TMS model and the vertical oculomotor system model, as well as code for data analysis and visualization will be available at https://github.com/EleBern/TMS_cerebellum once this work is published.

1.1.5 Dissertation structure

This work is divided as follows:

- The rest of Chapter 1 gives an introduction on the cerebellum and transcranial magnetic stimulation;
- Chapter 2 reviews the current state of the art and the main limitations relevant to the projects presented in this dissertation;
- Chapter 3 introduces the background information and tools and techniques needed to understand the rest of this dissertation;
- Chapter 4 outlines the biologically realistic model of the cerebellar cortex;
- Chapter 5 outlines the transcranial magnetic stimulation model and its coupling to the cerebellar model;
- Chapter 6 outlines the validation method for the transcranial stimulation model;
- Chapter 7 summarises my findings and suggests future work.

1.2 The cerebellum

The cerebellum, Latin for “little brain,” contains around one-half of the brain’s neurons, even though it makes up only 10% of its volume [11], [12]. It is a structure located at the back of the head, below the temporal and occipital lobes and above the brainstem (see Figure 1.1) [11]. It is well known for its involvement in motor control [11], [12], and increasing evidence shows it is also involved in cognitive aspects [11], [13]. Lesions to it can cause severe impairments and disorders such as hypotonia, ataxia, intention tremor and incoordination [12], [14].

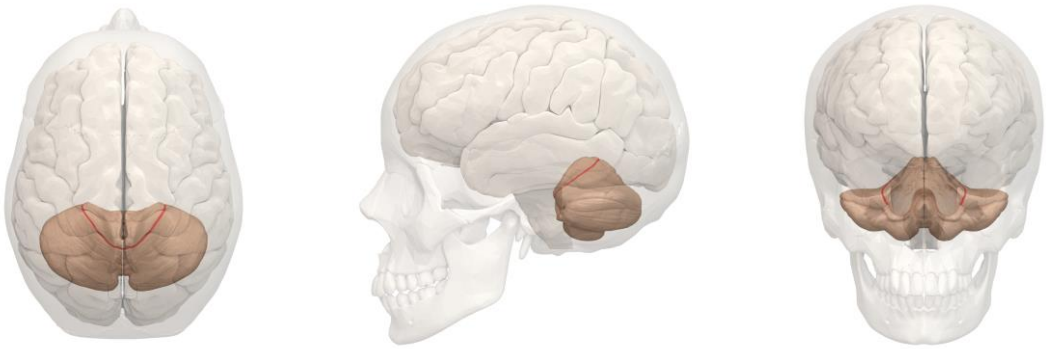


Figure 1.1 Location of the cerebellum in the brain, with the primary fissure highlighted in red. Image taken from "Primary fissure of cerebellum -- 01" [15], "Primary fissure of cerebellum -- 04" [16] and "Primary fissure of cerebellum -- 05" [17] by BodyParts3D generated by DBCLS and licensed under CC BY-SA 2.1.

The following subsections are all informed by the book “Principles of neural science” [14], unless stated otherwise.

1.2.1 Anatomy of the cerebellum

The cerebellum is composed of two main parts: the deep nuclei, which are the main output of the cerebellum, and the cerebellar cortex, a densely populated structure that provides input to the nuclei.

The cerebellum is divided into three lobes by two transverse fissures (see Figure 1.2): the primary fissure divides the cerebellum in the anterior and posterior lobes; the posterolateral fissure separates the flocculonodular lobe from the anterior and posterior lobes. In the orthogonal direction, the cerebellum can be divided into the vermis and two lateral hemispheres by two sulci.

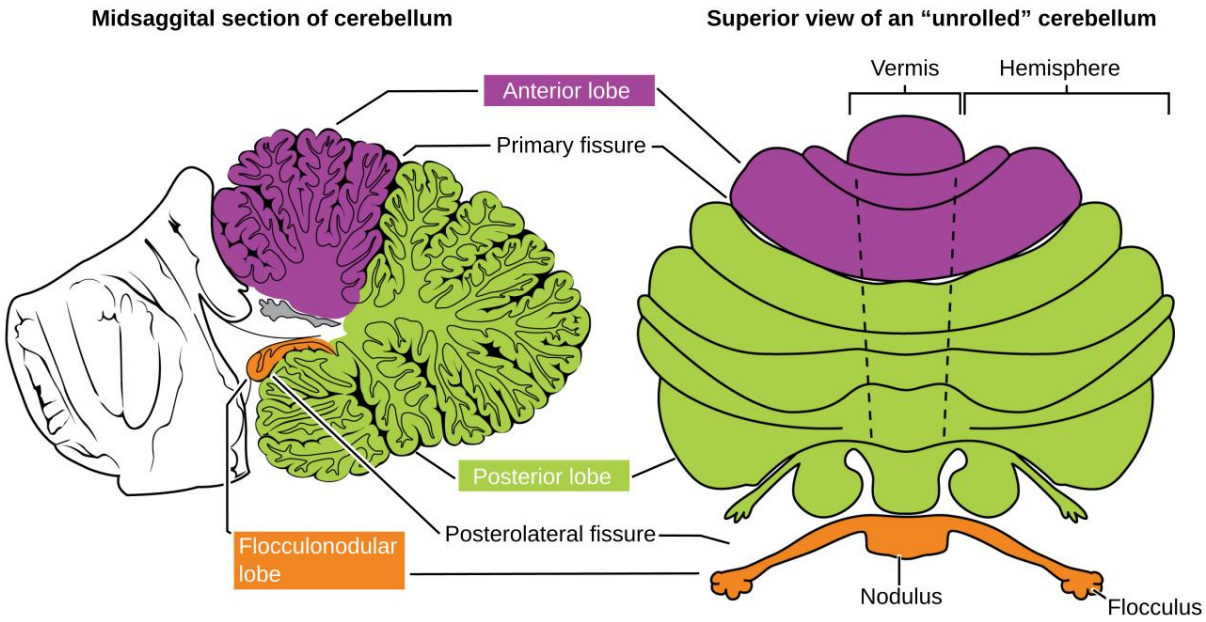


Figure 1.2 Subdivision of the cerebellum in its main anatomical regions: anterior (purple), posterior (green) and flocculonodular (orange) lobes. Image taken from “Major Regions of the Cerebellum” [18] by OpenStax College and licensed under CC BY 3.0.

There are three deep nuclei in the cerebellum: the fastigial nucleus, the interposed nuclei and the dentate nucleus. The fastigial nucleus receives inputs from the vermis and projects to cortical and brain stem regions that control proximal muscles. The interposed nuclei, composed of the emboliform and the globose nuclei [11], receive inputs from the medial areas of the cerebellar hemispheres and project to systems that control distal muscles of the limbs and digits. The dentate nucleus receives inputs from the lateral areas of the cerebellar hemispheres and projects to the motor, premotor and prefrontal cortex via the thalamus.

1.2.2 Cerebellar cortex

The cerebellar cortex is a convoluted structure characterised by many parallel folds called folia. It is a highly ordered structure composed of three layers: the granular layer, the Purkinje layer and the molecular layer (see Figure 1.3 for a schematic representation of the cerebellar cortex).

The granular layer is the innermost layer and contains primarily Golgi and granule cells. Golgi cells are inhibitory neurons that modulate the activity of granule cells. Granule cells are small but extremely numerous neurons - in the order of 50 billion in humans - and the only excitatory neurons in the cerebellar cortex. The axons of

granule cells ascend to the molecular layer, where they bifurcate in T-junctions giving rise to parallel fibres. Parallel fibres run along the molecular layer parallel to the folia and excite the interneurons found in the molecular layer.

The Purkinje layer contains the somata of the Purkinje cells. Purkinje cells are the sole output of the cerebellar cortex; their axons project to the deep cerebellar nuclei and to the brain stem. Purkinje cells have a rich dendritic tree which expands mostly in a plane in the molecular layer, perpendicular to the direction of parallel fibres. This characteristic structure allows ascending axons of a granule cell to make many synaptic contacts with a Purkinje cell, and allows the parallel fibres to make synaptic contacts with Purkinje cells far from the granule cell's soma. This allows granule cells to distribute information to a large number of distributed Purkinje cells.

The molecular layer is the outermost layer and contains the parallel fibres and the dendritic trees of the Purkinje cells, as well as two interneurons: stellate and basket cells. Both these interneurons are excited by parallel fibres and modulate the activity of Purkinje cells.

The cerebellar cortex receives its main afferent inputs through climbing fibres and mossy fibres, both of which are excitatory. Mossy fibres stem from the spinal cord and brain stem; their terminals synapse with granule cells in masses of nerve fibre terminals called glomeruli in the granular layer. They relay sensory information to granule cells. A single granule cell is contacted by few mossy fibres, but the mossy fibre inputs are distributed to a large number of Purkinje cells - each Purkinje cell receives inputs from 10^5 to 10^6 granule cells.

Climbing fibres are fibres that wrap around Purkinje cells, "climbing" up their soma and dendrites. This allows a climbing fibre to make multiple synapses with a Purkinje cell. Due to this, climbing fibres have a strong influence on the activity of Purkinje cells - climbing fibre inputs cause complex spikes in the Purkinje cell, a burst characterised by a first large-amplitude spike, followed by high-frequency lower amplitude spikes. Climbing fibres stem from the inferior olivary nucleus and relay sensory information to Purkinje cell dendrites. A Purkinje cell is only contacted by one climbing fibre, but one climbing fibre may contact up to ten Purkinje cells.

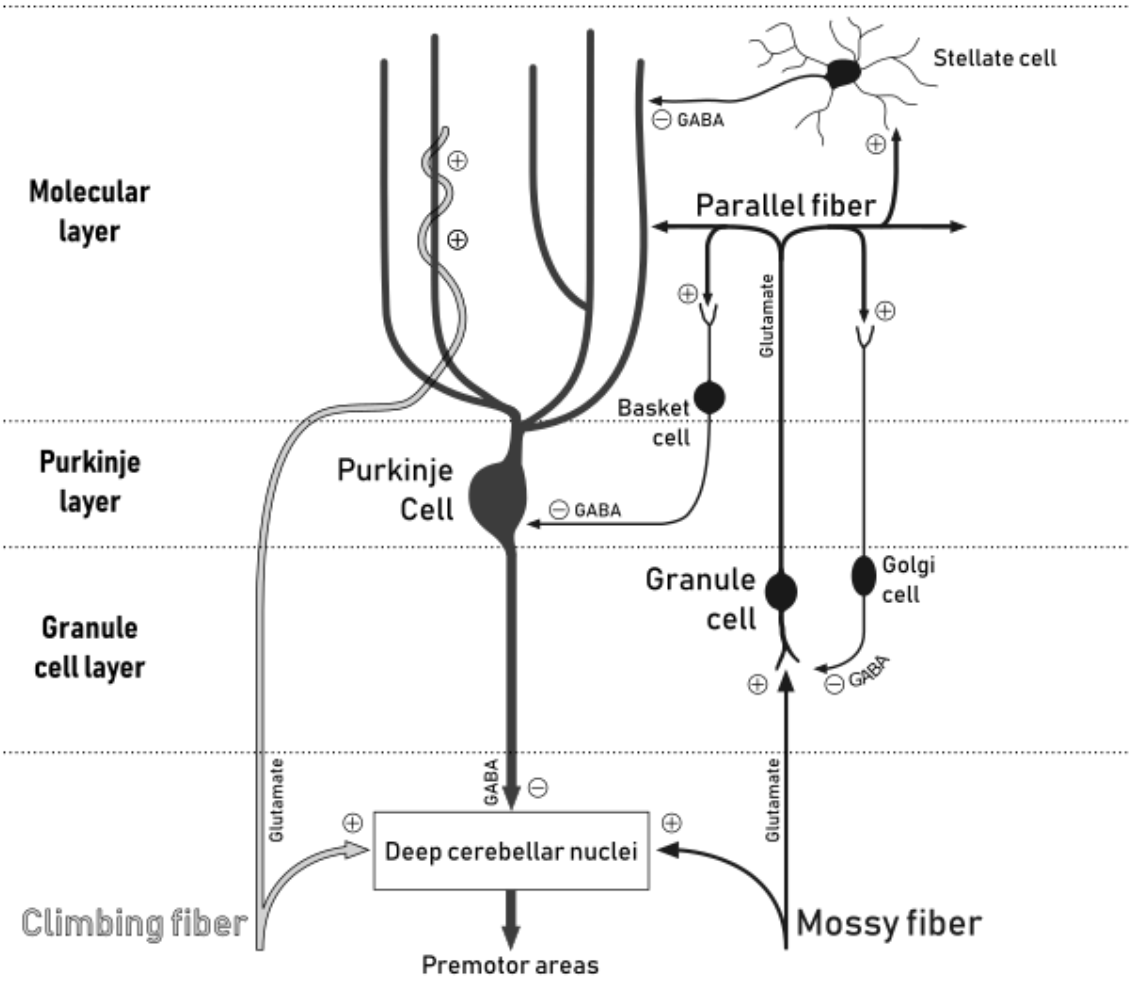


Figure 1.3 Circuitry of the cerebellar cortex. Taken from “Cerebellar Circuit.svg” by Tom282f3 [19] and licensed under CC BY-SA 3.0.

1.2.3 Functional roles of the cerebellum

The cerebellum is most commonly associated with motor control; however, it also plays a crucial role in cognitive [13], [14] and affective processes [13]. Accumulating evidence indicates that the cerebellum contributes to executive functions, linguistic skills, and also emotional control [13]. Consistent with these findings, cerebellar lesions have been linked not only to motor impairments but also to non-motor disorders, including autism spectrum disorders [13] and schizophrenia [20].

Different regions of the cerebellum account for different functional roles. The cerebellum is commonly divided into three functional subdivisions: the vestibulocerebellum, the spinocerebellum and the cerebrocerebellum. The

vestibulocerebellum comprises the floccular lobe, which mostly receives vestibular inputs. It primarily influences vestibular reflexes through its projections to the vestibular nuclei in the brain stem. It is involved in controlling axial muscles and limb extensors to assist in balance. As it also receives visual inputs, it also plays an important role in controlling eye movements, in particular smooth pursuit, and in coordinating head and eye movements.

The spinocerebellum is composed of the vermis and the medial parts of the cerebellar hemispheres. It mainly receives inputs from the spinal cord. In particular, the vermis primarily processes somatosensory and vestibular inputs from the proximal body and head, while the intermediate cerebellar hemispheres process inputs from the distal body regions, such as the limbs. The spinocerebellum projects to cortical and brain stem regions via the fastigial and interposed nuclei. It influences posture and locomotion by influencing both proximal and distal muscles. Given it receives head-related somatosensory inputs, the vermis also plays an important role in controlling eye movements, including saccades and smooth pursuit, especially within lobules V to VII.

The cerebellum is thought to influence movement by constructing internal kinematic and dynamic models of the body and using these models within a feedback control framework to achieve precise motor output. The spinocerebellum receives information about the external environment, the current state of the body through muscle and joint receptors, and planned motor commands. This enables the cerebellum to compare intended and executed movements, generate an error signal, and adjust motor output to minimise discrepancies and achieve the desired movement.

The cerebrocerebellum comprises the lateral parts of the cerebellar hemispheres. These areas are primarily connected to the cerebral cortex via the pontine nuclei and the thalamus. In particular, the cerebrocerebellum projects to the motor, pre-motor and prefrontal cortical areas. This area of the cerebellum is involved in the planning and execution of movement, as well as in higher-order cognitive functions attributed to the cerebellum, including motor learning, language, and working memory.

1.3 Non-invasive neurostimulation

Non-invasive neurostimulation of the cerebellum is a promising technique that could be beneficial for people suffering from cerebellar deficits [21], [22], [23]. Several studies are starting to demonstrate that neuromodulation of the cerebellum may have positive therapeutic outcomes [21], [22], [24], [25]. However, research in this field provides contrasting evidence of the effects that non-invasive stimulation has on the cerebellum, and there are still many limitations and open questions [21], [26], [27]. This is partly the result of not having a standard stimulation method and protocol [26]. Further limitations of non-invasive neurostimulation techniques include the large level of inter-individual variability [23], [25], the lack of an in depth study of the side effects [21] and the limited understanding of the influence that this stimulation has on the target neurons [26], [28], [29], [30].

The most widely used non-invasive neurostimulation technologies are transcranial magnetic stimulation (TMS) and transcranial electrical stimulation, in particular direct current stimulation [23], [27]. As the design of the model presented in this dissertation was informed by the experimental protocol planned within the group of Dr Barry Seemungal at Imperial College London, in this work I have focused on TMS.

1.3.1 Transcranial magnetic stimulation

The following section is informed by the book chapter Transcranial Magnetic Stimulation: Principles and Applications [31], unless stated otherwise.

Transcranial magnetic stimulation (TMS) is a non-invasive technique used to stimulate the brain. It operates by inducing an electric field within the brain through the placement of an electromagnetic coil on the scalp (see Figure 1.4). A rapidly changing current passes through the coil, generating a magnetic field that, in turn, induces an electric field in the underlying neural tissue. This induced electric field modulates neuronal ionic currents and, if sufficiently strong, can depolarise neurons and trigger action potentials. A more detailed discussion of the physical principles underlying TMS is provided in Section 3.2. TMS has been widely applied in research, diagnostics, and clinical treatment. It is a safe and well-tolerated technique that has been used for over three decades to modulate cortical excitability and is increasingly being applied in

therapeutic contexts and to non-cortical brain regions, such as the cerebellum [21], [23].

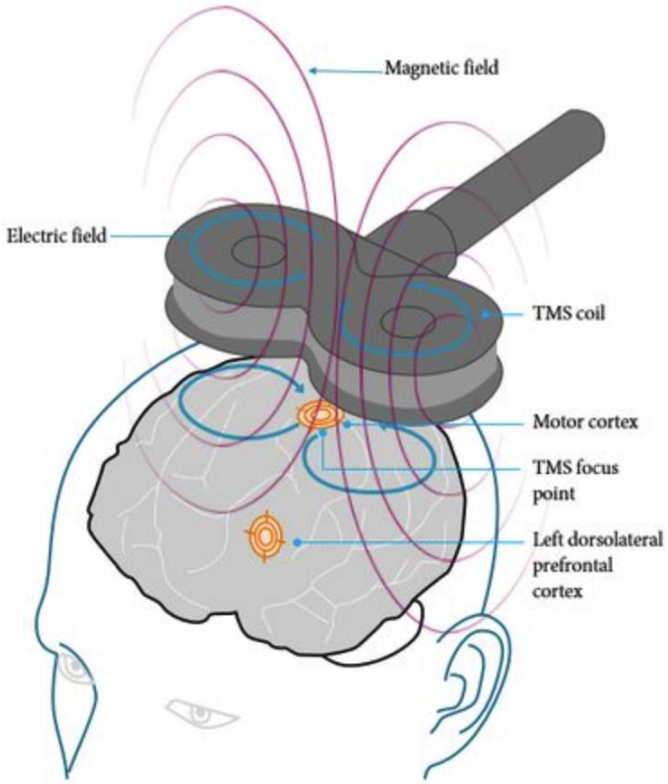


Figure 1.4 General mechanism of TMS. An electric field is induced in the brain by placing an electromagnetic coil near the scalp. Taken from “Transcranial_magnetic_stimulation_(TMS).png” [32] by Ilovestarbies and licensed under CC BY-SA 4.0.

The first TMS device was developed by Anthony Barker in 1985. Modern TMS systems consist of two main components: a pulse generator and an electromagnetic coil. The pulse generator produces the stimulation pulses, which can vary in waveform and amplitude depending on the selected protocol. The electromagnetic coil determines the spatial distribution of the induced electric field, which is shaped by the coil’s geometry and its position relative to the scalp.

Depending on the design of the pulse generator, TMS pulses may be monophasic, biphasic, or have more flexible waveforms. Several coil designs are available. The simplest is the circular coil, which induces a broadly distributed, circular electric field in the head. To achieve greater focality, figure-of-eight coils were developed. These coils consist of two adjacent circular windings with currents flowing in opposite directions, producing a peak electric field at the intersection of the two windings. A

variation of this design is the double-cone coil (see Figure 1.5), in which the two windings have a larger diameter and are angled relative to each other. This configuration increases the depth of stimulation at the expense of reduced focality.



Figure 1.5 Geometry of a double-cone coil. Taken from “Double_cone_coil.jpg” [33] by Baburov and licensed under CC BY-SA 4.0.

TMS pulse generators require high energy and power levels, which limits the range of achievable stimulation protocols and contributes to the size and complexity of the equipment. In addition, stimulation coils can heat rapidly; therefore, coils designed for repetitive stimulation typically incorporate active cooling systems. Despite these engineering constraints, a wide range of TMS protocols has been developed. Stimulation can be delivered as single pulses, paired pulses, or repetitive pulse trains, resulting in numerous possible protocol combinations.

Single-pulse TMS is commonly used to determine a subject’s motor threshold, defined as the minimum stimulus intensity required to elicit a motor-evoked potential of 50 μV peak-to-peak amplitude. Subsequent stimulation is often administered at a specified percentage of this threshold. In paired-pulse TMS, a conditioning stimulus is followed by a test stimulus after a short inter-stimulus interval. Depending on this interval, the response to the test stimulus may be facilitated or inhibited relative to a single-pulse response, allowing researchers to study intracortical connectivity, excitability, and inhibition.

Repetitive TMS (rTMS) consists of trains of pulses delivered at a specified frequency. Whereas single pulse and paired-pulse TMS produce only transient effects, rTMS can induce longer-lasting changes. In general, low-frequency rTMS (approximately 1 Hz) is associated with inhibitory effects, whereas high-frequency rTMS (typically 5–20 Hz) tends to produce excitatory effects. More complex temporal patterns can be used to enhance these effects, such as theta-burst stimulation, in which bursts of three pulses at 50 Hz are repeated at 5 Hz.

At the neuronal level, TMS can both alter the neuron's firing rate, but also induce sub-threshold responses such as altering the membrane resting potentials and thresholds [34]. It is generally assumed that a higher electric field magnitude will elicit a higher response in the neurons [34]. However, this is rather simplistic. For example, the angle between the neurons and the electric field can have a great impact on the outcomes of the stimulation [34]. This means that the orientation of the gyri and sulci as well as the neurons' morphologies will influence the efficacy of the stimulation [34]. As a result, the effects of the stimulation are highly patient specific.

TMS is widely used in neuroscience research, to study the roles of different brain regions and to explore the effects of specific stimulation protocols. In clinical settings, TMS serves both diagnostic and therapeutic purposes. At present, TMS has been approved by the U.S. Food and Drug Administration for the treatment of depression and obsessive-compulsive disorders, as well as for the alleviation of migraine symptoms.

1.4 Conclusion

In this chapter I introduced my research focus, my research outputs and provided an introduction on the cerebellum and transcranial magnetic stimulation. In the next chapter I will review the current state of the art and the main limitations relevant to the projects presented in this dissertation, including approaches to modelling the cerebellum and transcranial stimulation and the applications of transcranial magnetic stimulation targeting the cerebellum.

Chapter 2

Literature Review

This chapter reviews the current state of the art and the main limitations relevant to the projects presented in this dissertation. First, I describe existing approaches to modelling the cerebellum. Next, I review applications of transcranial magnetic stimulation targeting the cerebellum, with a particular focus on the cerebellar vermis. Finally, I present and discuss different modelling approaches used to simulate transcranial stimulation.

2.1 Models of the cerebellum

“All models are wrong, but some are useful” is a quote attributed to British statistician George E. P. Box [35] and it is particularly fitting in the context of computational neuroscience. The scale and complexity of the brain make complete biological realism unattainable in computational models. For example, the mouse brain contains on the order of 70 million neurons, whereas the human brain contains approximately 86 billion neurons [36]. Moreover, the human cerebral cortex alone contains an estimated 150×10^{12} synapses [37]. Each neuron has a unique morphology, a distinct set of ionic currents, and specific neurotransmitters, resulting in an extraordinary level of biological complexity.

Despite accounting for only about 10% of the brain’s total mass, the human cerebellum contains more than 50% of all neurons in the brain [36]. Accurately reproducing the entire cerebellum in silico, or even a single cerebellar lobe, is therefore not feasible. Instead, models must approximate the real system through informed simplifications and assumptions. A useful model must balance biological realism and computational tractability: it should be sufficiently detailed to capture the dynamics of interest, yet simple enough to avoid prohibitive computational costs.

The cerebellum, with its highly regular and stereotyped structure, is particularly well suited to computational modelling. Fifty years ago, the Marr–Albus–Ito theory was developed and it represents one of the most influential computational frameworks for understanding cerebellar function. Initially proposed in theoretical form by David Marr

[38] and James S. Albus [39], and later refined through experimental work by Masao Ito [40], the theory conceptualizes the cerebellar cortex as a supervised learning system that supports adaptive motor control.

Marr first proposed that learning in the cerebellar cortex arises through facilitation of synapses between parallel fibres and Purkinje cells driven by climbing fibre activity [38]. Building on Marr's theoretical framework, Albus suggested that the cerebellar cortex functions as a pattern-recognition device analogous to a perceptron, proposing an error-driven modification of parallel fibre to Purkinje cell synapses [39]. Experimental work by Ito and colleagues [40] demonstrated that coincident activation of climbing fibres and parallel fibres induces long-term depression at parallel fibre to Purkinje cell synapses. This synaptic learning rule provides a plausible cellular mechanism through which error signals conveyed by climbing fibres can guide adaptive changes in cerebellar circuitry during motor learning.

Since then, researchers have developed numerous computational models of the cerebellum to better understand its function [14], [41], [42]. For this dissertation, I reviewed published cerebellar models available on the database ModelDB [43], focusing on entries corresponding to the cerebellum and its principal cell types. Specifically, the search included the following categories:

- Species or Region
    - *Cerebellum*
- Cell type
    - *Cerebellum deep nucleus neuron*
    - *Cerebellum golgi cell*
    - *Cerebellum interneuron Golgi GABA cell*
    - *Cerebellum interneuron granule GLU cell*
    - *Cerebellum interneuron stellate GABA cell*
    - *Cerebellum Purkinje GABA cell*.

Duplicate models listed under multiple categories were removed, resulting in a total of 63 unique published models. These models are summarised in Table 2.1, which indicates whether each model represents a single neuron or a network, the types and number of cells included, and the modelling approach employed. The final six models listed in the table do not represent neurons or networks, but instead focus on finer-scale structures, such as synapses, dendritic spines, or protein kinetics associated with synaptic plasticity.

Authors	Network, single cells or mechanism	Modelled cells/ mechanism	Number of cells in network	Model type
Masoli et al, 2015 [44]	Single cell	Purkinje cell	Not applicable	Multi-compartment cell with 16 Hodgkin-Huxley like currents
Brown et al, 2011 [45]	Single cell	Purkinje cell	Not applicable	Multi-compartment cell with Hodgkin-Huxley like currents. Focus on reducing the number of compartments while preserving physiological behaviour
Forrest, 2015 [46]	Single cell	Purkinje cell	Not applicable	Two-compartment cell with 21 Hodgkin-Huxley like currents
Anwar et al, 2014 [47]	Single cell	Purkinje cell	Not applicable	Multi-compartment cell with Hodgkin-Huxley like potassium and calcium currents. Detailed calcium dynamics
Akemann et al, 2009 [48]	Single cell	Purkinje cell	Not applicable	Single compartment cell with six Hodgkin-Huxley like currents
Cirtala and De Schutter, 2024 [49]	Single cell	Purkinje cell	Not applicable	Multi-compartment cell with Hodgkin-Huxley like currents. Each dendritic branch has its specific ion channel conductance densities
Masoli et al, 2024 [50]	Single cell	Purkinje cell	Not applicable	Multi-compartment cell with Hodgkin-Huxley like currents. Cell morphology taken from a human Purkinje cell

Buchin et al, 2016 [51]	Single cell	Purkinje cell	Not applicable	Exponential integrate-and-fire model with adaptation
Gallimore et al, 2018 [52]	Single cell	Purkinje cell	Not applicable	Single compartment cell with Hodgkin-Huxley like currents. Models synaptic plasticity at parallel fibre to Purkinje cell synapses
Zang and De Schutter, 2021 [53]	Single cell	Purkinje cell	Not applicable	Multi-compartment cell with Hodgkin-Huxley like currents with the addition of climbing fibre inputs
Masoli and D'Angelo, 2017 [54]	Single cell	Purkinje cell	Not applicable	Multi-compartment cell with Hodgkin-Huxley like currents. Updates [44] to account for synaptic inputs to dendrites and to reproduce in vivo experiments
Anwar et al, 2013 [55]	Single cell	Purkinje cell	Not applicable	Multi-compartment cell with Hodgkin-Huxley like currents. Markov model for calcium channels
Marasco et al, 2013 [56]	Single cell	Purkinje cell	Not applicable	Multi-compartment cell with Hodgkin-Huxley like currents. Focus on reducing the geometrical complexity while accurately preserving the effects of arbitrarily located synaptic inputs
Cannon et al, 2010 [57]	Single cell	Purkinje cell	Not applicable	Multi-compartment cell with currents modelled with Markov models
Zang et al, 2018 [6]	Single cell	Purkinje cell	Not applicable	Multi-compartment cell with Hodgkin-Huxley like currents with detailed calcium dynamics
Akemann and Knöpfel, 2006 [58]	Single cell	Purkinje cell	Not applicable	Single compartment cell with Hodgkin-Huxley like currents. Extension of [59] including different types of sodium and potassium currents

Khaliq et al, 2003 [60]	Single cell	Purkinje cell	Not applicable	Multi-compartment cell with Hodgkin-Huxley like currents with one Markov model current
Anwar et al, 2012 [61]	Single cell	Purkinje cell	Not applicable	Single compartment cell with Hodgkin-Huxley like currents. Includes detailed calcium diffusion and buffering models
Genet et al, 2010 [62]	Single cell	Purkinje cell	Not applicable	Single compartment cell with Hodgkin-Huxley like currents, including calcium dynamics
Vetter and Häusser, 2001 [63]	Single cell	Purkinje cell	Not applicable	Multi-compartment cell with two Hodgkin-Huxley like currents
Couto et al, 2015 [64]	Single cell	Purkinje cell	Not applicable	Multi-compartment cell with Hodgkin-Huxley like currents with the inclusion of voltage fluctuations caused by ion channel noise
Reed and Blackwell, 2021 [65]	Single cell	Purkinje cell	Not applicable	Multi-compartment cell with Hodgkin-Huxley like currents. Focus on correct reconstruction of the dendritic tree and predicting the dendritic diameter from published neuron morphologies
Diwakar et al, 2009 [7]	Single cell	Granule cell	Not applicable	Multi-compartment cell with eight Hodgkin-Huxley like currents, including calcium dynamics in the soma
Gall and Dupont, 2019 [66]	Single cell	Granule cell	Not applicable	Single compartment cell with four Hodgkin-Huxley like currents
Rössert et al, 2014 [67]	Single cell	Granule cell	Not applicable	Single compartment cell with nine Hodgkin-Huxley like currents, including calcium dynamics
Masoli et al, 2020 [68]	Single cell	Granule cell	Not applicable	Multi-compartment cell with Hodgkin-Huxley like currents able to generate diverse response patterns

Dover et al, 2016 [69]	Single cell	Granule cell	Not applicable	Multi-compartment cell with ten Hodgkin-Huxley like currents
Gabbiani et al, 1994 [70]	Single cell	Granule cell	Not applicable	Multi-compartment cell with six Hodgkin-Huxley like currents in the soma
Solinas et al, 2007 [71]	Single cell	Golgi cell	Not applicable	Multi-compartment cell with eight Hodgkin-Huxley like currents. All compartments except the soma are passive
Masoli et al, 2020 [72]	Single cell	Golgi cell	Not applicable	Multi-compartment cell with 13 Hodgkin-Huxley like currents. Includes calcium dynamics modelled with Markov models
Geminiani et al, 2018 [73]	Single cell	Golgi cell	Not applicable	Extended generalized leaky integrate-and-fire neuron
Pali et al, 2025 [74]	Single cell	Golgi cell	Not applicable	Multi-compartment cell which includes synaptic plasticity at mossy fibre to Golgi cell connections
Luthman et al, 2011 [75]	Single cell	Deep cerebellar nucleus cell	Not applicable	Multi-compartment cell with Hodgkin-Huxley like currents including short term depression at Purkinje cell to deep cerebellar nucleus cell synapses
Steuber et al, 2011 [76]	Single cell	Deep cerebellar nucleus cell	Not applicable	Multi-compartment cell with six Hodgkin-Huxley like currents, including calcium dynamics
Masoli et al, 2025 [77]	Single cell	Basket cell	Not applicable	Multi-compartment cell with Hodgkin-Huxley like currents
Rizza et al, 2021 [78]	Single cell	Stellate cell	Not applicable	Multi-compartment cell with 14 Hodgkin-Huxley like and Markov model currents, including calcium dynamics
Szoboszlay et al, 2016 [79]	Network	Golgi cell	2	Multi-compartment passive cells connected via gap junctions

Zhang and Santaniello, 2019 [80]	Network	Olivocerebellar and thalamo-cortical loop. Modelled Purkinje and granule cells	425 cells in total, 265 cerebellar neurons	Single compartment cells with Hodgkin-Huxley like currents
Casellato et al, 2014 [81]	Network	Inferior olive neurons, granule cells, deep cerebellar nuclei cells, Purkinje cells	1580	Spiking neural network
Rössert et al, 2015 [82]	Network	Granule cells	1000	Firing rate model
Yamazaki and Tanaka, 2007 [83]	Network	Golgi and granule cells	1024 Golgi and 102400 granule cells	Single compartment leaky integrated and fire neurons
Maex and De Schutter, 1998 [84]	Network	Golgi and granule cells	Less than 30000	Single compartment cells with Hodgkin-Huxley like currents
Romano et al, 2025 [85]	Network	Cortical, thalamic and cerebellar populations	1 equation per population	Neural mass model
Zhang et al, 2021 [26]	Network	Purkinje, granule and deep cerebellar nuclei cells	3	Multi-compartment cells with Hodgkin-Huxley like currents
Garrido et al, 2013 [86]	Network	Granule, Golgi, Purkinje and deep cerebellar nuclei cells and interneurons	1 equation per cell type	Firing rate model
Luque et al, 2014 [87]	Network	Granular layer, Purkinje layer, mossy fibres, deep cerebellar nuclei	1 equation per layer	Firing rate model
Sudhakar et al, 2017 [3]	Network	Granule and Golgi cells	> 100,000	Multi-compartment Golgi cells, single compartment granule cells. Both with Hodgkin-Huxley like currents
Ma et al, 2020 [88]	Network	Purkinje cell, stellate cells	3	Multi-compartment cells with Hodgkin-Huxley like currents

Yousif et al, 2020 [89]	Network	Cortex, thalamus, deep cerebellar nuclei, globus pallidus, subthalamic nucleus, inhibitory reticular nucleus	1 equation per population	Neural mass model
Zang et al, 2020 [90]	Network	Purkinje cells	100	Multi-compartment cells with Hodgkin-Huxley like currents
Vervaeke et al, 2010 [91]	Network	Golgi cells	2 or more	Multi-compartment cells with Hodgkin-Huxley like currents
Cayco-Gajic et al, 2017 [92]	Network	Granule cells	Not stated	Comparison of integrate and fire cells and a firing frequency model
Luque et al, 2019 [93]	Network	Mossy fibres, granule cells, medial vestibular nuclei, Purkinje cells, and inferior olive cells	~2100	Single compartment Purkinje cells with Hodgkin-Huxley like currents. Leaky integrated and fire model for the other neurons
Hariani et al, 2023 [94]	Network	Unipolar brush cells	2	Single compartment cells with Hodgkin-Huxley like currents
Clopath et al, 2014 [95]	Network	Granule and Purkinje cells	100	Firing rate model
Yamazaki et al, 2015 [96]	Network	Mossy fibres, granule cells, Purkinje cells, climbing fibres, molecular layer interneurons, vestibular nuclear neurons	1 equation per population	Firing rate model
Traub et al, 2008 [97]	Network	Purkinje cell	1000	Multi-compartment cells with Hodgkin-Huxley like currents
Doi et al, 2005 [98]	Dendritic Purkinje cell spine	Not applicable	Not applicable	Kinetic model of calcium dynamics within a Purkinje dendritic spine
Lee et al, 2009 [99]	Synapse model	Not applicable	Not applicable	Intracellular biochemical processes of synaptic short-term plasticity.

Antunes and De Schutter, 2012 [100]	LTD model	Not applicable	Not applicable	Detailed kinetic model of the signalling and trafficking network involved in the induction of cerebellar LTD
Pinto et al, 2020 [101]	Biochemical model	Not applicable	Not applicable	Ordinary differential equations describing interactions of intracellular components
Hepburn et al, 2017 [102]	Biochemical model	Not applicable	Not applicable	Michaelis-Menten formulation of protein kinetics
Chimal and De Schutter, 2018 [103]	Biochemical model	Not applicable	Not applicable	Michaelis-Menten formulation of protein kinetics related to the effects of calcium in long term depression

Table 2.1 Summary of the reviewed cerebellar models published on ModelDB [43].

I used ModelDB as the primary source for the literature review on cerebellar models. However, this approach has some limitations. Several historically important models, such as the Marr [38] and Albus [39] models described above, were theoretical and were never implemented as simulations. In addition, many computational models have not been published on ModelDB. Therefore, although ModelDB is a valuable resource for sharing and accessing computational models, it does not constitute a comprehensive database from which to derive a complete literature review.

Given this limitation, it is important to acknowledge two influential models that are not summarised in Table 2.1. The first is the Purkinje cell model developed by De Schutter and Bower [4], [5], which is widely regarded as one of the most influential models of Purkinje cell electrophysiology. This model is based on a realistic Purkinje cell morphology, enabling detailed investigation of the relationship between structure and function. It includes ten active voltage-dependent ionic conductances and explicitly models active dendrites. Although several Purkinje cell models had been proposed previously, most did not include voltage-dependent conductances in the dendrites. Those that did typically incorporated only a subset of the ionic channels now known to exist.

The second model is the network model proposed by Medina and Mauk [104]. In this influential cerebellar network model, granule, Golgi, basket, and Purkinje cells are

represented as leaky integrate-and-fire neurons. The model provided a biologically plausible computational framework for understanding how the cerebellum supports timed, adaptive, and predictive motor behaviours, and it played an important role in linking theoretical models of cerebellar function with experimental observations, particularly in the study of eyeblink conditioning.

Published computational models of the cerebellum typically fall into one of two broad categories. Some focus on highly detailed representations of limited components of the cerebellum, ranging from individual neurons to the kinetics of single molecules [4], [6], [42], [44], [59], [102]. Others adopt large-scale but more abstract network representations [104], [105].

This diversity reflects the specific research questions motivating each modelling effort. For instance, Garrido et al. [86] developed a cerebellar network model to control a robotic manipulator, for which representing neuronal populations using firing-rate models was sufficient. In contrast, studies investigating how neuronal morphology and biophysical properties give rise to specific functional behaviours require more detailed representations. As an example, Cirtala and De Schutter [49] proposed a morphologically detailed Purkinje cell model in which individual dendritic branches possess distinct ion channel conductance densities to investigate how such heterogeneity influences input processing.

Despite this wide range of approaches, detailed, large-scale, biologically realistic computational models of the whole cerebellar circuit are still lacking [41], [106].

2.2 TMS targeting the cerebellum

Although transcranial magnetic stimulation (TMS) has traditionally been used to target the primary motor cortex [25], it is increasingly being applied on other brain regions, such as the cerebellum. To develop clinically meaningful and effective stimulation strategies, it is fundamental to study stimulation protocols that are tailored to specific brain areas. Given the substantial cytoarchitectural, neurophysiological and neurochemical differences across brain regions it cannot be assumed that the effects of TMS are invariant across targets [23], [25]. Stimulation outcomes depend on multiple factors, including the relative orientation of the neurons and the stimulation

induced electric field, neuronal type, morphology and excitability, the stimulation protocol, and coil characteristics, among others [23], [25].

Transcranial magnetic stimulation has been used both as a research tool to investigate cerebellar functions and as a potential therapeutic intervention. By transiently disrupting normal cerebellar activity, TMS can induce a localised “virtual lesion,” allowing the contribution of the cerebellum to specific behaviours to be inferred from changes in performance. In such paradigms, behavioural measures are typically obtained both at baseline and following stimulation, enabling each participant to serve as their own control and thereby reducing inter-individual variability [23]. Experimental studies have shown that TMS can effectively influence cerebellar activity both in motor and in cognitive domains, including motor adaptation and learning [107], [108], visually guided tracking tasks [107], [109], working memory [110], and social cognitive tasks [111].

From a clinical perspective, the cerebellum is implicated in several common and disabling neurological conditions for which effective treatments remain limited, including cerebellar ataxia, Parkinson’s disease, and essential tremor. This has made the cerebellum an attractive target for TMS-based therapeutic interventions [21], [112]. Table 2.2 summarises the articles reviewed in this dissertation that have investigated the feasibility of cerebellar TMS as a treatment modality.

Pathology	Study	Number of subjects	TMS protocol	Coil type	Main Findings
Progressive supranuclear palsy	Brusa et al, 2014 [113]	10 patients, 20 controls	10 sessions in 2 weeks of iTBS	Figure of 8	Improvement of dysarthria. Increase in the functional cerebellar-cortical connectivity measured by cerebellar cortical inhibition.

Cerebellar ataxia	Farzan et al, 2013 [114]	1 patient	21 TMS sessions	Circular	Improvement of limb coordination, speech, and gait.
	Shiga et al, 2002 [115]	39 patients, 35 sham	21 single pulse TMS sessions	Circular	Improvement in 10 m time, 10 m steps, and standing capacities.
	Kim et al, 2014 [116]	22 patients, 10 sham	5 15 minutes 1 Hz rTMS sessions	Figure of 8	Improvement in 10m time and balance.
	Bonnì et al, 2014 [117]	6 patients	10 sessions in 2 weeks of iTBS	Figure of 8	Improvement in posture and gait.
	França et al, 2020 [118]	24 patients	5 1 Hz rTMS sessions	Double-cone	Improvement in ataxia.
Cerebellar ataxia, tremor and dystonia	Cury et al, 2015 [119]	1 patient	2 single pulse TMS sessions	Double-cone	Improvement in tremor and ataxia, no improvement in dystonia.
Dystonia	Bradnam et al, 2016 [120]	8 patients, 8 sham	10 iTBS sessions	Figure of 8	Small improvement in dystonia severity. Improvement in hand dexterity.
	Bologna et al, 2016 [121]	26 patients, 13 controls	1 cTBS session	Figure of 8	No changes.
	Linssen et al, 2015 [122]	10 patients, 2 controls	1 cTBS session	Figure of 8	No changes.
	Koch et al, 2014 [123]	20 patients	10 cTBS sessions	Figure of 8	Small improvements in dystonia severity.
	Hoffland et al, 2013 [124]	11 patients, 8 controls	1 cTBS session	Figure of 8	Improvement in eyeblink classical conditioning which is impaired in dystonia.

Essential tremor	Bologna et al, 2015 [125]	16 patients, 11 controls	1 cTBS session	Figure of 8	No change in tremor severity.
	Popa et al, 2013 [126]	11 patients, 11 controls	5 1 Hz rTMS sessions in 1 week	Figure of 8	Improved tremor and reduced tremor amplitude.
	Gironell et al, 2002 [127]	10 patients	1 1Hz rTMS session	Butterfly	Improved tremor without lasting effects.
	Avanzino et al, 2009 [128]	15 patients	1 1 Hz rTMS session	Figure of 8	Decreased touch duration and increased inter tapping interval, restored to normal subject values.
	Shin et al, 2019 [129]	12 patients, 10 sham	5 1 Hz rTMS sessions in 5 days	Figure of 8	No effect.
	Olfati et al, 2020 [130]	13 patients, 10 sham	5 1 Hz rTMS sessions in 5 days	Figure of 8	No effect.
	Lv et al, 2023 [131]	20 patients, 18 control	10 sessions 1 Hz rTMS in 10 days	Figure of 8	Improvement in tremor severity.
	He et al, 2024 [132]	20 patients, 20 controls	20 sessions 1 Hz rTMS in 4 weeks	Not reported	Improvement in tremor severity.
	El-Adawy et al, 2024 [133]	23 patients, 22 sham	12 1 Hz rTMS daily sessions in 4 weeks	Figure of 8	Improvement in tremor severity.
Parkinson's disease	Bologna et al, 2015 [134]	13 patients, 10 controls	1 cTBS session	Figure of 8	No changes in tremor.
	Brusa et al, 2012 [135]	8 patients	5 cTBS sessions	Figure of 8	Reduction of dyskinesia.
	Minks et al, 2011 [136]	20 patients	1 1 Hz rTMS session	Conic	Improvement of gross motor skills, worsening of fine motor skills.
	Koch et al, 2009 [137]	20 patients	1 cTBS session	Figure of 8	Reduction of dyskinesia.

	Grobe-Einsler et al, 2024 [138]	18 patients, 17 sham	2 iTBS sessions at 48 Hz per day for 5 days	Figure of 8	Improved rigor, bradykinesia, and gait. No improvement in tremor.
	Grobe-Einsler et al., 2024 [139]	20 patients, 16 sham	3 iTBS sessions at 48 Hz per day for 5 days	Figure of 8	No improvement in postural instability.
Alzheimer's Disease	Yao et al, 2022 [140]	27 patients	20 5 Hz rTMS sessions in 4 weeks	Figure of 8	Improved cognitive functions.
Drug-resistant Epilepsy	Wang et al, 2025 [141]	18 patients, 20 sham	10 cTBS sessions in 2 weeks	Double-cone	Reduction of seizures.
Mal de Débarquement Syndrome	Cha et al, 2019 [142]	26 patients	1 cTBS session	Double-cone	Reduction in oscillating vertigo intensity.
Multiple system atrophy	Liu et al, 2018 [143]	9 patients	5 5 Hz rTMS sessions in 5 days	Circular	Improvement in motor performance.
	Song et al, 2020 [144]	20 patients, 25 controls	10 iTBS sessions in 10 days	Double-cone	Improvement in balance and reduction in ataxia.
	Li et al, 2025 [145]	13 patients, 13 controls	10 iTBS sessions in 10 days	Figure of 8	Improvement in ataxia, fatigue, depression and anxiety.
Multiple Sclerosis	Tramontano et al, 2020 [146]	10 patients, 10 sham	iTBS for 2 weeks	Figure of 8	Improved gait and balance abilities.
	Yassine et al, 2024 [147]	20 patients, 19 sham	48 iTBS sessions in 1 year	Figure of 8	Improvement in balance.
Post stroke	Johkura et al, 2018 [148]	6 patients	5 iTBS sessions in 5 days	Double-cone	Improvement in dizziness, disappearance of nystagmus.
	Koch et al, 2019 [149]	17 patients, 17 sham	2 iTBS daily sessions for 3 weeks	Figure of 8	Improvement of gait and balance.
	Liao et al, 2021 [150]	15 patients, 15 sham	1 daily iTBS session for 2 weeks	Figure of 8	Improvement in balance.

	Chen et al, 2021 [151]	16 patients, 16 sham	10 iTBS sessions in 2 weeks	Figure of 8	Improvement in upper limb spasticity.
	Li et al, 2021 [152]	30 patients	4 cTBS sessions in 1 day	Circular	Improvement in muscle spasticity and limb dyskinesia.
	Rao et al, 2022 [153]	35 patients, 35 sham	10 iTBS sessions in 2 weeks	Figure of 8	Improvement in swallowing function.
	Dong et al, 2022 [154]	12 bilaterally stimulated, 12 unilaterally stimulated, 12 sham	10 10 Hz rTMS sessions in 2 weeks	Circular	Improvement in swallowing function.
	Dai et al, 2023 [155]	14 bilaterally stimulated, 14 unilaterally stimulated, 14 sham	10 iTBS sessions in 2 weeks	Double-cone	Improvement in swallowing function.
	Zhu et al, 2024 [156]	19 patients, 19 sham	2 daily sessions of iTBS five times per week for 2 weeks	Figure of 8	Improvement in gait and balance.
	Liao et al, 2024 [157]	12 patients, 12 sham	15 iTBS sessions in 3 weeks	Figure of 8	Improvement in balance and motor recovery.
	Zhang et al, 2024 [158]	15 patients, 9 controls	10 iTBS sessions in 2 weeks	Double-cone	Improvement in emotional and cognitive function.
Spinocerebellar ataxia	Manor et al, 2019 [159]	10 patients, 10 sham	20 1 Hz rTMS sessions	Circular	Improvement in ataxia, no improvement in gate kinematics.
	Chen et al, 2022 [160]	9 patients, 9 sham	15 1 Hz rTMS sessions in 15 days	Figure of 8	Improvement in ataxia.
	Shi et al, 2023 [161]	40 rTMS, 40 iTBS, 40 sham	10 1 Hz rTMS or iTBS sessions in 2 weeks	Figure of 8	Improvement in ataxia.

	Zhou et al, 2024 [162]	8 patients, 8 sham	10 Hz rTMS for 2 weeks	Double-cone	Improvement in ataxia.
	Grobe-Einsler et al, 2024 [163]	15 patients, 18 sham	3 daily iTBS sessions for 5 days	Figure of 8	Improvement in ataxia.
Schizophrenia	Tikka et al, 2015 [164]	11 patients	10 iTBS sessions in 2 weeks	Double-cone	Improvement in negative syndrome and depression.
	Garg et al, 2016 [165]	20 patients, 20 sham	10 sessions of 5, 6 and 7 Hz rTMS in 2 weeks	Double-cone	Improvement in depressive symptoms.
	Brady et al, 2019 [20]	11 patients	2 daily iTBS sessions for 5 days	Figure of 8	Improvement in negative syndrome.
	Chauhan et al, 2021 [166]	19 patients, 17 sham	2 daily iTBS sessions for 2 weeks	Figure of 8	No effect.
	Zhu et al, 2021 [167]	32 patients, 32 controls	10 iTBS sessions in 2 weeks	Figure of 8	Improvement in negative syndrome.
	Basavaraju et al, 2021 [168]	15 patients, 15 sham	2 daily iTBS sessions for 5 days	Figure of 8	No effect.

Table 2.2 Summary of clinical applications of TMS targeting the cerebellum. The table includes the considered pathology, the TMS intervention protocol, the coil used and the observed effects of the stimulation.

Although many of the studies summarised in Table 2.2 have reported favourable outcomes in ameliorating symptoms of several pathologies [21] and have demonstrated that TMS is safe and well tolerated [21], [112], the overall evidence is inconclusive. Reported effects have been variable largely due to small sample size [112], heterogeneity in stimulation protocols, experimental designs and of outcome measures, and, in several cases, the lack of blinded experiments [21], [107]. It is also important to note that it is reasonable to assume publication bias towards positive findings is likely, suggesting that additional unpublished studies may exist that failed to demonstrate clinical benefit [21], [112].

In addition to the general limitations of TMS discussed in Chapter 1, cerebellar stimulation poses specific challenges. In contrast to the primary motor cortex, the

cerebellum lacks a direct non-invasively measurable output to quantify the effects of the stimulation [30], [169]. The effects of TMS on the cerebellum are typically inferred indirectly, for example through changes in cortical excitability. Eye movements represent a promising behavioural readout of cerebellar function [169], [170]. However, because coil placement near the inion may inadvertently stimulate the occipital cortex, careful consideration of the stimulation site is required, particularly in studies where visual cortical activation could confound interpretation of the results [30].

Targeting the cerebellar cortex is also intrinsically more difficult than targeting the primary motor cortex, as the distance between the scalp and the cerebellar cortex is greater and more variable across individuals [169]. Some studies suggest that effective cerebellar stimulation may require stimulator outputs up to twice those used for cortical stimulation, which could indicate that the cerebellar tissue is less excitable, not just deeper [30]. This could also mean that the coils commonly used to stimulate the cortex are not suitable for cerebellar applications. Alternative designs, such as double-cone coils that have a greater penetration effect may be more suitable than standard figure-8 coils [30].

To summarise, the mechanistic basis underlying the potential therapeutic effects of cerebellar stimulation in movement disorders remains poorly understood [21]. Further studies are needed to elucidate which neural structures in the cerebellum are mostly affected by TMS, and which cerebellar stimulation protocols are most effective, questions that can be addressed using in silico modelling approaches [26].

2.2.1 TMS targeting the cerebellar vermis

In this dissertation, I focus on modelling the stimulation of the cerebellar vermis, which represents a promising clinical target [20], [148]. As with other cerebellar regions, TMS has been applied to the vermis both to investigate its functional roles by creating a localised virtual lesion and to explore its potential for alleviating symptoms associated with cerebellar pathologies.

By inducing a virtual lesion in the cerebellar vermis via TMS, researchers have examined its involvement in swallowing [171], its causal role in biological motion discrimination [172] and its functional topography related to visuospatial functions [173]. From a clinical perspective, the cerebellar vermis has been investigated as a

possible target to treat the symptoms of a range of neurological and psychiatric conditions, including schizophrenia [20], [164], [166], [167], [168], [174], Parkinson's disease [138], [139], multiple sclerosis [147], mal de débarquement syndrome [142], spinocerebellar ataxia [159], [162], [163], as well as for the recovery of balance [175], [176] and reduction of dizziness [148] following stroke.

High frequency stimulation protocols have been predominantly employed in these studies, with intermittent theta burst stimulation being the most commonly used approach [20], [138], [139], [148], [163], [164], [166], [167], [168]. Only a limited number of studies have explored alternative protocols: one study employed continuous theta-burst stimulation [142], two studies used high-frequency repetitive TMS [162], [174], and only one study investigated low-frequency stimulation [159].

The cerebellum has long been known to play a critical role in the control of eye movements. Accordingly, TMS targeting the cerebellum has been widely used to investigate its effects on oculomotor behaviour, particularly saccadic eye movements [177], saccadic adaptation [108] and smooth pursuit [177], [178]. Reported effects include changes in amplitude and velocity of saccadic eye movements [109] and latency and peak velocity of reflexive saccades [179]. In Chapter 4 an experimental study is described in greater detail as it served as the experimental paradigm reproduced using the stimulation model developed in this work. This study evaluates the effects of cerebellar TMS in perturbing saccades and smooth pursuit [177].

2.3 Models of non-invasive stimulation

As the positive effects that non-invasive stimulation has on the brain become more evident, it is becoming increasingly important to understand the underlying mechanisms of its action. A deeper knowledge of how these techniques work will allow us to develop them much faster. This is why many researchers are developing in silico models of extracellular stimulation [29], [89], [180], [181].

Researchers have been investigating the effects of non-invasive stimulation mainly via three approaches [182]:

- Neuron-field models: These involve modelling a morphologically detailed isolated neuron, or a network of neurons, and applying an external field to

perturbate it. These models investigate how and what parts of the neurons are influenced by the stimulation.

- Head models: These involve modelling the structure of the human head and transcranial magnetic stimulation coils or transcranial electric stimulation electrodes. These models investigate how the electric field generated by the stimulation propagates through the head and the brain.
- Multi-scale models: These state of the art models involve incorporating both head models and isolated neurons allowing a more detailed and realistic analysis of the effects of the stimulation.

2.3.1 Neuron-field models

The first computational study to investigate the effect of extracellular stimulation on a nerve dates to the mid 1970s [183]. Early investigations only considered the effects that stimulation has on a nerve, neglecting the complex morphologies of neurons [183], [184].

McIntyre and Grill took into account more detailed morphologies and demonstrated that the axon is the part of the neuron that is most affected by extracellular stimulation [185]. This further pushed modelling efforts to focus on the excitability of axons [186]. However, this simplification overlooks more subtle effects that the stimulation has on the entire neuron, such as the potential to alter its firing rate [180].

To address this limitation, later computational studies applied non-invasive stimulation to isolated, morphologically detailed neurons [187], [188], [189], [190], [191]. In parallel, other researchers concentrated on applying non-invasive stimulation models to networks of neurons to research the impact of synaptic connections [181], [192], [193], [194]. In this context, the complexity of individual neuron models is reduced: the networks are modelled using single or few compartment neurons [181], [195]; Integrate-and-Fire neurons [196], [197]; Neural Mass Models [198], [199]; or Wilson-Cowan oscillators [200].

Across these various computational approaches, non-invasive stimulation is typically modelled in a simplified manner. Common stimulation models include uniform electric fields dependent only upon distance from the source [181], [188], [195], and currents

generated by undamped RLC circuits [191], [192], [193], [194]. In most studies, non-invasive stimulation is directly incorporated into the neurons either by current injection [188], [189], [191], [192], [193], [194] or by perturbation of the transmembrane voltage [181], [197], [198], [199] - but sometimes further assumptions are made and the stimulation is added by changing the synaptic conductances [196] or modifying the probability of synaptic release [197].

2.3.2 Head models

Computational forward models of transcranial stimulation are invaluable tools to guide clinical practice. These models are used to investigate and predict the propagation of the electric field in the brain. These models enable the exploration of various stimulation protocols, constituting the initial step in optimising protocols to target specific brain regions while ensuring safety [201], [202].

In the first forward models of transcranial stimulation, the head is represented with simplified morphologies. Typically, the head is approximated by concentric spheres characterising different head parts with differing electrical conductivity values, such as the scalp, skull and brain [203], [204] (see Figure 2.1). While these models can be solved analytically, they lack an accurate representation of the convoluted structure of the brain, which can exert a substantial influence on the propagation of the electric field [205].

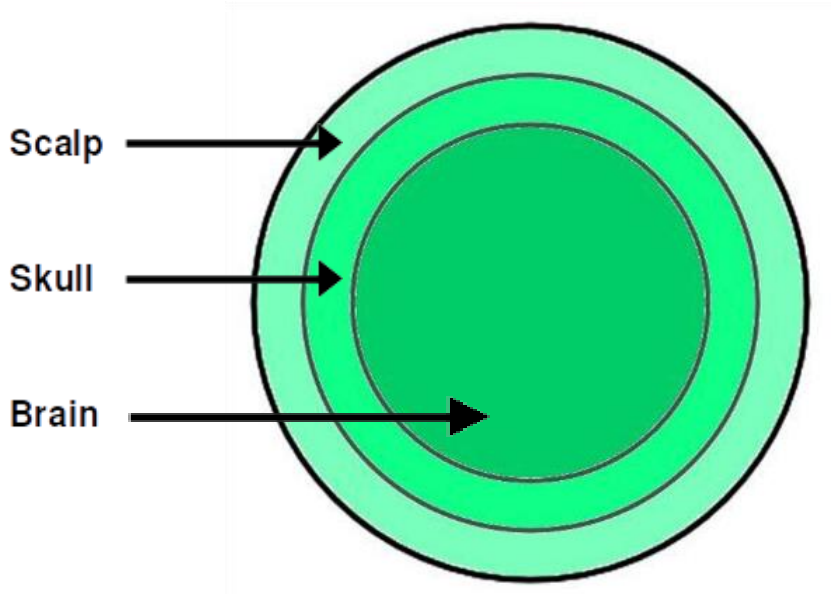


Figure 2.1 Three layer spherical head model.

To overcome this limitation, more realistic head models emerged, featuring explicit representations of human anatomy. These models are constructed by acquiring the subject's MRI images and segmenting them into distinct volumes such as white matter, grey matter, cerebrospinal fluid, bone, and scalp tissue [29], [206], [207], [208], [209], [210]. As the popularity of these models grew, an array of freely available software tools emerged to automate their generation.

The inclusion of anisotropic properties in the skull and the white matter regions employing diffusion tensor imaging (DTI) further improved the MRI generated head models [211], [212]. Additionally, patient specific head modelling gained increasing interest - not only are healthy adult subjects' heads modelled, but also individuals with brain lesions [213] and varying age groups [214]. However, it is crucial to note that increased model complexity does not necessarily equate to greater accuracy or clinical utility. It is the researcher's job to ensure the balance between complexity and precision, aligned with clinical requirements [201].

Though the exact process may vary, the generation of forward models from MRI images follows these steps [201], [202]:

1. Segmenting individual tissue types from high-resolution anatomical data, employing both automated and manual segmentation tools;
2. Modelling the physical attributes of the electrodes or magnetic coil and their placement within the segmented image data;
3. Generating meshes from the masks generated in point 1;
4. Assigning the electrical properties of the tissues and imposing boundary conditions, followed by solving the associated differential equations employing a finite element solver;
5. Visualising the data, plotting maps depicting the induced cortical electric field or current density.

2.3.3 Multi-scale models

The head models described in the previous subchapter have a limitation: they ignore the complex morphologies and electrical properties of neurons [182]. There is still a limited understanding of the effects that transcranial stimulation has on neurons. For example, it is unclear how spatial and temporal parameters of TMS influence the neuron's threshold and site of activation [215].

To overcome this, researchers are developing state of the art multi-scale models. Multi-scale models consist of the integration of head models and biological neuron models [182]. These models are usually generated in three steps:

1. The electric field generated by a stimulation protocol is calculated using a head model;
2. A region of interest (ROI) is populated by neurons (or fibres);
3. The modelled neurons are simulated, with the addition of the extracellular potential generated by the field calculated in point 1.

The development of multi-scale models is an ongoing research frontier, as combining head and neuron models comes with great technical difficulties. Developed multi-scale models have a wide range of complexity, both for the head model and the neuron models used. As described in the previous section, head models may be either MRI generated [211], [215], [216], [217], [218], [219], [220], [221], [222], [223], [224], [225], [226] or approximated by concentric spheres [195], [221], [227], [228], [229], [230], [231], [232]. White matter anisotropies may be included in anatomically realistic head models with the use of DTI [211], [224], [225], [226], [233]. Simulated neurons range from single compartment neurons or simple fibres [211], [222], [225], [226], [228], [229], [230], [232], [233], [234] (especially when combined with DTI generated head models), to morphologically realistic ones [215], [216], [217], [218], [220], [221], [223], [224], [231].

Most often, multi-scale models only include the neurons that are most likely to be affected by the stimulation, such as pyramidal neurons and basket cells [182]. This simplifies the technical and computational difficulty. Another simplification is to simulate isolated neurons, rather than networks [182] (see Figure 2.2).

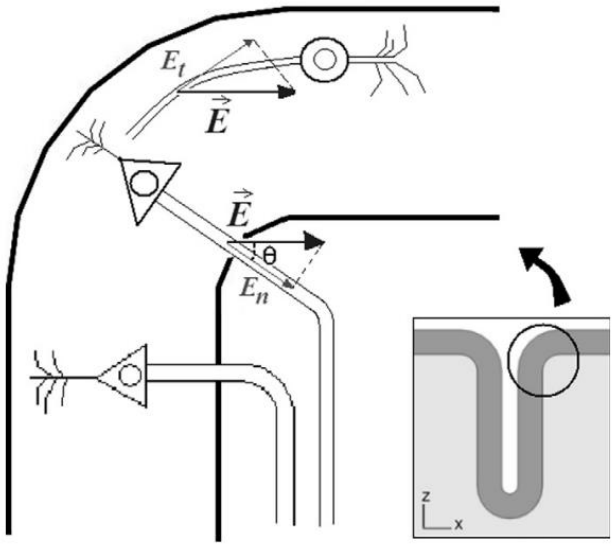


Figure 2.2 Schematic representation of simple neurons in a cortical sulcus. Figure taken from [232].

Using concentric spheres based head models offers a distinct advantage: the placement of the neurons in the head model is highly simplified. However, this approximation may introduce modelling errors that may then result in an inaccurate depiction of the neuronal excitability [205], [221], [227]. An accurate representation of the head anatomy generates a more precise estimate of the stimulus-induced electric field, which could lead to a more faithful prediction of neuronal activation [205], [221]. However, positioning the neurons in an MRI generated head model is an arduous task. Neurons have different spatial orientations according to the folds in the brain, this has to be reflected in the positioning of the neurons in the model [182] (see Figure 2.3).

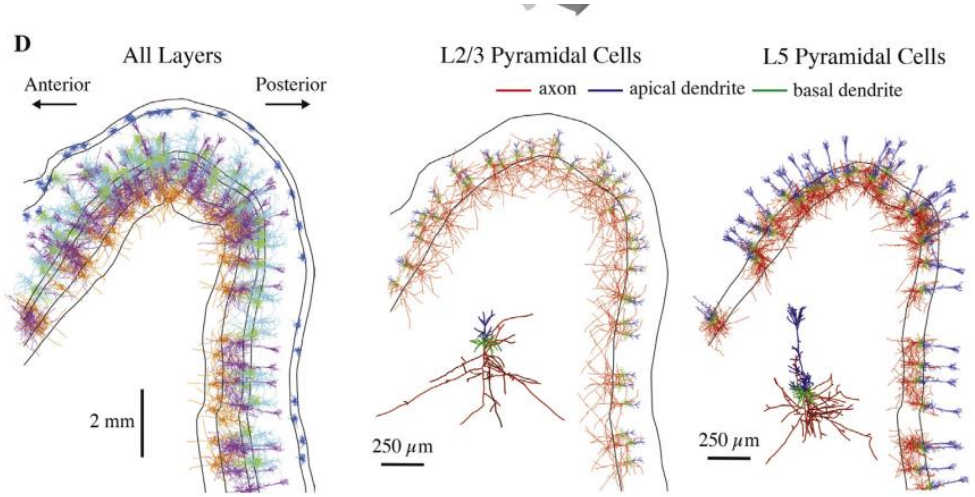


Figure 2.3 Model neurons located in the crown of the pre-central gyrus between the grey matter and white matter surfaces. Figure taken from [215].

Multi-scale models of transcranial stimulation encounter several notable limitations. One of the foremost challenges lies in the validation of these models [226]. Additionally, a source of considerable uncertainty arises from the nature of neuronal representations within these models: neurons are often simplified or fitted on data extrapolated from animal studies due to a lack of comprehensive human-specific neuronal data [182]. Another significant limitation is the absence of synaptic connections within these models. This restricts their ability to fully capture the intricate network dynamics and communication essential for understanding the effects of transcranial stimulation on neural circuits [215]. These limitations collectively underscore the need for ongoing studies to enhance the reliability and predictive capabilities of multi-scale models.

2.4 Conclusion

In this chapter, I reviewed the current state of the art and the principal limitations of cerebellar models, transcranial stimulation models, and applications of TMStargeting the cerebellum. I highlighted the need for further studies to elucidate the mechanisms underlying the effects of TMS on the cerebellum, as well as the need for large-scale, biologically realistic models of the cerebellum and multiscale models of TMS that explicitly account for stimulation effects at the network level.

In the next chapter, I provide the background knowledge required to understand the remainder of this dissertation, including the mathematical and physical principles underlying neuron modelling, TMS, and computational modelling of TMS.

Chapter 3

Tools and techniques

In this chapter I provide the background knowledge needed to understand the rest of this dissertation. I start by describing how neurons can be characterised by mathematical equations to model them. I then describe the physics of transcranial magnetic stimulation. Finally, I describe how transcranial magnetic stimulation is modelled in SimNIBS, the transcranial stimulation simulator I employed.

3.1 Modelling neurons

Computational neuroscience is a branch of neuroscience which uses mathematical equations to describe and simulate the brain, or more properly a portion of it. Neurons have properties that are comparable to those of electrical components. It is possible to model neurons using equivalent electric circuits and to simulate neurons by solving the differential equations describing the equivalent circuit. One of the most influential biophysical models of neurons is the Hodgkin-Huxley model [235], proposed in 1952 and still widely used today. To understand how to develop biophysical computational models of neurons, it is first necessary to examine some fundamental concepts of neuronal electrophysiology. The following subsections are all informed by the book "Principles of Computational Modelling in Neuroscience" [236], unless stated otherwise.

3.1.1 Neuron electrophysiology

Neurons are the fundamental units of the brain and nervous system. In general, neurons can be divided into three parts (see Figure 3.1) [237]:

- Soma: it is the body of the neuron. The inputs to the neuron are summed at the soma;
- Dendrites: they are branch-like structures that extend from the soma and receive the inputs from other neurons;
- Axon: it is a fibre that transmits the action potential to other neurons.

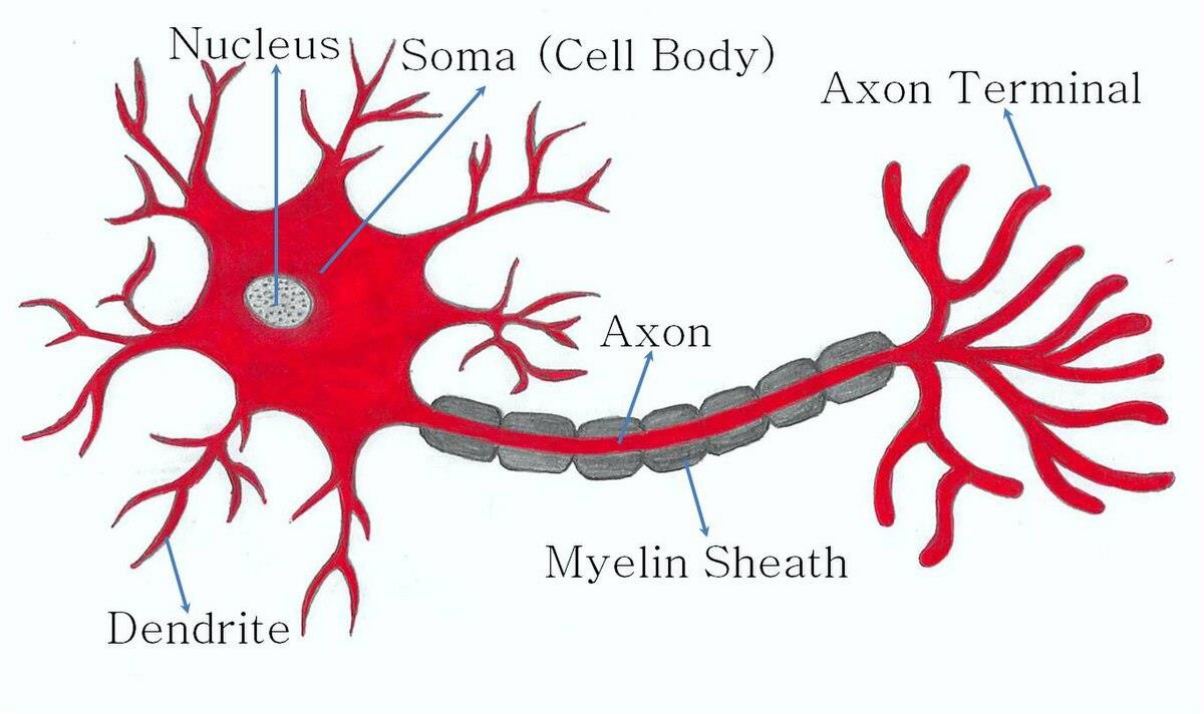


Figure 3.1 Typical structure of a neuron. Image taken from "Neuron typical structure" [235] by Ajimonthomas and licensed under CC BY-SA 4.0.

Neuronal electrical activity arises due to ionic currents flowing through the neuron's membrane via complex proteins that form ion channels. The majority of these currents are generated by sodium and potassium ions. These ions have different concentrations inside and outside the cell, with the cell membrane impeding the free flow of ions: the cell membrane is characterised by a capacitor in parallel with a number of resistors [238].

At rest, the neuron's voltage is negative, usually between -60 mV and -80 mV. When the neuron is at its resting potential, both sodium and potassium channels are closed. The sodium channels rapidly open when the membrane potential increases, such as when the neuron receives an excitatory input. Sodium ions enter the neuron, depolarising it. This results in a fast and large increase in the membrane potential. The sodium channels then inactivate, preventing further sodium ions from entering the neuron. Concurrently, potassium channels activate and potassium ions flow outside of the neuron. Finally, potassium channels deactivate; the resting potential is restored by actively transporting the potassium and sodium ions back inside and outside the neuron through the sodium-potassium pump. The described rapid sequence of changes in the voltage across the neuron's membrane is called an action potential (see Figure 3.2) [239].

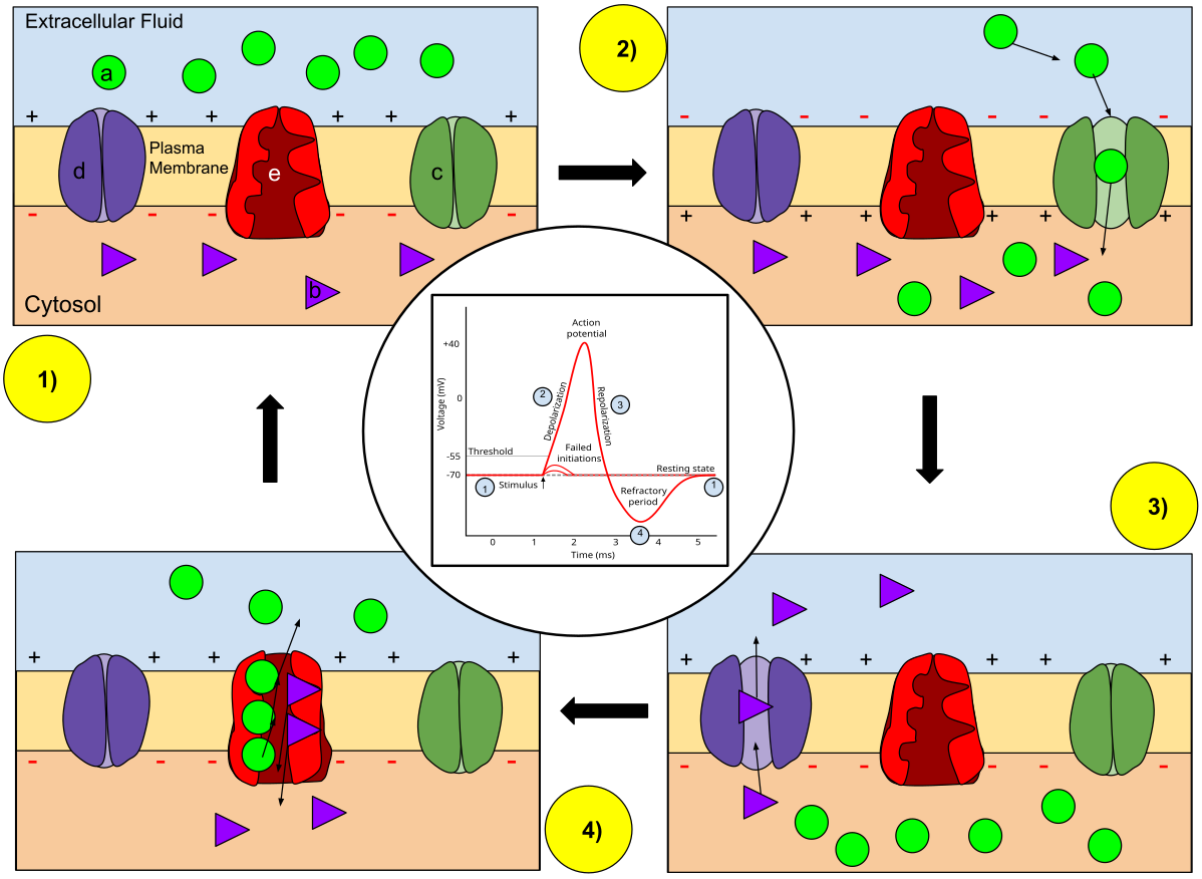


Figure 3.2 The stages of an action potential:

At rest, sodium (green circles) and potassium (purple triangles) ions are unable to cross the neuron's membrane.

The neuron depolarises. Sodium ions enter the cell through the sodium ion channels (in green).

The sodium channels close, the potassium channels open (in purple), and potassium ions flow outside the neuron. The neuron repolarises.

Potassium channels close. Potassium and sodium ions are actively transported through the cell membrane via sodium-potassium pumps (in red), restoring the resting potential.

Image taken from "Membrane Permeability of a Neuron During an Action Potential" [240] by CThompson02 and licensed under CC BY-SA 4.0.

During an action potential, except when actively transported, ions flow through the cell membrane according to their electrochemical gradient. The ion's flux depends on two factors: drift and diffusion. Diffusion is due to different concentrations of the ion species inside and outside the cell. Drift is caused by the fact that the ion is a charge carrier and is moved by an electric potential gradient. At the equilibrium potential, these two forces counterbalance each other out, giving no net current flowing through the cell. This equilibrium potential, E_{ion}, can be calculated with Nernst's equation:

$$E_{ion} = \frac{RT}{zF} ln\left(\frac{c_{out}}{c_{in}}\right) \quad (3.1)$$

Here, R is the universal gas constant, T is the temperature, z is the valence of the ion, F is Faraday's constant and c_{out} and c_{in} are the ion's concentration respectively outside and inside the cell.

If the membrane potential is equal to the Nernst potential of an ion, the current flowing across the cell membrane generated by that ion will be zero. If the membrane potential lies at a different value, the ion will generate a current, I_{ion}, proportional to the potential difference:

$$I_{ion} = g_{ion} * (V - E_{ion}) \quad (3.2)$$

Here, V is the membrane voltage, E_{ion} is the ion's reversal potential and g_{ion} is the channel conductance.

The channel conductances are not fixed but depend on different factors, such as time, voltage, and intracellular and extracellular agents such as calcium concentration or neurotransmitters. The dependence on voltage was modelled by Hodgkin and Huxley by introducing gating variables. These gating variables can be of activating or inactivating kind, and they act as a switch for the channel shifting it between open and closed states (see Figure 3.3) [238]. The channel conductance can be described as follows:

$$g_{ion} = \bar{g}_{ion} * m^a * h^b \quad (3.3)$$

Here, $\bar{g}_{ion}$ represents the maximal channel conductance, m and h are the gating variables which define the probability of the gates being in the open and inactivated state. Their exponents, a and b, can be interpreted as the number of activation and inactivation gates per channel [235].

The gating variables depend on the voltage as so:

$$\frac{dx}{dt} = \alpha_x * (1 - x) - \beta_x * x \quad (3.4)$$

Here, x is a generic gating variable, and α_x and β_x are its rate constants, which depend on the membrane voltage, V.

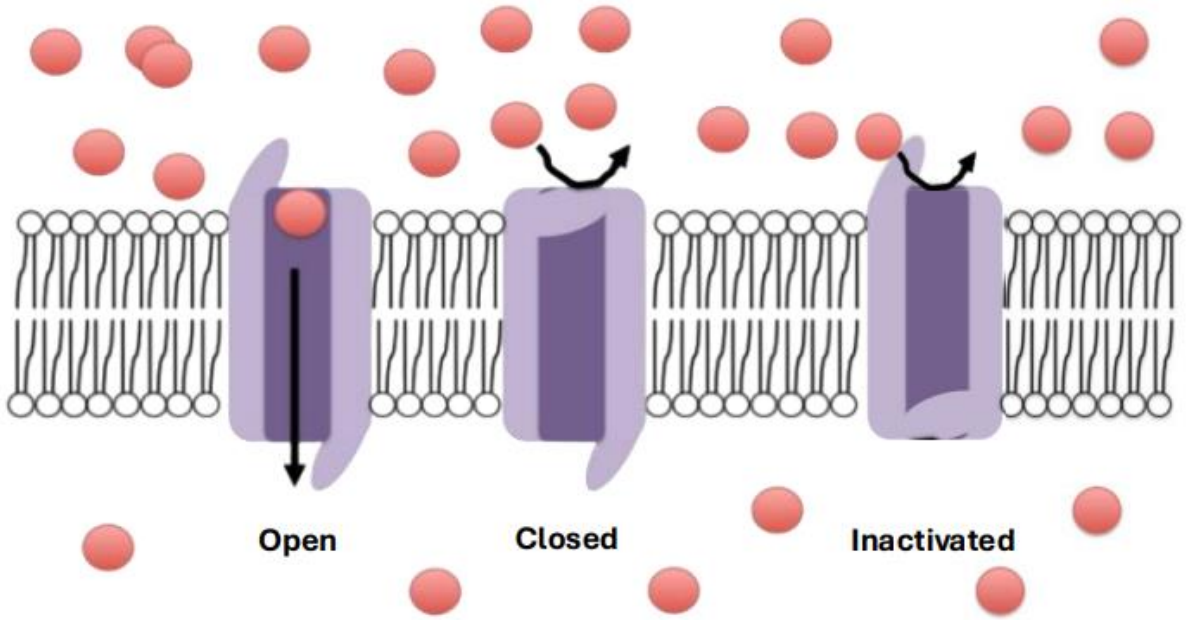


Figure 3.3 Transition states of voltage-gated sodium channels. At resting potential, the activation gate is closed, so no ions may flow through the channel. When the cell is depolarized, the channel switches to the activated state. In this configuration, sodium ions may flow through the channel. Finally, the channel stops conducting ions since the inactivation gate blocks it. Image taken from "Open and closed conformations of ion channels" [241] by Efazzari and licensed under CC BY-SA 4.0. Modified to add the inactivated state.

3.1.2 The Hodgkin-Huxley model

The Hodgkin-Huxley model is one of the most influential models in computational neuroscience. Alan Hodgkin and Andrew Huxley were able, using pioneering techniques for the time, to disentangle the contributions of sodium and potassium currents to action potentials in the squid giant axon. They advanced a circuit model of a neuron (see Figure 3.4), the mathematical equations associated with it and derived the equations of the sodium and potassium gating particles.

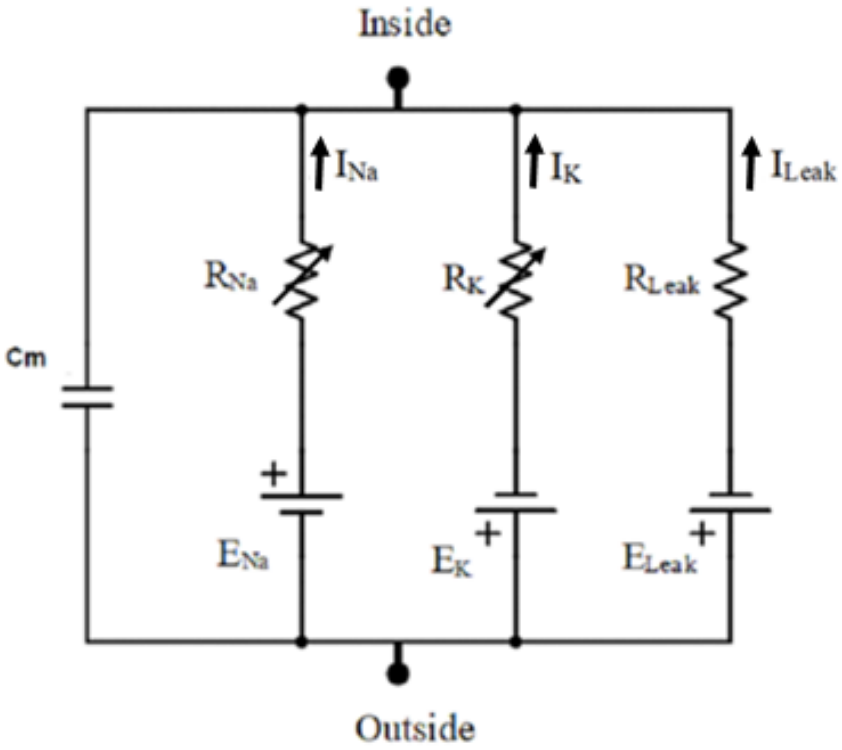


Figure 3.4 Neuron electrical circuit as proposed by Hodgkin and Huxley. R_{leak} is considered constant, while R_{Na} and R_K vary with the membrane potential and time. Reproduced from [235].

The total membrane current per unit area, I, can be expressed as:

$$I = C_m \frac{dV}{dt} + I_{ions} \tag{3.5}$$

By convention, I is positive if flowing into the cell. Here, C_m is the membrane capacitance per unit area, V is the membrane potential and I_{ions} is the sum of all ionic currents, that is the sodium current, I_{Na}, the potassium current, I_k, and the leak current, I_{leak}.

Leak channels account for the natural permeability of the membrane to ions. The conductance, $\bar{g}_{Leak}$ is a constant. Thus, the leak current can be described as:

$$I_{Leak} = \bar{g}_{Leak} * (V - E_{Leak}) \tag{3.6}$$

Hodgkin and Huxley described the sodium and potassium currents as [235]:

$$I_{Na} = \bar{g}_{Na} * m^3 * h * (V - E_{Na}) \tag{3.7}$$

$$I_K = \bar{g}_K * n^4 * (V - E_K) \tag{3.8}$$

The gating variables m, h and n are described by equation 3.4. Below are the functions presented by Hodgkin and Huxley for their rate constants [235]:

$$\alpha_n = \frac{0.01[10-(V_{rest}-V)]}{e^{\frac{10-V}{10}}-1} \qquad \beta_n = 0.125\, e^{-\frac{V_{rest}-V}{80}}$$

$$\alpha_m = \frac{0.1[25-(V_{rest}-V)]}{e^{\frac{25-V}{10}}-1} \qquad \beta_m = 4 * e^{-\frac{V_{rest}-V}{18}} \tag{3.9}$$

$$\alpha_h = 0.07 * e^{-\frac{V_{rest}-V}{20}} \qquad \beta_h = \frac{1}{e^{\frac{30-(V_{rest}-V)}{10}}+1}$$

Here, V_{rest} is the neuron's resting state voltage.

3.1.3 Beyond the Hodgkin-Huxley neuron

The rate constants of the gating variables are strongly dependent on temperature. The data obtained by Hodkin and Huxley was recorded at 6.3°C [235]. When modelling a different temperature, the rate constants must be scaled by the following temperature scaling factor:

$$Q_{10}^{\frac{T-T_0}{10}} \tag{3.10}$$

Here, Q_{10} is a temperature coefficient, typically between 2 and 3 [242], T is the temperature at which the model simulations are conducted and T_0 is the temperature at which Hodgkin and Huxley conducted their electrophysiological experiment.

The Hodgkin and Huxley model is still largely used as a biophysical neuronal model. It often serves as a basis from which to add the contribution of other ionic currents. This allows to reproduce various firing behaviours that the Hodgkin and Huxley model is not able to replicate, such as adaptation, bursts or post-inhibitory rebound, among others.

The Hodgkin-Huxley model describes a single point neuron. However, real neurons are often characterised by a rich morphology that cannot be simplified to a sphere. Synaptic inputs arriving at different locations may generate substantially different outputs. To include this aspect in computational models, continuous dendritic trees are simplified using a network of discrete compartments. Each compartment's dynamics follows the Hodgkin-Huxley equations, or a variation of them. The

compartments are coupled to each other via conductances describing the flow of ions between them [238].

A limitation of the Hodgkin-Huxley model is that it assumes that ion permeation processes are continuous and deterministic. This is not the case. A neuron's membrane is studded with discrete ion channels undergoing random fluctuations between open and closed stable states [243]. Markov multistate transition models allow to overcome this limitation.

3.1.4 Markov multistate transition models

Markov multistate transition models are a type of statistical model used to describe systems that move between multiple states over time in which the future state depends only on the current state, not on the sequence of past states or the time the system has spent in the current state. Markov multistate transition models are widely used in neuroscience to model biological processes that involve stochastic transitions between different states, particularly in synaptic and ion channel dynamics.

When modelling ion channels with Markov multistate transition models, the ion channels are considered to have a finite number of discrete stable states separated by large energy barriers. The time evolution of the probability of a state, S_i, is described by:

$$\frac{dP(S_i)}{dt} = \sum_{j=1}^{n} P(S_j)P(S_j \rightarrow S_i) - \sum_{i=1}^{n} P(S_i)P(S_i \rightarrow S_j) \quad (3.11)$$

Here, the channel is characterised by n stable states. $P(S_j)$ is the probability of being in the state S_j at time t and $P(S_j \rightarrow S_i)$ is the probability to transition from the state S_j to the state S_i. In the limit of large numbers of identical channels, the probability of being in the state S_j becomes the fraction of channels in the state S_j and the probability of transitioning from one state to another becomes the rate constant of the transition reaction.

Given O_{ion} the only state in which the ion channel is open, the current generated by an ion per unit area, I_{ion}, can be described as follows:

$$I_{ion} = \bar{g}_{ion} * O_{ion} * (V - E_{ion}) \quad (3.12)$$

3.1.5 Neural synapses

To understand the inner workings of the brain, it is not sufficient to develop and study a model of a single neuron in great detail. Networks of neurons can be created by linking computational models of single neurons with synaptic models.

Synapses are the fundamental units of communication in the nervous system, acting as junctions between neurons where information is transmitted. The concept of synapses was first described by Santiago Ramon y Cajal [244], though the term synapse, from the Greek meaning "to clasp together" was coined later by Charles Sherrington [245]. Synapses can be broadly categorised into electrical and chemical synapses.

Electrical synapses transmit signals through gap junctions: direct electrical connections between neurons. This connection allows for the rapid and bidirectional transfer of ions, enabling nearly instantaneous communication.

Electrical synapses are modelled as conductive pathways between neurons, where the current, I_{ij}, between two neurons i and j is proportional to the voltage difference across the gap junction:

$$I_{ij} = -g_{gap} * (V_i - V_j) \tag{3.13}$$

Here, g_{gap} represents the conductance of the gap junction, and V_i and V_j are the membrane potentials of the connected neurons.

Chemical synapses are more complex and involve the release of neurotransmitters from the presynaptic neuron into the synaptic cleft (see Figure 3.5). These neurotransmitters then bind to receptors on the postsynaptic neuron, resulting in either an excitatory or inhibitory postsynaptic potential (EPSP or IPSP). The delay associated with neurotransmitter release, diffusion, and receptor binding makes chemical synapses slower than electrical synapses, but they offer greater flexibility in modulating synaptic strength and plasticity.

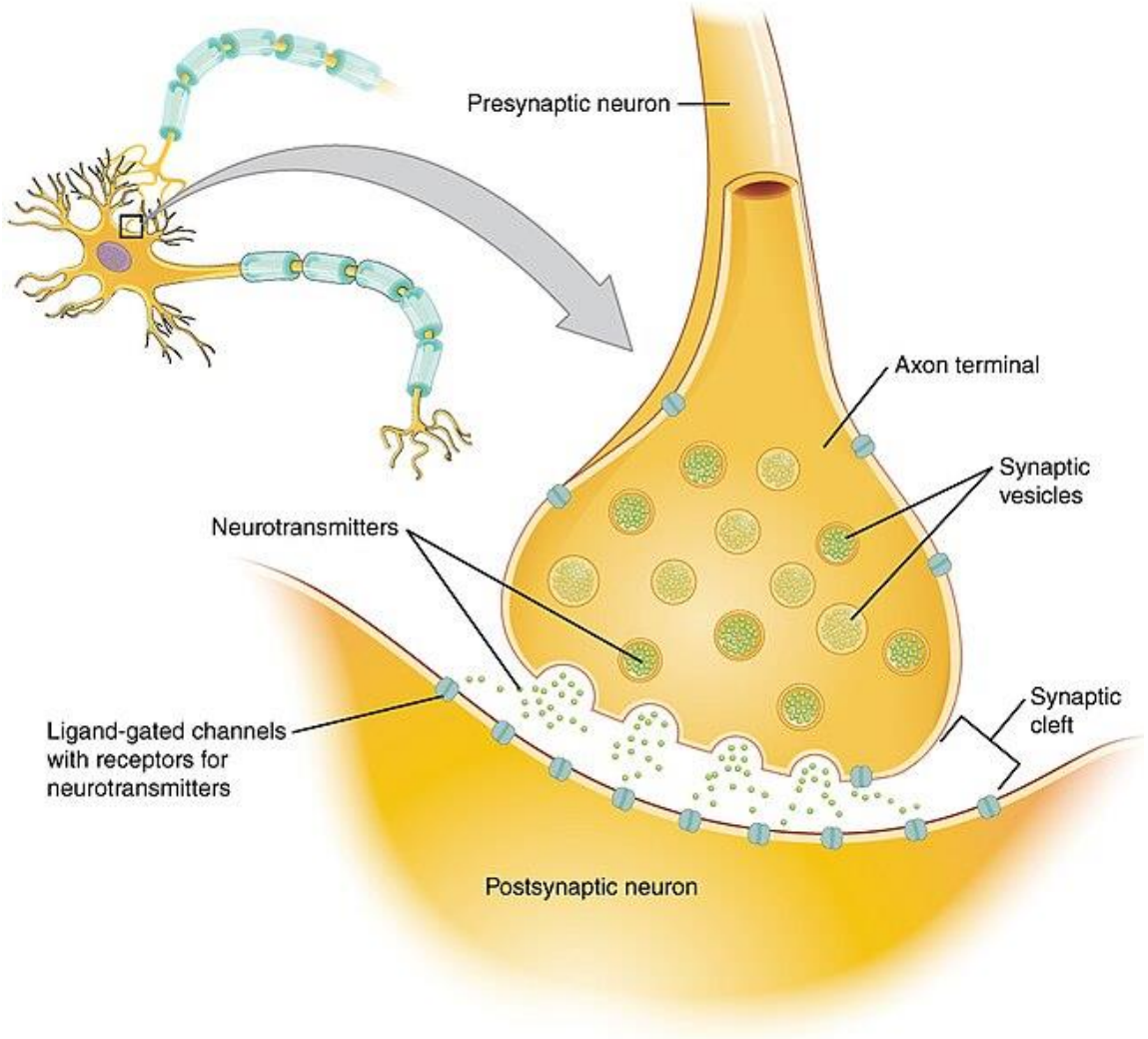


Figure 3.5 Chemical synapse. Image taken from "1225 Chemical Synapse" [246] by Young, KA., Wise, JA., DeSaix, P., Kruse, DH., Poe, B., Johnson, E., Johnson, JE., Korol, O., Betts, JG., & Womble, M. licensed under CC BY 4.0.

Modelling chemical synapses involves capturing the dynamics of neurotransmitter release, postsynaptic receptors activation, and postsynaptic response. Researchers proposed several models varying in complexity to describe them. In this work, synapses are modelled with conductance-based models and Markov multistate transition models.

In conductance-based models, the synaptic current, I_{syn}, can be described as below [237]:

$$I_{syn} = g_{syn} * (\mathrm{V} - E_{syn}) \tag{3.14}$$

Here, g_{syn} is the synaptic conductance, V is the membrane potential and E_{syn} is the synapse reversal potential.

The time course of the synaptic conductance, g_{syn}, is often modelled as a difference of exponentials:

$$g_{syn} = \bar{g}_{syn} * \left(e^{-\frac{t-t_S}{\tau_{decay}}} - e^{-\frac{t-t_S}{\tau_{rise}}} \right) \tag{3.15}$$

with the rise representing neurotransmitter release and receptor activation, and the decay reflecting neurotransmitter clearance. Here, $\bar{g}_{syn}$ is the maximum synaptic conductance, τ_{rise} and τ_{decay} are the exponentials' rise and decay time constants and t_s is the time of arrival of a presynaptic spike.

3.2 Physics of transcranial magnetic stimulation

When a subject is stimulated via transcranial magnetic stimulation, the stimulation coil acts as an electromagnet, generating a time varying magnetic field. This induces an electric field in the underlying tissues of the subject's head. The electromagnetic field is governed by Maxwell's equations:

$$\nabla \cdot \boldsymbol{E} = \frac{\rho}{\varepsilon_0} \tag{3.16}$$

$$\nabla \cdot \boldsymbol{B} = 0 \tag{3.17}$$

$$\nabla \times \boldsymbol{E} = -\frac{\partial \boldsymbol{B}}{\partial t} \tag{3.18}$$

$$\nabla \times \boldsymbol{B} = \mu_0 \boldsymbol{J} + \mu_0 \varepsilon_0 \frac{\partial \boldsymbol{E}}{\partial t} \tag{3.19}$$

Here $\boldsymbol{E}$ is the electric field, $\boldsymbol{B}$ is the magnetic field, ρ is electric charge density, $\boldsymbol{J}$ is the current density, ε_0 is the vacuum permittivity and μ_0 is the vacuum permeability.

TMS coils typically operate at frequencies in the range of 1-10 kHz. The electromagnetic wavelength at those frequencies is 30-300 km. As the dimension of the head, which is the relevant length scale for TMS, is much smaller than the electromagnetic wavelength, we can assume a quasi-static state: the displacement currents are negligible. Ampère-Maxwell law (equation 3.19) reduces to:

$$\nabla \times \boldsymbol{B} = \mu_0 \boldsymbol{J} \tag{3.20}$$

3.2.1 Magnetic field generated by the TMS coil

In a quasi-static state, the magnetic field can be described by Biot-Savart's law:

$$\boldsymbol{B}(\boldsymbol{r}) = \frac{\mu_0}{4\pi}\int \frac{\boldsymbol{J}(\boldsymbol{r}')\times(\boldsymbol{r}-\boldsymbol{r}')}{|\boldsymbol{r}-\boldsymbol{r}'|^3} d^3\boldsymbol{r}' \tag{3.21}$$

Here $\boldsymbol{B}(\boldsymbol{r})$ is the magnetic field at point $\boldsymbol{r}$ and $\boldsymbol{r}'$ is the position vector at the source point. As the radius of the coil wire is much smaller than the distance of the coil to the cortex, we can assume the coil wire to be infinitely narrow. Equation 3.21 can be simplified to:

$$\boldsymbol{B}(\boldsymbol{r}) = \frac{\mu_0}{4\pi}\oint \frac{Idl\times(\boldsymbol{r}-\boldsymbol{r}')}{|\boldsymbol{r}-\boldsymbol{r}'|^3} \tag{3.22}$$

Here I is the current and dl is the wire path.

As the conductivity of biological tissues is very low, the magnetic field generated by the currents induced in the subject's body by TMS is insignificant. We can assume a magnetostatic regime and equation 3.22 further simplifies to:

$$\boldsymbol{B}(\boldsymbol{r}) = \frac{\mu_0 I}{4\pi}\oint \frac{dl\times(\boldsymbol{r}-\boldsymbol{r}')}{|\boldsymbol{r}-\boldsymbol{r}'|^3} \tag{3.23}$$

The magnetic field, $\boldsymbol{B}$, can be expressed as the curl of the magnetic vector potential, $\boldsymbol{A}$:

$$\boldsymbol{B} = \nabla\times\boldsymbol{A} \tag{3.24}$$

Equation 3.24 comes from Gauss's law (equation 3.17), and the identity $\nabla\cdot(\nabla\times\boldsymbol{A}) = 0$, where $\boldsymbol{A}$ is any continuously twice-differentiable vector field.

To express equation 3.23 in terms of the magnetic vector potential, $\boldsymbol{A}$, first consider the identity:

$$\frac{\boldsymbol{r}-\boldsymbol{r}'}{|\boldsymbol{r}-\boldsymbol{r}'|^3} = -\nabla\left(\frac{1}{|\boldsymbol{r}-\boldsymbol{r}'|}\right) \tag{3.25}$$

Substituting 3.25 in 3.23 we obtain:

$$\boldsymbol{B}(\boldsymbol{r}) = -\frac{\mu_0 I}{4\pi}\oint dl\times\nabla\left(\frac{1}{|\boldsymbol{r}-\boldsymbol{r}'|}\right) \tag{3.26}$$

Considering the vector identity $\nabla\times(fc) = -c\times\nabla f$, where f is a scalar function and c is a constant vector, and setting $f = \frac{1}{|\boldsymbol{r}-\boldsymbol{r}'|}$ and $c = dl$, we get:

$$\nabla \times \left(\frac{dl}{|\boldsymbol{r}-\boldsymbol{r}'|}\right) = -dl \times \nabla\left(\frac{1}{|\boldsymbol{r}-\boldsymbol{r}'|}\right) \quad (3.27)$$

Substituting equation 3.27 in equation 3.26, and exchanging the order of the curl and the integral, we get:

$$\boldsymbol{B}(\boldsymbol{r}) = \frac{\mu_0 I}{4\pi}\oint \nabla \times \left(\frac{dl}{|\boldsymbol{r}-\boldsymbol{r}'|}\right) = \nabla \times \left(\frac{\mu_0 I}{4\pi}\oint \frac{dl}{|\boldsymbol{r}-\boldsymbol{r}'|}\right) \quad (3.28)$$

Given equations 3.24 and 3.28, we can identify:

$$\boldsymbol{A}(\boldsymbol{r}) = \frac{\mu_0 I}{4\pi}\oint \frac{dl}{|\boldsymbol{r}-\boldsymbol{r}'|} \quad (3.29)$$

Knowing the magnetic vector potential, $\boldsymbol{A}$, of a TMS coil, it is possible to calculate the induced electric field in the head.

3.2.2 Electric field induced in the head

Substituting equation 3.24 in equation 3.18, and considering that the curl operator and the partial derivative operator are commutative, we have:

$$\nabla \times \boldsymbol{E} = -\frac{\partial}{\partial t}\nabla \times \boldsymbol{A} = -\nabla \times \frac{\partial \boldsymbol{A}}{\partial t} \quad (3.30)$$

Rearranging equation 3.30 by bringing all the terms to the left, we obtain:

$$\nabla \times \left(\boldsymbol{E} + \frac{\partial \boldsymbol{A}}{\partial t}\right) = 0 \quad (3.31)$$

Since the curl of the gradient of any continuously twice-differentiable scalar field is the zero vector ($\nabla \times (\nabla\varphi) = 0$), the vector field $\boldsymbol{E}+\frac{\partial \boldsymbol{A}}{\partial t}$ in equation 3.31 can be described by the electric scalar potential, φ:

$$-\nabla\varphi = \boldsymbol{E}+\frac{\partial \boldsymbol{A}}{\partial t} \quad (3.32)$$

Isolating the electric field we obtain:

$$\boldsymbol{E} = -\frac{\partial \boldsymbol{A}}{\partial t} - \nabla\varphi \quad (3.33)$$

The electric field can be split into a primary and a secondary field. The primary field, $-\frac{\partial \boldsymbol{A}}{\partial t}$, is a direct result of the change in the magnetic field. The secondary field, $-\nabla\varphi$, arises from the accumulation of charges at tissue interfaces caused by the primary field. The minus sign is for convention as the secondary electric field opposes the primary field [31].

Equation 3.33 describes the electric field induced in the head by transcranial magnetic stimulation given the magnetic vector potential, $\boldsymbol{A}$, and the electric scalar potential, φ. To solve equation 3.33, numerical methods are needed. SimNIBS is a transcranial stimulation simulator that allows estimating the electric field generated by transcranial magnetic stimulation in realistic head models.

3.3 Modelling transcranial magnetic stimulation using SimNIBS

SimNIBS is an open-source software package that simulates the electric field induced by transcranial magnetic stimulation and transcranial electric stimulation in realistic head models [247].

SimNIBS relies on GMSH, FreeSurfer, GetFEM and FSL. GMSH is an open-source 3D finite element mesh generator. FreeSurfer is an open-source software to process, analyse and visualise human brain magnetic resonance images. GetFEM is an open-source library to solve systems of partial differential equations with the finite element method [248]. FSL is a software for analysing magnetic resonance imaging data.

A basic SimNIBS workflow consists of three main parts:

- Generation of realistic head models from magnetic resonance images;
- Calculation of the electric field induced in the head;
- Visualisation and analysis of the results.

3.3.1 Generating head models from MR images

SimNIBS generates a tetrahedral volume mesh of the head given 4 magnetic resonance images, two T1-weighted images and two T2-weighted images, one fat suppressed image for each.

The first step is to segment the magnetic resonance images into the white matter, grey matter, skull, skin and cerebrospinal fluid using FreeSurfer and FSL (see Figure 3.6). The FreeSurfer software reconstructs topologically correct, closed surface models of the cerebral hemispheres separately, artificially cutting the corpus callosum [249]. To decouple these areas, it is assumed that each surface is embedded into the next.

Starting from the outermost layer, the boundaries between the areas are delimited creating the outer surfaces of each area.



Figure 3.6 Segmentation and meshing results for “Ernie”, an exemplary subject whose pre-built head model is available on SimNIBS. A: View of the surfaces of the final meshes, including skin, skull, cerebrospinal fluid, grey matter and white matter. B: Coronal and axial slices of the T1-weighted image with the segmented tissue boundaries in red. Image taken from [250].

These meshed surfaces are represented by triangular elements. The surface meshes are preprocessed removing overlapping and degenerate triangles and optimizing the spatial uniformity of the distribution of the vertices. The corpus callosum is added back to join the two hemispheres.

The surface meshes define the five subvolumes white matter, grey matter, skull, skin and cerebrospinal fluid. Using GMSH, each subvolume is populated with tetrahedral elements, generating the head mesh. The final meshes contain around 500,000 nodes and 3,500,000 tetrahedra [251]. Finally, each tissue type is assigned a conductivity value: 0.126, 0.276, 1.654, 0.010, 0.456 S/m for the white matter, grey matter, cerebrospinal fluid, skull and skin [250].

SimNIBS provides several datasets of pre-built example head models [252].

3.3.2 Electric field calculation

The electric field induced in the head model by transcranial magnetic stimulation is predicted by:

- Positioning the desired coil model above the desired target;
- Calculating the magnetic vector potential generated by the coil;

- Estimating the induced electric field.

SimNIBS provides several pre-built TMS coil models [253]. The coil position, its distance from the scalp and its rate of change of current can be set by the user.

In Section 3.2, I explained how the induced electric field can be expressed in terms of the magnetic vector potential and the electric scalar potential. In order to estimate the induced electric field using the finite element method, the electric scalar potential, φ, needs to be expressed in terms of the magnetic vector potential, $\boldsymbol{A}$.

The current density $\boldsymbol{J}$, is determined by Ohm's law as:

$$\boldsymbol{J} = \sigma \boldsymbol{E} \tag{3.34}$$

where σ is the conductivity of the tissue. Substituting $\boldsymbol{E}$ from equation 3.33 in equation 3.34 we get:

$$\boldsymbol{J} = -\sigma \nabla \varphi - \sigma \frac{\partial \boldsymbol{A}}{\partial t} \tag{3.35}$$

In the quasi-static state, the charge density continuity equation gives:

$$\nabla \cdot \boldsymbol{J} = 0 \tag{3.36}$$

Substituting $\boldsymbol{J}$ from equation 3.35 we get:

$$\nabla \cdot (\sigma \nabla \varphi) = -\nabla \cdot \left(\sigma \frac{\partial \boldsymbol{A}}{\partial t} \right) \tag{3.37}$$

Equation 3.37 is solved using GetFEM. The time derivative of the magnetic vector potential, $\boldsymbol{A}$, of the chosen TMS coil is used as input to the FEM calculations (see Section 3.2.1, equation 3.29). The FEM solver determines the electric scalar potential, φ, at each node. Given the primary electric field described by $\boldsymbol{A}$, and the secondary electric field described by φ, the induced electric field is determined in each mesh element based on equation 3.33.

3.4 Conclusion

In this chapter I provided the background knowledge required to understand the remainder of this dissertation, including the mathematical and physical principles underlying neuron modelling, TMS, and computational models of TMS. In the next chapter, I describe the computational model of the cerebellar cortex I developed.

Chapter 4

Model of the cerebellar cortex

This chapter describes the biologically realistic model of the cerebellar cortex that I developed. The model is based on the cerebellar network proposed by Katakura et al. [2]. The chapter is structured as follows. First, I present the model introduced by Katakura et al. [2] and describe its main components. Next, I introduce my extended model and detail the equations governing its dynamics. Finally, I present results demonstrating that the extended model reproduces key physiological behaviours reported in experimental studies and the behaviour of the original cerebellar network proposed by Katakura et al. [2].

The work presented in this chapter addresses *The lack of a biologically realistic model of the cerebellar cortex*, which, as presented in Chapter 1, is the first gap in the literature tackled in my PhD.

4.1 Cerebellar model by Katakura et al.

The cerebellar model by Katakura's et al. [2] is made up of the granular layer model by Sudhakar et al. [3] connected to the De Schutter & Bower Purkinje cell [4], [5] in a feedforward manner (see Figure 4.1). In the granular layer, granule and Golgi cells are explicitly modelled.

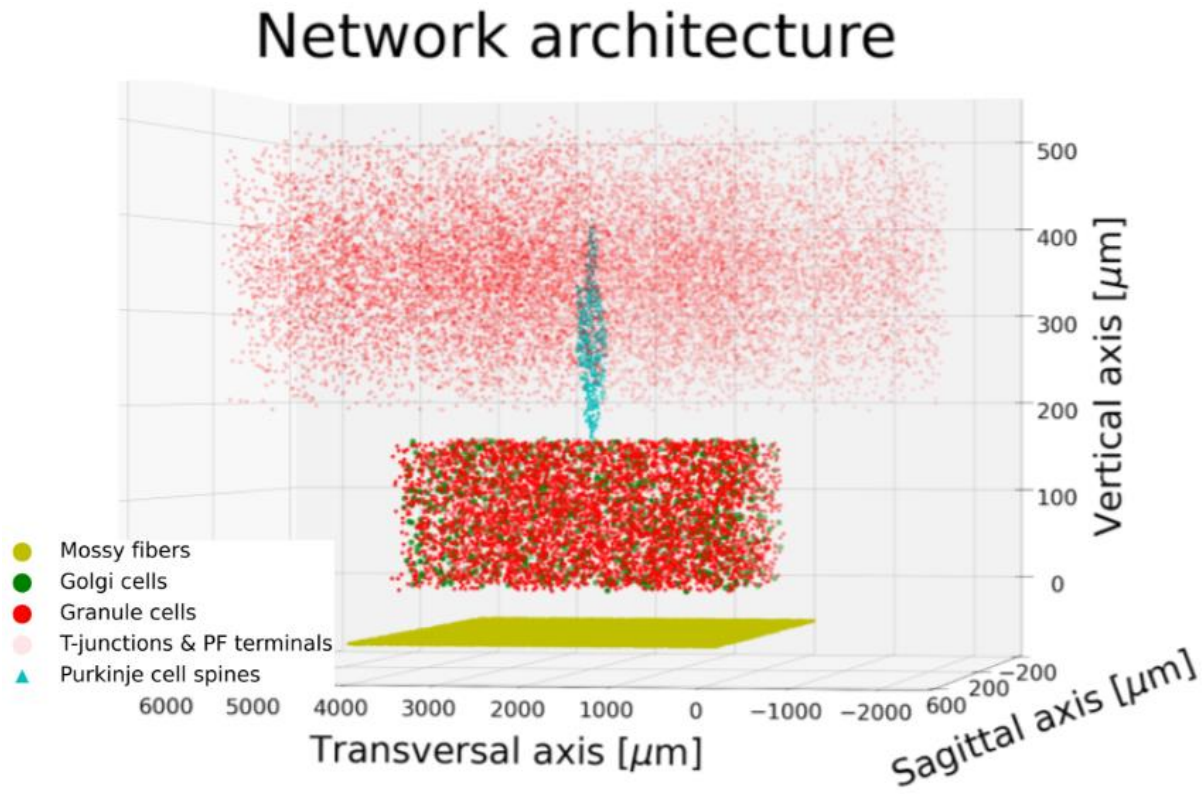


Figure 4.1 Network architecture of the cerebellar model. Light green dots represent the mossy fibre locations, dark green dots represent Golgi cells soma, dark red dots represent granule cells soma, transparent red dots represent the T-junction and the parallel fibre terminals of each granule cell and blue triangles represent the location of the spines of the Purkinje cell.

To reduce computational requirements, the granular layer network and the Purkinje cell are simulated separately. First, the granular layer network is simulated and the spike times of the granule cells are recorded. These spike trains are then used to drive the Purkinje cell model. In the next sections I will describe the granular layer model, the Purkinje cell model and the synaptic connections in the network.

4.1.1 Granular layer network model

The granular layer model is based on the work of Sudhakar et al. [3]. It contains 491,520 single-compartment granule cells [254] and 1,228 multi-compartment Golgi cells [71]. Both cell types include biologically plausible ion channels, which are modelled either using the Hodgkin–Huxley formalism or as Markov multistate transition models (see Chapter 3 for a description of how ionic channels are modelled).

The network spans 4000 μm × 400 μm × 510 μm along the transversal, sagittal, and vertical axes. The heights of the granular layer, Purkinje layer, and molecular layer are set to 160 μm, 30 μm, and 320 μm, resulting in a total vertical extent of 510 μm.

The density of Golgi cells is set to 4,800 cells/mm^3, and the number of granule cells is determined by imposing a granule-to-Golgi cell ratio of 400. The somatic centres of all neurons are uniformly distributed within the granular layer.

Mossy fibres are arranged in a plane below the granular layer. This plane measures 4208 μm × 768 μm along the transversal and sagittal axes. The mossy fibre density is set to 5,000 cells/mm^3, resulting in 16,158 mossy fibres within the network. Mossy fibre activity is modelled as Poisson spike trains with a mean firing rate of 5 Hz.

Golgi cells consist of a soma, two basolateral dendrites, and two apical dendrites. The basolateral dendrites project downward to receive mossy fibre inputs, whereas the apical dendrites extend upwards into the molecular layer to connect with parallel fibres. To account for biological variability, the orientation of Golgi cell dendrites varies randomly.

The angles defined by the vertical straight line passing through the soma and each apical dendrite, θ_{a1} and θ_{a2}, are uniformly distributed between 30° and 120°, while the angles defined by the same straight line and each basolateral dendrite, θ_{b1} and θ_{b2}, are uniformly distributed between -20° and -240° (see Figure 4.2). θ_{b1} and θ_{b2} are negative by convention, to indicate that the basolateral dendrites extend downwards. θ_{a1} and θ_{a2} are set independently from θ_{b1} and θ_{b2}, as there is no experimental data documenting a spatial relationship between apical and basolateral dendrites in a Golgi cell.

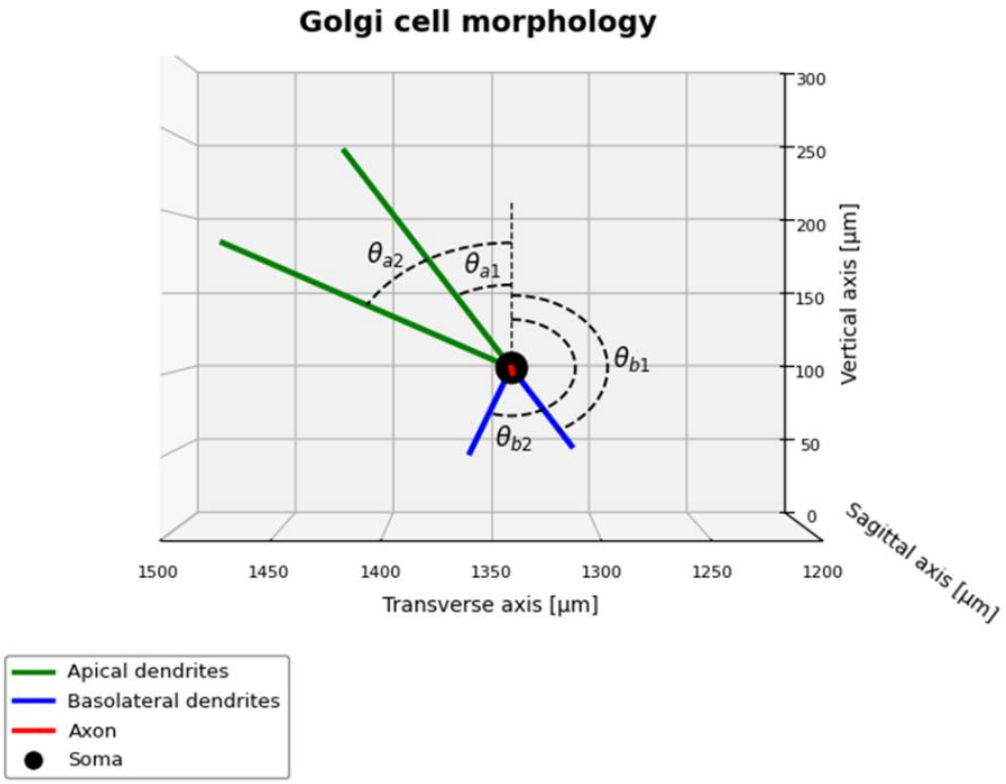


Figure 4.2 Golgi cell morphology. Soma in black, basolateral dendrites in blue, apical dendrites in green and axon in red. The angles formed by the straight line parallel to the vertical axis passing through the soma and the apical dendrites, θ_{a1} and θ_{a2}, and the basolateral dendrites, θ_{b1} and θ_{b2}, are shown.

To account for biological variability, random variations are introduced in cellular and synaptic parameters. Specifically, the soma diameters of Golgi and granule cells vary uniformly by up to 20%, and their initial resting membrane potentials are uniformly distributed between –60 mV and –75 mV. In addition, the maximum synaptic conductance of all synapses follows a normal distribution with a coefficient of variation of 0.25.

4.1.2 Purkinje cell model

The Purkinje cell model used in the cerebellar network proposed by Katakura et al. [2] is a biologically realistic neuron with a detailed morphology and ionic currents modelled using the Hodgkin–Huxley formalism [4], [5]. The cell consists of a soma, 1,599 dendritic compartments, of which 1,472 are spiny dendrites, and one spine per spiny dendrite [5].

Spines are represented by a cylindrical spine neck (length 0.66 µm, diameter 0.20 µm) connected to the centre of the spiny dendrite, and a spherical spine head (diameter

0.5 μm) attached to the distal end of the neck. The spine dimensions are taken from experimental measurements of rat Purkinje cell spines by Harris and Stevens [255].

The soma of the Purkinje cell is positioned at the centre of the network in the transversal and sagittal planes, and at the centre of the Purkinje layer along the vertical axis.

4.1.3 Synaptic connections

The synaptic connectivity within the network is organised as follows. Mossy fibres provide excitatory input to both granule cells and Golgi cells. Granule cells, in turn, excite Golgi cells and the Purkinje cell. Golgi cells connect to other Golgi cells through both inhibitory chemical synapses and electrical coupling via gap junctions, and they also inhibit granule cells. Signal transmission includes a delay that depends on the distance between neurons. The conduction velocity of the granule cell axons is set to 0.5 m/s [256], while the conduction velocity of all other axons and fibres is set to 2 m/s [257].

4.1.3.1 Synaptic model

All synapses, except those between mossy fibres and granule cells, are modelled with a double exponential formulation (see Section 3.1.5 for a description of synaptic models). As described in Section 3.1.5, the synaptic current, I_{syn}, is given by:

$$I_{syn} = g_{syn}(V - E_{syn}) \tag{4.1}$$

where E_{syn} is the reversal potential, and the synaptic conductance, g_{syn} is modelled as a difference of two exponentials:

$$g_{syn} = \bar{g}_{syn} * N * \left(e^{-\frac{t-t_s}{\tau_{decay}}} - e^{-\frac{t-t_s}{\tau_{rise}}} \right) \tag{4.2}$$

where $\bar{g}_{syn}$ is the maximum synaptic conductance, τ_{rise} and τ_{decay} are the rise and decay time constants, t_s is the time of arrival of a presynaptic spike and N is a normalisation factor that ensures that the peak conductance equals $\bar{g}_{syn}$.

4.1.3.2 Mossy fibre to Golgi cells connections

Mossy fibres connect to Golgi cells through a specialised synaptic terminal called a rosette. Mossy fibre rosettes connect to the basolateral dendrites of Golgi cells within a sphere of radius 100 μm with a probability of 0.03. These synapses only contain AMPA receptors. Parameters to calculate the synaptic current (equation 4.1) are as follows: $\bar{g}_{syn} = 300\ pS$, $\tau_{rise} = 0.13\ ms$, $\tau_{decay} = 1.1\ ms$ and $E_{syn} = 0\ mV$.

4.1.3.3 Golgi cells to granule cells connections

Golgi cells connect to granule cells within a range of 650 μm and 180 μm along the sagittal and transversal axes, with a connection probability of one sixth. The distance is calculated between the somata of the two cells.

The decay consists of two components, a transient and a spillover component:

$$\frac{1}{\tau_{decay}} = \frac{1}{\tau_{transient}} + \frac{1}{\tau_{spill}} \tag{4.3}$$

where $\tau_{transient} = 5\ ms$ and $\tau_{spill} = 35\ ms$.

These synapses only contain GABA receptors. Parameters to calculate the synaptic current (equation 4.1) are as follows: $\bar{g}_{syn} = 100\ pS$, $\tau_{rise} = 3\ ms$ and $E_{syn} = -80\ mV$.

4.1.3.4 Granule cells to Golgi cells connections

Parallel fibres and ascending axons are not explicitly modelled for computational costs. Instead, they are represented conceptually as straight lines in order to estimate distances to postsynaptic neurons. Ascending axons are conceptualised as straight lines parallel to the vertical axis, with lengths normally distributed between 200 μm and 360 μm and presynaptic terminals spaced every 50 μm. Parallel fibres are represented as straight lines parallel to the transversal axis extending 2000 μm on either side of the T-junction, with presynaptic terminals every 7.5 μm.

Connections between granule cells and Golgi cells are formed within a radius of 15 μm and 5 μm between the apical dendrites of Golgi cells and the presynaptic terminals of ascending axons and parallel fibres. One sixth of ascending axons and 90% of randomly selected parallel fibres within this range form synapses with the Golgi cell, with a maximum of 1,000 connections (prioritising the closest connections).

These synapses only contain AMPA receptors. In the case of excitatory inputs from parallel fibres, the parameters to calculate the synaptic current (equation 4.1) are as follows: $\bar{g}_{syn} = 200\,pS$, $\tau_{rise} = 0.06\,ms$ and $\tau_{decay} = 0.6\,ms$ and $E_{syn} = 0\,mV$. In the case of excitatory inputs from ascending axons, parameters to calculate the synaptic current (equation 4.1) are as follows: $\bar{g}_{syn} = 240\,pS$, $\tau_{rise} = 0.06\,ms$, $\tau_{decay} = 0.5\,ms$ and $E_{syn} = 0\,mV$.

4.1.3.5 Golgi cells to Golgi cells connections

Golgi cells are interconnected via inhibitory synapses and gap junctions. Golgi cells are allowed to connect if they are within a distance, x, of 150 µm of each other as seen experimentally [91]. The probability of connection, p, depends on the distance between cells and is defined as:

$$p = \frac{A_1 - A_2}{1 + e^{\frac{x - x_0}{\Delta x}}} + A2 \tag{4.4}$$

where x is the distance between the source and target cells' soma. For gap junctions, $A_1 = 0.91$, $A_2 = -17.45$ and $\Delta x = 55\,\mu m$; for inhibitory connections, $A_1 = 1.71$, $A_2 = -19.45$ and $dx = 118\,\mu m$. The parameter $x_0 = 376\,\mu m$ is used in both cases.

For chemical synapses mediated by GABA receptors, parameters to calculate the synaptic current (equation 4.1) are as follows: $\bar{g}_{syn} = 330\,pS$, $\tau_{rise} = 1.9\,ms$, $\tau_{decay} = 14.1\,ms$ and $E_{syn} = -80\,mV$.

For a pair of Golgi cells i and j, with membrane potentials V_i and V_j, the gap junction current is given by:

$$I_{gap} = -g_{gap} * d_{ij} * (V_i - V_j) \tag{4.5}$$

where d_{ij} is the distance between the soma of the two Golgi cells. The gap junction conductance, g_{gap}, decays as a function of distance:

$$g_{gap}(d_{ij}) = \bar{g}_{gap} * e^{-\lambda d_{ij}} \tag{4.6}$$

Where $\bar{g}_{gap} = 1.659\,nS$ is the maximum synaptic conductance and $\lambda = 0.01259\,\mu m^{-1}$ is the length constant.

4.1.3.6 Purkinje cell connections

Each Purkinje cell spine connects to the $\lfloor d_s L \rfloor$ closest presynaptic terminals from parallel fibres and ascending axons, where $d_s = 13\ \mu m^{-1}$ is the spine density, L is the length of the spiny dendrite and $\lfloor x \rfloor$ denotes the floor function. In total, the Purkinje cell receives 143,724 excitatory synaptic inputs distributed across 1,474 spines.

Signal transmission delays are determined by the length of the ascending axon plus the distance from the spine to the T-junction, assuming a transmission velocity of 0.5 m/s.

The Purkinje cell also receives inhibitory inputs from stellate cells, which are modelled as Poisson spike trains with a mean firing rate of 1 Hz. The model includes one inhibitory input per dendrite (both smooth and spiny), and each inhibitory input is unique.

Both excitatory and inhibitory synapses onto the Purkinje cell are modelled using the double-exponential formulation described in equation 4.1. For excitatory inputs, the parameters are $\bar{g}_{syn} = 1\ nS,\ \tau_{rise} = 0.5\ ms,\ \tau_{decay} = 1.2\ ms$ and $E_{syn} = 0\ mV$. For inhibitory inputs, the parameters are $\tau_{rise} = 0.93\ ms,\ \tau_{decay} = 26.50\ ms$ and $E_{syn} = -80\ mV$. The maximum conductance is $\bar{g}_{syn} = 1.4 \times 10^{-5}\ \mu S/\mu m^2$ for synapses targeting smooth dendrites and $\bar{g}_{syn} = 7.0 \times 10^{-5}\ \mu S/\mu m^2$ for inputs targeting spiny dendrites.

4.1.3.7 Mossy fibre to granule cell connections

Connections between mossy fibre rosettes and granule cells' soma were established within a maximum distance of 30 μm. Experimental evidence suggests that granule cells have on average four dendrites and a maximum of seven dendrites, each connecting with one rosette [258]. To reflect this in the model, each granule cell can receive up to seven mossy fibre inputs. The probability of forming connections decreases as the number of established inputs increases. Assuming that at least seven rosettes are present within a 30 μm radius of a granule cell soma, the first three inputs occur with a probability of 100%. The probabilities for the fourth, fifth, sixth, and seventh inputs are 90%, 45%, 3%, and 2%.

Synapses between mossy fibres and granule cells are modelled using a detailed representation of presynaptic dynamics that accounts for short-term potentiation and depression, following the approach described in [254] which is a development of [259]. This modelling choice was motivated by the fact that NMDA receptors expressed in cerebellar granule cells exhibit a characteristically low open probability (~0.04) [260], a property that cannot be adequately represented by a phenomenological model.

Both AMPA and NMDA receptors are represented using Markov state models (see Section 3.1.4 for a description of Markov models for ion channels). For the AMPA receptor, the synaptic current, I_{syn}, is defined as:

$$I_{syn} = \bar{g}_{syn} * O_{syn} * \left(V - E_{syn}\right) \tag{4.7}$$

where $\bar{g}_{syn} = 1200\, pS$ is the maximum synaptic conductance, $E_{syn} = 0\, mV$ is the reversal potential and O_{syn} represents the fraction of receptors in the open state.

The AMPA receptor kinetics include three states: closed, C, open, O, and deactivated, D. Transitions between these states are governed by the kinetics below:

$$\mathrm{D} \underset{r_4}{\overset{R_3}{\rightleftarrows}} \mathrm{C} \underset{R_2}{\overset{r_1}{\rightleftarrows}} \mathrm{O} \tag{4.8}$$

where $R_2 = 0.82\, ms^{-1}$, $R_3 = 0.013\, ms^{-1}$, while the transition rates r_1 and r_4 depend on glutamate concentration according to the equation below:

$$r_i = R_i * \frac{T^2}{(T + k_B)^2} \tag{4.9}$$

where $k_B = 0.44\, mM$, $R_1 = 5.4\, ms^{-1}mM^{-1}$, $R_4 = 1.12\, ms^{-1}mM^{-1}$ and T is the effective glutamate concentration in the synaptic cleft.

The glutamate concentration is obtained by combining a synaptic pulse component, T_s, with a diffusion component, T_d:

$$T(t) = T_s(t) + T_d(t) = Y(t)(\bar{T}_s + \bar{T}_d) \tag{4.10}$$

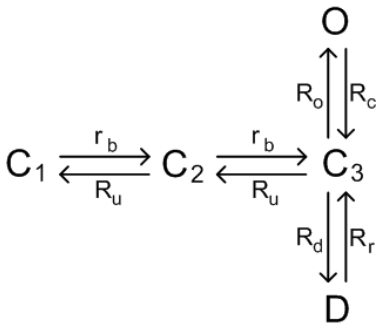
where $\bar{T}_s = 1\, mM$, $\bar{T}_d = 0.83\, mM$. Y represents the fraction of released neurotransmitters, the dynamics of which are defined later (see equation 4.14).

For NMDA receptors, the synaptic current also depends on a voltage-dependent magnesium block. Although magnesium concentration is not explicitly modelled, its effect is incorporated through an exponential term:

$$I_{syn} = \bar{g}_{syn} * O_{syn} * \left(V - E_{syn}\right) * \frac{1}{1 + e^{\frac{v - v_{block}}{k_{block}}}} \tag{4.11}$$

where $v_{block} = -20\ mV$, $k_{block} = 13\ mV$, $\bar{g}_{syn} = 18{,}800\ pS$ and $E_{syn} = -3.7\ mV$.

NMDA receptors can occupy five states: three closed states, C_1, C_2, C_3, one deactivated state, D, and one open state O. Transitions between these states are governed by the kinetics below:



(4.12)

where $R_u = 0.1\ ms^{-1}$, $R_d = 21\text{x}10^{-4}\ ms^{-1}$, $R_r = 9\text{x}10^{-3}\ ms^{-1}$, $R_o = 3\text{x}10^{-2}\ ms^{-1}$, $R_c = 0.966\ ms^{-1}$ and $r_b = R_b * T(t)$, with $R_b = 5\ ms^{-1}mM^{-1}$. In this case, glutamate concentration only depends on diffusion, so equation 4.10 becomes:

$$T(t) = Y(t) * \bar{T}_d \tag{4.13}$$

with $\bar{T}_d = 0.83\ mM$.

The presynaptic dynamics model tracks three pools of neurotransmitter resources: available, X, released, Y, and recovered, Z. Neurotransmitter release depends on the release probability, P, and the dynamics are described by:

$$\frac{dX}{dt} = \frac{Z}{\tau_R} - P * X * \delta\left(t - t_{spike}\right)$$

$$\frac{dY}{dt} = -\frac{Y}{\tau_I} + P * X * \delta\left(t - t_{spike}\right) \tag{4.14}$$

$$\frac{dZ}{dt} = \frac{Y}{\tau_I} - \frac{Z}{\tau_R}$$

$$\frac{dP}{dt} = -\frac{P}{\tau_F} + p(1 - P) * X * \delta\left(t - t_{spike}\right)$$

where $\tau_F = 10.8\,ms$, $\tau_R = 35.1\,ms$ and $\tau_I = 3\,ms$ are the time constants of synaptic facilitation, recovery of the releasable neurotransmitters and synaptic inactivation. The function δ denotes the Dirac's delta function, and p represents the initial value for the release probability P.

At the time of a presynaptic spike, a proportion P of the available neurotransmitters is released. When the pool of available neurotransmitters, X, becomes depleted, synaptic depression occurs. Changes in the release probability, P, governs synaptic facilitation.

This presynaptic dynamics model was developed by Tsodyks et al. [261], [262] and fitted to mossy fibre data by Nieus et al. [254]. The rationale behind this modelling choice is that mossy fibre to granule cell synapses exhibit both depression and facilitation [263]: this model allows to capture both phenomena simultaneously and interactively as a consequence of a single resource pool.

4.2 Updated cerebellar cortex model

I have updated the original model of the cerebellum by employing a more recent Purkinje cell model [6] and by switching the single compartment granule cells in the granular layer model to multi-compartment neurons [7]. This modification was necessary to couple the TMS model to all neuronal types in a consistent manner. I coupled the TMS model to the neurons through an extracellular voltage (see Section 5.2.3). In a single-compartment neuron, the extracellular voltage is uniform across the entire membrane, so it produces no net driving force on the transmembrane current and has no effect on the neuron's dynamics.

For computational costs, I reduced the size of the granular layer to 2000 μm × 200 μm and that of the mossy fibre plane to 2008 μm × 568 μm along the transversal and sagittal axes. I did not vary the network extension along the vertical axis. This results in 6,270 mossy fibres, 307 Golgi cells and 122,880 granule cells (see Table 4.1 for a summary of the number of modelled cells in the network). The model is simulated using the NEURON simulator.

Explicitly modelled neurons		
Granule cells	Golgi cells	Purkinje cells
122,880	307	1
Poisson spike trains		
Mossy fibres	Stellate cells	Basket cells
6,270	9	4

Table 4.1 Summary of the modelled cells. Granule, Golgi and Purkinje cells are explicitly modelled. Mossy fibres, stellate cells and basket cells are modelled as Poisson spike trains.

Interneurons inhibiting the Purkinje cell (see Table 4.1 and Section 4.2.5) are not explicitly modelled for computational costs. Neuronal morphology correlates with neuronal polarization caused by TMS-induced electric fields [215], [264]. Interneurons are small, symmetrical neurons: the effects of TMS on interneurons is expected to be modest and can be neglected as a first approximation.

In the next sections, first I introduce the notation that will be used in the rest of the chapter to characterise the ionic channels of the cells. Then I characterize each modelled cell: its morphology, its passive properties and the equations describing the dynamics of its ionic channels. Then I describe the synaptic connections. Finally, I detail the analysis done to ensure that the network maintains the desired behaviour after the changes made.

4.2.1 Ionic current notation

Most ionic currents are modelled following the Hodgkin-Huxley formalism (see Chapter 3 for a description of the Hodgkin-Huxley formalism). The ionic current, I, is given by:

$$I_{ion} = \bar{g}_{ion} * m^a * h^b \tag{4.15}$$

where $\bar{g}_{ion}$ represents the maximal channel conductance, m and h are the gating variables and their exponents, a and b, are the number of activation and inactivation gates per channel.

A generic gating variable, x, dynamics are:

$$\frac{dx}{dt} = \frac{x_\infty - x}{\tau_x} \tag{4.16}$$

where the steady state of the gating variable, x_∞, and its time constant, τ_x, are defined as below:

$$x_\infty = \frac{\alpha_x}{\alpha_x + \beta_x}$$
$$\tau_x = \frac{1}{\alpha_x + \beta_x} \quad (4.17)$$

where α_x and β_x are rate constants that depend on voltage. Tables 4.2, 4.3, 4.6, 4.8 and 4.9 summarise the maximum conductance of each ionic channel and the passive properties of the cell. All equations in the tables 4.4, 4.7 and 4.10 describe the rate constants for each channel. In a few cases, the gating variables do not follow equations 4.16 and 4.17. In those instances, the equations for the gating variables are provided in the table as well. Ionic currents that do not follow the standard Hodgkin-Huxley formalism are denoted with an asterisk, and the current equation is detailed below the corresponding table.

All simulations are performed at 37°C. To account for the fact that experimental recordings were performed at different temperatures, the rate constants must be scaled by the following temperature scaling factor:

$$Q_{10}^{\frac{T-T_0}{10}} \quad (4.18)$$

Tables 4.5 and 4.12 summarise the Q_{10} factor, and the experimental temperature T_0 of each ionic channel.

4.2.2 Granule cell model

The employed granule cell model [7] consists of a soma, four dendrites, an axon and an axon initial segment (hillock) and four passive branches (see Figure 4.3). The explicitly modelled axon represents part of the ascending axon that can connect to other cells. For computational constraints, parallel fibres are not explicitly modelled.

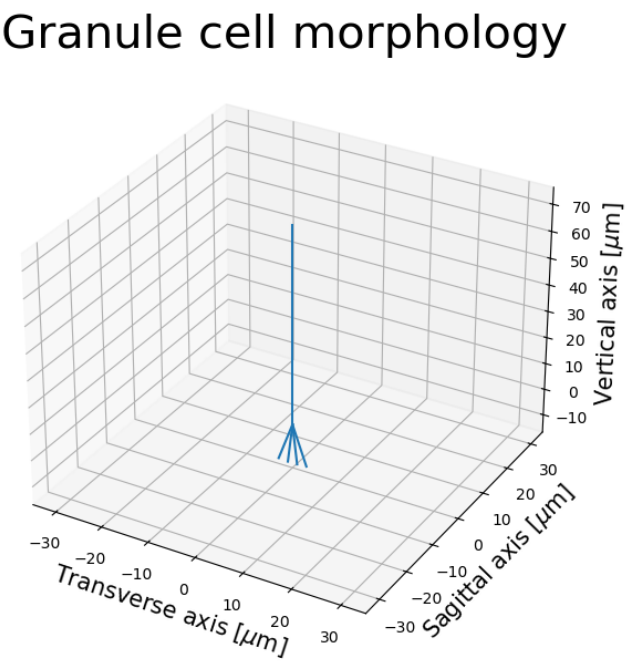


Figure 4.3 Granule cell morphology.

The passive properties of the granule cells are summarised in Table 4.2.

Passive properties	**Axon**	**Hillock**	**Soma**	**Dendrites**	**Branches**
Membrane capacitance $\frac{\mu F}{cm^2}$	1	1	1	1	1
Membrane conductance $\frac{S}{cm^2}$	$8.58x10^{-6}$	$9.62x10^{-5}$	$1.07x10^{-4}$	$4.51x10^{-5}$	$5x10^{-9}$
Axial resistance Ωcm	100	100	100	100	100

Table 4.2 Passive properties of the granule cell for each compartment type. The specific membrane capacitance is expressed in μF/cm², the specific membrane conductance is expressed in S/cm² and the specific axial resistance is expressed in Ωcm.

The cell contains a sodium current (I_{Na}); five potassium currents including a delayed rectifier current $(I_{K_{DR}})$, a fast current (I_{K_A}), an inward rectifier current $(I_{K_{IR}})$, a calcium dependent current $(I_{K_{CA}})$ and a slow repolarising current $(I_{K_{slow}})$; and a calcium current (I_{Ca}). The branches of the granule cells are passive. Table 4.3 summarises the maximum conductances of each ionic current for each section in the granule cell. If the ionic channel is not present in a section, no value for the conductance is given.

Maximum conductance $\left(\frac{\mu S}{cm^2}\right)$	**Axon**	**Hillock**	**Soma**	**Dendrites**
Na	$2.71\text{x}10^{-2}$	$2.45\text{x}10^{-2}$		
K_{DR}	$4.47\text{x}10^{-3}$	$1.81\text{x}10^{-3}$		
K_A			$9.06\text{x}10^{-3}$	
K_{IR}			$2.55\text{x}10^{-3}$	
K_{Ca}				0.38
Ca				$5.84\text{x}10^{-3}$
K_{slow}			0.00025	

Table 4.3 Maximum conductance of the ionic currents of the granule cell expressed in μS/cm². If the channel is not present in a section, no value for the conductance is given.

The reversal potential is set to 87.39 mV for the sodium current, to -84.68 mV for all potassium currents and to 129.33 mV for the calcium current. Table 4.4 summarises the rate constants of all modelled channels. Gating variable dynamics follow equations 4.16 and 4.17. If the steady state of the gating variable or its time constant does not follow equation 4.17, their equation is provided in the table below the rate constants for the corresponding channel. All ionic currents are given by equation 4.15, unless the channel is noted by an asterisk, in which case the current equation is provided below the table.

Channel	**Exponent**	**Rate constant α**	**Rate constant β**
Ca	2	$\alpha_m = 0.15e^{-0.063(V+29.06)}$	$\beta_m = 0.089e^{-0.039(V+18.66)}$
	1	$\alpha_h = 0.0039e^{-0.055(V+48)}$	$\beta_h = 0.0039e^{0.012(V+48)}$
K_{slow}	1	$\alpha_m = 0.008e^{0.025(V+30)}$	$\beta_m = 0.008e^{-0.05(V+30)}$
		$m_\infty = \frac{1}{1+e^{-\frac{V+30}{6}}}$	

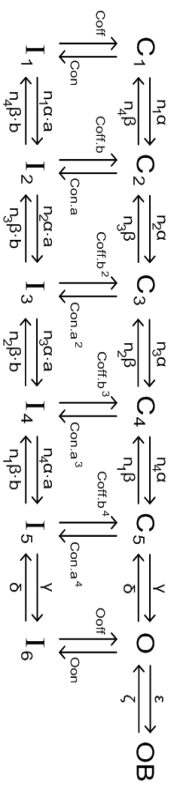
* Na	N.A.		$\alpha = 353.9e^{\frac{V}{13.9}}\ ms^{-1}$ $\beta = 31.272e^{\frac{V}{13.9}}\ ms^{-1}$ $\gamma = 150\ ms^{-1}$ $\delta = 40\ ms^{-1}$ $n_1 = 5.42$ $n_2 = 3.28$ $n_3 = 1.83$ $n_4 = 0.74$ $Con = 0.005\ ms^{-1}$ $Coff = 0.5\ ms^{-1}$ $Oon = 0.75\ ms^{-1}$ $Ooff = 0.005\ ms^{-1}$ $\varepsilon = 1.75\ ms^{-1}$ $\varsigma = 0.03201\ ms^{-1}$ $a = \left(\frac{Oon}{Con}\right)^{\frac{1}{4}}$ $b = \left(\frac{Ooff}{Coff}\right)^{\frac{1}{4}}$
K_V	4	$\alpha_m = \frac{0.13(V+25)}{1-e^{-\frac{V+25}{10}}}$	$\beta_m = 1.69e^{-0.0125(V+35)}$
K_A	3	$\alpha_m = \frac{2.445}{1+e^{-\frac{V+9.17}{23.32}}}$	$\beta_m = 0.497e^{-\frac{V+18.28}{19.47}}$
	1	$\alpha_h = \frac{0.11}{1+e^{\frac{V+111.33}{12.84}}}$	$\beta_h = \frac{0.103}{1+e^{-\frac{V+49.95}{8.9}}}$
		$m_\infty = \frac{1}{1+e^{-\frac{V+46.7}{19.8}}}$	$h_\infty = \frac{1}{1+e^{\frac{V+78.8}{8.4}}}$
K_{IR}	1	$\alpha_m = 0.4e^{-0.041(V+83.94)}$	$\beta_m = 0.51e^{-0.028(V+83.94)}$
K_{Ca}	1	$\alpha_m = \frac{2.5}{1+\frac{0.15*10^{-3}*e^{-0.085V}}{[Ca]}}$	$\beta_m = \frac{1.5}{1+\frac{[Ca]}{0.15*10^{-3}*e^{-0.085V}}}$

Table 4.4 Rate constants of the ionic channels of the granule cell. Gating variable dynamics follow equations 4.16 and 4.17. If the steady state of the time constant of the gating variable does not follow equation 4.17, their equation is provided below the rate constants for the corresponding channel. m denotes activating gating variables, h denotes inactivating gating variables. The exponents denote the number of activation and inactivation channels (a and b in equation 4.15).

The sodium current is modelled with a Markov multistate model. The sodium current, I_{Na}, is given by:

$$I_{Na} = \bar{g}_{Na} * O_{Na} * (V - E_{Na}) \quad (4.19)$$

Where O_{Na} denotes the fraction of open channels.

A potassium current, K_{Ca}, depends on the intracellular calcium concentration, $[Ca]$. The dynamics of intracellular calcium concentration, $[Ca]$, are as below:

$$\frac{d[Ca]}{dt} = -\frac{I_{Ca}}{2FAd} - \beta_{Ca}([Ca] - [Ca]_0) \quad (4.20)$$

where A is the surface area of the dendrite in which the calcium concentration is modelled, $d = 200\,nm$ is the depth of a shell adjacent to the cell where the calcium concentration is measured, $\beta_{Ca} = 0.6$ determines the loss of calcium ions from the shell approximating the effect of fluxes, ionic pumps, diffusion, and buffers, $F = 96.485\,C/mol$ is the Faraday constant and $[Ca]_0 = 100\,nM$ is the resting calcium concentration. Calcium dynamics were modelled only in the dendrites, as no other section has a calcium dependent potassium current.

Gating kinetics were corrected using a Q_{10} factor of 3 for all currents according to equation 4.18 to account for temperature differences between experimental recordings and the simulations. Table 4.5 summarises the experimental temperature at which the recordings were done (T_0 in equation 4.18).

	K_V	Na_{rsg}	K_A	K_{IR}	K_{Ca}	Ca	K_{slow}
T_0	6.3℃	20℃	25.5℃	20℃	30℃	20℃	22℃

Table 4.5 Temperature at which the ionic currents were recorded.

4.2.3 Golgi cell model

I did not alter the Golgi cell model [71]. All compartments, except for the soma, are passive. All compartments have a membrane resistance of 47.6 KΩcm^2, an axial resistance of 100 Ωcm and a membrane capacitance of 1 μF/cm^2.

Below I characterise the dynamics of its somatic ionic channel. The soma contains three sodium currents including a transient current (I_{Na_T}), a resurgent current (I_{Na_R}), and a persistent current (I_{Na_P}); five potassium currents including a voltage dependent

current (I_{K_V}), a fast current (I_{K_A}), a calcium dependent current $(I_{K_{CA}})$, a slow repolarising current $(I_{K_{slow}})$ and a voltage independent, calcium activated current $(I_{K_{SK2}})$; two calcium currents including a high $(I_{Ca_{HVA}})$ and a low threshold activated current $(I_{Ca_{LVA}})$; and two H-currents including slow and fast response channels ($I_{H_{CN1}}$ and $I_{H_{CN2}}$). Table 4.6 summarises the maximum conductances of each ionic current.

Channel	Maximum conductance $\left(\frac{\mu S}{cm^2}\right)$
Na_t	0.048
Na_r	0.0017
Na_p	$1.9\text{x}10^{-4}$
K_V	0.032
K_A	0.008
K_{Ca}	0.009
K_{slow}	0.001
Ca_{HVA}	$4.6\text{x}10^{-4}$
Ca_{LVA}	$2.5\text{x}10^{-4}$
K_{SK2}	0.038
H_{CN1}	$5\text{x}10^{-5}$
H_{CN2}	$8\text{x}10^{-5}$

Table 4.6 Maximum conductance of the ionic currents of the Golgi cells expressed in μS/cm^2.

The reversal potential is set to 77.39 mV for all sodium currents, to -94.6 mV for all potassium currents and to -30 mV for both H-type currents. Table 4.7 summarises the rate constants of all modelled currents. Gating variable dynamics follow equations 4.16 and 4.17. If the steady state of the gating variable, or its time constant does not follow equation 4.17, their equation is provided in the table below the rate constants for the corresponding current. All ionic currents are given by equation 4.15, unless the current is noted by an asterisk, in which case the current equation is provided below the table.

Channel	Exponent	Rate constant α	Rate constant β
Na_t	3	$\alpha_m = \frac{0.417(V+35)}{1-e^{-\frac{V+35}{10}}}$	$\beta_m = 16.68e^{-0.055(V+60)}$
	1	$\alpha_h = 0.292e^{-0.3(V+60)}$	$\beta_h = \frac{4.17}{1+e^{-\frac{V+27}{5}}}$
Na_r	1	$\alpha_m = \frac{1.11-68.5(V+6.48)}{10^4(e^{-\frac{V+6.48}{6.8}}-1)}$	$\beta_m = \frac{66+21.7(V+54)}{10^3(e^{\frac{V+54}{0.11}}-1)}$
	1	$\alpha_h = 0.443e^{-\frac{(V+90)}{62.5}}$	$\beta_h = 0.014e^{\frac{(V+93.3)}{16.1}}$
Na_p	1	$\alpha_m = \frac{0.421(V+50)}{1-e^{-\frac{V+50}{5}}}$	$\beta_m = \frac{-0.287(V+50)}{1-e^{-\frac{V+50}{5}}}$
		$m_\infty = \frac{1}{1+e^{\frac{53-V}{5}}}$	$\tau_\infty = \frac{5}{\alpha_m+\beta_m}$
K_V	4	$\alpha_m = \frac{0.062(V+36)}{1-e^{-\frac{V+36}{10}}}$	$\beta_m = 0.78e^{-\frac{(V+46)}{80}}$
K_A	3	$\alpha_m = \frac{0.62}{1+e^{-\frac{V+19.17}{23.32}}}$	$\beta_m = 0.126e^{-\frac{V+28.28}{19.47}}$
	1	$\alpha_h = \frac{0.028}{1+e^{\frac{V+121}{12.84}}}$	$\beta_h = \frac{0.026}{1+e^{-\frac{V+59.95}{8.9}}}$
		$m_\infty = \frac{1}{1+e^{-\frac{V+48}{17}}}$	$h_\infty = \frac{1}{1+e^{\frac{V+88.8}{8.4}}}$
K_{Ca}	1	$\alpha_m = \frac{3.2}{1+\frac{0.0015e^{-\frac{V+10}{11.7}}}{[Ca]}}$	$\beta_m = \frac{0.46}{1+\frac{[Ca]}{0.00015e^{-\frac{V+10}{11.7}}}}$
K_{slow}	1	$\alpha_m = 0.0037e^{\frac{V+40}{40}}$	$\beta_m = 0.0037e^{-\frac{V+40}{20}}$
		$m_\infty = \frac{1}{1+e^{-\frac{V+45}{6}}}$	
Ca_{HVA}	2	$\alpha_m = 0.0687e^{0.063(V+39)}$	$\beta_m = 0.115e^{-0.039(V+28.66)}$
	1	$\alpha_h = 1.8*10^{-3}*e^{-\frac{(V+58)}{18}}$	$\beta_h = 1.8*10^{-3}*e^{\frac{(V+58)}{83}}$

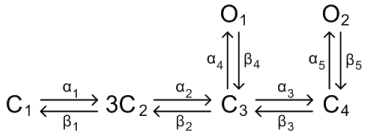
Ca_{LVA}	2	$m_\infty = \frac{1}{1+e^{-\frac{V+62}{7.4}}}$	$\tau_m = \frac{3}{0.5} + \frac{0.85}{e^{-\frac{V+30}{10}} + e^{-\frac{V+112}{15}}}$
	1	$h_\infty = \frac{1}{1+e^{-\frac{V+90}{5}}}$	$\tau_h = \frac{85}{0.9} + \frac{0.9}{e^{-\frac{V+58}{4}} + e^{-\frac{V+417}{50}}}$
$^*K_{SK2}$			$\alpha_1 = 200\ ms^{-1}$ $\beta_1 = 0.08\ ms^{-1}$ $\alpha_2 = 160\ ms^{-1}$ $\beta_2 = 0.08\ ms^{-1}$ $\alpha_3 = 80\ ms^{-1}$ $\beta_3 = 0.2\ ms^{-1}$ $\alpha_4 = 0.16\ ms^{-1}$ $\beta_4 = 1\ ms^{-1}$ $\alpha_5 = 1.2\ ms^{-1}$ $\beta_5 = 0.1\ ms^{-1}$
H_{CN1}	1	$r = 0.0021(V+10) + 0.97$ $x_{fast} = \frac{r}{1+e^{0.11(V+82.5)}}$ $x_{slow} = 1 - \frac{r}{1+e^{0.11(V+82.5)}}$	$\tau_{fast} = e^{2.3(0.014V+13.37)}$ $\tau_{slow} = e^{2.3(0.014V+14.07)}$
H_{CN2}	1	$r = 0.00227(V+10) - 1.47$ $x_{fast_\infty} = \frac{r}{1+e^{0.16(V+91.9)}}$ $x_{slow_\infty} = 1 - \frac{r}{1+e^{0.16(V+91.9)}}$	$\tau_{fast} = e^{2.3(0.027V+15.6)}$ $\tau_{slow} = e^{2.3(0.015V+15.3)}$

Table 4.7 Rate constants of the ionic currents of the Golgi cell. Gating variable dynamics follow equations 4.16 and 4.17. If the steady state of the time constant of the gating variable does not follow equation 4.17, their equation is provided below the rate constants for the corresponding channel. m denotes activating gating variables, h denotes inactivating gating variables. The exponents denote the number of activation and inactivation channels (a and b in equation 4.15).

H-currents have slow and fast channels. The conductance of the H-currents is given by:

$$g_H = \bar{g}_H\left(x_{fast} + x_{slow}\right) \tag{4.21}$$

where the dynamics of both x_{fast} and x_{slow} are described by equation 4.16.

The calcium activated potassium current is modelled with a Markov multistate model. The potassium current, $I_{K_{SK2}}$ is given by:

$$I_{K_{SK2}} = \bar{g}_K * O_K * (V - E_K) \tag{4.22}$$

where $O_K = O_1 + O_2$ denotes the fraction of open channels.

A potassium current, K_{Ca}, depends on the intracellular calcium concentration, $[Ca]$. Calcium dynamics are modelled the same as in the granule cell model (equation 4.20) with the following parameters: $d = 200\,nm,\ \beta_{Ca} = 1.3,\ F = 96.485\,C/mol,\ [Ca]_0 = 50\,nM$. Calcium dynamics were modelled only in the soma, as no other section has a calcium dependent potassium current.

Gating kinetics were corrected using a Q_{10} factor of 5 for Ca_{LVA} [265] and a Q_{10} factor of 3 for all the other currents [266] according to equation 4.18 to account for temperature differences between experimental recordings and the simulations. All currents were measured experimentally at 23°C except for I_{K_V} which was measured at 6.3°C.

4.2.4 Purkinje cell model

Instead of the De Schutter-Bower Purkinje cell [4], [5], I employed the more recent Zang et al. Purkinje cell model [6]. The employed Purkinje cell has 1,135 dendrites, 1,105 of which are spiny and 30 are main dendrites, a soma and an axon initial segment. It is based on a reconstructed rat Purkinje cell morphology (cell four in the paper [267]).

I rotated the Purkinje cell model so that the dendritic tree lies in the sagittal-vertical plane, perpendicular to parallel fibres (see Figure 4.4).

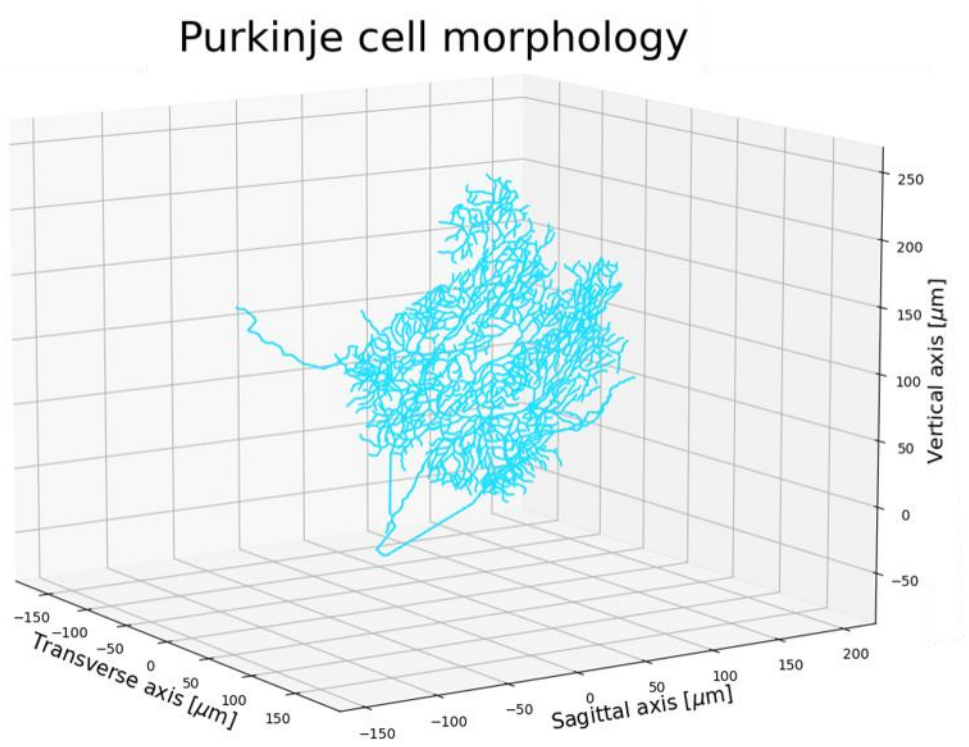


Figure 4.4 Rotated Purkinje cell morphology

The passive properties of the Purkinje cells are summarised in Table 4.8. Spiny and main dendrites have different membrane capacitance and resistance from other compartments to account for the fact that spines are not explicitly modelled (see Section 4.2.4.1).

Passive properties		**Soma**	**Axon initial segment**	**Main dendrites**	**Spiny dendrites and spine necks**	**Spine heads**
Membrane capacitance	$\frac{\mu F}{cm^2}$	0.64	0.64	$1.2 * 0.64$	$F_d * 0.64$	$F_d * 0.64$
Membrane resistance	Ωcm^2	120236	120236	$\frac{120236}{1.2}$	$\frac{120236}{F_d}$	$\frac{120236}{F_d}$
Axial resistance	Ωcm	120	120	120	120	240

Table 4.8 Passive properties of the Purkinje cell for each compartment type. The specific membrane capacitance is expressed in μF/cm^2, the specific membrane resistance is expressed in Ωcm^2 and the specific axial resistance is expressed in Ωcm. The compensation factors 1.2 and F_d account for the fact that not all spines are explicitly modelled.

4.2.4.1 Spine model

The Purkinje cell I employed did not have spines explicitly modelled. To account for the lack of spines, a compensation factor, F, was introduced by the authors of the passive Purkinje cell model [267]. The compensation factor, F was calculated as:

$$F = \frac{N_{spines} * A_{spine} + A_{dend}}{A_{dend}} \quad (4.23)$$

Where N_{spines} is the number of spines on a spiny dendrite, A_{spine} is the mean surface area of a spine (1.12 μm^2 [255]) and A_{dend} is the surface area of the spiny dendrite. This calculation was done for two dendritic segments presented in [255] and averaged to obtain a compensation factor of 5.3.

I modelled one spine per spiny dendrite compartment maintaining the same model as described in Section 4.1.2. I adjusted the compensation factor, F, to account for the explicitly modelled spines, obtaining a unique compensation factor, F_d, for each dendrite. For each dendrite, I first calculated the expected number of spines from equation 4.24 below. This equation comes from rearranging equation 4.23, substituting 5.3 for F and removing the explicitly modelled spine.

$$N_{spines} = \frac{(5.3 - 1) * A_{dend}}{A_{spine}} - 1 \quad (4.24)$$

I then calculated the adjusted compensation factor, F_d, for each dendrite using equation 4.23, substituting the number of spines, N_{spines}, previously obtained, rather than the average number of spines measured experimentally. In total, the Purkinje cell has 122,613 spines, of which I explicitly modelled 1,105.

4.2.4.2 Ionic currents

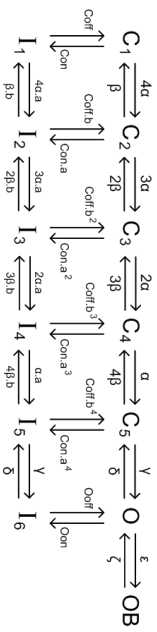
The Purkinje cell contains two types of sodium currents, including a resurgent current $\left(I_{Na_{rsg}}\right)$ and a persistent current $\left(I_{Na_P}\right)$; a H-current (I_h), two types of calcium currents, T- and P-type; and six types of potassium currents including three voltage dependent channels $(I_{Kv1}, I_{Kv3}\ and\ I_{Kv4})$, two high-conductance, calcium-activated currents $\left(I_{BKfast}\ and\ I_{BKslow}\right)$, and a voltage independent, calcium activated current $\left(I_{K_{SK2}}\right)$. Spines are passive compartments. Table 4.9 summarises the maximum conductances

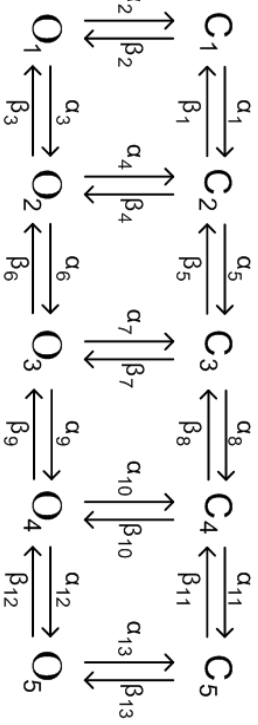
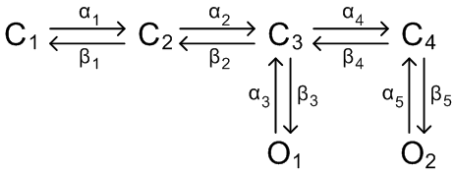
of each ionic current for each section in the Purkinje cell. If the ionic channel is not present in a section, no value for the conductance is given.

Maximum conductance $\left(\frac{\mu S}{cm^2}\right)$	**Axon initial segment**	**Soma**	**Main dendrites**	**Spiny dendrites**
Na_{rsg}	0.56	0.0317		
Na_P	0.0023	$1.4\text{x}10^{-4}$		
H	$1.08\text{x}10^{-4}$	$1.08\text{x}10^{-4}$	$2.16\text{x}10^{-4}$	$3.24\text{x}10^{-4}$
$T-type\ Ca^{2+}\ \left(\frac{cm}{s}\right)$	$1.28\text{x}10^{-4}$		$2.7\text{x}10^{-5}$	$1.08\text{x}10^{-4}$
$P-type\ Ca^{2+}\ \left(\frac{cm}{s}\right)$	0.00228	$1.9\text{x}10^{-4}$	$1.9\text{x}10^{-4}$	$7.6\text{x}10^{-4}$
$BKfast$	6	0.8736	0.21504	0.0448
$BKslow$	1.05	0.3		
$SK2$	0.0278	0.0075	$3.6\text{x}10^{-4}$	$3.6\text{x}10^{-4}$
$Kv3$	115	1.8	0.1512	0.2268
$Kv4$			0.015	0.015
$Kv1$			0.002	0.001

Table 4.9 Maximum conductance of the ionic currents of the Purkinje cell expressed in μS/cm². If the channel is not present in a section, no value for the conductance is given.

The reversal potential is set to 63 mV for all sodium currents, to -80 mV for all potassium currents and to -30 mV for the H-current. Table 4.10 summarises the gating variable dynamics and the rate constants of all modelled channels. All ionic currents are given by equation 4.15, unless the channel is noted by an asterisk, in which case the current equation is provided below the table.

Channel	Exponent	Gating variable dynamics	Rate constants α and β
* Na_{rsg}	N.A.		$\alpha = 150e^{\frac{V}{20}}\ ms^{-1}$ $\beta = 3e^{-\frac{V}{20}}\ ms^{-1}$ $\gamma = 150\ ms^{-1}$ $\delta = 40\ ms^{-1}$ $Con = 0.005\ ms^{-1}$ $Coff = 0.5\ ms^{-1}$ $Oon = 0.75\ ms^{-1}$ $Ooff = 0.005\ ms^{-1}$ $\varepsilon = 1.75\ ms^{-1}$ $\varsigma = 0.03e^{-\frac{V}{25}}\ ms^{-1}$ $a = \left(\frac{Oon}{Con}\right)^{\frac{1}{4}}$ $b = \left(\frac{Ooff}{Coff}\right)^{\frac{1}{4}}$
Na_p	3	$m_\infty = \frac{1}{1+e^{-\frac{V+66}{5}}}$ $\tau_m = \frac{1}{\alpha_m + \beta_m}$	$\alpha_m = \frac{17.235}{1+e^{\frac{V+27.58}{-11.47}}}$ $\beta_m = \frac{17.235}{1+e^{\frac{V+86.2}{19.8}}}$
I_h	1	$m_\infty = \frac{1}{1+e^{\frac{V+96.3}{9.67}}}$ $\tau_m = \frac{1000}{0.806\left(e^{-\frac{V+68}{22}} + e^{\frac{V+68}{7.14}}\right)}$	N.A.
* $T-type\ Ca^{2+}$	3	$m_\infty = \frac{1}{1+e^{-\frac{V-35.606}{4.7}}}$ $\tau_m = \frac{1}{1.2757 + \alpha_m + \beta_m}$	$\alpha_m = \frac{-2.3199}{1+e^{\frac{V+41.448}{-30.655}}}$ $\beta_m = \frac{2.5712}{1+e^{\frac{V+21.7866}{-9.6306}}}$
	1	$h_\infty = \frac{1}{1+e^{\frac{V+81.718}{6.4635}}}$ $\tau_h = \frac{1}{0.0076 + \alpha_h + \beta_h}$	$\alpha_h = \frac{0.17746}{1+e^{\frac{V+41.448}{-30.655}}}$ $\beta_h = \frac{0.13402}{1+e^{\frac{V+94.836}{-5.5845}}}$
* $P-type\ Ca^{2+}$	1	$m_\infty = \frac{1}{1+e^{-\frac{V-25.5}{4.113}}}$ $\tau_m = 0.2 + 0.7031e^{-\left(\frac{V+25}{14}\right)^2}$	N.A.

* BK_{fast}	N.A.		$\alpha_1 = 9189.59[Ca_i^{2+}]\ \ ms^{-1}$ $\beta_1 = 19.83\ ms^{-1}$ $\alpha_2 = 9.04e^{-\frac{0.67V}{310.15}}\ ms^{-1}$ $\beta_2 = 5.50 * 10^3 * e^{\frac{0.73V}{310.15}}\ ms^{-1}$ $\alpha_3 = 9189.59[Ca_i^{2+}]\ \ ms^{-1}$ $\beta_3 = 1.51\ ms^{-1}$ $\alpha_4 = 1.58e^{-\frac{0.67V}{310.15}}\ ms^{-1}$ $\beta_4 = 1.26 * 10^2 * e^{\frac{0.73V}{310.15}}\ ms^{-1}$ $\alpha_5 = 6892.19[Ca_i^{2+}]\ \ ms^{-1}$ $\beta_5 = 39.65\ ms^{-1}$ $\alpha_6 = 6892.19[Ca_i^{2+}]\ \ ms^{-1}$ $\beta_6 = 3.02\ ms^{-1}$ $\alpha_7 = 0.54e^{-\frac{0.67V}{310.15}}\ ms^{-1}$ $\beta_7 = 5.66 * 10^2 * e^{\frac{0.73V}{310.15}}\ ms^{-1}$ $\alpha_8 = 4594.79[Ca_i^{2+}]\ \ ms^{-1}$ $\beta_8 = 59.48\ ms^{-1}$ $\alpha_9 = 4594.79[Ca_i^{2+}]\ \ ms^{-1}$ $\beta_9 = 4.52\ ms^{-1}$ $\alpha_{10} = 0.24e^{-\frac{0.67V}{310.15}}\ ms^{-1}$ $\beta_{10} = 0.33 * e^{\frac{0.73V}{310.15}}\ ms^{-1}$ $\alpha_{11} = 2297.40[Ca_i^{2+}]\ \ ms^{-1}$ $\beta_{11} = 79.31\ ms^{-1}$ $\alpha_{12} = 2297.40[Ca_i^{2+}]\ \ ms^{-1}$ $\beta_{12} = 6.03\ ms^{-1}$ α_{13} $= 2.68 * 10^2 * e^{-\frac{0.67V}{310.15}}\ ms^{-1}$ $\beta_{13} = 4.85 * 10^1 * e^{\frac{0.73V}{310.15}}\ ms^{-1}$
BK_{slow}	1	$m_\infty = \frac{1}{1 + e^{\frac{-56.449 + 104.52e^{\left[-0.22964 * \left[Ca_i^{2+}\right]\right]} + 295.68e^{\left[-2.1571 * \left[Ca_i^{2+}\right]\right]}}{15.625}}}$ $\tau_m = \frac{1}{10 * \left(e^{-\frac{V}{63.6}} + e^{\frac{V-150}{63.6}}\right)} - 5.2$	
* $SK2$	N.A.		$\alpha_1 = 803.41[Ca_i^{2+}]\ \ ms^{-1}$ $\beta_1 = 0.32\ ms^{-1}$ $\alpha_2 = 642.73[Ca_i^{2+}]\ \ ms^{-1}$ $\beta_2 = 0.32\ ms^{-1}$ $\alpha_3 = 4.02\ ms^{-1}$ $\beta_3 = 0.64\ ms^{-1}$ $\alpha_4 = 321.37[Ca_i^{2+}]\ \ ms^{-1}$ $\beta_4 = 0.80\ ms^{-1}$ $\alpha_5 = 0.40\ ms^{-1}$ $\beta_5 = 4.82\ ms^{-1}$

$Kv3$	4	$m_\infty = \frac{\alpha_m}{\alpha_m + \beta_m}$ $\tau_\infty = \frac{1}{\alpha_m + \beta_m}$	$\alpha_m = 0.22e^{\frac{V+16}{26.5}}$ $\beta_m = 0.22e^{-\frac{V+16}{26.5}}$
$Kv4$	4	$m_\infty = \frac{1}{1+e^{\frac{V+49}{-12.5}}}$ $\tau_m = \frac{1}{\alpha_m + \beta_m}$	$\alpha_m = \frac{0.1342}{1 + e^{\frac{V+60}{32.19976}}}$ $\beta_m = \frac{0.15743}{1 + e^{\frac{V+57}{37.51346}}}$
	1	$h_\infty = \frac{1}{1 + e^{\frac{V+75.30348}{6.06329}}}$ $\tau_{hf} = \frac{1}{\alpha_{hf} + \beta_{hf}}$	$\alpha_{hf} = \frac{0.01342}{1 + e^{\frac{V+60}{7.86476}}}$ $\beta_{hf} = \frac{0.04477}{1 + e^{\frac{V+54}{-11.6315}}}$
$Kv1$	4	$m_\infty = \frac{\alpha_m}{\alpha_m + \beta_m}$ $\tau_m = \frac{1}{\alpha_m + \beta_m}$	$\alpha_m = 0.12889e^{\frac{V+45}{33.90877}}$ $\beta_m = 0.12889e^{-\frac{V+45}{12.42101}}$
	1	$h_\infty = \frac{1}{1 + e^{\frac{V+66.16}{6.1881}}}$ $\tau_h = 1000$	N.A.

Table 4.10 Gating variable dynamics and rate constants of the ionic channels of the Purkinje cell. m denotes activating gating variables, h denotes inactivating gating variables. The exponents denote the number of activation and inactivation channels (a and b in equation 4.15).

The resurgent sodium current $\left(I_{Na_{rsg}}\right)$, a high-conductance, calcium-activated potassium current $\left(I_{BK_{fast}}\right)$ and the voltage independent, calcium activated potassium current $\left(I_{K_{SK2}}\right)$ are modelled with a Markov multistate model. The sodium current, $I_{Na_{rsg}}$, is given by:

$$I_{Na_{rsg}} = \bar{g}_{Na} * O_{Na} * (V - E_{Na}) \tag{4.25}$$

The calcium-activated potassium current, $I_{BK_{fast}}$, is given by:

$$I_{BK_{fast}} = \bar{g}_K * O_{BK_{fast}} * (V - E_K) \tag{4.26}$$

where $O_{BK_{fast}} = O_1 + O_2 + O_3 + O_4 + O_5$ denotes the fraction of open channels.

The calcium activated potassium current, $I_{K_{SK2}}$, is given by:

$$I_{K_{SK2}} = \bar{g}_K * O_{K_{SK2}} * (V - E_K) \tag{4.27}$$

where $O_{K_{SK2}} = O_1 + O_2$ denotes the fraction of open channels.

The two calcium currents, I_{Ca_T} and I_{Ca_P}, depend on calcium concentration, $c(V)$ and are given as below:

$$\begin{aligned} I_{Ca_T} &= \bar{g}_{Ca_T} * m^3 * h * c(V) \\ I_{Ca_P} &= \bar{g}_{Ca_P} * m * c(V) \\ c(V) &= 19.297\text{x}10^{-2} * \left(Ca_{in} - Ca_0 * e^{-\frac{19.297*10^4*V}{2578.91}}\right) * \left(1 + \frac{9.6485 * 10^4 * V}{2578.91}\right) \end{aligned} \tag{4.28}$$

where Ca_{in} and Ca_0 are the concentrations of calcium ions inside the cell and at rest.

4.2.4.3 Calcium dynamics

The calcium concentration was modelled following the approach described in [61], which builds on the formulation proposed in [268]. The model represents intracellular calcium dynamics using two calcium pools with distinct temporal properties: one characterised by a fast decay and the other by a slow decay. Both pools depend on the total calcium current flowing through P- and T-type Ca^{2+} channels. The model also includes the calcium-binding proteins calbindin and parvalbumin as buffers, together with a calcium pump that regulates intracellular calcium levels.

Fast and slow Ca^{2+} transients, $[Ca_i^{2+}]_f$ and $[Ca_i^{2+}]_s$, were modeled using two pools with different decay time constants $(\beta_f \text{ and } \beta_s, \text{with } \beta_f > \beta_s)$, and different shell depths $(d_f \text{ and } d_s, \text{with } d_f < d_s)$. Shells define the effective volume used to compute calcium concentration. In the model, 20 shells for the soma, 4 shells for dendrites, and 10 shells for the axon initial segment were used. The total intracellular Ca^{2+} concentration, $[Ca_i^{2+}]$, was computed as the weighted sum of fast and slow Ca^{2+} transients:

$$[Ca_i^{2+}] = f_f[Ca_i^{2+}]_f + f_s[Ca_i^{2+}]_s \tag{4.29}$$

where $f_f = 0.994$ and $f_s = 0.006$.

The exponentially decaying calcium pool generated by influx was modelled as:

$$\frac{d[Ca_i^{2+}]_{influx}}{dt} = \frac{I_{Ca^{2+}}}{2Fd} - \beta([Ca_i^{2+}] - [Ca_i^{2+}]_{rest}) \quad (4.30)$$

where $[Ca^{2+}]_{influx}$ is the intracellular calcium concentration in the i-th shell resulting from calcium influx, $[Ca_i^{2+}]_{rest} = 45\ nM$ is the resting calcium concentration, $I_{Ca^{2+}}$ is the total Ca^{2+} current through P- and T-type Ca^{2+} channels, $\beta = 3.77\ ms^{-1}$ for fast Ca^{2+} transients and $\beta = 0.00306\ ms^{-1}$ for slow Ca^{2+} transients, $F = 9.648\text{x}10^4\ C/mol$ is Faraday's constant and d is the depth of the submembrane shell. The shell depths are $d_f = 0.351\ \mu m$ and $d_s = 0.928\ \mu m$.

In addition to calcium influx, intracellular calcium concentration depends on buffering by calbindin and parvalbumin. Calbindin contains four calcium-binding sites, whereas parvalbumin contains two. Calcium dynamics associated with buffering were modelled as:

$$\frac{d[Ca_i^{2+}]_{buffer}}{dt} = -k_{on}[Ca_i^{2+}][BS] + k_{off}[CaBS] \quad (4.31)$$

where $[BS]$ and $[CaBS]$ denote the concentrations of free binding sites and calcium-bound binding sites. The reaction parameters are summarised in Table 4.11. Calbindin contributes both to slow and fast calcium transients, whereas parvalbumin does not exhibit separate transients but instead depends on magnesium binding.

For calbindin, the relationship between free and occupied binding sites is given by:

$$\frac{d[BS]}{dt} = -\frac{d[CaBS]}{dt} \quad (4.32)$$

Parvalbumin also binds magnesium ions, and therefore the occupancy of its binding sites depends on both calcium and magnesium binding:

$$\frac{d[BS]}{dt} = -\frac{d[CaBS]}{dt} - \frac{d[MgBS]}{dt} \quad (4.33)$$

Magnesium binding was modelled using the same dynamics as calcium binding (equation 4.31). The intracellular magnesium concentration was kept constant at 590 μm.

A calcium pump was included to regulate intracellular calcium concentration:

$$\frac{d[Ca_i^{2+}]_{pump}}{dt} = -v_{max}\frac{A[Ca_i^{2+}]}{V([Ca_i^{2+}] + K_m)} \quad (4.34)$$

where A and V are the surface area and volume of the neuron compartment in which the calcium dynamics are modelled, $v_{max} = 150\, pmol/\mathrm{cm}^2 s$ is the maximal pump velocity and $K_m = 3\, \mu M$ is the Michaelis-Menten constant.

To maintain a stable resting calcium concentration, $[Ca_i^{2+}]_{rest} = 45\, nM$, the calcium removal from the pump was balanced by a leak current:

$$\frac{d[Ca_i^{2+}]_{leak}}{dt} = v_{max}\frac{A[Ca_i^{2+}]_{rest}}{V([Ca_i^{2+}]_{rest} + K_m)} \quad (4.35)$$

The total intracellular calcium concentration was then computed as the sum of the influx, buffer, pump, and leak components:

$$[Ca_i^{2+}] = [Ca_i^{2+}]_{influx} + [Ca_i^{2+}]_{buffer} + [Ca_i^{2+}]_{pump} + [Ca_i^{2+}]_{leak} \quad (4.36)$$

The reaction parameters governing the calcium dynamics associated with the buffers calbindin and parvalbumin (equation 4.31) are summarised in Table 4.11.

	Calbindin	**Paravalbumin**
Concentration	$0.16\, mM$	$0.08\, mM$
k_{on}	Fast $43.5\, ms^{-1}mM^{-1}$ Slow $5.5\, ms^{-1}mM^{-1}$	Calcium binding $107\, ms^{-1}mM^{-1}$ Magnesium binding $0.8\, ms^{-1}mM^{-1}$
k_{off}	Fast $3.58\text{x}10^{-2}\, ms^{-1}mM^{-1}$ Slow $0.26\text{x}10^{-2}\, ms^{-1}mM^{-1}$	Calcium binding $9.5\text{x}10^{-4}\, ms^{-1}mM^{-1}$ Magnesium binding $2.5\text{x}10^{-2}\, ms^{-1}mM^{-1}$

Table 4.11 Reaction parameters describing the calcium dynamics in relation to the two buffers, calbindin and paravalbumin.

4.2.4.4 Temperature correction

Gating kinetics were corrected according to equation 4.18 to account for temperature differences between experimental recordings and the simulations. Table 4.12 summarises the Q_{10} factor and the experimental temperature at which the recordings were done (T_0 in equation 4.18).

Channel	Q_{10}	T_0
Na_{rsg}	2.7	22
Na_P	2.7	22
I_h	2	25
$T-type\ Ca^{2+}$	1.0913	32
$P-type\ Ca^{2+}$	3	22
$BKfast$	2	22
$BKslow$	3	34
$SK2$	2.7	23
$Kv3$	2.7	22
$Kv4$	3	23
$Kv1$	3	22

Table 4.12 Q_{10} factor and temperature at which the ionic channels were recorded.

4.2.5 Connectivity

Connectivity parameters within the granular layer remain unvaried, as detailed in Section 4.1.3, except for the maximum synaptic conductances of connections with granule cells as post-synaptic neurons. To maintain the intended granular layer network behaviour after updating granule cell model, I have modified the synaptic conductances from 1200 pS to 2000 pS, from 18,800 pS to 20,000 pS and from 1000 pS to 756.35 pS for synaptic connections involving AMPA, NMDA and GABA receptors.

Synaptic parameters of excitatory connections to the Purkinje cell remain unvaried. However, as the number of spines in the cell decreased, the number of excitatory inputs decreased. I modelled inhibitory inputs as in [53], a computational study employing the same Purkinje cell model. The Purkinje cell receives 144 inhibitory inputs from nine stellate cells to sixteen randomly selected spiny dendrites and 80 inhibitory inputs from four basket cells to the soma. Both stellate cells and basket cells are modelled as Poisson spike trains with a mean firing rate of 12.3 Hz [269]. Synaptic

parameters are as follows $\bar{g}_{syn} = 0.5\,nS$, $\tau_{rise} = 0.93\,ms$, $\tau_{decay} = 26.50\,ms$ and $E_{syn} = -80\,mV$.

Purkinje cell results presented in this chapter pertain to the isolated Purkinje cell. Results presented in the next two chapters pertain to the Purkinje cell connected to the granular layer network, with the synaptic parameters described above.

4.2.6 Analysis

To ensure that updating the granule cell model did not alter the intended behaviour of the granular layer network, I reproduced the population responses of granule and Golgi cells using both the original granular layer network [2] and the updated network incorporating the multi-compartment granule cell model. To allow a fair comparison, I reduced the size of the single compartment network to match that of the multi-compartment network. I stimulated the granular layer network with mossy fibre inputs ranging from 10 to 130 Hz in 10 Hz steps, as higher stimulation frequencies produced artefacts in the single compartment network. I simulated the network for 1 s and calculated the mean firing rate of each population discarding the first 500 ms of simulation to avoid transient effects.

To verify that I tuned the parameters of the Purkinje cell model correctly after adding dendritic spines, I first confirmed that the model still exhibited spontaneous firing [270] and that its input–output relationship maintained a linear part [51], [269], both of which are key physiological properties of Purkinje cells. I then measured the total capacitance of the Purkinje cell under three conditions: without spines, with one spine per spiny dendrite, and with all spines explicitly modelled. I calculated the total cell capacitance as:

$$\sum_{i=1}^{N} C_{m_i} * Area_i \tag{4.37}$$

where N is the total number of compartments in the Purkinje cell model, C_{m_i} is the membrane capacitance of the i-th compartment and $Area_i$ is the surface area of that compartment.

Next, I examined the passive behaviour of the Purkinje cell with and without spines. To do so, I removed all ionic currents and synaptic inputs and stimulated the cell using

a clamping current. I evaluated three configurations: the Purkinje cell without spines, the Purkinje cell with one spine per spiny dendrite, and the Purkinje cell with all spines explicitly modelled. In the first analysis, I injected a step current into the soma. I then injected a step current into an arbitrarily selected spiny dendrite or, when present, into the spine head located at the centre of that dendrite to assess whether the cellular responses were comparable across conditions. The clamping current had an amplitude of 0.5 nA, it started after 500 ms of simulation, and the total simulation time was 1.5 s.

Finally, I reproduced the frequency–current (F–I) curve of the model reported in Figure 1F of the original study in which this Purkinje cell model was introduced [6] (see Figure 4.5). I applied a clamping current to the isolated Purkinje cell while retaining all ionic currents. I introduced the clamping current after 100 ms of simulation, and each simulation lasted 1.5 s. I calculated the mean firing rate of the cell discarding the first 500 ms of simulation to avoid transient effects. I injected currents ranging from −0.5 to 1.5 nA in increments of 0.25 nA. I repeated the simulations twice: once with one spine per spiny dendrite and once with all spines explicitly modelled.

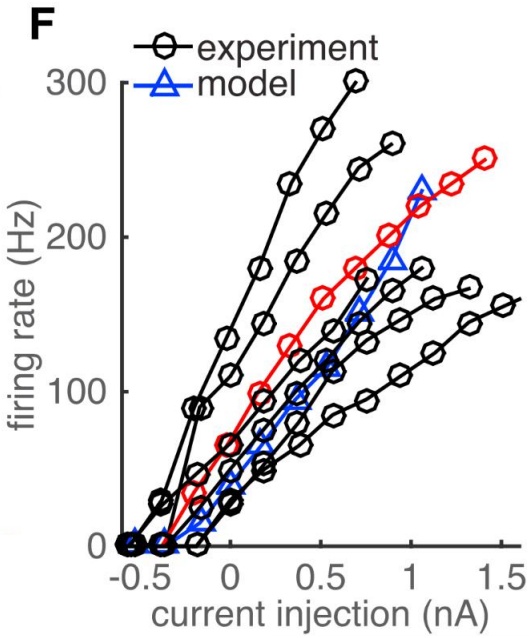


Figure 4.5 F-I curve of the Purkinje cell model (blue triangles). Taken from the original modelling study where this Purkinje cell model was proposed [6].

4.3 Results

First, I generated the population response of the granular layer network with the single compartment granule cell (see Figure 4.6).

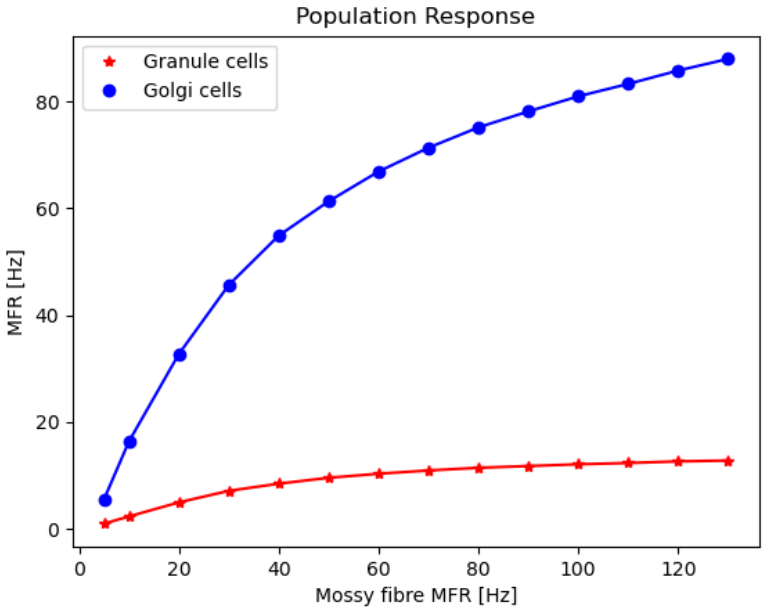


Figure 4.6 Population response of granule (red stars) and Golgi (blue dots) cells obtained simulating the granular layer network with single compartment granule cells.

The maximum mean firing rate is 12.82 Hz for the granule cell population, and 87.94 Hz for the Golgi cell population, obtained when the network is excited by mossy fibres firing at 130 Hz.

I then generated the population response of the granular layer network with the multi-compartment granule cell (see Figure 4.7).

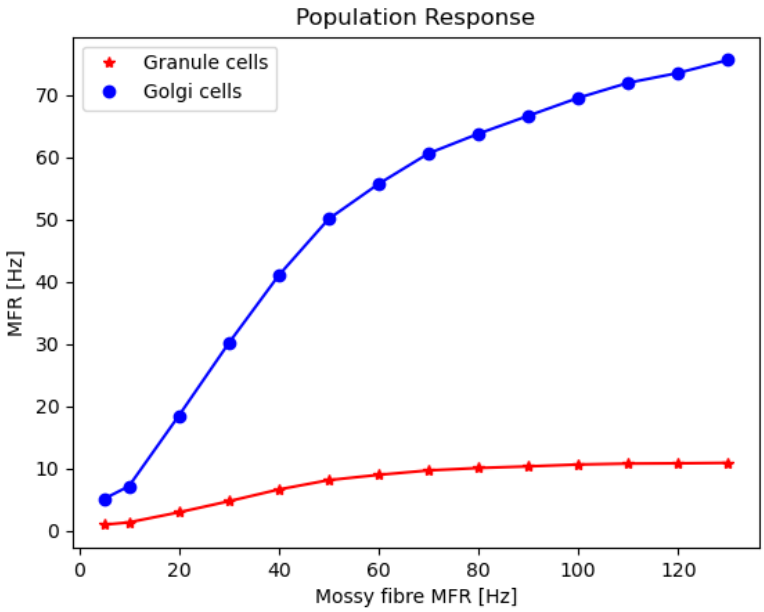


Figure 4.7 Population response of granule (red stars) and Golgi (blue dots) cells obtained simulating the granular layer network with multi-compartment granule cells.

The maximum mean firing rate is 10.92 Hz for the granule cell population, and 75.64 Hz for the Golgi cell population, obtained when the network is excited by mossy fibres firing at 130 Hz.

To verify that I tuned the parameters of the Purkinje cell model correctly after adding dendritic spines, I calculated the total cell capacitance of the cell in three configurations: without spines, with one spine per spiny dendrite, and with all spines explicitly modelled. (see Table 4.13).

	No spines	**One spine**	**All spines**
Total cell capacitance	1159.35 pF	1138.71 pF	1168.01 pF

Table 4.13 Total cell capacitance, in pF, of the Purkinje cell model in the three analysed configurations: without spines, with one spine per spiny dendrite, and with all spines explicitly modelled.

I then assessed the passive behaviour of the Purkinje cell in the three configurations. First, I injected a step current in the soma of the cell. The steady state voltage reached in the cell soma is of -27.59 mV, -27.00 mV, -27.84 mV for the cell without spines, with one spine per spiny dendrite, and with all spines explicitly modelled.

I then repeated the simulations injecting a step current in a spiny dendrite or, when present, into the spine head located at the centre of that dendrite. The steady state voltage reached in the cell soma is of -32.66 mV, -32.05 mV, -32.91 mV for the cell without spines, with one spine per spiny dendrite, and with all spines explicitly modelled (see Figure 4.8).

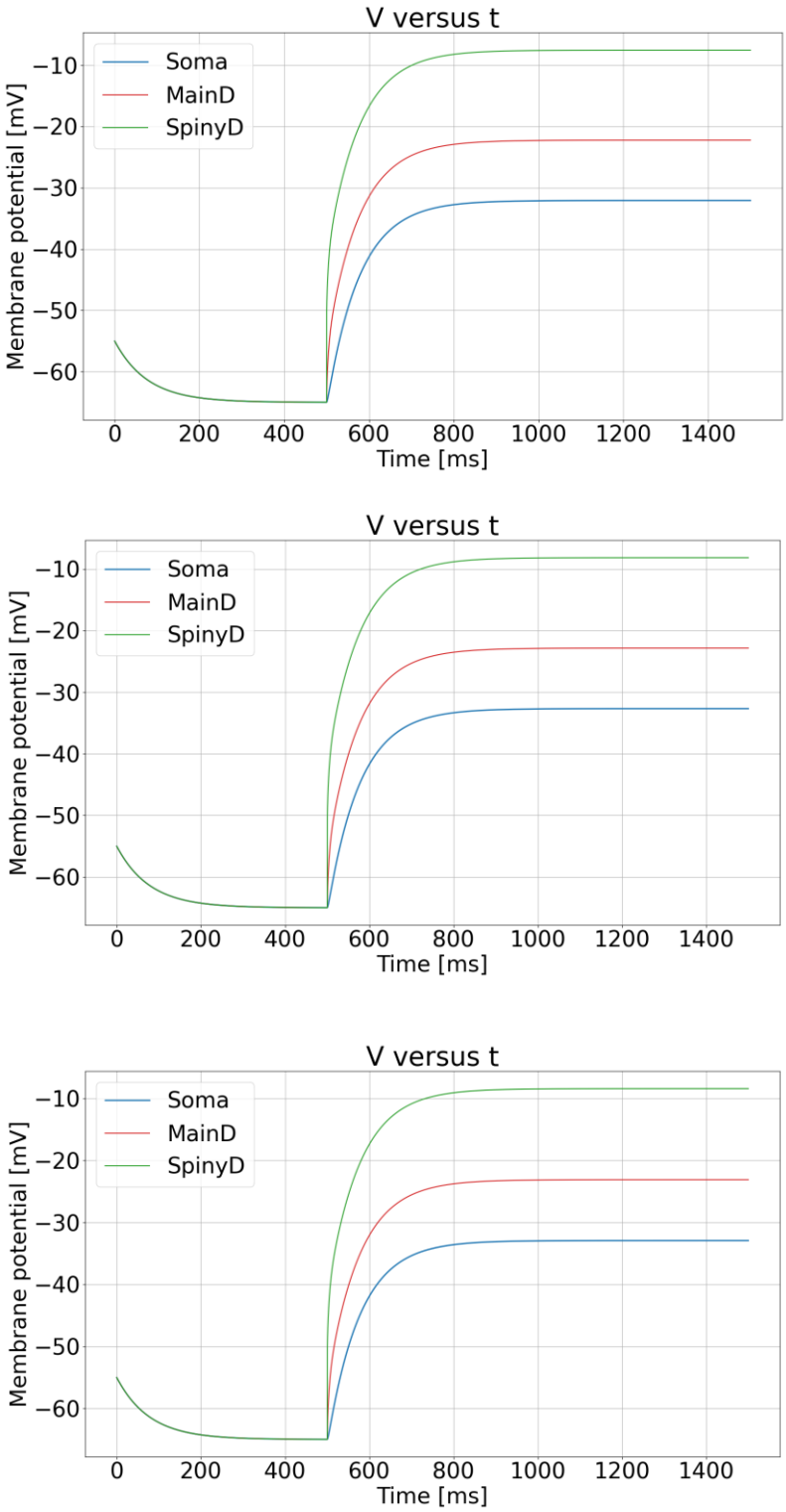


Figure 4.8 Passive behaviour of the Purkinje cell when injecting a step current in a spiny dendrite or, when present, into the spine head located at the centre of that dendrite. Voltage traces of the soma (blue), a main dendrite, parent of the clamped spiny dendrite (red), and the current clamped spiny dendrite (green) are shown.

Finally, I generated the frequency-current (F-I) curve of the Purkinje cell in two configurations: with one spine per spiny dendrite, and with all spines explicitly modelled. The F-I curve of the Purkinje cell without spines is shown in Figure 4.5. From Figure 4.9 it can be seen that the Purkinje cell fires spontaneously, with a mean firing frequency of 56 Hz, and its input-output curve has a linear part.

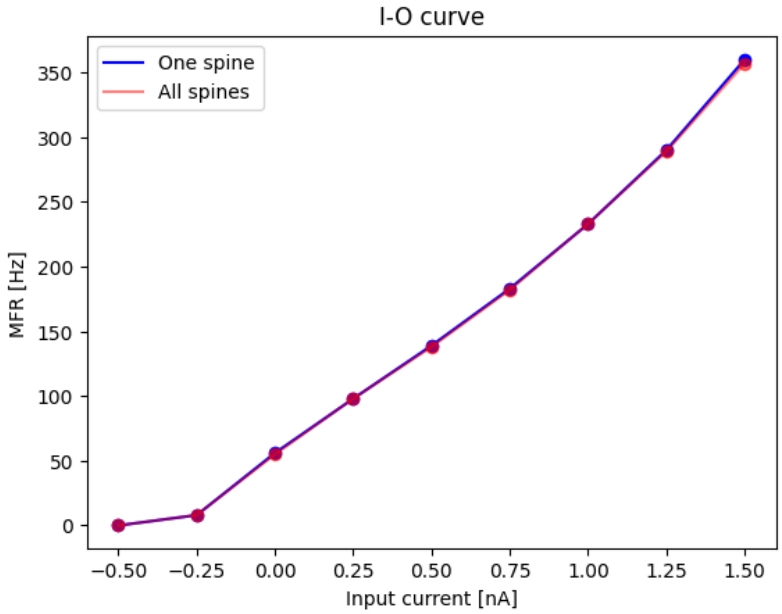


Figure 4.9 F-I curve of the Purkinje cell with one spine per spiny dendrite modelled explicitly (in blue) and F-I curve of the Purkinje cell with all spines modelled explicitly (in red).

When one spine is modelled explicitly, the cell reaches a maximum firing rate of 360 Hz, when all spines are modelled explicitly, the cell reaches a maximum firing rate of 357 Hz. In both cases, the maximum firing rate is obtained with an injected current of 1.5 nA (see Figure 4.9).

4.4 Discussion

Modifying biologically realistic neural network models inevitably alters their behaviour. However, it is essential to preserve key physiological properties when introducing such changes. In this work, I demonstrated that the population responses of Golgi and granule cells remain qualitatively consistent with those of the original model. Specifically, granule cells exhibit a response curve that rapidly saturates at low firing frequencies, while Golgi cells show a rapidly increasing response curve (see Figure 4.6 And 4.7).

The addition of dendritic spines did not substantially alter the behaviour of the Purkinje cell. The model continues to display spontaneous firing (see Figure 4.9), maintains an input–output relationship with a linear part (see Figure 4.9), and both the frequency-current curve (see Figure 4.9) and the passive electrophysiological behaviour (see Figure 4.8) are comparable to those observed in the version without explicitly modelled spines.

The model reproduces both the behaviour of the previous implementation and key physiological characteristics, indicating that the updated cerebellar cortex model remains suitable for further investigations

As with all models, the proposed cerebellar model comes with limitations. The following limitations are relevant to discuss:

- The model represents a general cerebellar cortex network rather than a region-specific implementation. In particular, it does not explicitly model the vermis, which is the cerebellar region targeted in the experimental study reproduced in the following chapter.
- The cerebellar network is implemented as a feedforward architecture, only a single Purkinje cell is modelled, and interneurons are not explicitly included. This represents a simplification of the underlying biological circuitry. These modelling choices were made to reduce computational costs.
- The model is based on experimental data obtained from rodents. More recent models, such as [50], incorporate the morphology of human neurons (while still relying on ion channel models derived from rodent data). The experimental data used to evaluate the stimulation model, as well as the stimulation model itself, are based on human studies. This introduces a potential cross-species inconsistency.
- Although Golgi cells include variability in dendritic orientation, the morphology of granule cells does not vary across the population. This simplification was introduced to reduce computational cost, given the large number of granule cells in the network. However, it limits the model's ability to capture biological variability within this cell population.

4.5 Conclusion

In this chapter I presented the cerebellar cortex model I developed and I have shown that it reproduces key modelling and experimental results. The described model addresses the gap in the literature #1 - *The lack of a biologically realistic model of the cerebellar cortex.* In the next chapter, I will describe the transcranial magnetic stimulation model I employed.

Chapter 5

Model of transcranial magnetic stimulation

This chapter describes the computational model of a transcranial magnetic stimulation (TMS) protocol and its coupling to the cerebellar network. The model is intended to be used in conjunction with experiments, both to assess the model's validity and to gain insights on the underlying effects of the stimulation which are not measurable in experimental settings. Accordingly, the design of the model was informed by the experimental protocol planned within the group of Dr Barry Seemungal at Imperial College London.

Dr Seemungal suggested focusing on stimulation of the cerebellar vermis, as it represents a promising clinical target [162], [165]. He also proposed using eye movements as the primary readout of the model, as they are straightforward to measure and his laboratory has the necessary experimental setup. The model used to predict eye movements is discussed in greater detail in Chapter 6. As the planned experiments had not yet commenced at the time of this work, an existing experimental study [177] was reproduced to assess the validity of the TMS model.

This chapter is structured as follows. First, I present the experimental study selected for reproduction using the model. Next, I describe the implementation of a 2 s continuous theta-burst stimulation (cTBS) protocol targeting the cerebellar vermis. Finally, I show the resulting simulation outcomes.

The work presented in this chapter addresses my research questions 1 *Are the neurons in the cerebellar vermis, lobules VI–VII, affected by TMS?* and 2 *How does the cTBS protocol affect the neurons in terms of mean firing rate, instantaneous firing rate and spike timing?* The work presented in this chapter also addresses *The lack of a multi-scale non-invasive stimulation model including synaptic connections*, which, as presented in Chapter 1, is the second gap in the literature tackled in my PhD.

5.1 Reproduced experimental setup

The objective of this work is to reproduce the experimental setup described by Colnaghi and colleagues [177] using the proposed model. In their experiment, the authors investigated the effects of transcranial magnetic stimulation (TMS) on reflexive saccades and smooth pursuit eye movements.

Continuous theta burst stimulation (cTBS) was delivered to eight healthy participants across three separate recording sessions: one session with 20 s of stimulation, one session with 40 s of stimulation, and one control session delivering sham stimulation. Eye movements were recorded for a period of 30 minutes following the stimulation using video-oculography.

Stimulation was delivered using a MagStim Super Rapid magnetic stimulator (Magstim Company, Whitland, UK) connected to a figure-of-eight coil with a diameter of 70 mm. TMS pulses were applied at 100% of the resting motor threshold, corresponding to 42.9 ± 3.8% (mean ± standard deviation) of the maximum stimulator output.

The coil position and orientation were calibrated using a neuronavigation system, targeting the coordinates [7, −60, −40] in the stereotaxic Talairach coordinate system. This target corresponds to vermal lobules VI–VII of the cerebellum. No information was provided regarding the specific coil orientation. The coil was positioned over the occiput on the right side, in the region caudal to the inion.

Eye movement recording began immediately after stimulation and was repeated every five minutes for a total duration of 30 minutes. In each recording block, participants performed 30 reflexive saccades and 20 smooth pursuit trials. For reflexive saccades, a target initially appeared at the central fixation point and then moved randomly to the left or right of the participant's sagittal plane. The target remained stationary until the saccade was completed. For smooth pursuit trials, the central fixation point disappeared randomly and was simultaneously replaced by a tracking target that appeared randomly to the left or right of the sagittal plane. The tracking target moved at a constant velocity and stopped at a random time.

Eye movements were analysed using the following parameters: amplitude, peak velocity, duration, and latency for reflexive saccades; and acceleration, latency, and velocity for smooth pursuit movements. The authors reported that 20 s of cerebellar

vermis stimulation had no effect on either reflexive saccades or smooth pursuit movements. In contrast, 40 s of cTBS produced a significant increase in the amplitude of ipsilateral reflexive saccades and in the acceleration of ipsilateral smooth pursuit movements. These effects persisted throughout the entire 30 minute recording period. No other measured parameters were affected by the 40 s stimulation protocol.

5.2 Methods

To model a continuous theta-burst stimulation (cTBS) protocol, I assumed a quasi-static approximation [31], [250] which allowed me to decouple the electric field in its spatial and temporal components. I modelled a cTBS protocol and coupled it to the cerebellar network as follows:

1. I estimated the spatial electric field generated in a realistic head model by a figure of 8 coil using SimNIBS. SimNIBS is an open-source software package that simulates the electric field induced by TMS in realistic head models [247] which I described in more detail in Chapter 3;

2. I generated a time-varying electric field by multiplying the mean electric field in a region of interest (ROI) by a cTBS pulse waveform.

3. I derived an extracellular voltage from the resulting time-varying electric field for each neuron in the cerebellar network. I coupled this extracellular voltage to the cerebellar model via the *extracellular* mechanism of the NEURON simulator.

See Figure 5.1 for a schematic representation of the aforementioned steps.

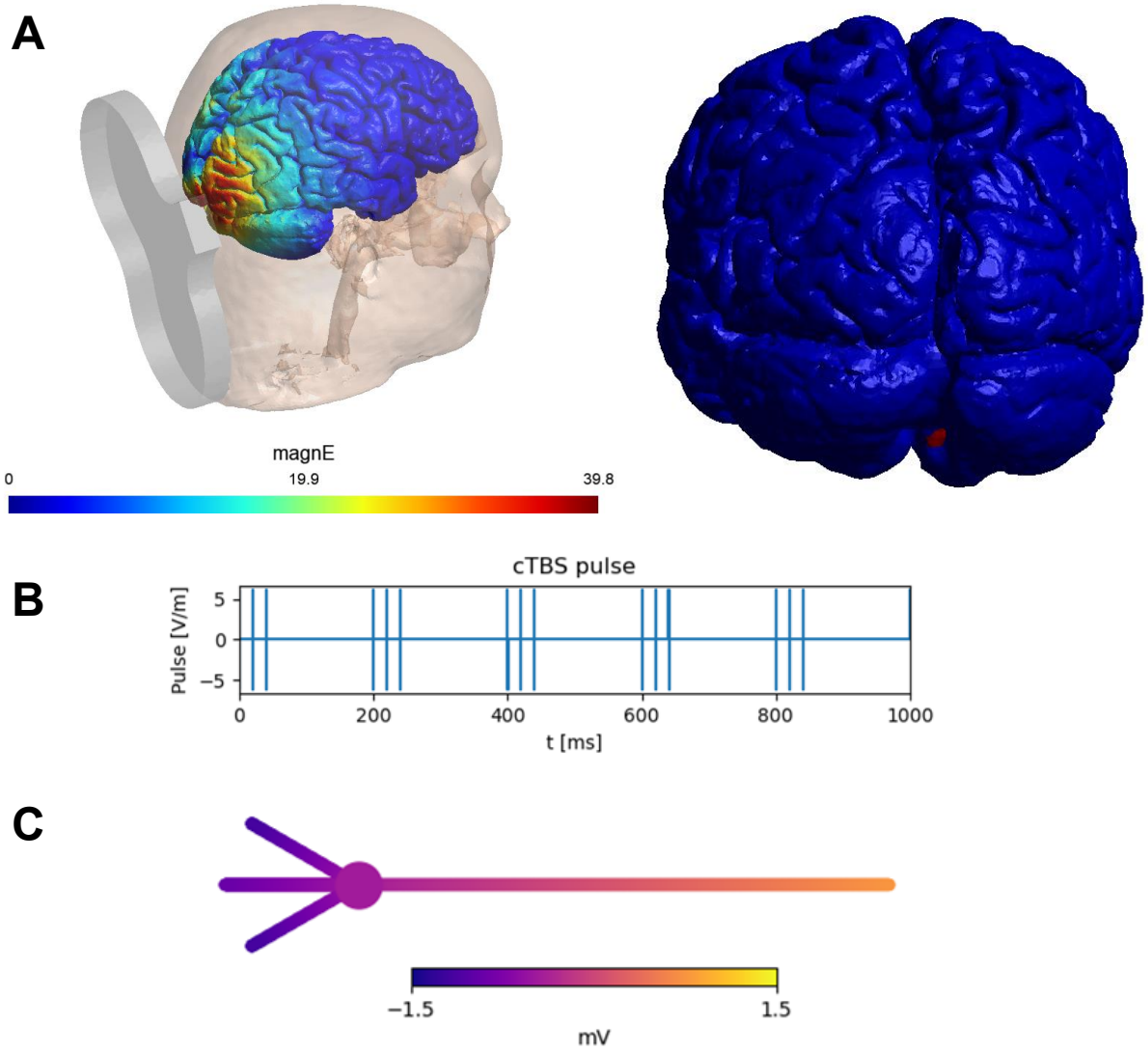


Figure 5.1 Schematics of TMS model.

A: Left - Estimated electric field in a realistic head model. Right - Location of the region of interest (in red) in the grey matter. Caudal view of the grey matter rotated 10° around the vertical axis and 10° around the horizontal axis for a clearer view of the ROI.

B: Time-varying electric field, showing 1 s of a continuous theta burst pulse.

C: Extracellular potential across a simple neuron model including a soma, an axon and three dendrites. A dipole is generated by coupling the extracellular voltage to the neuron.

To reduce the model complexity, the electric field in the ROI was assumed to be spatially uniform, consistent with the quasi-uniform field assumption commonly adopted in transcranial stimulation modelling [271]. The reasoning for this assumption is discussed in Section 5.4.

This modelling approach was informed by the work of Aberra and colleagues. The methods described in this chapter correspond to their study of the effects of a time-

varying, spatially uniform electric field on isolated neurons [215]. The key distinction is that in the present work I modelled a network of interconnected neurons rather than isolated neurons; its consequence is described in Section 5.2.3.

5.2.1 Estimation of the spatial electric field

I estimated the electric field generated by a TMS pulse in a realistic head model using SimNIBS. SimNIBS allows the user to set the following parameters: the head model, the coil model, the distance of the coil from the scalp, the coil position and the speed of variation of the current through the coil $\left(\frac{dI}{dt}\right)$.

I utilised the MRI generated head model *ernie* [272] and the validated model of a MagStim D70 figure of 8 coil [253], both provided with the SimNIBS simulator. I placed the coil 4 mm away from the skin, the default value in SimNIBS, as no details were provided in the experimental paper chosen to reproduce.

No specific information was provided on the coil position and orientation in the experimental paper. In the experiment, the coil was positioned over the occiput on the right side, in the region caudal to the inion. I positioned the coil 1 cm caudal [167], [176], [273] and 7 mm to the right [178] of the inion as done in other experiments targeting the cerebellar vermis. I placed the coil at a 10° angle with respect to the vertical so that it is tangent to the scalp. I tested 19 different orientations, orienting the coil handle across the 360° circle with a 18.95° step. I selected the orientation that generated the lowest possible polar angle, the angle between the electric field and the network's z-axis (see Figure 5.2), and highest possible mean electric field in the ROI.

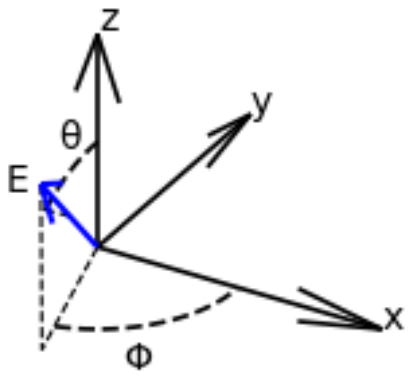


Figure 5.2 Representation of polar, ϑ, and azimuth, Φ, angles. The blue vector represents the mean electric field in the ROI. The x, y and z axes are the cerebellar network axes, with the z-axis being parallel to the neurons' axons. The polar angle, ϑ, is the angle between the electric field and the z-axis; the azimuth angle, Φ, is the angle between the electric field and the x-axis.

I set the speed of variation of the current through the coil, $\frac{dI}{dt}$, to $49.2063 \text{ x } 10^6\ A/s$. The speed of variation of the current through the coil depends approximately linearly on the pulse intensity set by the user, β [274]:

$$\frac{dI}{dt} = \beta\ * \frac{dI_{max}}{dt} \tag{5.1}$$

The peak speed of variation of the current through the coil, $\frac{dI_{max}}{dt}$, is a value provided by the manufacturer for a specific coil type. It is not provided by MagStim for the D70 coil, but it is estimated to be $114.7\ A/\mu s$ [253]. In the experiment, a mean of 42.9% of maximum stimulator output was used to stimulate the participants, which gives $\beta = 0.429$. Substituting β and the estimated $\frac{dI_{max}}{dt}$ in equation 5.1 I obtained:

$$\frac{dI}{dt} = 0.429\ *\ 114.7\ A/\mu s\ =\ 49.2063 \text{ x } 10^6\ A/s \tag{5.2}$$

With this setup, SimNIBS estimated the spatial electric field in each tetrahedral element of the head mesh. I calculated the mean electric field in a sphere of radius 2 mm centred in the stimulation target: [7, -60, -40] in Talairach space as reported in the experimental paper. I used the resulting mean electric field magnitude to generate a time-varying pulse.

5.2.2 Generation of the time-varying electric field

Assuming the quasi-static approximation [31], [250] I multiplied the mean electric field magnitude obtained in the region of interest (ROI) by the desired pulse. I used a cTBS protocol as in the experimental paper. This consists of three-pulse bursts at 50 Hz repeated every 200 Hz. For computational costs, the simulated protocol lasted a maximum of 3 s rather than 20 or 40 s as in the experiment.

5.2.3 Generation and coupling of the extracellular voltage to the cerebellar model

I first calculated the voltage generated by the time varying electric field for each neuron compartment in the cerebellar model. I then coupled the extracellular voltage to each neuron compartment with NEURON's *extracellular* mechanism.

To calculate the voltage, I decoupled the electric field in its three components along the three axes:

$$E_x = \bar{E} * sin(\vartheta) * cos(\phi)$$

$$E_y = \bar{E} * sin(\vartheta) * sin(\phi) \quad (5.3)$$

$$E_z = b * cos(\vartheta)$$

Where $\bar{E}$ is the mean electric field magnitude, ϑ is the polar angle and ϕ is the azimuth angle (see Figure 5.2 above for a representation of the polar and azimuth angles).

The extracellular voltage is calculated as:

$$V_{extracellular} = E_x * (x_0 - x) + E_y * (y_0 - y) + E_z * (z_0 - z) \quad (5.4)$$

Where x, y, and z are the centre points of the neuron compartment, and x_0, y_0 and z_0 are the coordinates of the reference point. I calculated $V_{extracellular}$ for each neuron compartment in the cerebellar network.

In the work of Aberra and colleagues, each isolated neuron has its own reference point, arbitrarily set to the soma of the neuron. The potential at the reference point is set to $0\,V$ [215]. In my model, I arbitrarily chose the approximate centre of the cerebellar network, $[1000, 100, 80]$, as a reference point for all neurons in the network and set it at voltage zero.

The cerebellar cortex is structured in an organised manner with the parallel fibres running along the cerebellar folds, while the ascending axons and the axons of the other neurons are perpendicular to the folds [275]. Based on this structure, to obtain the polar angle, ϑ, I aligned the z-axis of the cerebellar network with the head mesh surface element normals in the following steps:

- Defining the z-axis of the cerebellar network as the unit vector with origin in the approximate network centre, $[1000, 100, 80]$, and direction parallel to the ascending axons;
- Calculating the weighted (by the volume of the element) mean electric field in the ROI;
- Determining the unit normal vectors to the white and grey matter surfaces in the closest proximity of the ROI (a maximum distance between the ROI and grey matter of 5.5 mm and a maximum distance between the ROI and white matter of 3 mm);
- Computing the weighted mean of the unit normal vectors obtained above and aligning the z-axis of the cerebellar model along this mean unit vector (see Figure 5.3);
- Deriving the polar angle, ϑ, as the angle defined by the z-axis of the cerebellar network and the mean electric field vector.

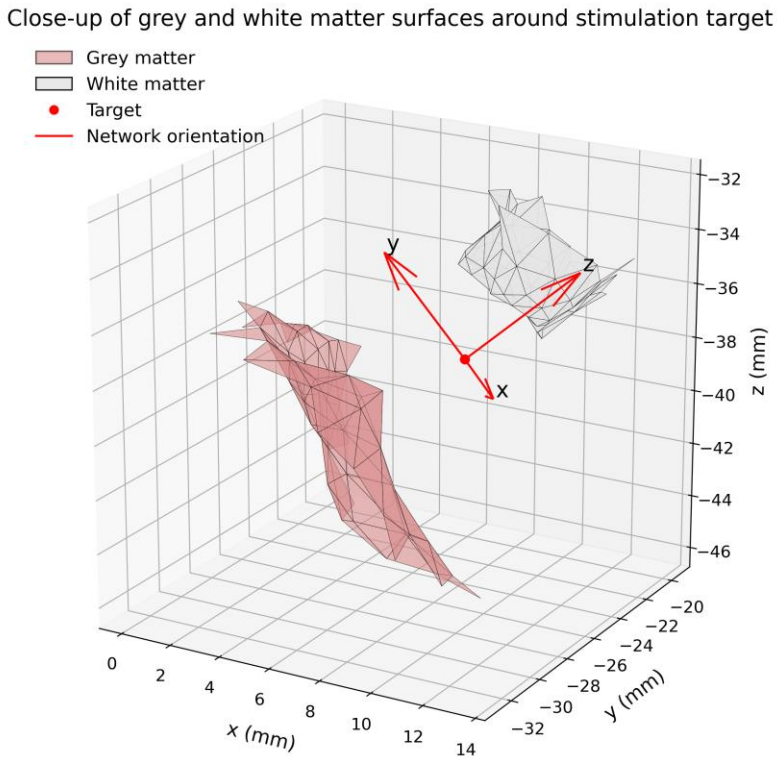


Figure 5.3 Placement and orientation of the axes of the cerebellar network in the head model. The white and grey matter surface elements in proximity to the ROI are shown in grey and in pink. The axes of the cerebellar network are placed with the origin in the stimulation target (red dot). The z-axis is aligned with the weighted mean of the grey and white matter unit normal vectors. The x- and y-axes are oriented arbitrarily.

The azimuth angle, ϕ, depends on the orientations of the neurons around their z-axis and is not anatomically constrained as the polar angle, ϑ. I have tested 36 azimuth angles, ϕ, from 0° to 350° in 10° steps. For computational costs, these tests have only been performed on the isolated Purkinje cell, with simulations lasting 1 s. The best azimuth angle, ϕ, measured as the angle that generated the highest response in the Purkinje cell's instantaneous firing rate (see Section 5.2.4), has then been used for the subsequent granular layer and Purkinje cell simulations.

I ran granular layer and Purkinje cell simulations adding the TMS induced extracellular potential, $V_{extracellular}$, to all compartments of all cells. For computational costs, the cerebellar network simulations lasted a maximum of 3 s rather than 20 to 40 s as in the experiment. For both granular layer and Purkinje cell simulations, the stimulation was applied from the beginning to the end of the simulation. I simulated the granular layer for 3 s and the Purkinje cell for 2.4 s as the first 600 ms of the granular layer spike trains were discarded to allow the network to reach its steady state.

5.2.4 Analysis

I quantified the effects of the stimulation employing the following metrics:

- Mean firing rate of granule, Golgi and Purkinje cells;
- Instantaneous firing rate of an isolated Purkinje cell;
- Spike timing following a stimulation burst comparing the network affected by two stimulation conditions.

The mean firing rate, mfr, for each cell population was calculated as:

$$mfr = \frac{n_{spikes}}{n_{cells} * t} \tag{5.5}$$

Where n_{spikes} is the total number of spikes generated in the time interval t by n_{cells} granule or Golgi cells ($n_{cells} = 1$ in the case of the Purkinje cell). To exclude transient effects, the first 600 ms of each simulation were discarded when calculating the mean firing rate.

To select the azimuth angle, ϕ, I measured the angle that generated the strongest response on the instantaneous firing rate of the isolated Purkinje cell. To quantify stimulation-induced changes in the instantaneous firing rate, I fitted the instantaneous firing rate with a straight line (equation 5.6) using a least-squares optimisation procedure with a maximum of 10,000 iterations.

$$y = ax + b \tag{5.6}$$

For the initial parameters, I set b to the maximum instantaneous firing rate observed and a to 0.

I calculated the root mean square error and the coefficient of determination of the best fit discarding the first 300 ms of the simulations allowing the Purkinje cell to reach its steady state. This analysis was performed on simulations of the isolated cell without synaptic inputs. I selected the azimuth angle, ϕ, that gives the highest mean square error and lowest coefficient of determination, indicating that the stimulation disrupts the regular spiking of the Purkinje cell.

To quantify the effects of the stimulation at the network level, I employed the stimulus-triggered average technique. I stimulated the network with the model described previously in this chapter under two conditions: a low-amplitude condition and a high-

amplitude condition. The low-amplitude condition reproduces the experimental paper [177]. I increased the mean electric field magnitude fivefold in the high-amplitude condition. For each neuron, the mean difference in spike timing between the two conditions was computed over a 100 ms window following the stimulation bursts. As in previous analyses, I discarded the first 600 ms of each simulation to allow the network to reach steady state. I excluded from the analysis cells that did not exhibit the same number of spikes in the analysed time window across both conditions.

5.3 Results

I first placed the cerebellar network in the head model, orienting the z-axis of the network parallel to the weighted mean surface unit normal vectors (see Figure 5.4).

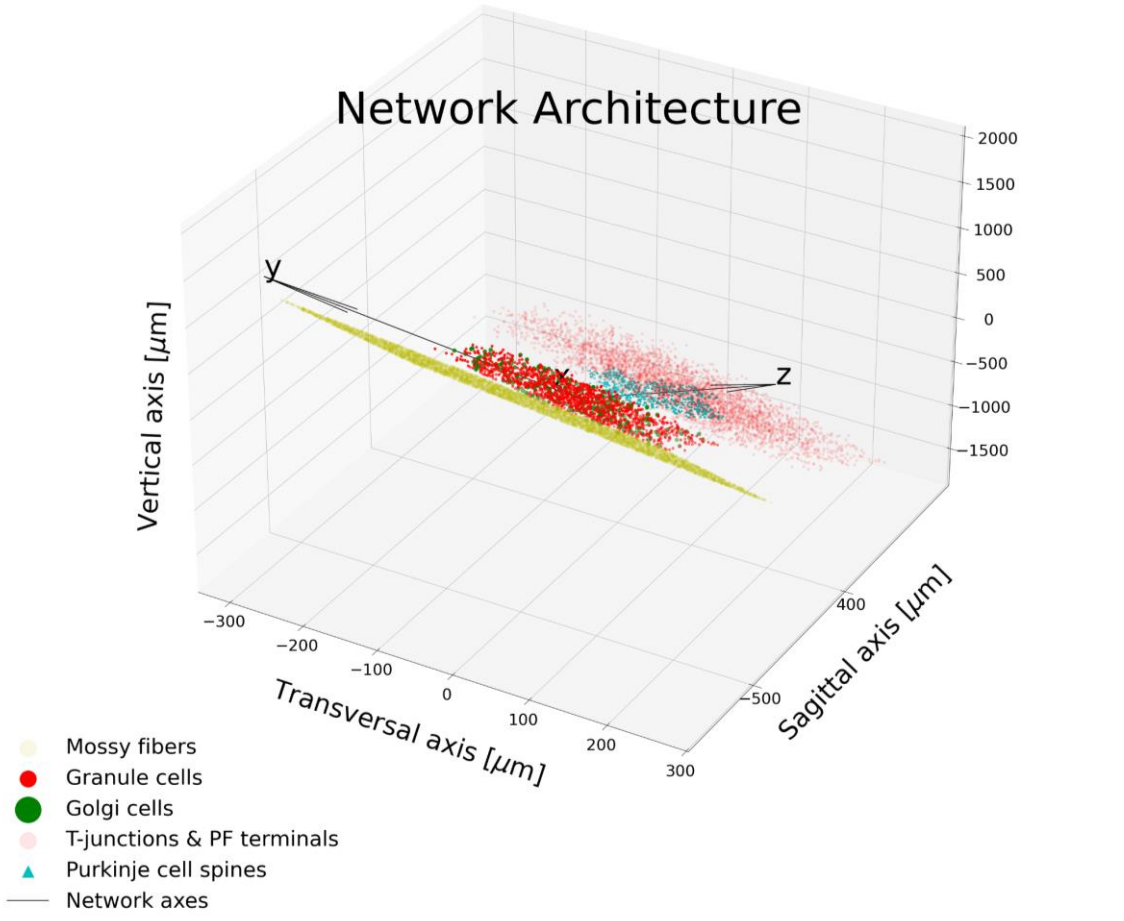


Figure 5.4 Cerebellar network architecture oriented according to the brain structure in the ROI in the head model. The z-axis is parallel to the ascending axons. The x and y-axes are arbitrarily set.

5.3.1 Coil orientation

I established the coil orientation that generated an electric field best aligned with the cerebellar network in the region of interest. I tested 19 orientations, starting with the coil handle pointing downwards (see Figure 5.5) and rotating the coil clockwise around its z-axis in equally spaced steps.

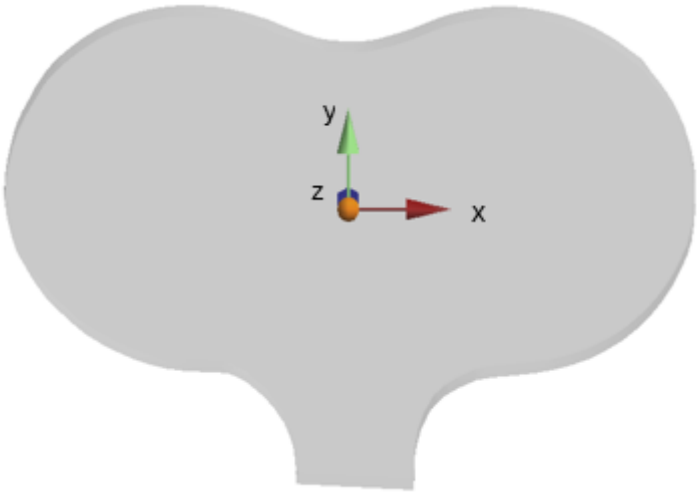


Figure 5.5 Coil starting position. The coil handle is pointing downwards. The coil is rotated around its z-axis, in blue in the figure.

Figure 5.6 below summarises the polar angle, ϑ, and the mean electric field magnitude in the region of interest (ROI) obtained from the 19 simulations performed varying the coil orientation. I selected a coil orientation of 246.32° which produces the lowest polar angle, ϑ. All further results presented are obtained with this coil orientation.

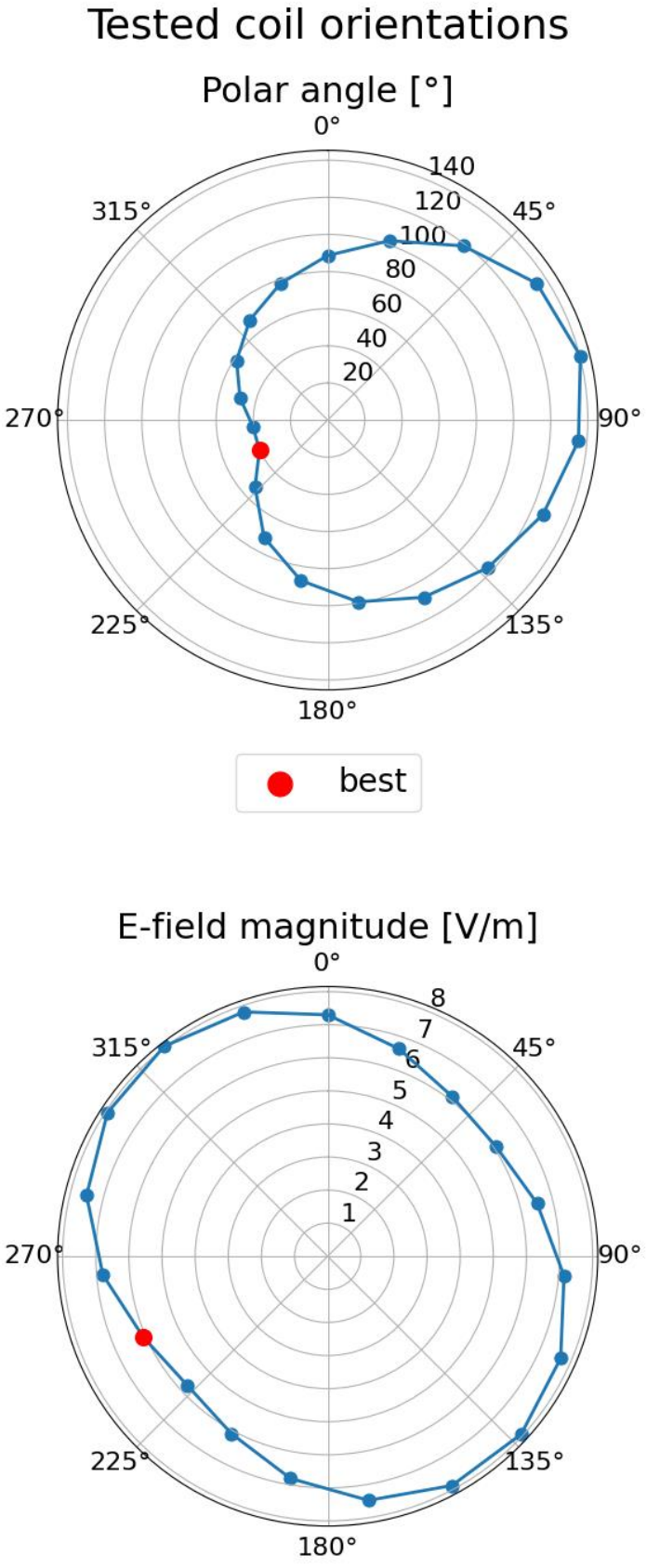


Figure 5.6 Polar angle (top) and mean electric field magnitude (bottom) for the tested coil orientations. The selected coil orientation is highlighted in red.

5.3.2 Electric field in ROI

With a coil orientation of 246.32°, I obtained a polar angle, ϑ, of 40.07°. See Figure 5.7 for a representation of how the electric field is placed with respect to the cerebellar network.

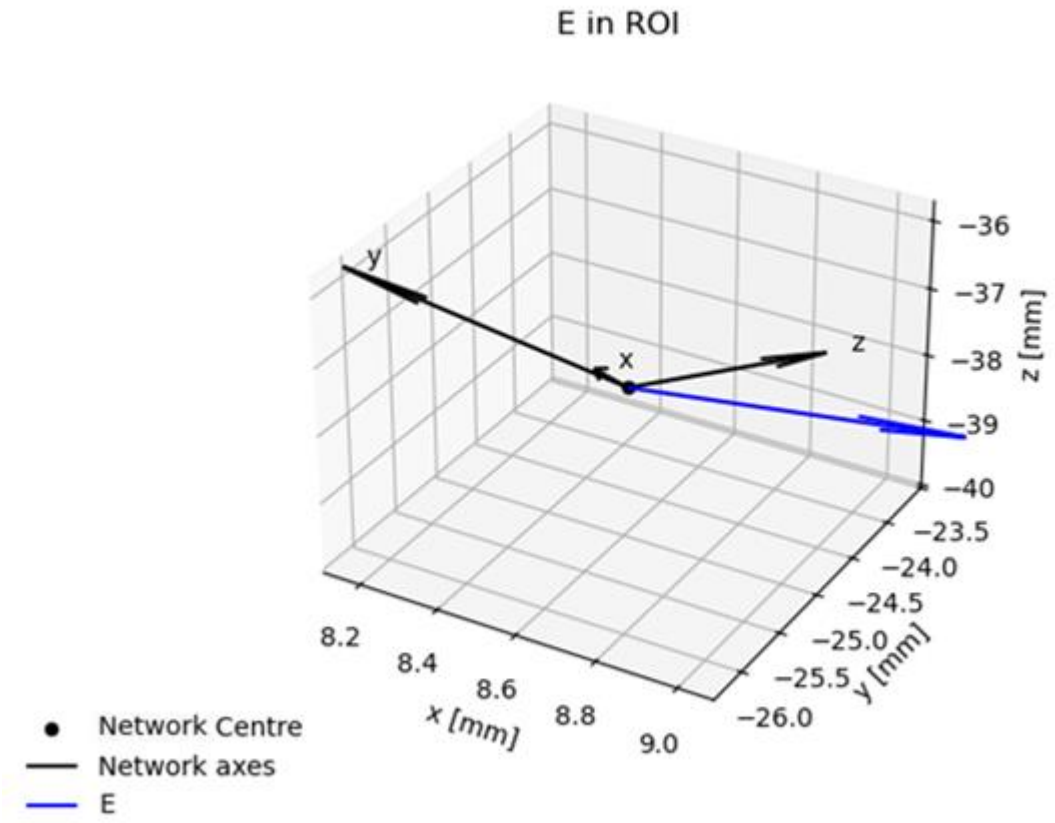


Figure 5.7 Mean electric field in the ROI. In black the axes of the cerebellar network, in blue the mean electric field unit vector. The network centre, black dot, is located at the stimulation target, [7, −60, −40] in the stereotaxic Talairach coordinate system.

As expected, superficial areas under the coil are affected by a stronger electric field. The deeper the area, the weaker the induced electric field. The peak electric field magnitude obtained in the head model is of 39.8 V/m. In the ROI, the mean electric field magnitude is of 6.08 V/m (see Figure 5.8).

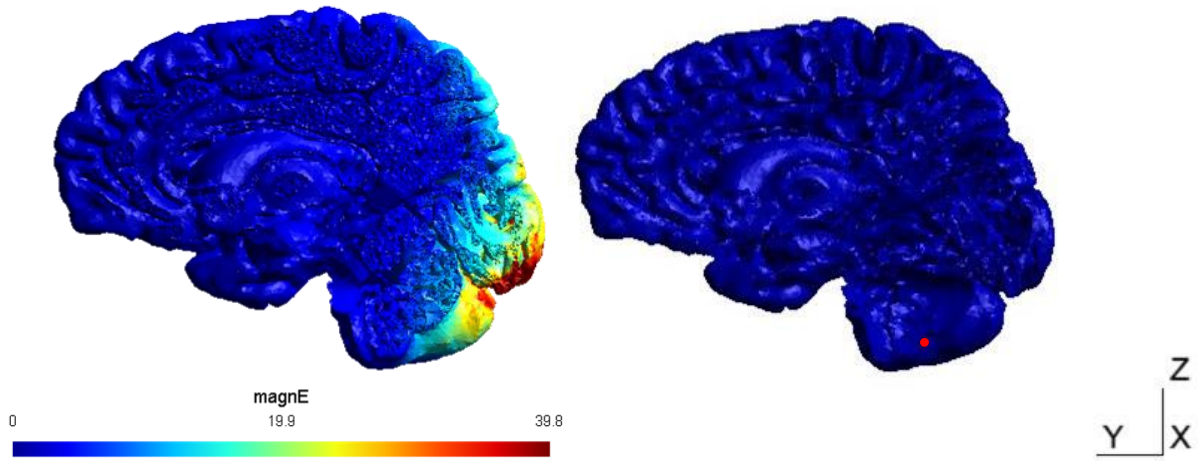


Figure 5.8 Sagittal section of the grey matter showing the electric field magnitude, in V/m, on the left and the ROI location highlighted with a red dot on the right.

5.3.3 Azimuth angle

To define the azimuth angle I tested 36 different azimuth angles running simulations of the isolated Purkinje cell. With a mean electric field magnitude of 6.08 V/m, the stimulation does not affect the instantaneous firing rate of the Purkinje cell, regardless of the azimuth angle. See Figure 5.9 as an example plot of the instantaneous firing rate of the isolated Purkinje cell stimulated with mean electric field magnitude of 6.08 V/m and an azimuth angle, ϕ, of 30°.

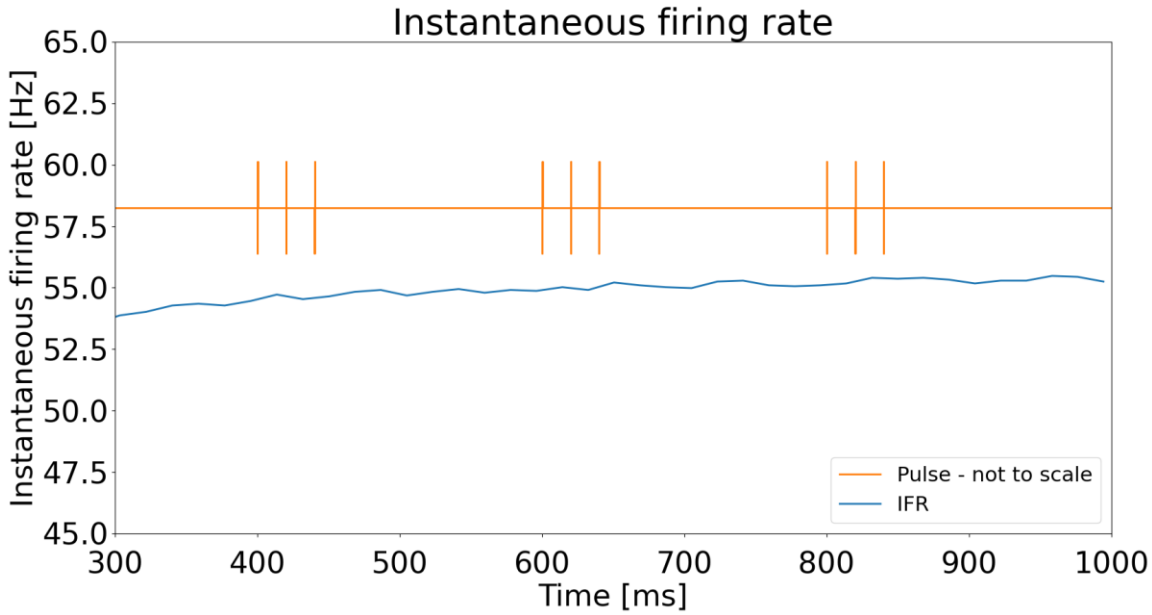


Figure 5.9 Instantaneous firing rate of the isolated Purkinje cell, in blue, stimulated by a uniform electric field with magnitude 6.08 V/m. In orange the stimulation pulse, the pulse amplitude is not to scale. The results shown are obtained with an azimuth angle, ϕ, of 30°.

To quantify stimulation-induced changes in the instantaneous firing rate of the Purkinje cell, I fitted the instantaneous firing rate with a straight line, discarding the first 300 ms of the simulation to remove transient effects (see Figure 5.10). I then quantified how much the stimulation affects the regular firing of the Purkinje cell by measuring how far from the perfect fit the instantaneous firing rate is, by means of root mean square error and coefficient of determination.

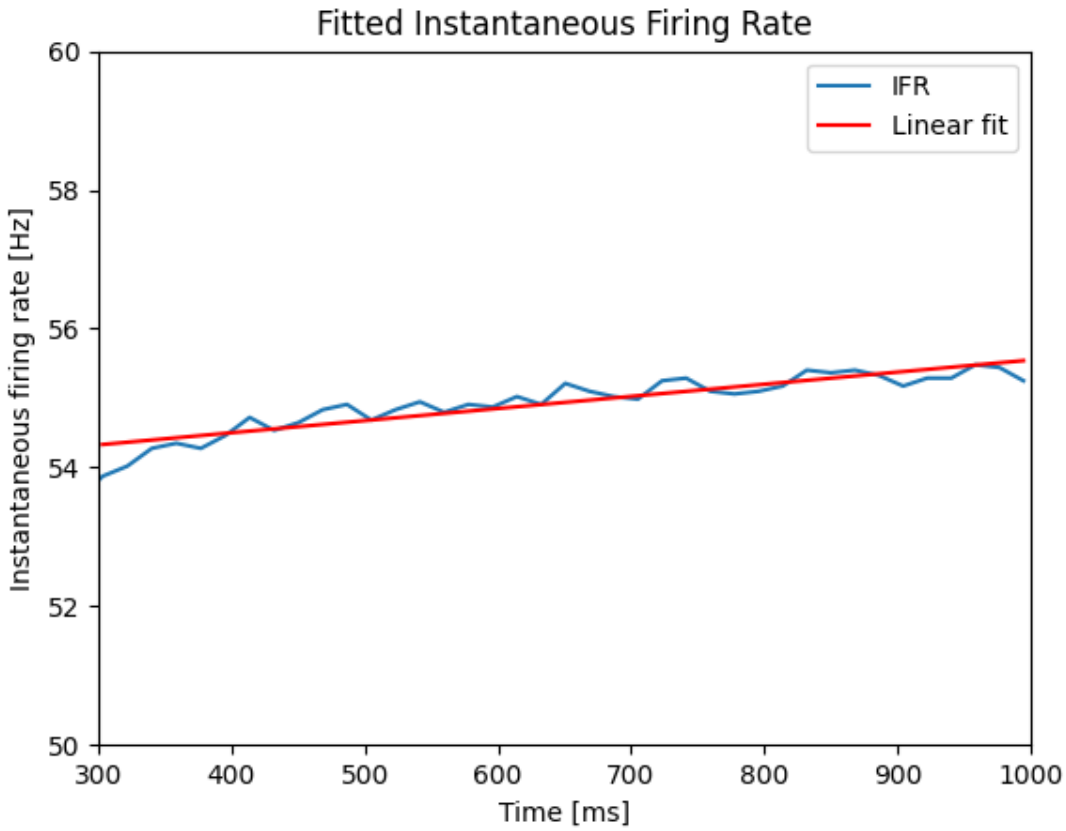


Figure 5.10 Instantaneous firing rate, in blue, of the isolated Purkinje cell stimulated with mean electric field magnitude of 6.08 V/m and an azimuth angle, ϕ, of 30°. Best linear fit in red.

Figure 5.11 summarises the root mean square error (RMSE) and the coefficient of determination (R2) of the best linear fit for each tested azimuth angle. From the figure, as the coefficient of determination is close to one and the root mean square error is very low, it is evident that the instantaneous firing rate is not affected by the stimulation.

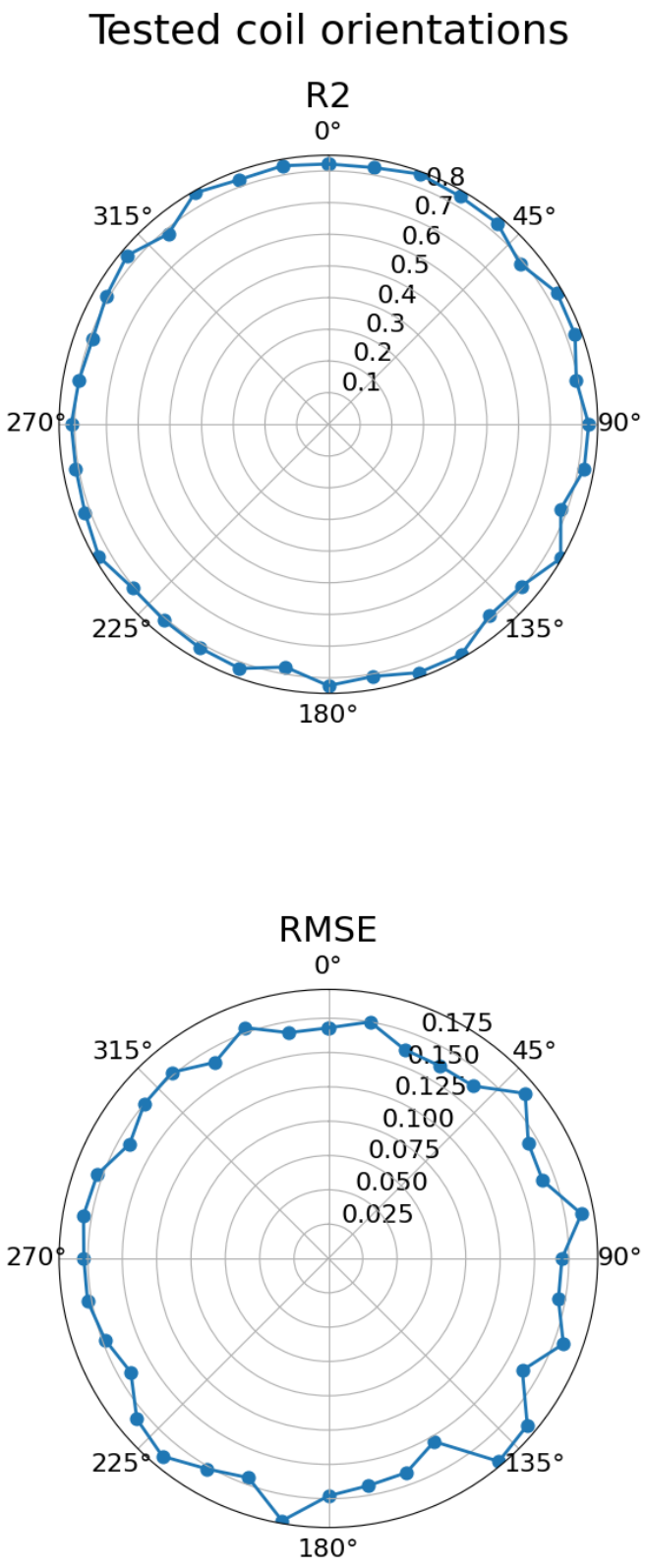


Figure 5.11 Coefficient of determination, R2, (top) and root mean square error, RMSE, (bottom) of the best linear fit for the instantaneous firing rate of the isolated Purkinje cell. The cell is stimulated with a uniform electric field of mean magnitude 6.08 V/m. The azimuth angle, ϕ, is varied between 0° and 360° in 10° steps.

To generate a response in the instantaneous firing rate of the Purkinje cell, I increased the mean electric field fivefold. In these conditions the instantaneous firing rate is affected by the stimulation and the choice of the azimuth angle, ϕ, greatly affects the behaviour of the Purkinje cell (see Figure 5.12).

I chose an azimuth angle, ϕ, of 30°. It has the second highest root mean square error and the lowest coefficient of determination (see Figure 5.13) and for each pulse after the Purkinje cell has reached its steady state, its instantaneous firing rate is affected (see Figure 5.12 above). All simulations of the full cerebellar network were run with an azimuth angle, ϕ, of 30°.

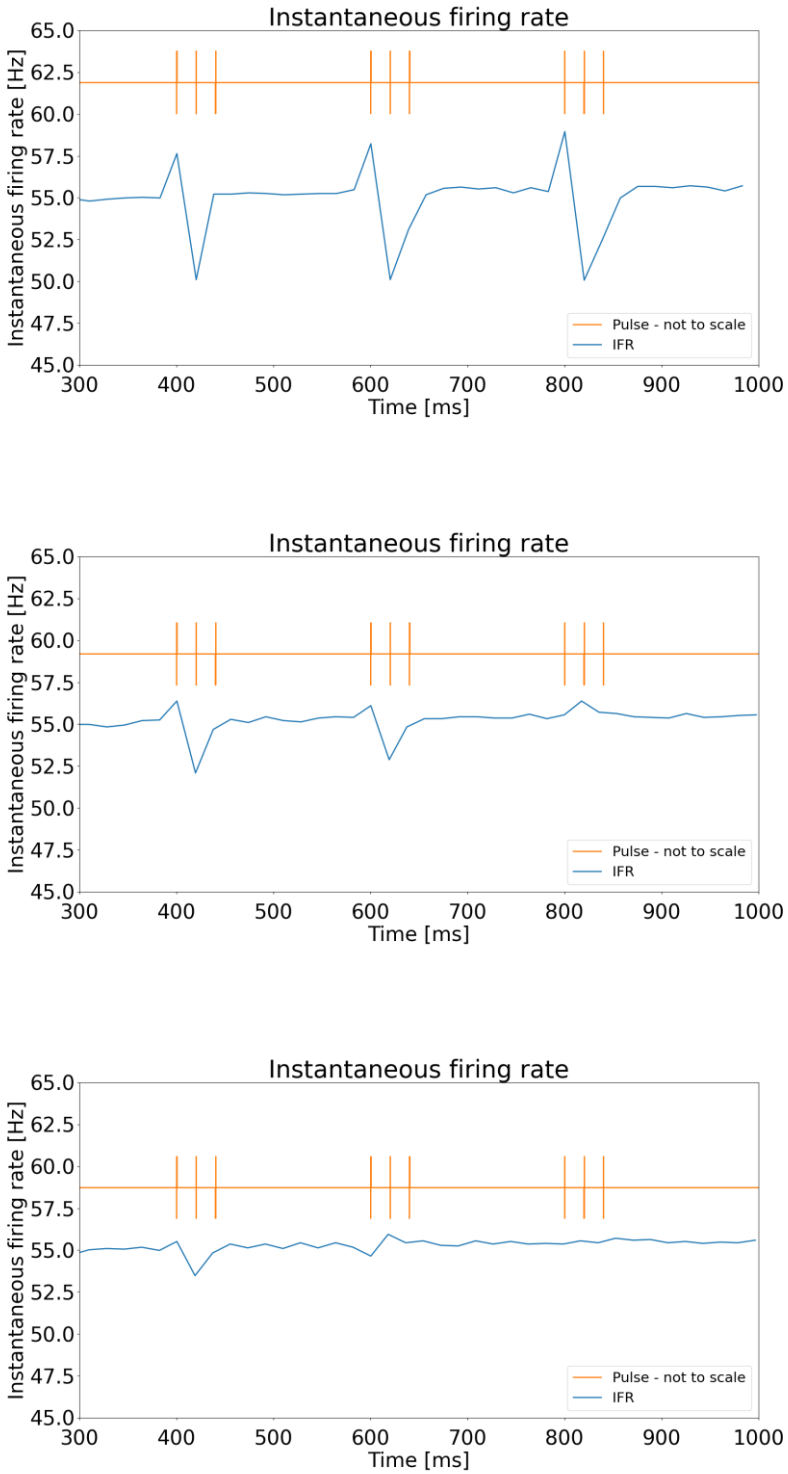


Figure 5.12 Instantaneous firing rate of the isolated Purkinje cell, in blue, stimulated by a uniform electric field with magnitude 30.4 V/m. In orange the stimulation pulse, the pulse amplitude is not to scale. The results shown are obtained with an azimuth angle, ϕ, of 30°, 200° and 150° from top to bottom.

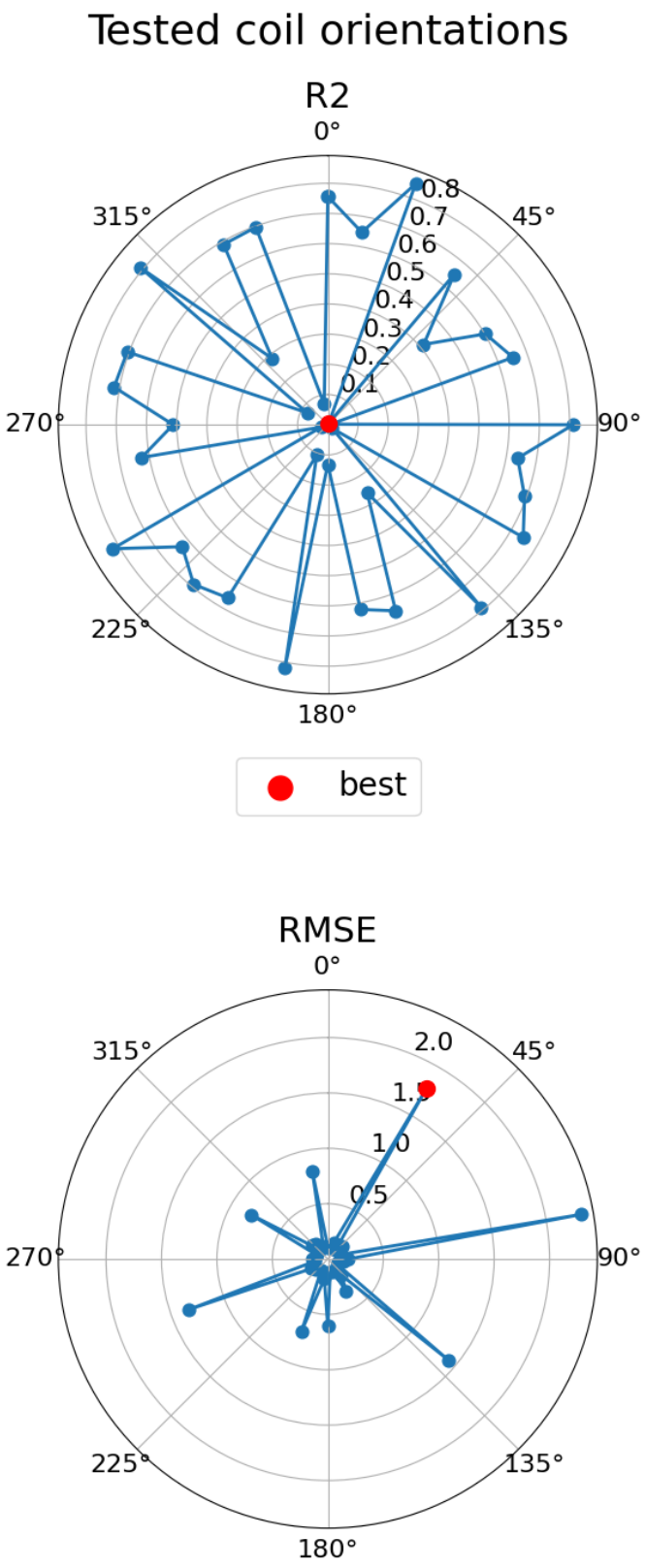


Figure 5.13 Coefficient of determination, R2, (top) and root mean square error, RMSE, (bottom) of the best linear fit for the instantaneous firing rate of the isolated Purkinje cell. The cell is stimulated with a uniform electric field of mean magnitude 30.4 V/m. The azimuth angle, ϕ, is varied between 0° and 360° in 10° steps. The chosen azimuth angle, 30°, is highlighted in red.

5.3.4 Stimulation effect at network level

The effects of the stimulation on the isolated Purkinje cell are presented in the previous section. In this section I present the effects of the stimulation on the network in terms of mean firing rate and stimulus-triggered average.

I compared the mean firing rate of each cell population in three conditions: without any stimulation, a low-amplitude condition and a high-amplitude condition. I increased the mean electric field magnitude fivefold in the high-amplitude condition, from 6.08 V/m to 30.4 V/m. The stimulation does not highly affect the mean firing rate of the granule and Golgi cells, and it has no effect on the mean firing rate of the isolated Purkinje cell. However, it decreases the mean firing rate of the Purkinje cell when connected to the granular layer network. Table 5.1 summarises the mean firing rate of Golgi, granule and Purkinje cells.

Cell type	No stimulation [Hz]	Low-amplitude [Hz]	High-amplitude [Hz]
Golgi cells	22.69	22.64	22.69
Granule cells	3.38	3.38	3.39
Isolated Purkinje cell	55.42	55.42	55.42
Purkinje cell	66.67	56.67	66.11

Table 5.1 Mean firing rate of Golgi, granule and Purkinje cells in three conditions: the network is not stimulated (no stimulation), the network is stimulated with and electric field magnitude of 6.08 V/m (low-amplitude) and an electric field magnitude of 30.4 V/m (high-amplitude). The mean firing rate of the Purkinje cell is shown both without receiving any synaptic inputs (isolated Purkinje cell) and when receiving the granular layer inputs (Purkinje cell).

I also analysed the spike timing following a stimulation burst comparing the network affected by the low-amplitude and the high-amplitude stimulation conditions.

The Golgi cells stimulated in the high-amplitude condition spiked on average 0.30 ± 7.75 ms later than the Golgi cells stimulated in the low-amplitude condition (see Figure 5.14). The average was calculated over 394 Golgi cells.

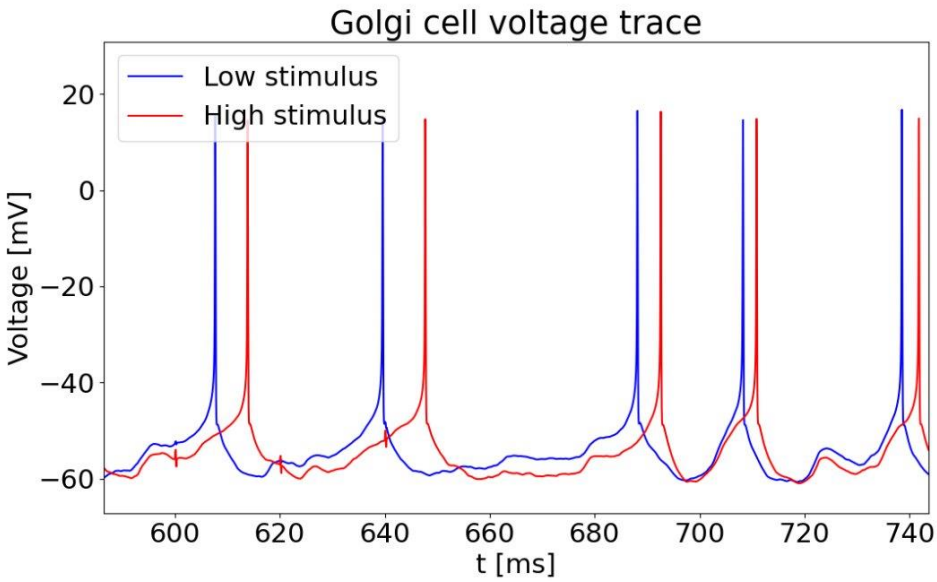


Figure 5.14 Golgi cell voltage trace at a spike following a stimulation burst. In blue the voltage trace of the Golgi cell stimulated with the low-amplitude condition. In red the voltage trace of the Golgi cell stimulated with the high-amplitude condition. The spikelets present at 600, 620 and 640 ms are caused by the stimulation pulses.

The granule cells stimulated in the high-amplitude condition spiked on average 0.055 ± 9.06 ms sooner than the granule cells stimulated in the low-amplitude condition (see Figure 5.15). The average was calculated over 133,370 granule cells.

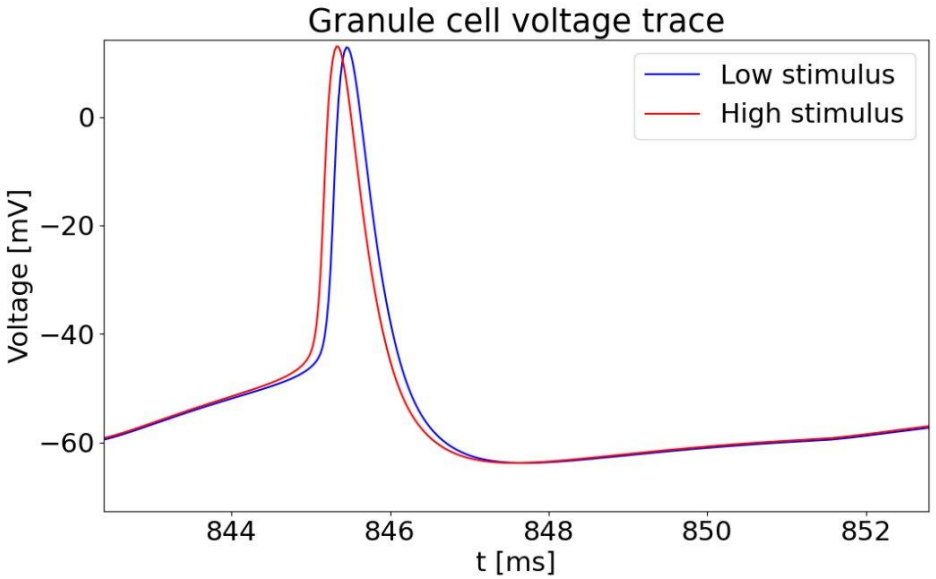


Figure 5.15 Granule cell voltage trace at a spike following a stimulation burst. In blue the voltage trace of the granule cell stimulated with the low-amplitude condition. In red the voltage trace of the granule cell stimulated with the high-amplitude condition.

The isolated Purkinje cell stimulated in the high-amplitude condition spiked on average 0.54 ± 1.27 ms sooner than the Purkinje cell stimulated in the low-amplitude condition in all analysed time windows (see Figure 5.16). The opposite is true for the Purkinje cell in the context of the cerebellar network, where it is affected both by the stimulation and the inputs from the granule cells receiving the same stimulation. When receiving the granular layer inputs, the Purkinje cell stimulated in the high-amplitude condition spiked on average 3.29 ± 9.95 ms later than the Purkinje cell stimulated in the low-amplitude condition (see Figure 5.17). However, in 50% of the analysed time windows, the Purkinje cell stimulated in the high-amplitude condition spiked more times than the Purkinje cell stimulated in the low-amplitude condition.

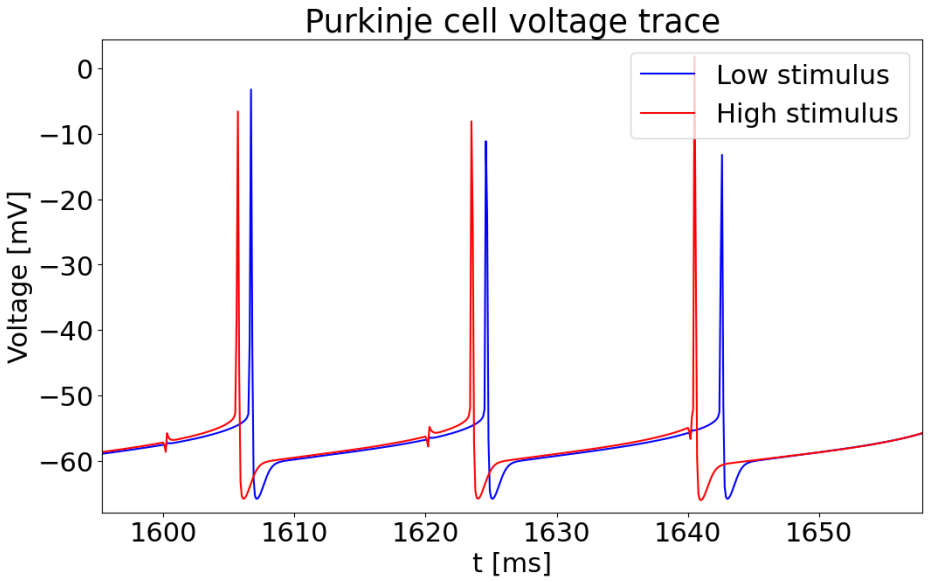


Figure 5.16 Isolated Purkinje cell voltage trace at a spike following a stimulation burst. In blue the voltage trace of the Purkinje cell stimulated with the low-amplitude condition. In red the voltage trace of the Purkinje cell stimulated with the high-amplitude condition. The spikelets present at 1600, 1620 and 1640 ms are caused by the stimulation pulses.

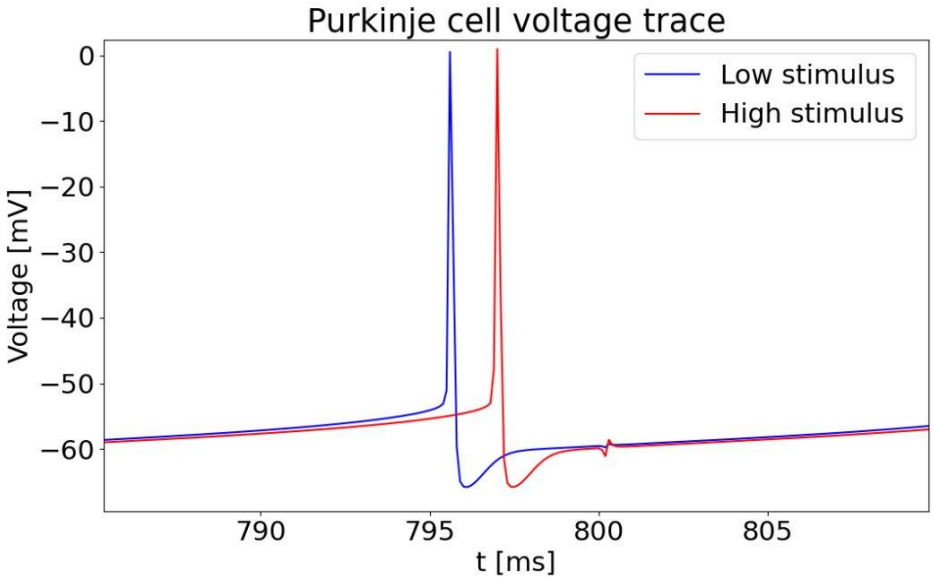


Figure 5.17 Purkinje cell voltage trace at a spike following a stimulation burst. In blue the voltage trace of the Purkinje cell stimulated with the low-amplitude condition. In red the voltage trace of the Purkinje cell stimulated with the high-amplitude condition. The spikelet present at 800 ms is caused by a stimulation pulse.

5.4 Discussion

I have shown that the Golgi and granule neurons are not affected by a 2 s cTBS stimulation at 42% of stimulation intensity in terms of their mean firing rate as shown in Table 5.1. The mean firing rate of the isolated Purkinje cell is not affected by the stimulation. However, in the context of the network, the stimulation reduces the cell's mean firing rate. As the Purkinje cell is bistable [51], [276], even small inputs can alter the cell's state from tonic firing to quiescence, causing the changes observed in the mean firing rate.

The instantaneous firing rate of the isolated Purkinje cell is not affected by the low-amplitude stimulation (see Figure 5.11), and requires a stronger electric field to observe a stimulus-induced effect (see Figure 5.13). However, in the context of the network, the Purkinje cell is affected even by the low-amplitude stimulation - its mean firing rate decreases (see Table 5.1). Notably, the low-amplitude stimulation condition appears to produce a greater reduction in mean firing rate than the high-amplitude condition. This result should be interpreted with caution, as it is based on a single simulation per condition (baseline, low-amplitude stimulation, and high-amplitude stimulation).

With the stimulus-triggered averaging technique, I showed that while the mean firing rate of Golgi and granule cells is unaffected by the stimulation, the spike times are altered. The two cell populations are affected by the stimulation in opposite ways. A high-amplitude condition makes the granule cells spike a fraction sooner, while the Golgi cells spike later compared to the low-amplitude condition.

As with all models, the proposed stimulation model comes with limitations. The following limitations are relevant to discuss:

- The findings presented in this chapter were obtained by analysing one simulation per condition (baseline, low-amplitude stimulation and high-amplitude stimulation). Given the small changes and high variability in spike timing observed using the stimulus-triggered averaging technique, these findings require validation through repeated simulations. The same limitation applies to the analysis of mean firing rates across the cell populations. Therefore, although the current results suggest that the network is affected by the stimulation, the lack of repeated simulations prevents a robust quantification of these effects. To draw more reliable conclusions, the analyses should be repeated across multiple simulations.

- I assumed a uniform electric field in the ROI. While this is a simplification that ignores regional differences in morphology and biophysics, it is a reasonable approximation when considering a small ROI [271]. Given that the polar and azimuth angles are set for the network and do not vary among neurons, a spatially-varying electric field in a very small ROI would not change enough to produce meaningful differences in polarisation of the neurons. Another reason for this choice is that SimNIBS does not provide precise estimates of the electric field and surface normals for the cerebellum, which is discussed in the next point. As such, small differences in the electric field and brain fold orientation are not to be taken as accurate, making the uniform assumption necessary.

- The surface model of the cerebellum in SimNIBS is coarse [250], which means SimNIBS does not provide an accurate estimate of the electric field in the cerebellum. This does not influence the validity of my results. Given that I use a uniform electric field rather than a spatially varying field, I do not require particular accuracy in the electric field calculation. If the model were to be used

to test stimulation protocols in clinical settings, then a more precise representation of the cerebellum would be necessary.

- All neurons in the network are orientated along the same z-axis. Although this is a simplification, given that the network is small (2 mm in the longest direction) it is reasonable to assume that the network lies in the same flat plane.

- There is no variability in the modelled granule cells. Given that all modelled granule cells share the same morphology, the stimulation generates the same potential difference across each cell. As discussed in the previous chapter, this was done for computational reasons as simulating in the order of a hundred thousand multi-compartment cells is extremely computationally expensive.

- The azimuth angle was chosen based on its effect on simulations of the isolated Purkinje cell. This was done for computational costs of running multiple granular layer simulations. It could be that the granular layer is more sensitive to a different azimuth angle.

- The 3D location of the sections of granule and Golgi cells is not coded in NEURON using NEURON's *pt3d* function for computational reasons. As discussed in the previous chapter, Golgi cells have some variability in the angles formed by their dendrites and the vertical axis. This variability is taken into account when forming the synaptic connections between granule and Golgi cells and mossy fibres and Golgi cells. However, it is not coded in NEURON when simulating the network. This can affect the extracellular potentials, $V_{extracellular}$, affecting those cell populations.

- I simulated a maximum of 3 s, the stimulation protocol in the reproduced experimental paper lasted 20 to 40 s. This was done to reduce computational costs. However, the cerebellar network reaches a steady state by the end of the 3 s simulation, so simulating for longer would not affect the presented results. The fact that a 40 s stimulation was needed to influence the measured eye movements could be due to synaptic plasticity, which is not accounted for in the cerebellar model.

5.5 Conclusion

In this chapter I presented my transcranial stimulation model. The development of the described model addresses the gap in the literature #2 - *the lack of a multi-scale non-invasive stimulation model including synaptic connections*. In this chapter, I addressed my research questions 1 and 2.

1. *Are the neurons in the cerebellar vermis, lobules VI–VII, affected by TMS?* From the results shown in Figure 5.8, the stimulation target chosen by the experimental paper is located in a very deep region that therefore is exposed to a low magnitude electric field. From the results shown in Table 5.1 it is possible to conclude that a cTBS protocol at 42% intensity of the maximum stimulator output does not generate any significant effect in the Golgi and granule cell's mean firing rate. It does, however, alter the behaviour of the Purkinje cell.
2. *How does a cTBS protocol affect the neurons in terms of mean firing rate, instantaneous firing rate and spike timing?* The mean firing rate of granule and Golgi cells is not affected by the stimulation. The stimulus decreases the Purkinje cell's firing rate. The instantaneous firing rate of the Purkinje cell is not affected by the modelled stimulation protocol; a higher mean electric field magnitude is required to disrupt the regular spiking of the Purkinje cell (see Section 5.3.3). On average, the high-amplitude condition makes the granule cells spike sooner, the Golgi cells later and the Purkinje cell more frequently than the low-amplitude condition.

In the next chapter, I will describe the vertical oculomotor system model and how I used it to link the simulation results to a measurable behavioural outcome, validating the non-invasive stimulation model.

Chapter 6

Validation method for the model of transcranial magnetic stimulation

This chapter describes the validation approach used for the transcranial magnetic stimulation (TMS) model. I validated the TMS model by linking the output of the cerebellar network to a measurable behaviour: eye movements. Specifically, I compared predicted eye movements under baseline conditions and eye movements in stimulated conditions with experimental measurements reported by Colnaghi and colleagues [177] (see Section 5.1 for a description of the experimental study).

This chapter is structured as follows. First, I describe the physiological mechanisms underlying the generation of eye movements, with particular emphasis on the role of the cerebellum in this process. Next, I introduce the vertical oculomotor system model [1] employed as the validation framework for the TMS model. Then, I describe how I integrated the vertical oculomotor system model [1] with the cerebellar network output to predict eye movements. Finally, I present the eye movements predicted by my simulations.

The work presented in this chapter addresses my research question 3 *Is a vertical oculomotor system model [1] suitable as a validation method for transcranial stimulation models targeting the cerebellum?* The work presented in this chapter also addresses *The lack of validation methods for non-invasive stimulation models*, which, as presented in Chapter 1, is the third gap in the literature tackled in my PhD.

6.1 Eye movements

For the purpose of this dissertation, I will focus on vertical saccades and gaze holding, the eye movements predicted by the vertical oculomotor system model [1] I employed.

6.1.1 Saccades

Saccades are rapid eye movements that shift the direction of gaze toward an object of interest, either in response to visual stimuli or during visual scene exploration [170], [277].

Saccade generation is initiated when visual information from the retina activates neurons in the frontal and parietal cortices [170]. This information is subsequently transmitted to the reticulotegmental nucleus and the superior colliculus [170], two structures located in the brainstem [278]. The superior colliculus modulates the activity of the reticulotegmental nucleus, and also projects directly to the saccadic burst generator in the brainstem [170].

The reticulotegmental nucleus projects to the cerebellar vermis, which exerts inhibitory control over one of the cerebellar deep nuclei, the caudal fastigial nucleus [170]. The caudal fastigial nucleus, in turn, influences the saccadic burst generator both directly and indirectly via thalamic projections [170]. The saccadic burst generator ultimately produces premotor commands for saccade execution [170]. These commands are transmitted to the extraocular muscles, resulting in the initiation of a saccadic eye movement [279].

6.1.2 Gaze holding

Gaze holding is the ability to hold the eyes steady looking away from the centre (straight-ahead) position, called an eccentric gaze position [279].

During gaze holding, the extraocular muscles must contract to sustain an eccentric eye position [280]. The continuous neural activity necessary to produce this muscle contraction is generated by a sophisticated neuronal mechanism, the oculomotor integrator [280]. The oculomotor integrator converts the transient bursts corresponding to eye velocity into steady state firing corresponding to eye position [280]. The oculomotor integrator responsible for vertical gaze holding is the interstitial nucleus of Cajal [280], a structure located in the brainstem [278].

6.1.3 Role of the cerebellum

As discussed in Section 1.2.3, the cerebellum is thought to influence movement by constructing internal kinematic and dynamic models of the body and using these models within a feedback control framework to achieve precise motor output [14].

Several experimental observations suggest that saccadic eye movements are subject to feedback control [14], [170]. Gaze holding also relies on feedback mechanisms, as neural integrators responsible for maintaining stable eye position are inherently imperfect, leading to slow eye drifts that must be corrected through external feedback loops [279]. In both cases, the cerebellum plays a key role within these feedback control systems [170], [279].

It is hypothesised that the cerebellum contains an internal model of the oculomotor plant, enabling it to estimate eye velocity [14]. This estimated eye velocity is compared with the desired eye velocity, and the resulting error signal is transmitted back to the brainstem contributing to the fine control of eye movements [14], [279].

6.2 Vertical oculomotor system model

The research group led by Stephen Glasauer proposed several control theory models to predict eye movements, in particular to study downbeat nystagmus and the contribution of cerebellar feedback to oculomotor control [1], [279]. In this work, I employed a simplified version of the vertical oculomotor system model [1] capable of simulating vertical saccades and gaze holding (see Figure 6.1 for an outline of the model). The structure and governing equations of the model are described below.

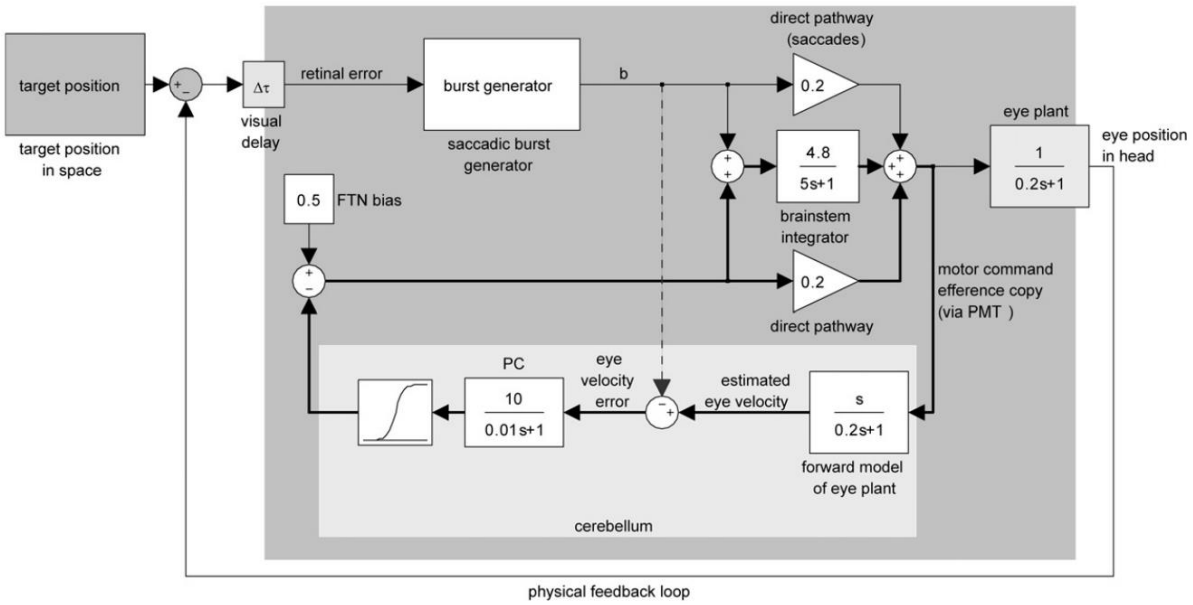


Figure 6.1 Outline of the vertical oculomotor system model. The model of the cerebellum is highlighted in light grey. Figure taken from [1].

In this model, the visual information (given by the target position block) drives the saccadic burst generator, which produces the saccadic motor command. This motor command is then transformed into eye movements by the eye plant block. In parallel, the motor command is relayed to the cerebellum (light grey area), which provides feedback control.

The transmission of the visual information from the retina to the saccadic burst generator is only modelled by delaying the arrival of the visual signals (visual delay block). The brainstem integrator block represents the interstitial nucleus of Cajal and enables gaze holding.

The cerebellar component models the floccular lobe and functions as a feedback loop. This floccular lobe contains a forward model of the eye plant, allowing the transformation of motor commands into an estimate of the eye velocity. The estimated eye velocity is compared with the target velocity provided by the burst generator. The resulting error signal drives the Purkinje cell population, which is modelled using a firing-rate representation. The Purkinje cell output is then transmitted back to the brainstem.

6.2.1 Model equations

The model equations are expressed in Laplace notation, where s denotes the complex frequency.

The input to the model is the target position, t. The target position, t, was arbitrarily defined such that the eye initially fixates the centre position, then moves upward by 20°, downward to −20°, and finally returns to the centre position within a 10 s interval. The output of the model is the vertical eye position, e_v (see equation 6.5).

The delayed retinal error, r_e, defined as the delayed difference between the target position, t, and the vertical eye position, e_v, drives the burst generator:

$$r_e = (t - e_v) * e^{-\Delta t * s} \tag{6.1}$$

where $\Delta t = 100\ ms$ represents the time delay due to visual processing.

The burst generator operates as follows: it remains inactive when the retinal error, r_e, is below a threshold of 2°. Otherwise, it produces a constant burst until the retinal error reaches zero:

$$b = 10 * sign(r_e) \tag{6.2}$$

where $sign()$ denotes the sign function. The saccadic burst, b, encodes the target velocity.

The burst generator contributes to the generation of the motor command both through a direct pathway with gain 0.2, which supports saccade generation, and indirectly via the brainstem integrator, which supports gaze holding.

The output of the brainstem integrator, e_i, is given by:

$$e_i = (b - p) * \frac{\tau_b - \tau_e}{1 + \tau_b s} \tag{6.3}$$

where $\tau_b = 5\ s$ is the brainstem integrator time constant, $\tau_e = 0.2\ s$ is the eye plant time constant, p is the Purkinje cell population discharge (see equation 6.7) and b is the saccadic burst.

The motor command, m, is defined as the sum of the contributions from the brainstem integrator output, e_i, the saccadic burst, b, the Purkinje cell population discharge, p,

and a bias at the level of floccular target neurons that compensates for the resting discharge of the Purkinje cells, $c_{ft} = 0.5$:

$$m = (b - p + c_{ft}) * \tau_e + e_i \tag{6.4}$$

The eye plant block transforms the motor command, m, into the vertical eye position, e_v:

$$e_v = m * \frac{1}{1 + \tau_e * s} \tag{6.5}$$

where $\tau_e = 0.2\ s$ is the eye plant time constant.

The cerebellar model functions as a feedback loop. It contains an internal model of the eye plant used to estimate eye velocity, v_e, given a copy of the motor command, m:

$$v_e = \frac{s}{1 + \tau_e * s} * m \tag{6.6}$$

At the level of the Purkinje cell population, the estimated eye velocity, v_e, is compared with the saccadic burst, b, generating the Purkinje cell population discharge, p:

$$p = F\left(g * (v_e - b) * \frac{1}{1 + \tau_{PC} * s}\right) \tag{6.7}$$

where $F(x)$ is the Purkinje cell population activation function (described in the next section), $\tau_{PC} = 0.01\ s$ is the time constant of the Purkinje cells, and $g = 10$ is the gain, which is the only free parameter in the model.

6.2.2 Purkinje cell activation function

The activation function was obtained by normalising the response of a population of Purkinje cells.

The population response was generated as follows:

1. The input–output curve of a biologically realistic Purkinje cell model [9] was obtained by stimulating the model with Poisson spike trains with mean firing rates ranging from 0 to 200 Hz in 2 Hz increments. The Purkinje cell was simulated for 600 ms and its mean firing rate was calculated discarding the first 100 ms.

2. Physiological variability across Purkinje cells was simulated by repeating the input–output simulations 2000 times. For each input-output simulation the Purkinje cell received different background inputs (Poisson spike trains with a mean firing rate normally distributed 0±50 spikes/s, mean±SD) and its overall synaptic strength was varied (normally distributed 1.0±0.5).

3. The 2000 input-output curves were then combined to obtain the population response: for each input frequency, the output was calculated as the mean output of the 2000 cells for that input frequency.

The resulting population response was normalised by:

1. Scaling the output to a maximum value of one;

2. Scaling the population response to achieve a maximum slope of one;

3. Shifting the population response such that the point of maximal slope occurs at zero input.

The activation function generated through this procedure was then applied to the vertical oculomotor system model [1] by replacing the sigmoid function block within the cerebellar component of the model.

In [1], a healthy subject and a subject with downbeat nystagmus were modelled. The scaling parameters were calculated for a healthy subject, then the same parameters were used to scale the population response of the subject with downbeat nystagmus.

6.3 Methods

I predicted the eye movements in three conditions:

1. A baseline condition. The network is not excited by the transcranial magnetic stimulation (TMS) model.
2. A low-amplitude stimulation condition. The network is stimulated by a continuous theta burst stimulation (cTBS) protocol, in which the electric field magnitude is 6.08 V/m, as resulting from the SimNIBS simulations described in the previous chapter.

3. A high-amplitude stimulation condition (control condition). The network is stimulated by a continuous theta burst stimulation (cTBS) protocol, in which the electric field magnitude is 30.4 V/m, five times the electric field magnitude in the low-amplitude condition.

There are three steps to predicting eye movements using the vertical oculomotor system model:

1. Generation of the population response.
2. Generation of the activation function.
3. Simulation of the vertical oculomotor system model.

Each step is described in a separate section below.

6.3.1 Generation of the population response

I generated the population response following the methodology presented in the vertical oculomotor system modelling study [1], with two main modifications. First, I excited the Purkinje cell using inputs derived from granular layer simulations rather than Poisson spike trains. Second, I simulated the physiological variability across Purkinje cells by varying inhibitory inputs instead of introducing background input noise and modifying the synaptic strength.

To generate the population response, I first ran simulations of the granular layer network while increasing mossy fibre input firing rates from 0 to 150 Hz in steps of 3 Hz. I reduced the mossy fibre firing frequency range compared with the Poisson spike train inputs used in the original modelling study to reduce computational cost. I simulated the granular layer network for 3 s and discarded the first 600 ms of the granule cells' spike trains to remove transient activity.

I then used the granule cell spike trains to excite the Purkinje cell model and simulated the Purkinje cell for 2.4 s. As described in Chapter 4, the Purkinje cell should contain 122,613 spines; however, I explicitly modelled only one spine per spiny dendrite, for a total of 1,105 spines. The Purkinje cell received 122,613 excitatory inputs from granule cells to the spines, distributed according to the number of anatomical spines associated with each spiny dendrite. I set the maximum excitatory synaptic conductance to 1 nS.

To prevent excessive Purkinje cell firing, I added inhibitory inputs that were not included in the original modelling study [1]. The Purkinje cell received 144 inhibitory synaptic inputs from nine stellate cells, modelled as Poisson spike trains with a mean firing rate of 12.3 Hz [269]. Each stellate cell contacted 16 randomly selected spiny dendrites. The Purkinje cell also received 80 inhibitory synaptic inputs from four basket cells, modelled as Poisson spike trains with a mean firing rate of 12.3 Hz [269], targeting the soma. I set the maximum inhibitory synaptic conductance to 0.5 nS. I reproduced the inhibitory synapse locations, the number of inhibitory inputs, and the maximum synaptic conductances from the study by Zang and colleagues [53], which employed the same Purkinje cell model.

To simulate a population of Purkinje cells using a single Purkinje cell model, I repeated the Purkinje cell simulations ten times instead of 2,000 times, due to computational constraints. For each repetition, I varied the random seed of the spike train generators for the stellate and basket cell inputs. I arbitrarily set the random seed values from 1 to 64 in increments of 7.

I calculated the mean firing rate of the Purkinje cell during the final second of each simulation.

6.3.2 Generation of the activation function

To generate the activation function, I fitted the resulting population response using a logistic function using a least-squares optimisation procedure:

$$y = \frac{L}{1 + e^{-k(x-x_0)}} + b \tag{6.8}$$

I allowed a maximum of 10,000 fitting iterations and used the following initial parameter estimates: the maximum observed mean firing rate for L, 0 for b, 0.05 for k, and 75 for x_0.

To incorporate the population response into the vertical oculomotor system model, I normalised the best logistic fit obtained under baseline conditions. I performed normalisation by scaling the function to a maximum output of one, scaling it to achieve a maximum slope of one, and shifting it such that the point of maximal slope occurred at zero input:

$$x_{norm} = \frac{x - x_0}{L} \tag{6.9}$$

$$y_{norm} = \frac{1}{1 + e^{-k*c*(x-x_0)}} \tag{6.10}$$

where x_{norm} and y_{norm} represent the normalised population input and output, L, x_0 and k are the parameters of the best logistic fit, and c is a scaling parameter. As the slope at x_0 is $\frac{L*k}{4}$, to obtain a slope of one it needs to be scaled by $c = \frac{4}{L*k}$.

I used the same scaling parameters to normalise the best logistic fit of the population responses obtained under low- and high-amplitude stimulation conditions.

6.3.3 Simulation of the vertical oculomotor system model

To predict eye movements, I first replaced the activation function in the vertical oculomotor system model with the activation function generated under baseline conditions. I then fitted the model's free parameter (the gain of the Purkinje cell block) to reproduce the response of a healthy subject. Finally, using the fitted gain value, I ran the vertical oculomotor system model with the activation functions generated under low- and high-amplitude stimulation conditions.

6.4 Results

I first obtained the Purkinje cell population response under baseline conditions and fitted it using a logistic function. Table 6.1 presents the parameters of the best logistic fit, together with the root mean square error (RMSE) and coefficient of determination (R2).

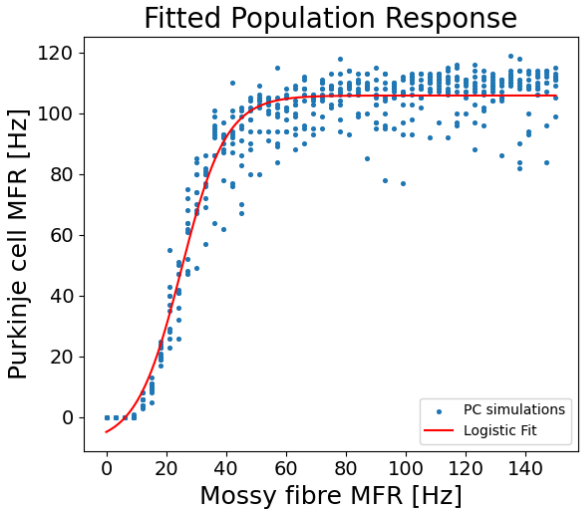
Condition	L	k	x_0	b	RMSE	R2
Baseline	114.61	0.13	25.04	-8.81	7.54	0.96
Low-amplitude stimulation	111.95	0.15	24.99	-7.34	7.04	0.96
High-amplitude stimulation	113.73	0.15	23.38	-7.95	6.01	0.97

Table 6.1 Parameters of the best logistic fit of the population response of the Purkinje cells in the three tested conditions, along with the root mean square error (RMSE) and coefficient of determination (R2) of the fit.

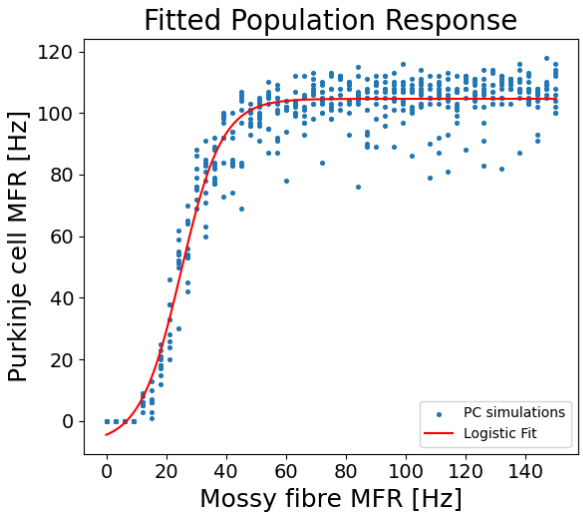
I then normalised the baseline population response to generate the activation function used in the oculomotor system model (see Figure 6.2A and 6.3).

Next, I generated the Purkinje cell population responses under low- and high-amplitude stimulation conditions (see Figure 6.2 B and C). I used the previously estimated values for the parameters L, x_0, b and k to scale the population responses of the network in the stimulated conditions (see Table 6.1 above for the parameters of the best logistic fit in the low- and high-amplitude stimulation conditions). The resulting activation functions are shown in Figure 6.3.

A


Fitted Population Response
Purkinje cell MFR [Hz]
Mossy fibre MFR [Hz]
PC simulations
Logistic Fit

B


Fitted Population Response
Purkinje cell MFR [Hz]
Mossy fibre MFR [Hz]
PC simulations
Logistic Fit

C

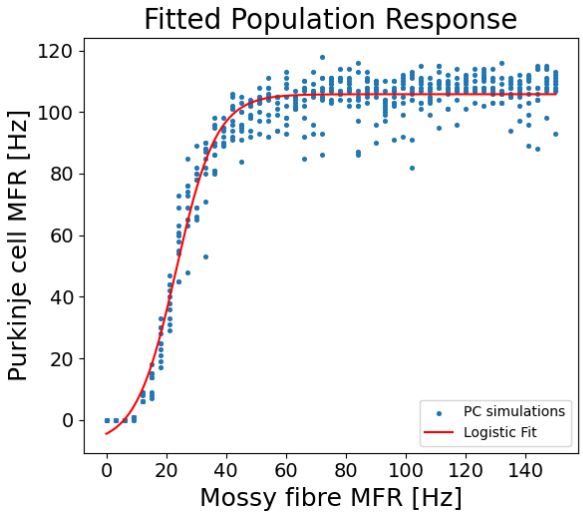

Fitted Population Response
Purkinje cell MFR [Hz]
Mossy fibre MFR [Hz]
PC simulations
Logistic Fit

Figure 6.2 Response of a population of Purkinje cells fitted with a logistic function. In blue, mean firing rate of each Purkinje cell simulation. In red, best logistic fit.
Top (A): Simulations obtained without stimulating the network with the TMS model (baseline condition).
Middle (B): Simulations obtained stimulating the network with the TMS model with an electric field magnitude of 6.08 V/m (low-amplitude stimulation condition).
Bottom (C): Simulations obtained stimulating the network with the TMS model with an electric field magnitude of 30.4 V/m (high-amplitude stimulation condition).

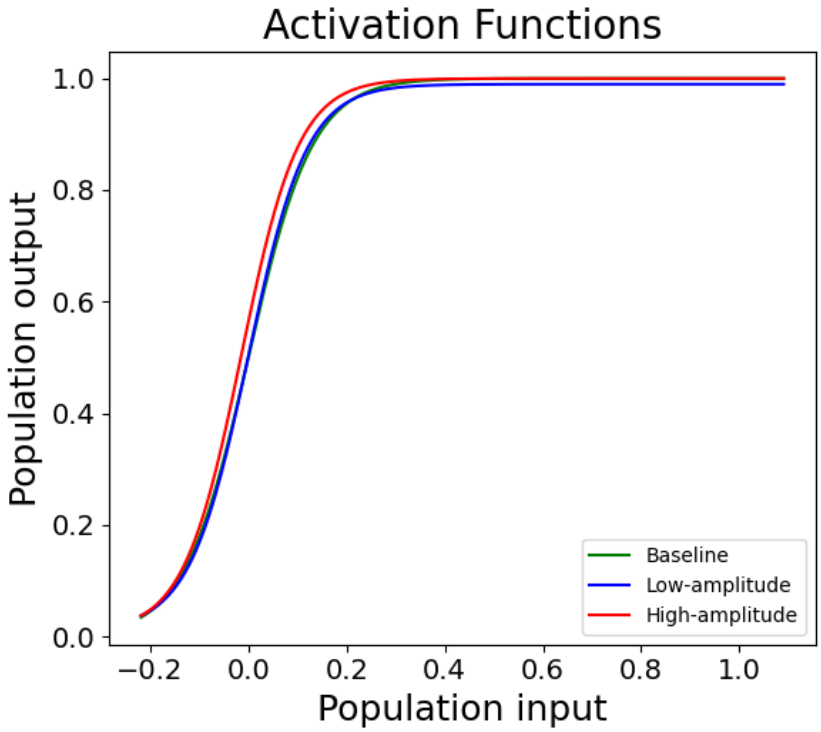


Figure 6.3 Activation functions to be used in the vertical oculomotor system model, generated by normalising the best logistic fits (see Figure 6.2). Baseline, low-amplitude stimulation and high-amplitude stimulation conditions are shown in green, blue and red.

After substituting the activation function obtained under baseline conditions into the vertical oculomotor system model and reducing the gain parameter to 5, I successfully reproduced the eye movement patterns of a healthy subject, as reported in the modelling study [1] (see Figure 6.4, solid green line, overlayed by the solid blue line).

The low-amplitude stimulation condition does not alter the predicted eye movements (see Figure 6.4, solid blue line). In contrast, the high-amplitude stimulation condition affects the predicted eye movements, producing a downward drift during gaze holding (see Figure 6.4, solid red line).

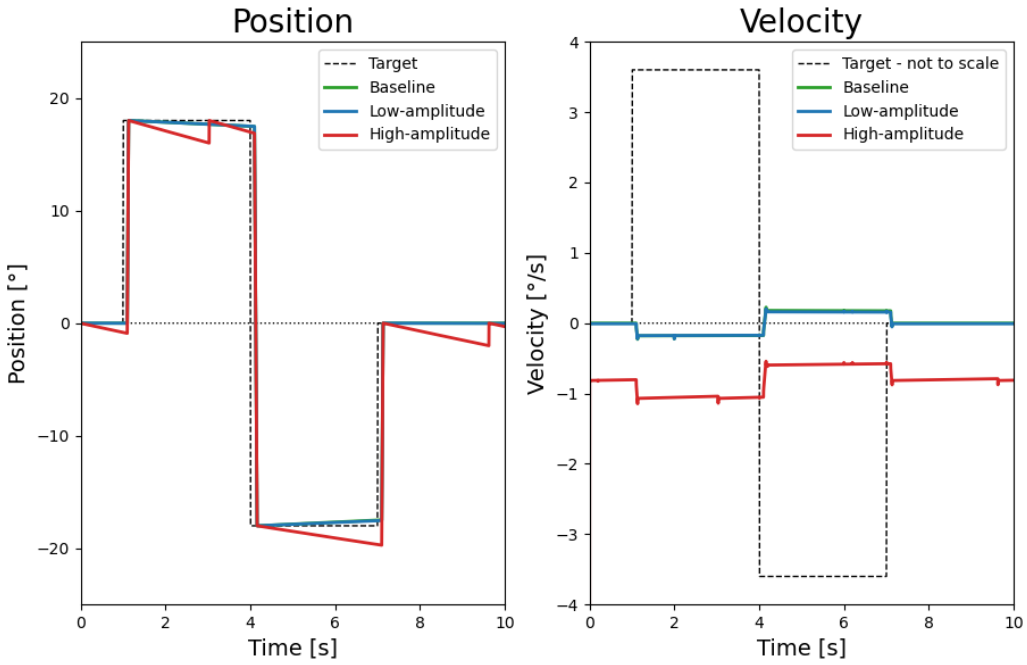


Figure 6.4 Position and slow phase velocity of predicted eye movements. On the left, target position (dashed line) and predicted eye position (solid line). On the right, predicted slow phase velocity of the eye (solid line) and target position (dashed line, not to scale). In green, predicted eye movements obtained employing the activation function generated without stimulating the network with the TMS model (baseline condition). In blue, predicted eye movements employing the activation function generated stimulating the network with the TMS model with an electric field magnitude of 6.08 V/m (low-amplitude stimulation condition). In red, predicted eye movements employing the activation function generated stimulating the network with the TMS model with an electric field magnitude of 30.4 V/m (high-amplitude stimulation condition). Note that the solid green line is not visible as it is overlayed by the solid blue line.

6.5 Discussion

By comparing the predicted eye movements with those observed experimentally [177], it is evident that this modelling framework does not account for all variables influencing eye movements, as it does not accurately reproduce the experimental findings. Although the vertical oculomotor system model predicts a drift during gaze holding, saccades remain unaffected by stimulation. Furthermore, the low-amplitude stimulation condition, which most closely reproduces the experimental setup, does not alter the predicted eye movements.

These findings may suggest that the eye movement changes reported by Colnaghi and colleagues [177] are not primarily driven by neuronal activity within the targeted

cerebellar region, as neurons in this region may not be sufficiently excited by the applied stimulation. Instead, the observed experimental effects may arise from activation of more superficial neural structures, or from neighbouring regions not included in my model. For example, the visual cortex, which lies close to the cerebellum, may be inadvertently stimulated contributing to the experimentally observed eye movement changes. According to the results presented in Figure 5.8, the visual cortex is stimulated by the modelled protocol. In particular, the mean electric field magnitude is of 10.7 V/m in a region of 2 mm around a superficial area of the visual cortex ([0, -84, -4] in Montreal Neurological Institute coordinates) in the low-amplitude stimulation condition.

Despite these discrepancies, the vertical oculomotor system model produces observable differences in predicted eye movements following stimulation, even when the mean firing rate of the cerebellar network is only minimally altered. This suggests that the model can serve as a validation framework for transcranial magnetic stimulation models. However, its applicability is limited to models targeting cerebellar circuits involved in saccades and gaze holding. Additionally, caution is required when using this model for validation purposes, as it captures qualitative differences between stimulated and non-stimulated conditions but does not fully reproduce the magnitude of effects observed experimentally.

As with all models, the proposed validation framework comes with limitations. The following limitations are relevant to discuss:

- The use of a simplified vertical oculomotor system model. More detailed versions of the model (for example [279]) incorporate additional eye movements, such as smooth pursuit, which may be more sensitive to stimulation and could better reproduce a broader range of experimental findings.
- The employed vertical oculomotor system model represents saccade generation in a simplified manner. Employing a more physiologically detailed model of saccade generation could alter the predicted outcomes and potentially improve agreement with experimental observations.
- An inherent limitation of the chosen model arises from transitioning from a spiking neuron model to a firing-rate representation when incorporating the

Purkinje cell activation function into the control-theory framework. TMS may induce subthreshold neuronal changes and changes in spike timing that influence saccade generation but are not captured by firing-rate models. This modelling approach may underestimate subtle but functionally relevant stimulation effects.

6.6 Conclusion

In this chapter I presented the validation method for the TMS model I employed. The described methodology addresses the gap in the literature #3 - *The lack of validation methods for non-invasive stimulation models*. In this chapter, I also addressed my research question 3: *Is a vertical oculomotor system model [1] suitable as a validation method for transcranial stimulation models targeting the cerebellum?* The vertical oculomotor system model produces observable differences in predicted eye movements following stimulation. This suggests that the model can serve as a validation framework for transcranial magnetic stimulation models targeting cerebellar circuits involved in saccades and gaze holding. In the next chapter, I will conclude this dissertation summarising my findings.

Chapter 7

Conclusion

In this dissertation I presented a computational framework that integrates a model of the cerebellar cortex, a model of transcranial magnetic stimulation (TMS) and a validation method for the latter with the objective of expanding the current knowledge on the feasibility of non-invasive neurostimulation to treat neurological disorders linked to cerebellar pathologies.

Using this integrated framework, I demonstrated that a commonly used cerebellar stimulation protocol [177] predominantly produces subthreshold effects in neurons of the cerebellar cortex. Under these conditions, the stimulation is not sufficient to produce measurable changes in behaviour, specifically in eye movements. The simulations indicate that substantially higher stimulation intensities would be required to directly alter cerebellar activity to a degree that influences eye movement control.

These findings suggest that the eye movement changes reported experimentally in [177] are unlikely to be primarily driven by neuronal activity within the targeted cerebellar region. Instead, the observed effects may result from the activation of more superficial neural structures or neighbouring brain regions that are not included in the present model, such as the visual cortex.

Overall, these results highlight the importance of carefully considering the stimulation protocol parameters such as the coil type, positioning and stimulation intensity when designing neurostimulation experiments. Accurate targeting is essential to ensure that the intended neural structures are effectively stimulated and to correctly interpret the behavioural effects observed in experimental studies.

Looking ahead, this framework could serve as a valuable tool for identifying optimal treatment protocols in clinical settings. Developing clinically meaningful and effective stimulation strategies requires studying protocols that are tailored to the specific brain regions being targeted. The present modelling framework has already provided insights into how a cTBS protocol affects granule, Golgi, and Purkinje cells, and it could be extended in future work to test a range of protocols and coil positions to

identify the most suitable treatment approach. For instance, downbeat nystagmus is thought to result from a reduction in Purkinje cell firing rate [1]; this framework could therefore be used to simulate candidate protocols and assess whether they produce the desired increase in Purkinje cell activity before being applied to patients.

7.1 Answers to my research questions

I have addressed the following three research questions in this work:

1. *Are the neurons in the cerebellar vermis, lobules VI–VII, affected by TMS?* The stimulation target is located in a deep cerebellar region, resulting in a low electric field magnitude in that area. A cTBS protocol at 42% intensity of the maximum stimulator output does not generate any significant effect in the Golgi and granule cell's mean firing rate. It does, however, reduce the Purkinje cell's firing rate. This has been discussed in Chapter 5.

2. *How does a cTBS protocol affect the neurons in terms of mean firing rate, instantaneous firing rate and spike timing?* The stimulation does not affect the mean firing rate of granule and Golgi cells, while it decreases the Purkinje cell's firing rate. The instantaneous firing rate of the Purkinje cell is not affected by the modelled stimulation protocol; a higher mean electric field magnitude is required to disrupt the regular spiking of the Purkinje cell. On average, the high-amplitude condition makes the granule cells spike sooner, the Golgi cells later and the Purkinje cell more frequently than the low-amplitude condition. This has been discussed in Chapter 5.

3. *Is a vertical oculomotor system model [1] suitable as a validation method for transcranial stimulation models targeting the cerebellum?* The model can serve as a validation framework for transcranial magnetic stimulation models targeting cerebellar circuits involved in saccades and gaze holding. This has been discussed in Chapter 6.

7.2 Addressed gaps in the literature

I have addressed the following gaps in the field:

1. *The lack of a biologically realistic model of the cerebellar cortex.* I further developed Katakura et al.'s cerebellar model [2] by employing a more recent Purkinje cell model and by switching the single compartment granule cells in the granular layer model to multi-compartment neurons. This has been discussed in Chapter 4.

2. *The lack of a multi-scale non-invasive stimulation model including synaptic connections.* I excited my cerebellar model with an electric field estimated by a MRI-generated head model. This has been discussed in Chapter 5.

3. *The lack of validation methods for non-invasive stimulation models.* I linked the output of the cerebellar model to a measurable behaviour - slow phase velocity eye movements. This step serves as a validation method for the non-invasive stimulation model. This has been discussed in Chapter 6.

7.3 Future work

Future work could further extend and refine the modelling framework presented in this dissertation in several directions.

First, the cerebellar network could be expanded by explicitly modelling interneuron populations. This would allow further development of the network architecture and enable the investigation of TMS effects on additional neuronal types within the cerebellar cortex.

The cerebellar network could also be expanded by including multiple Purkinje cells within the network. Modelling interactions among Purkinje cells would provide a more realistic representation of cerebellar circuitry and allow the investigation of population-level dynamics that cannot be captured with a single-cell representation.

The spatial organisation of the cerebellar network could be improved by modelling neurons according to anatomical orientations that follow the brain's sulci and gyri, rather than placing them on a planar structure. Incorporating random rotations of neurons around their z-axis would further increase anatomical realism. Such improvements would enhance both the biological fidelity of the cerebellar network and the spatial accuracy of the TMS model.

Another important extension would involve improving the TMS model by incorporating a spatially varying electric field instead of assuming a uniform electric field across the network, as done by [215]. This would provide a more realistic representation of the stimulation delivered in vivo. Also, to robustly quantify the effects of the stimulation on the network, the analyses presented in Chapter 5 should be repeated across multiple simulations.

The validation framework for the TMS model could be improved by employing a more sophisticated vertical oculomotor system model (for example [279]), allowing for the prediction of a broader range of eye movements, such as smooth pursuit.

Finally, integrating the computational model more closely with experimental studies would help provide further insights into the mechanisms underlying TMS. Such collaboration could inform experimental design while also guiding future refinements of the model.

Bibliography

[1] S. Glasauer and C. Rössert, ‘Modelling drug modulation of nystagmus’, *Prog. Brain Res.*, vol. 171, pp. 527–534, 2008, doi: 10.1016/S0079-6123(08)00675-4.

[2] O. Katakura, R. Maex, S. Kadir, and V. Steuber, ‘Clustered stimuli and oscillations can improve pattern recognition in a detailed model of cerebellar cortex’, *J. Comput. Neurosci.*, vol. 51, no. 1, p. P102, Jan. 2023, doi: https://doi.org/10.1007/s10827-022-00841-9.

[3] S. K. Sudhakar *et al.*, ‘Spatiotemporal network coding of physiological mossy fiber inputs by the cerebellar granular layer’, *PLOS Comput. Biol.*, vol. 13, no. 9, p. e1005754, Sep. 2017, doi: 10.1371/journal.pcbi.1005754.

[4] E. De Schutter and J. M. Bower, ‘An active membrane model of the cerebellar Purkinje cell. I. Simulation of current clamps in slice’, *J. Neurophysiol.*, vol. 71, no. 1, pp. 375–400, Jan. 1994, doi: 10.1152/jn.1994.71.1.375.

[5] E. De Schutter and J. M. Bower, ‘An active membrane model of the cerebellar Purkinje cell II. Simulation of synaptic responses’, *J. Neurophysiol.*, vol. 71, no. 1, pp. 401–419, Jan. 1994, doi: 10.1152/jn.1994.71.1.401.

[6] Y. Zang, S. Dieudonné, and E. De Schutter, ‘Voltage- and Branch-Specific Climbing Fiber Responses in Purkinje Cells’, *Cell Rep.*, vol. 24, no. 6, pp. 1536–1549, Aug. 2018, doi: 10.1016/j.celrep.2018.07.011.

[7] S. Diwakar, J. Magistretti, M. Goldfarb, G. Naldi, and E. D’Angelo, ‘Axonal Na+ channels ensure fast spike activation and back-propagation in cerebellar granule cells’, *J. Neurophysiol.*, vol. 101, no. 2, pp. 519–532, Feb. 2009, doi: 10.1152/jn.90382.2008.

[8] E. Bernasconi, N. Yousif, and V. Steuber, ‘32nd Annual Computational Neuroscience Meeting: CNS*2023 - P194 Development of a biologically realistic cerebellar model to study the effects of non-invasive stimulation’, *J. Comput. Neurosci.*, vol. 52, no. 1, pp. 3–166, Oct. 2024, doi: 10.1007/s10827-024-00871-5.

[9] E. Bernasconi, S. Glasauer, N. Yousif, and V. Steuber, ‘33rd Annual Computational Neuroscience Meeting: CNS*2024 - P015 Predicting eye movements with a detailed network model of the cerebellar cortex’, *J. Comput. Neurosci.*, vol. 53, no. 1, pp. 3–89, Feb. 2025, doi: 10.1007/s10827-024-00889-9.

[10] E. Bernasconi, N. Yousif, and V. Steuber, ‘34th Annual Computational Neuroscience Meeting: CNS*2025 - P021 Studying the effects of TMS on the cerebellum with a realistic model of the cerebellar cortex’, *J. Comput. Neurosci.*, vol. 54, no. 1, pp. 3–395, Feb. 2026, doi: 10.1007/s10827-025-00915-4.

[11] J. Knierim, *Neuroscience Online*. 2020. Accessed: Oct. 02, 2024. [Online]. Available: https://nba.uth.tmc.edu/neuroscience/m/s3/chapter05.html

[12] E. D’Angelo, ‘Chapter 6 - Physiology of the cerebellum’, in *Handbook of Clinical Neurology*, vol. 154, M. Manto and T. A. G. M. Huisman, Eds, in The Cerebellum: From Embryology to Diagnostic Investigations, vol. 154. , Elsevier, 2018, pp. 85–108. doi: 10.1016/B978-0-444-63956-1.00006-0.

[13] J. D. Schmahmann, ‘The cerebellum and cognition’, *Neurosci. Lett.*, vol. 688, pp. 62–75, Jan. 2019, doi: 10.1016/j.neulet.2018.07.005.

[14] E. Kandel, J. Schwartz, T. Jessell, S. Siegelbaum, and A. J. Hudspeth, *Principles of Neural Science*, 5th edition. New York: McGraw-Hill Education / Medical, 2012.

[15] B. is generated by DBCLS, *English: Primary fissure of cerebellum (Shown in red).* 2019. Accessed: Feb. 10, 2026. [Online]. Available: https://commons.wikimedia.org/w/index.php?curid=77846103
[16] B. is generated by DBCLS, *English: Primary fissure of cerebellum (Shown in red).* 2019. Accessed: Feb. 10, 2026. [Online]. Available: https://commons.wikimedia.org/w/index.php?curid=77846106
[17] B. is generated by DBCLS, *English: Primary fissure of cerebellum (Shown in red).* 2019. Accessed: Feb. 10, 2026. [Online]. Available: https://commons.wikimedia.org/w/index.php?curid=77846109
[18] O. file created by O. College, *English: Major regions of the cerebellum. SVG text version. Original file is File:1613 Major Regions of the Cerebellum-02.jpg.* 2019. Accessed: Feb. 10, 2026. [Online]. Available: https://commons.wikimedia.org/wiki/File:1613_Major_Regions_of_the_Cerebellum-02.svg
[19] Tom282f3, *English: Diagram of the cerebellar circuitry.* 2019. Accessed: Feb. 10, 2026. [Online]. Available: https://commons.wikimedia.org/wiki/File:Cerebellar_Circuit.svg
[20] R. O. Brady *et al.*, 'Cerebellar-Prefrontal Network Connectivity and Negative Symptoms in Schizophrenia', *Am. J. Psychiatry*, vol. 176, no. 7, pp. 512–520, Jul. 2019, doi: 10.1176/appi.ajp.2018.18040429.
[21] C. França *et al.*, 'Effects of cerebellar neuromodulation in movement disorders: A systematic review', *Brain Stimulat.*, vol. 11, no. 2, pp. 249–260, Apr. 2018, doi: 10.1016/j.brs.2017.11.015.
[22] C. D. Workman, A. C. Fietsam, E. Y. Uc, and T. Rudroff, 'Cerebellar Transcranial Direct Current Stimulation in People with Parkinson's Disease: A Pilot Study', *Brain Sci.*, vol. 10, no. 2, Art. no. 2, Feb. 2020, doi: 10.3390/brainsci10020096.
[23] A. Valero-Cabré, J. L. Amengual, C. Stengel, A. Pascual-Leone, and O. A. Coubard, 'Transcranial magnetic stimulation in basic and clinical neuroscience: A comprehensive review of fundamental principles and novel insights', *Neurosci. Biobehav. Rev.*, vol. 83, pp. 381–404, Dec. 2017, doi: 10.1016/j.neubiorev.2017.10.006.
[24] S. Koganemaru *et al.*, 'Cerebellar transcranial alternating current stimulation modulates human gait rhythm', *Neurosci. Res.*, vol. 156, pp. 265–270, Jul. 2020, doi: 10.1016/j.neures.2019.12.003.
[25] R. Polanía, M. A. Nitsche, and C. C. Ruff, 'Studying and modifying brain function with non-invasive brain stimulation', *Nat. Neurosci.*, vol. 21, no. 2, Art. no. 2, Feb. 2018, doi: 10.1038/s41593-017-0054-4.
[26] X. Zhang, R. Hancock, and S. Santaniello, 'Transcranial direct current stimulation of cerebellum alters spiking precision in cerebellar cortex: A modeling study of cellular responses', *PLOS Comput. Biol.*, vol. 17, no. 12, p. e1009609, Dec. 2021, doi: 10.1371/journal.pcbi.1009609.
[27] C. Sanches *et al.*, 'Past, Present, and Future of Non-invasive Brain Stimulation Approaches to Treat Cognitive Impairment in Neurodegenerative Diseases: Time for a Comprehensive Critical Review', *Front. Aging Neurosci.*, vol. 12, 2021, Accessed: Nov. 29, 2022. [Online]. Available: https://www.frontiersin.org/articles/10.3389/fnagi.2020.578339
[28] R. Jalali, A. Chowdhury, M. Wilson, R. C. Miall, and J. M. Galea, 'Neural changes associated with cerebellar tDCS studied using MR spectroscopy', *Exp. Brain Res.*, vol. 236, no. 4, pp. 997–1006, Apr. 2018, doi: 10.1007/s00221-018-5170-1.

[29] M. Parazzini, E. Rossi, R. Ferrucci, I. Liorni, A. Priori, and P. Ravazzani, ‘Modelling the electric field and the current density generated by cerebellar transcranial DC stimulation in humans’, *Clin. Neurophysiol. Off. J. Int. Fed. Clin. Neurophysiol.*, vol. 125, no. 3, pp. 577–584, Mar. 2014, doi: 10.1016/j.clinph.2013.09.039.
[30] R. M. Hardwick, E. Lesage, and R. C. Miall, ‘Cerebellar transcranial magnetic stimulation: the role of coil geometry and tissue depth’, *Brain Stimulat.*, vol. 7, no. 5, pp. 643–649, 2014, doi: 10.1016/j.brs.2014.04.009.
[31] L. M. Koponen and A. V. Peterchev, ‘Transcranial Magnetic Stimulation: Principles and Applications’, in *Neural Engineering*, B. He, Ed., Cham: Springer International Publishing, 2020, pp. 245–270. doi: 10.1007/978-3-030-43395-6_7.
[32] Ilovestarbies, *English: Figure 1: Image derived from psych scene hub displaying the general mechanism of TMS. A small coil is placed near the scalp, whereby a magnetic field is applied to induce an electrical field within the brains outer cortex. The coil is generally directed above the motor cortex (region which primarily generates neural impulses).* 2023. Accessed: Feb. 10, 2026. [Online]. Available: https://commons.wikimedia.org/wiki/File:Transcranial_magnetic_stimulation_%28TMS%29.png
[33] Baburov, *English: Идуктор «восьмерка» для транскраниальной магнитной стимуяции*. 2014. Accessed: Feb. 10, 2026. [Online]. Available: https://commons.wikimedia.org/wiki/File:Double_cone_coil.jpg
[34] T. Wagner, J. Rushmore, U. Eden, and A. Valero-Cabre, ‘Biophysical foundations underlying TMS: setting the stage for an effective use of neurostimulation in the cognitive neurosciences’, *Cortex J. Devoted Study Nerv. Syst. Behav.*, vol. 45, no. 9, pp. 1025–1034, Oct. 2009, doi: 10.1016/j.cortex.2008.10.002.
[35] M. R. Nester, ‘An Applied Statistician’s Creed’, *J. R. Stat. Soc. Ser. C Appl. Stat.*, vol. 45, no. 4, pp. 401–410, 1996, doi: 10.2307/2986064.
[36] S. Herculano-Houzel, K. Catania, P. R. Manger, and J. H. Kaas, ‘Mammalian Brains Are Made of These: A Dataset of the Numbers and Densities of Neuronal and Nonneuronal Cells in the Brain of Glires, Primates, Scandentia, Eulipotyphlans, Afrotherians and Artiodactyls, and Their Relationship with Body Mass’, *Brain. Behav. Evol.*, vol. 86, no. 3–4, pp. 145–163, 2015, doi: 10.1159/000437413.
[37] B. Pakkenberg *et al.*, ‘Aging and the human neocortex’, *Exp. Gerontol.*, vol. 38, no. 1, pp. 95–99, Jan. 2003, doi: 10.1016/S0531-5565(02)00151-1.
[38] D. Marr, ‘A theory of cerebellar cortex’, *J. Physiol.*, vol. 202, no. 2, pp. 437–470, 1969, doi: 10.1113/jphysiol.1969.sp008820.
[39] J. S. Albus, ‘A theory of cerebellar function’, *Math. Biosci.*, vol. 10, no. 1, pp. 25–61, Feb. 1971, doi: 10.1016/0025-5564(71)90051-4.
[40] M. Ito, M. Sakurai, and P. Tongroach, ‘Climbing fibre induced depression of both mossy fibre responsiveness and glutamate sensitivity of cerebellar Purkinje cells’, *J. Physiol.*, vol. 324, pp. 113–134, Mar. 1982, doi: 10.1113/jphysiol.1982.sp014103.
[41] E. D’Angelo *et al.*, ‘Modeling the Cerebellar Microcircuit: New Strategies for a Long-Standing Issue’, *Front. Cell. Neurosci.*, vol. 10, 2016, Accessed: Nov. 28, 2022. [Online]. Available: https://www.frontiersin.org/articles/10.3389/fncel.2016.00176
[42] S. Solinas, T. Nieus, and E. D‘Angelo, ‘A realistic large-scale model of the cerebellum granular layer predicts circuit spatio-temporal filtering properties’,

Front. Cell. Neurosci., vol. 4, 2010, Accessed: Aug. 31, 2022. [Online]. Available: https://www.frontiersin.org/articles/10.3389/fncel.2010.00012
[43] R. A. McDougal *et al.*, 'Twenty years of ModelDB and beyond: building essential modeling tools for the future of neuroscience', *J. Comput. Neurosci.*, vol. 42, no. 1, pp. 1–10, Feb. 2017, doi: 10.1007/s10827-016-0623-7.
[44] S. Masoli, S. Solinas, and E. D'Angelo, 'Action potential processing in a detailed Purkinje cell model reveals a critical role for axonal compartmentalization', *Front. Cell. Neurosci.*, vol. 9, 2015, doi: 10.3389/fncel.2015.00047.
[45] S.-A. Brown, I. I. Moraru, J. C. Schaff, and L. M. Loew, 'Virtual NEURON: a strategy for merged biochemical and electrophysiological modeling', *J. Comput. Neurosci.*, vol. 31, no. 2, pp. 385–400, Oct. 2011, doi: 10.1007/s10827-011-0317-0.
[46] M. D. Forrest, 'Simulation of alcohol action upon a detailed Purkinje neuron model and a simpler surrogate model that runs >400 times faster', *BMC Neurosci.*, vol. 16, p. 27, Apr. 2015, doi: 10.1186/s12868-015-0162-6.
[47] H. Anwar, C. J. Roome, H. Nedelescu, W. Chen, B. Kuhn, and E. De Schutter, 'Dendritic diameters affect the spatial variability of intracellular calcium dynamics in computer models', *Front. Cell. Neurosci.*, vol. 8, p. 168, 2014, doi: 10.3389/fncel.2014.00168.
[48] W. Akemann, A. Lundby, H. Mutoh, and T. Knöpfel, 'Effect of Voltage Sensitive Fluorescent Proteins on Neuronal Excitability', *Biophys. J.*, vol. 96, no. 10, pp. 3959–3976, May 2009, doi: 10.1016/j.bpj.2009.02.046.
[49] G. Cirtala and E. De Schutter, 'Branch-specific clustered parallel fiber input controls dendritic computation in Purkinje cells', *iScience*, vol. 27, no. 9, p. 110756, Sep. 2024, doi: 10.1016/j.isci.2024.110756.
[50] S. Masoli *et al.*, 'Human Purkinje cells outperform mouse Purkinje cells in dendritic complexity and computational capacity', *Commun. Biol.*, vol. 7, no. 1, p. 5, Jan. 2024, doi: 10.1038/s42003-023-05689-y.
[51] A. Buchin, S. Rieubland, M. Häusser, B. S. Gutkin, and A. Roth, 'Inverse Stochastic Resonance in Cerebellar Purkinje Cells', *PLoS Comput. Biol.*, vol. 12, no. 8, p. e1005000, Aug. 2016, doi: 10.1371/journal.pcbi.1005000.
[52] A. R. Gallimore, T. Kim, K. Tanaka-Yamamoto, and E. De Schutter, 'Switching On Depression and Potentiation in the Cerebellum', *Cell Rep.*, vol. 22, no. 3, pp. 722–733, Jan. 2018, doi: 10.1016/j.celrep.2017.12.084.
[53] Y. Zang and E. D. Schutter, 'The Cellular Electrophysiological Properties Underlying Multiplexed Coding in Purkinje Cells', *J. Neurosci.*, vol. 41, no. 9, pp. 1850–1863, Mar. 2021, doi: 10.1523/JNEUROSCI.1719-20.2020.
[54] S. Masoli and E. D'Angelo, 'Synaptic Activation of a Detailed Purkinje Cell Model Predicts Voltage-Dependent Control of Burst-Pause Responses in Active Dendrites', *Front. Cell. Neurosci.*, vol. 11, p. 278, 2017, doi: 10.3389/fncel.2017.00278.
[55] H. Anwar, I. Hepburn, H. Nedelescu, W. Chen, and E. De Schutter, 'Stochastic calcium mechanisms cause dendritic calcium spike variability', *J. Neurosci. Off. J. Soc. Neurosci.*, vol. 33, no. 40, pp. 15848–15867, Oct. 2013, doi: 10.1523/JNEUROSCI.1722-13.2013.
[56] A. Marasco, A. Limongiello, and M. Migliore, 'Using Strahler's analysis to reduce up to 200-fold the run time of realistic neuron models', *Sci. Rep.*, vol. 3, p. 2934, Oct. 2013, doi: 10.1038/srep02934.
[57] R. C. Cannon, C. O'Donnell, and M. F. Nolan, 'Stochastic ion channel gating in dendritic neurons: morphology dependence and probabilistic synaptic activation

of dendritic spikes', *PLoS Comput. Biol.*, vol. 6, no. 8, p. e1000886, Aug. 2010, doi: 10.1371/journal.pcbi.1000886.
[58] W. Akemann and T. Knöpfel, 'Interaction of Kv3 potassium channels and resurgent sodium current influences the rate of spontaneous firing of Purkinje neurons', *J. Neurosci. Off. J. Soc. Neurosci.*, vol. 26, no. 17, pp. 4602–4612, Apr. 2006, doi: 10.1523/JNEUROSCI.5204-05.2006.
[59] Z. M. Khaliq, N. W. Gouwens, and I. M. Raman, 'The contribution of resurgent sodium current to high-frequency firing in Purkinje neurons: an experimental and modeling study', *J. Neurosci. Off. J. Soc. Neurosci.*, vol. 23, no. 12, pp. 4899–4912, Jun. 2003.
[60] Z. M. Khaliq, N. W. Gouwens, and I. M. Raman, 'The contribution of resurgent sodium current to high-frequency firing in Purkinje neurons: an experimental and modeling study', *J. Neurosci. Off. J. Soc. Neurosci.*, vol. 23, no. 12, pp. 4899–4912, Jun. 2003.
[61] H. Anwar, S. Hong, and E. De Schutter, 'Controlling Ca2+-activated K+ channels with models of Ca2+ buffering in Purkinje cells', *Cerebellum Lond. Engl.*, vol. 11, no. 3, pp. 681–693, Sep. 2012, doi: 10.1007/s12311-010-0224-3.
[62] S. Genet, L. Sabarly, E. Guigon, H. Berry, and B. Delord, 'Dendritic signals command firing dynamics in a mathematical model of cerebellar Purkinje cells', *Biophys. J.*, vol. 99, no. 2, pp. 427–436, Jul. 2010, doi: 10.1016/j.bpj.2010.04.056.
[63] P. Vetter, A. Roth, and M. Häusser, 'Propagation of action potentials in dendrites depends on dendritic morphology', *J. Neurophysiol.*, vol. 85, no. 2, pp. 926–937, Feb. 2001, doi: 10.1152/jn.2001.85.2.926.
[64] J. Couto, D. Linaro, E. De Schutter, and M. Giugliano, 'On the firing rate dependency of the phase response curve of rat Purkinje neurons in vitro', *PLoS Comput. Biol.*, vol. 11, no. 3, p. e1004112, Mar. 2015, doi: 10.1371/journal.pcbi.1004112.
[65] J. D. Reed and K. T. Blackwell, 'Prediction of Neural Diameter From Morphology to Enable Accurate Simulation', *Front. Neuroinformatics*, vol. 15, p. 666695, 2021, doi: 10.3389/fninf.2021.666695.
[66] D. Gall and G. Dupont, 'Tonic Activation of Extrasynaptic NMDA Receptors Decreases Intrinsic Excitability and Promotes Bistability in a Model of Neuronal Activity', *Int. J. Mol. Sci.*, vol. 21, no. 1, p. 206, Dec. 2019, doi: 10.3390/ijms21010206.
[67] C. Rössert, S. Solinas, E. D'Angelo, P. Dean, and J. Porrill, 'Model cerebellar granule cells can faithfully transmit modulated firing rate signals', *Front. Cell. Neurosci.*, vol. 8, p. 304, 2014, doi: 10.3389/fncel.2014.00304.
[68] S. Masoli, M. Tognolina, U. Laforenza, F. Moccia, and E. D'Angelo, 'Parameter tuning differentiates granule cell subtypes enriching transmission properties at the cerebellum input stage', *Commun. Biol.*, vol. 3, no. 1, p. 222, May 2020, doi: 10.1038/s42003-020-0953-x.
[69] K. Dover *et al.*, 'FHF-independent conduction of action potentials along the leak-resistant cerebellar granule cell axon', *Nat. Commun.*, vol. 7, p. 12895, Sep. 2016, doi: 10.1038/ncomms12895.
[70] F. Gabbiani, J. Midtgaard, and T. Knopfel, 'Synaptic integration in a model of cerebellar granule cells', *J. Neurophysiol.*, Aug. 1994, doi: 10.1152/jn.1994.72.2.999.
[71] S. Solinas, L. Forti, E. Cesana, J. Mapelli, E. De Schutter, and E. D'Angelo, 'Computational reconstruction of pacemaking and intrinsic electroresponsiveness

in cerebellar Golgi cells', *Front. Cell. Neurosci.*, vol. 1, p. 2, 2007, doi: 10.3389/neuro.03.002.2007.
[72] S. Masoli, A. Ottaviani, S. Casali, and E. D'Angelo, 'Cerebellar Golgi cell models predict dendritic processing and mechanisms of synaptic plasticity', *PLoS Comput. Biol.*, vol. 16, no. 12, p. e1007937, Dec. 2020, doi: 10.1371/journal.pcbi.1007937.
[73] A. Geminiani, C. Casellato, F. Locatelli, F. Prestori, A. Pedrocchi, and E. D'Angelo, 'Complex Dynamics in Simplified Neuronal Models: Reproducing Golgi Cell Electroresponsiveness', *Front. Neuroinformatics*, vol. 12, p. 88, 2018, doi: 10.3389/fninf.2018.00088.
[74] E. Pali, S. Masoli, D. Di Domenico, T. Sorbo, F. Prestori, and E. D'Angelo, 'Coincidence detection between apical and basal dendrites drives STDP in cerebellar Golgi cells', *Commun. Biol.*, vol. 8, no. 1, p. 731, May 2025, doi: 10.1038/s42003-025-08153-1.
[75] J. Luthman *et al.*, 'STD-dependent and independent encoding of input irregularity as spike rate in a computational model of a cerebellar nucleus neuron', *Cerebellum Lond. Engl.*, vol. 10, no. 4, pp. 667–682, Dec. 2011, doi: 10.1007/s12311-011-0295-9.
[76] V. Steuber, N. W. Schultheiss, R. A. Silver, E. De Schutter, and D. Jaeger, 'Determinants of synaptic integration and heterogeneity in rebound firing explored with data-driven models of deep cerebellar nucleus cells', *J. Comput. Neurosci.*, vol. 30, no. 3, pp. 633–658, Jun. 2011, doi: 10.1007/s10827-010-0282-z.
[77] S. Masoli *et al.*, 'Cerebellar basket cell filtering of Purkinje cell responses elicited by low frequency parallel fibre transmission', *Sci. Rep.*, vol. 15, no. 1, p. 25192, Jul. 2025, doi: 10.1038/s41598-025-09964-2.
[78] M. F. Rizza *et al.*, 'Stellate cell computational modeling predicts signal filtering in the molecular layer circuit of cerebellum', *Sci. Rep.*, vol. 11, no. 1, p. 3873, Feb. 2021, doi: 10.1038/s41598-021-83209-w.
[79] M. Szoboszlay, A. Lőrincz, F. Lanore, K. Vervaeke, R. A. Silver, and Z. Nusser, 'Functional Properties of Dendritic Gap Junctions in Cerebellar Golgi Cells', *Neuron*, vol. 90, no. 5, pp. 1043–1056, Jun. 2016, doi: 10.1016/j.neuron.2016.03.029.
[80] X. Zhang and S. Santaniello, 'Role of cerebellar GABAergic dysfunctions in the origins of essential tremor', *Proc. Natl. Acad. Sci. U. S. A.*, vol. 116, no. 27, pp. 13592–13601, Jul. 2019, doi: 10.1073/pnas.1817689116.
[81] C. Casellato *et al.*, 'Adaptive robotic control driven by a versatile spiking cerebellar network', *PloS One*, vol. 9, no. 11, p. e112265, 2014, doi: 10.1371/journal.pone.0112265.
[82] C. Rössert, P. Dean, and J. Porrill, 'At the Edge of Chaos: How Cerebellar Granular Layer Network Dynamics Can Provide the Basis for Temporal Filters', *PLoS Comput. Biol.*, vol. 11, no. 10, p. e1004515, Oct. 2015, doi: 10.1371/journal.pcbi.1004515.
[83] T. Yamazaki and S. Tanaka, 'A spiking network model for passage-of-time representation in the cerebellum', *Eur. J. Neurosci.*, vol. 26, no. 8, pp. 2279–2292, Oct. 2007, doi: 10.1111/j.1460-9568.2007.05837.x.
[84] R. Maex and E. De Schutter, 'Synchronization of golgi and granule cell firing in a detailed network model of the cerebellar granule cell layer', *J. Neurophysiol.*, vol. 80, no. 5, pp. 2521–2537, Nov. 1998, doi: 10.1152/jn.1998.80.5.2521.

[85] V. Romano *et al.*, ‘Stage-dependent cerebrocerebellar communication during sensorimotor processing’, *Nat. Commun.*, vol. 16, no. 1, p. 8812, Oct. 2025, doi: 10.1038/s41467-025-64592-8.
[86] J. A. Garrido, N. R. Luque, E. D’Angelo, and E. Ros, ‘Distributed cerebellar plasticity implements adaptable gain control in a manipulation task: a closed-loop robotic simulation’, *Front. Neural Circuits*, vol. 7, p. 159, 2013, doi: 10.3389/fncir.2013.00159.
[87] N. R. Luque, J. A. Garrido, R. R. Carrillo, E. D’Angelo, and E. Ros, ‘Fast convergence of learning requires plasticity between inferior olive and deep cerebellar nuclei in a manipulation task: a closed-loop robotic simulation’, *Front. Comput. Neurosci.*, vol. 8, p. 97, 2014, doi: 10.3389/fncom.2014.00097.
[88] M. Ma *et al.*, ‘Molecular layer interneurons in the cerebellum encode for valence in associative learning’, *Nat. Commun.*, vol. 11, no. 1, p. 4217, Aug. 2020, doi: 10.1038/s41467-020-18034-2.
[89] N. Yousif, P. G. Bain, D. Nandi, and R. Borisyuk, ‘A Population Model of Deep Brain Stimulation in Movement Disorders From Circuits to Cells’, *Front. Hum. Neurosci.*, vol. 14, Mar. 2020, Accessed: Jun. 29, 2022. [Online]. Available: https://www.frontiersin.org/article/10.3389/fnhum.2020.00055
[90] Y. Zang, S. Hong, and E. De Schutter, ‘Firing rate-dependent phase responses of Purkinje cells support transient oscillations’, *eLife*, vol. 9, p. e60692, Sep. 2020, doi: 10.7554/eLife.60692.
[91] K. Vervaeke, A. Lorincz, P. Gleeson, M. Farinella, Z. Nusser, and R. A. Silver, ‘Rapid desynchronization of an electrically coupled interneuron network with sparse excitatory synaptic input’, *Neuron*, vol. 67, no. 3, pp. 435–451, Aug. 2010, doi: 10.1016/j.neuron.2010.06.028.
[92] N. A. Cayco-Gajic, C. Clopath, and R. A. Silver, ‘Sparse synaptic connectivity is required for decorrelation and pattern separation in feedforward networks’, *Nat. Commun.*, vol. 8, no. 1, p. 1116, Oct. 2017, doi: 10.1038/s41467-017-01109-y.
[93] N. R. Luque, F. Naveros, R. R. Carrillo, E. Ros, and A. Arleo, ‘Spike burst-pause dynamics of Purkinje cells regulate sensorimotor adaptation’, *PLoS Comput. Biol.*, vol. 15, no. 3, p. e1006298, Mar. 2019, doi: 10.1371/journal.pcbi.1006298.
[94] H. N. Hariani, A. B. Algstam, C. T. Candler, I. F. Witteveen, J. K. Sidhu, and T. S. Balmer, ‘A system of feed-forward cerebellar circuits that extend and diversify sensory signaling’, *BioRxiv Prepr. Serv. Biol.*, p. 2023.04.11.536335, Dec. 2023, doi: 10.1101/2023.04.11.536335.
[95] C. Clopath, A. Badura, C. I. De Zeeuw, and N. Brunel, ‘A cerebellar learning model of vestibulo-ocular reflex adaptation in wild-type and mutant mice’, *J. Neurosci. Off. J. Soc. Neurosci.*, vol. 34, no. 21, pp. 7203–7215, May 2014, doi: 10.1523/JNEUROSCI.2791-13.2014.
[96] T. Yamazaki, S. Nagao, W. Lennon, and S. Tanaka, ‘Modeling memory consolidation during posttraining periods in cerebellovestibular learning’, *Proc. Natl. Acad. Sci. U. S. A.*, vol. 112, no. 11, pp. 3541–3546, Mar. 2015, doi: 10.1073/pnas.1413798112.
[97] R. D. Traub, S. J. Middleton, T. Knöpfel, and M. A. Whittington, ‘Model of very fast (> 75 Hz) network oscillations generated by electrical coupling between the proximal axons of cerebellar Purkinje cells’, *Eur. J. Neurosci.*, vol. 28, no. 8, pp. 1603–1616, Oct. 2008, doi: 10.1111/j.1460-9568.2008.06477.x.
[98] T. Doi, S. Kuroda, T. Michikawa, and M. Kawato, ‘Inositol 1,4,5-trisphosphate-dependent Ca2+ threshold dynamics detect spike timing in cerebellar Purkinje

cells', *J. Neurosci. Off. J. Soc. Neurosci.*, vol. 25, no. 4, pp. 950–961, Jan. 2005, doi: 10.1523/JNEUROSCI.2727-04.2005.
[99] C.-C. J. Lee, M. Anton, C.-S. Poon, and G. J. McRae, 'A kinetic model unifying presynaptic short-term facilitation and depression', *J. Comput. Neurosci.*, vol. 26, no. 3, pp. 459–473, Jun. 2009, doi: 10.1007/s10827-008-0122-6.
[100] G. Antunes and E. De Schutter, 'A stochastic signaling network mediates the probabilistic induction of cerebellar long-term depression', *J. Neurosci. Off. J. Soc. Neurosci.*, vol. 32, no. 27, pp. 9288–9300, Jul. 2012, doi: 10.1523/JNEUROSCI.5976-11.2012.
[101] T. M. Pinto, M. J. Schilstra, A. C. Roque, and V. Steuber, 'Binding of Filamentous Actin to CaMKII as Potential Regulation Mechanism of Bidirectional Synaptic Plasticity by β CaMKII in Cerebellar Purkinje Cells', *Sci. Rep.*, vol. 10, no. 1, p. 9019, Jun. 2020, doi: 10.1038/s41598-020-65870-9.
[102] I. Hepburn, A. Jain, H. Gangal, Y. Yamamoto, K. Tanaka-Yamamoto, and E. De Schutter, 'A Model of Induction of Cerebellar Long-Term Depression Including RKIP Inactivation of Raf and MEK', *Front. Mol. Neurosci.*, vol. 10, p. 19, 2017, doi: 10.3389/fnmol.2017.00019.
[103] C. G. Zamora Chimal and E. De Schutter, 'Ca2+ Requirements for Long-Term Depression Are Frequency Sensitive in Purkinje Cells', *Front. Mol. Neurosci.*, vol. 11, p. 438, 2018, doi: 10.3389/fnmol.2018.00438.
[104] J. F. Medina and M. D. Mauk, 'Computer simulation of cerebellar information processing', *Nat. Neurosci.*, vol. 3 Suppl, pp. 1205–1211, Nov. 2000, doi: 10.1038/81486.
[105] T. Yamazaki and S. Nagao, 'A Computational Mechanism for Unified Gain and Timing Control in the Cerebellum', *PLOS ONE*, vol. 7, no. 3, p. e33319, Mar. 2012, doi: 10.1371/journal.pone.0033319.
[106] S. Casali, E. Marenzi, C. Medini, C. Casellato, and E. D'Angelo, 'Reconstruction and Simulation of a Scaffold Model of the Cerebellar Network', *Front. Neuroinformatics*, vol. 13, 2019, Accessed: Aug. 31, 2022. [Online]. Available: https://www.frontiersin.org/articles/10.3389/fninf.2019.00037
[107] G. Grimaldi *et al.*, 'Non-invasive cerebellar stimulation--a consensus paper', *Cerebellum Lond. Engl.*, vol. 13, no. 1, pp. 121–138, Feb. 2014, doi: 10.1007/s12311-013-0514-7.
[108] N. Jenkinson and R. C. Miall, 'Disruption of saccadic adaptation with repetitive transcranial magnetic stimulation of the posterior cerebellum in humans', *Cerebellum Lond. Engl.*, vol. 9, no. 4, pp. 548–555, Dec. 2010, doi: 10.1007/s12311-010-0193-6.
[109] M. Hashimoto and K. Ohtsuka, 'Transcranial magnetic stimulation over the posterior cerebellum during visually guided saccades in man', *Brain J. Neurol.*, vol. 118 (Pt 5), pp. 1185–1193, Oct. 1995, doi: 10.1093/brain/118.5.1185.
[110] C. Ferrari *et al.*, 'TMS Over the Cerebellum Interferes with Short-term Memory of Visual Sequences', *Sci. Rep.*, vol. 8, no. 1, p. 6722, Apr. 2018, doi: 10.1038/s41598-018-25151-y.
[111] C. Ferrari, A. Ciricugno, M. Arioli, and Z. Cattaneo, 'Functional Segregation of the Human Cerebellum in Social Cognitive Tasks Revealed by TMS', *J. Neurosci. Off. J. Soc. Neurosci.*, vol. 43, no. 20, pp. 3708–3717, May 2023, doi: 10.1523/JNEUROSCI.1818-22.2023.
[112] A. Ciricugno, S. Paternò, N. Barbati, R. Borgatti, Z. Cattaneo, and C. Ferrari, 'Advances in Cerebellar TMS Therapy: An Updated Systematic Review on Multi-

Session Interventions', *Biomedicines*, vol. 13, no. 7, p. 1578, Jun. 2025, doi: 10.3390/biomedicines13071578.
[113] L. Brusa *et al.*, 'Theta burst stimulation modulates cerebellar-cortical connectivity in patients with progressive supranuclear palsy', *Brain Stimulat.*, vol. 7, no. 1, pp. 29–35, 2014, doi: 10.1016/j.brs.2013.07.003.
[114] F. Farzan *et al.*, 'Cerebellar TMS in treatment of a patient with cerebellar ataxia: evidence from clinical, biomechanics and neurophysiological assessments', *Cerebellum Lond. Engl.*, vol. 12, no. 5, pp. 707–712, Oct. 2013, doi: 10.1007/s12311-013-0485-8.
[115] Y. Shiga *et al.*, 'Transcranial magnetic stimulation alleviates truncal ataxia in spinocerebellar degeneration', *J. Neurol. Neurosurg. Psychiatry*, vol. 72, no. 1, pp. 124–126, Jan. 2002, doi: 10.1136/jnnp.72.1.124.
[116] W.-S. Kim, S. H. Jung, M. K. Oh, Y. S. Min, J. Y. Lim, and N.-J. Paik, 'Effect of repetitive transcranial magnetic stimulation over the cerebellum on patients with ataxia after posterior circulation stroke: A pilot study', *J. Rehabil. Med.*, vol. 46, no. 5, pp. 418–423, May 2014, doi: 10.2340/16501977-1802.
[117] S. Bonnì, V. Ponzo, C. Caltagirone, and G. Koch, 'Cerebellar theta burst stimulation in stroke patients with ataxia', *Funct. Neurol.*, vol. 29, no. 1, pp. 41–45, 2014.
[118] C. França *et al.*, 'Effects of cerebellar transcranial magnetic stimulation on ataxias: A randomized trial', *Parkinsonism Relat. Disord.*, vol. 80, pp. 1–6, Nov. 2020, doi: 10.1016/j.parkreldis.2020.09.001.
[119] R. G. Cury *et al.*, 'Neuronavigation-guided transcranial magnetic stimulation of the dentate nucleus improves cerebellar ataxia: A sham-controlled, double-blind n = 1 study', *Parkinsonism Relat. Disord.*, vol. 21, no. 8, pp. 999–1001, Aug. 2015, doi: 10.1016/j.parkreldis.2015.05.010.
[120] L. V. Bradnam, M. N. McDonnell, and M. C. Ridding, 'Cerebellar Intermittent Theta-Burst Stimulation and Motor Control Training in Individuals with Cervical Dystonia', *Brain Sci.*, vol. 6, no. 4, p. 56, Nov. 2016, doi: 10.3390/brainsci6040056.
[121] M. Bologna *et al.*, 'Effects of cerebellar theta-burst stimulation on arm and neck movement kinematics in patients with focal dystonia', *Clin. Neurophysiol. Off. J. Int. Fed. Clin. Neurophysiol.*, vol. 127, no. 11, pp. 3472–3479, Nov. 2016, doi: 10.1016/j.clinph.2016.09.008.
[122] M. W. Linssen, J. van Gaalen, M. A. M. Munneke, B. S. Hoffland, W. Hulstijn, and B. P. C. van de Warrenburg, 'A single session of cerebellar theta burst stimulation does not alter writing performance in writer's cramp', *Brain J. Neurol.*, vol. 138, no. Pt 6, p. e355, Jun. 2015, doi: 10.1093/brain/awu321.
[123] G. Koch *et al.*, 'Effects of two weeks of cerebellar theta burst stimulation in cervical dystonia patients', *Brain Stimulat.*, vol. 7, no. 4, pp. 564–572, 2014, doi: 10.1016/j.brs.2014.05.002.
[124] B. S. Hoffland *et al.*, 'Cerebellum-dependent associative learning deficits in primary dystonia are normalized by rTMS and practice', *Eur. J. Neurosci.*, vol. 38, no. 1, pp. 2166–2171, Jul. 2013, doi: 10.1111/ejn.12186.
[125] M. Bologna *et al.*, 'Cerebellar continuous theta burst stimulation in essential tremor', *Cerebellum Lond. Engl.*, vol. 14, no. 2, pp. 133–141, Apr. 2015, doi: 10.1007/s12311-014-0621-0.
[126] T. Popa *et al.*, 'Cerebellar rTMS stimulation may induce prolonged clinical benefits in essential tremor, and subjacent changes in functional connectivity: an

open label trial', *Brain Stimulat.*, vol. 6, no. 2, pp. 175–179, Mar. 2013, doi: 10.1016/j.brs.2012.04.009.
[127] A. Gironell, J. Kulisevsky, J. Lorenzo, M. Barbanoj, B. Pascual-Sedano, and P. Otermin, 'Transcranial magnetic stimulation of the cerebellum in essential tremor: a controlled study', *Arch. Neurol.*, vol. 59, no. 3, pp. 413–417, Mar. 2002, doi: 10.1001/archneur.59.3.413.
[128] L. Avanzino *et al.*, 'Cerebellar involvement in timing accuracy of rhythmic finger movements in essential tremor', *Eur. J. Neurosci.*, vol. 30, no. 10, pp. 1971–1979, Nov. 2009, doi: 10.1111/j.1460-9568.2009.06984.x.
[129] H.-W. Shin, M. Hallett, and Y. H. Sohn, 'Cerebellar repetitive transcranial magnetic stimulation for patients with essential tremor', *Parkinsonism Relat. Disord.*, vol. 64, pp. 304–307, Jul. 2019, doi: 10.1016/j.parkreldis.2019.03.019.
[130] N. Olfati *et al.*, 'Cerebellar repetitive transcranial magnetic stimulation (rTMS) for essential tremor: A double-blind, sham-controlled, crossover, add-on clinical trial', *Brain Stimulat.*, vol. 13, no. 1, pp. 190–196, 2020, doi: 10.1016/j.brs.2019.10.003.
[131] Y. Lv *et al.*, 'Cerebellar repetitive transcranial magnetic stimulation versus propranolol for essential tremor', *Brain Behav.*, vol. 13, no. 3, p. e2926, 2023, doi: 10.1002/brb3.2926.
[132] R. He *et al.*, 'Prediction of rTMS Efficacy in Patients With Essential Tremor: Biomarkers From Individual Resting-State EEG Network', *IEEE Trans. Neural Syst. Rehabil. Eng. Publ. IEEE Eng. Med. Biol. Soc.*, vol. 32, pp. 3719–3728, 2024, doi: 10.1109/TNSRE.2024.3469576.
[133] A. F. I. El-Adawy *et al.*, 'Efficacy of Cerebellar Transcranial Magnetic Stimulation in Treating Essential Tremor: A Randomized, Sham-Controlled Trial', *J. Clin. Neurol. Seoul Korea*, vol. 20, no. 4, pp. 378–384, Jul. 2024, doi: 10.3988/jcn.2023.0348.
[134] M. Bologna, F. Di Biasio, A. Conte, E. Iezzi, N. Modugno, and A. Berardelli, 'Effects of cerebellar continuous theta burst stimulation on resting tremor in Parkinson's disease', *Parkinsonism Relat. Disord.*, vol. 21, no. 9, pp. 1061–1066, Sep. 2015, doi: 10.1016/j.parkreldis.2015.06.015.
[135] L. Brusa *et al.*, 'Metabolic changes induced by theta burst stimulation of the cerebellum in dyskinetic Parkinson's disease patients', *Parkinsonism Relat. Disord.*, vol. 18, no. 1, pp. 59–62, Jan. 2012, doi: 10.1016/j.parkreldis.2011.08.019.
[136] E. Minks, R. Mareček, T. Pavlík, P. Ovesná, and M. Bareš, 'Is the cerebellum a potential target for stimulation in Parkinson's disease? Results of 1-Hz rTMS on upper limb motor tasks', *Cerebellum Lond. Engl.*, vol. 10, no. 4, pp. 804–811, Dec. 2011, doi: 10.1007/s12311-011-0290-1.
[137] G. Koch *et al.*, 'Cerebellar magnetic stimulation decreases levodopa-induced dyskinesias in Parkinson disease', *Neurology*, vol. 73, no. 2, pp. 113–119, Jul. 2009, doi: 10.1212/WNL.0b013e3181ad5387.
[138] M. Grobe-Einsler, V. Baljasnikowa, A. Faikus, T. Schaprian, and O. Kaut, 'Cerebellar transcranial magnetic stimulation improves motor function in Parkinson's disease', *Ann. Clin. Transl. Neurol.*, vol. 11, no. 10, pp. 2673–2684, Oct. 2024, doi: 10.1002/acn3.52183.
[139] M. Grobe-Einsler, A. Lupa, J. Weller, and O. Kaut, 'RTMS of the Cerebellum Using an Accelerated Stimulation Protocol Improved Gait in Parkinson's Disease', *Neurorehabil. Neural Repair*, vol. 38, no. 7, pp. 539–550, Jul. 2024, doi: 10.1177/15459683241257518.

[140] Q. Yao *et al.*, ‘Effect of cerebellum stimulation on cognitive recovery in patients with Alzheimer disease: A randomized clinical trial’, *Brain Stimulat.*, vol. 15, no. 4, pp. 910–920, 2022, doi: 10.1016/j.brs.2022.06.004.
[141] Y.-Y. Wang *et al.*, ‘Cerebellar transcranial magnetic stimulation to treat drug-resistant epilepsy: A randomized, controlled, crossover clinical trial’, *Epilepsia*, vol. 66, no. 1, pp. 240–252, Jan. 2025, doi: 10.1111/epi.18168.
[142] Y.-H. Cha, D. Gleghorn, and B. Doudican, ‘Occipital and Cerebellar Theta Burst Stimulation for Mal De Debarquement Syndrome’, *Otol. Neurotol. Off. Publ. Am. Otol. Soc. Am. Neurotol. Soc. Eur. Acad. Otol. Neurotol.*, vol. 40, no. 9, pp. e928–e937, Oct. 2019, doi: 10.1097/MAO.0000000000002341.
[143] Z. Liu *et al.*, ‘Effects of Multi-Session Repetitive Transcranial Magnetic Stimulation on Motor Control and Spontaneous Brain Activity in Multiple System Atrophy: A Pilot Study’, *Front. Behav. Neurosci.*, vol. 12, p. 90, 2018, doi: 10.3389/fnbeh.2018.00090.
[144] P. Song, S. Li, S. Wang, H. Wei, H. Lin, and Y. Wang, ‘Repetitive transcranial magnetic stimulation of the cerebellum improves ataxia and cerebello-fronto plasticity in multiple system atrophy: a randomized, double-blind, sham-controlled and TMS-EEG study’, *Aging*, vol. 12, no. 20, pp. 20611–20622, Oct. 2020, doi: 10.18632/aging.103946.
[145] D. Li *et al.*, ‘Repeated transcranial magnetic stimulation on the bilateral cerebellum to improve symptoms of ataxia with multiple system atrophy: a prospective, randomized, sham-controlled pilot study’, *Neurol. Sci. Off. J. Ital. Neurol. Soc. Ital. Soc. Clin. Neurophysiol.*, vol. 46, no. 4, pp. 1875–1882, Apr. 2025, doi: 10.1007/s10072-025-08001-4.
[146] M. Tramontano *et al.*, ‘Cerebellar Intermittent Theta-Burst Stimulation Combined with Vestibular Rehabilitation Improves Gait and Balance in Patients with Multiple Sclerosis: a Preliminary Double-Blind Randomized Controlled Trial’, *Cerebellum Lond. Engl.*, vol. 19, no. 6, pp. 897–901, Dec. 2020, doi: 10.1007/s12311-020-01166-y.
[147] I. A. Yassine *et al.*, ‘Effect of high frequency repetitive transcranial magnetic stimulation (rTMS) on the balance and the white matter integrity in patients with relapsing-remitting multiple sclerosis: A long-term follow-up study’, *Mult. Scler. Relat. Disord.*, vol. 83, p. 105471, Mar. 2024, doi: 10.1016/j.msard.2024.105471.
[148] K. Johkura *et al.*, ‘Effects of cerebellar magnetic stimulation on chronic post-lateral medullary infarction dizziness: A proof-of-principle cohort study’, *J. Neurol. Sci.*, vol. 392, pp. 56–62, Sep. 2018, doi: 10.1016/j.jns.2018.07.007.
[149] G. Koch *et al.*, ‘Effect of Cerebellar Stimulation on Gait and Balance Recovery in Patients With Hemiparetic Stroke: A Randomized Clinical Trial’, *JAMA Neurol.*, vol. 76, no. 2, pp. 170–178, Feb. 2019, doi: 10.1001/jamaneurol.2018.3639.
[150] L.-Y. Liao, Y.-J. Xie, Y. Chen, and Q. Gao, ‘Cerebellar Theta-Burst Stimulation Combined With Physiotherapy in Subacute and Chronic Stroke Patients: A Pilot Randomized Controlled Trial’, *Neurorehabil. Neural Repair*, vol. 35, no. 1, pp. 23–32, Jan. 2021, doi: 10.1177/1545968320971735.
[151] Y. Chen *et al.*, ‘Cerebellar Intermittent Theta-Burst Stimulation Reduces Upper Limb Spasticity After Subacute Stroke: A Randomized Controlled Trial’, *Front. Neural Circuits*, vol. 15, p. 655502, 2021, doi: 10.3389/fncir.2021.655502.
[152] D. Li, A. Cheng, Z. Zhang, Y. Sun, and Y. Liu, ‘Effects of low-frequency repetitive transcranial magnetic stimulation combined with cerebellar continuous theta burst stimulation on spasticity and limb dyskinesia in patients with stroke’,

BMC Neurol., vol. 21, no. 1, p. 369, Sep. 2021, doi: 10.1186/s12883-021-02406-2.
[153] J. Rao *et al.*, 'Bilateral Cerebellar Intermittent Theta Burst Stimulation Combined With Swallowing Speech Therapy for Dysphagia After Stroke: A Randomized, Double-Blind, Sham-Controlled, Clinical Trial', *Neurorehabil. Neural Repair*, vol. 36, no. 7, pp. 437–448, Jul. 2022, doi: 10.1177/15459683221092995.
[154] L.-H. Dong *et al.*, 'High-Frequency Cerebellar rTMS Improves the Swallowing Function of Patients with Dysphagia after Brainstem Stroke', *Neural Plast.*, vol. 2022, p. 6259693, 2022, doi: 10.1155/2022/6259693.
[155] M. Dai *et al.*, 'Effect of cerebellar transcranial magnetic stimulation with double-cone coil on dysphagia after subacute infratentorial stroke: A randomized, single-blinded, controlled trial', *Brain Stimulat.*, vol. 16, no. 4, pp. 1012–1020, 2023, doi: 10.1016/j.brs.2023.05.023.
[156] P.-A. Zhu *et al.*, 'Can cerebellar theta-burst stimulation improve balance function and gait in stroke patients? A randomized controlled trial', *Eur. J. Phys. Rehabil. Med.*, vol. 60, no. 3, pp. 391–399, Jun. 2024, doi: 10.23736/S1973-9087.24.08307-2.
[157] L.-Y. Liao *et al.*, 'Intermittent Theta-Burst Stimulation for Stroke: Primary Motor Cortex Versus Cerebellar Stimulation: A Randomized Sham-Controlled Trial', *Stroke*, vol. 55, no. 1, pp. 156–165, Jan. 2024, doi: 10.1161/STROKEAHA.123.044892.
[158] H. Zhang *et al.*, 'EEG microstates analysis after TMS in patients with subacute stroke during the resting state', *Cereb. Cortex N. Y. N 1991*, vol. 34, no. 1, p. bhad480, Jan. 2024, doi: 10.1093/cercor/bhad480.
[159] B. Manor, P. E. Greenstein, P. Davila-Perez, S. Wakefield, J. Zhou, and A. Pascual-Leone, 'Repetitive Transcranial Magnetic Stimulation in Spinocerebellar Ataxia: A Pilot Randomized Controlled Trial', *Front. Neurol.*, vol. 10, p. 73, Feb. 2019, doi: 10.3389/fneur.2019.00073.
[160] X.-Y. Chen *et al.*, 'Effects of Repetitive Transcranial Magnetic Stimulation on Cerebellar Metabolism in Patients With Spinocerebellar Ataxia Type 3', *Front. Aging Neurosci.*, vol. 14, p. 827993, 2022, doi: 10.3389/fnagi.2022.827993.
[161] Y. Shi *et al.*, 'Efficacy of cerebellar transcranial magnetic stimulation in spinocerebellar ataxia type 3: a randomized, single-blinded, controlled trial', *J. Neurol.*, vol. 270, no. 11, pp. 5372–5379, Nov. 2023, doi: 10.1007/s00415-023-11848-2.
[162] M. Zhou *et al.*, 'Effectiveness of High-Frequency Repetitive Transcranial Magnetic Stimulation in Patients With Spinocerebellar Ataxia Type 3', *J. ECT*, vol. 40, no. 1, pp. 15–19, Mar. 2024, doi: 10.1097/YCT.0000000000000925.
[163] M. Grobe-Einsler, F. Bork, A. Faikus, R. Hurlemann, and O. Kaut, 'Effects of cerebellar repetitive transcranial magnetic stimulation plus physiotherapy in spinocerebellar ataxias - A randomized clinical trial', *CNS Neurosci. Ther.*, vol. 30, no. 6, p. e14797, Jun. 2024, doi: 10.1111/cns.14797.
[164] S. K. Tikka, S. Garg, V. K. Sinha, S. H. Nizamie, and N. Goyal, 'Resting State Dense Array Gamma Oscillatory Activity as a Response Marker for Cerebellar-Repetitive Transcranial Magnetic Stimulation (rTMS) in Schizophrenia', *J. ECT*, vol. 31, no. 4, pp. 258–262, Dec. 2015, doi: 10.1097/YCT.0000000000000242.
[165] S. Garg, V. K. Sinha, S. K. Tikka, P. Mishra, and N. Goyal, 'The efficacy of cerebellar vermal deep high frequency (theta range) repetitive transcranial magnetic stimulation (rTMS) in schizophrenia: A randomized rater blind-sham

controlled study', *Psychiatry Res.*, vol. 243, pp. 413–420, Sep. 2016, doi: 10.1016/j.psychres.2016.07.023.
[166] P. Chauhan, S. Garg, S. K. Tikka, and S. Khattri, 'Efficacy of Intensive Cerebellar Intermittent Theta Burst Stimulation (iCiTBS) in Treatment-Resistant Schizophrenia: a Randomized Placebo-Controlled Study', *Cerebellum Lond. Engl.*, vol. 20, no. 1, pp. 116–123, Feb. 2021, doi: 10.1007/s12311-020-01193-9.
[167] L. Zhu *et al.*, 'Cerebellar theta burst stimulation for the treatment of negative symptoms of schizophrenia: A multicenter, double-blind, randomized controlled trial', *Psychiatry Res.*, vol. 305, p. 114204, Nov. 2021, doi: 10.1016/j.psychres.2021.114204.
[168] R. Basavaraju *et al.*, 'Intermittent theta burst stimulation of cerebellar vermis enhances fronto-cerebellar resting state functional connectivity in schizophrenia with predominant negative symptoms: A randomized controlled trial', *Schizophr. Res.*, vol. 238, pp. 108–120, Dec. 2021, doi: 10.1016/j.schres.2021.10.005.
[169] H. R. Siebner *et al.*, 'Transcranial magnetic stimulation of the brain: What is stimulated? – A consensus and critical position paper', *Clin. Neurophysiol.*, vol. 140, pp. 59–97, Aug. 2022, doi: 10.1016/j.clinph.2022.04.022.
[170] S. Colnaghi, S. Ramat, E. D'Angelo, and M. Versino, 'Transcranial magnetic stimulation over the cerebellum and eye movements: state of the art', *Funct. Neurol.*, vol. 25, no. 3, pp. 165–171, 2010.
[171] A. Sasegbon *et al.*, 'The Effects of Midline Cerebellar rTMS on Human Pharyngeal Cortical Activity in the Intact Swallowing Motor System', *Cerebellum Lond. Engl.*, vol. 20, no. 1, pp. 101–115, Feb. 2021, doi: 10.1007/s12311-020-01191-x.
[172] C. Ferrari, A. Ciricugno, L. Battelli, E. D. Grossman, and Z. Cattaneo, 'Distinct Cerebellar regions for Body Motion Discrimination', *Soc. Cogn. Affect. Neurosci.*, vol. 17, no. 1, pp. 72–80, Dec. 2019, doi: 10.1093/scan/nsz088.
[173] A. Ciricugno, C. Ferrari, M. L. Rusconi, and Z. Cattaneo, 'The left posterior cerebellum is involved in orienting attention along the mental number line: An online-TMS study', *Neuropsychologia*, vol. 143, p. 107497, Jun. 2020, doi: 10.1016/j.neuropsychologia.2020.107497.
[174] S. Garg, V. K. Sinha, S. K. Tikka, P. Mishra, and N. Goyal, 'The efficacy of cerebellar vermal deep high frequency (theta range) repetitive transcranial magnetic stimulation (rTMS) in schizophrenia: A randomized rater blind-sham controlled study', *Psychiatry Res.*, vol. 243, pp. 413–420, Sep. 2016, doi: 10.1016/j.psychres.2016.07.023.
[175] L. Wang *et al.*, 'Effects of the Intermittent Theta Burst Stimulation of the Cerebellar Vermis on Balance Recovery After Stroke: A Study Protocol for a Randomized Controlled Trial', *Front. Aging Neurosci.*, vol. 14, p. 881311, 2022, doi: 10.3389/fnagi.2022.881311.
[176] Y. Chen *et al.*, 'Effectiveness of cerebellar vermis intermittent theta-burst stimulation in improving trunk control and balance function for patients with subacute stroke: a randomised controlled trial protocol', *BMJ Open*, vol. 13, no. 1, p. e066356, Jan. 2023, doi: 10.1136/bmjopen-2022-066356.
[177] S. Colnaghi, P. Colagiorgio, S. Ramat, E. D'Angelo, G. Koch, and M. Versino, 'After Effects of Cerebellar Continuous Theta Burst Stimulation on Reflexive Saccades and Smooth Pursuit in Humans', *Cerebellum Lond. Engl.*, vol. 16, no. 4, pp. 764–771, Aug. 2017, doi: 10.1007/s12311-017-0852-y.

[178] K. Ohtsuka and T. Enoki, ‘Transcranial magnetic stimulation over the posterior cerebellum during smooth pursuit eye movements in man’, *Brain J. Neurol.*, vol. 121 (Pt 3), pp. 429–435, Mar. 1998, doi: 10.1093/brain/121.3.429.
[179] M. Nagel and W. H. Zangemeister, ‘The effect of transcranial magnetic stimulation over the cerebellum on the synkinesis of coordinated eye and head movements’, *J. Neurol. Sci.*, vol. 213, no. 1–2, pp. 35–45, Sep. 2003, doi: 10.1016/s0022-510x(03)00145-x.
[180] N. Yousif, N. Purswani, R. Bayford, D. Nandi, P. Bain, and X. Liu, ‘Evaluating the impact of the deep brain stimulation induced electric field on subthalamic neurons: A computational modelling study’, *J. Neurosci. Methods*, vol. 188, no. 1, pp. 105–112, Apr. 2010, doi: 10.1016/j.jneumeth.2010.01.026.
[181] H. de C. B. Terra, F. da S. Borges, M. F. D. Moraes, and V. R. Cota, ‘Implementation of Intra and Extracellular Nonperiodic Scale-Free Stimulation in silico for the NEURON Simulator’, in *Computational Neuroscience*, P. R. de A. Ribeiro, V. R. Cota, D. A. C. Barone, and A. C. M. de Oliveira, Eds, in Communications in Computer and Information Science. Cham: Springer International Publishing, 2022, pp. 119–131. doi: 10.1007/978-3-031-08443-0_8.
[182] H. Seo and S. C. Jun, ‘Multi-Scale Computational Models for Electrical Brain Stimulation’, *Front. Hum. Neurosci.*, vol. 11, p. 515, 2017, doi: 10.3389/fnhum.2017.00515.
[183] D. R. McNeal, ‘Analysis of a Model for Excitation of Myelinated Nerve’, *IEEE Trans. Biomed. Eng.*, vol. BME-23, no. 4, pp. 329–337, Jul. 1976, doi: 10.1109/TBME.1976.324593.
[184] F. Rattay, ‘Analysis of Models for External Stimulation of Axons’, *IEEE Trans. Biomed. Eng.*, vol. BME-33, no. 10, pp. 974–977, Oct. 1986, doi: 10.1109/TBME.1986.325670.
[185] C. C. McIntyre and W. M. Grill, ‘Excitation of central nervous system neurons by nonuniform electric fields’, *Biophys. J.*, vol. 76, no. 2, pp. 878–888, Feb. 1999, doi: 10.1016/S0006-3495(99)77251-6.
[186] C. C. McIntyre, S. Mori, D. L. Sherman, N. V. Thakor, and J. L. Vitek, ‘Electric field and stimulating influence generated by deep brain stimulation of the subthalamic nucleus’, *Clin. Neurophysiol. Off. J. Int. Fed. Clin. Neurophysiol.*, vol. 115, no. 3, pp. 589–595, Mar. 2004, doi: 10.1016/j.clinph.2003.10.033.
[187] Y. Kamitani, V. M. Bhalodia, Y. Kubota, and S. Shimojo, ‘A model of magnetic stimulation of neocortical neurons’, *Neurocomputing*, vol. 38–40, pp. 697–703, Jun. 2001, doi: 10.1016/S0925-2312(01)00447-7.
[188] T. Pashut *et al.*, ‘Mechanisms of Magnetic Stimulation of Central Nervous System Neurons’, *PLoS Comput. Biol.*, vol. 7, no. 3, p. e1002022, Mar. 2011, doi: 10.1371/journal.pcbi.1002022.
[189] T. Wu, J. Fan, K. S. Lee, and X. Li, ‘Cortical neuron activation induced by electromagnetic stimulation: a quantitative analysis via modelling and simulation’, *J. Comput. Neurosci.*, vol. 40, no. 1, pp. 51–64, Feb. 2016, doi: 10.1007/s10827-015-0585-1.
[190] A. S. Aberra, A. V. Peterchev, and W. M. Grill, ‘Biophysically realistic neuron models for simulation of cortical stimulation’, *J. Neural Eng.*, vol. 15, no. 6, p. 066023, Dec. 2018, doi: 10.1088/1741-2552/aadbb1.
[191] M. Memarian Sorkhabi, K. Wendt, M. T. Wilson, and T. Denison, ‘Estimation of the Motor Threshold for Near-Rectangular Stimuli Using the Hodgkin-Huxley Model’, *Comput. Intell. Neurosci.*, vol. 2021, p. 4716161, 2021, doi: 10.1155/2021/4716161.

[192] C. V. Rusu, M. Murakami, U. Ziemann, and J. Triesch, ‘A model of TMS-induced I-waves in motor cortex’, *Brain Stimulat.*, vol. 7, no. 3, pp. 401–414, 2014, doi: 10.1016/j.brs.2014.02.009.
[193] B. Moezzi *et al.*, ‘Simulation of electromyographic recordings following transcranial magnetic stimulation’, *J. Neurophysiol.*, vol. 120, no. 5, pp. 2532–2541, Nov. 2018, doi: 10.1152/jn.00626.2017.
[194] N. Schaworonkow and J. Triesch, ‘Ongoing brain rhythms shape I-wave properties in a computational model’, *Brain Stimulat.*, vol. 11, no. 4, pp. 828–838, 2018, doi: 10.1016/j.brs.2018.03.010.
[195] W. S. Anderson, P. Kudela, J. Cho, G. K. Bergey, and P. J. Franaszczuk, ‘Studies of stimulus parameters for seizure disruption using neural network simulations’, *Biol. Cybern.*, vol. 97, no. 2, pp. 173–194, Aug. 2007, doi: 10.1007/s00422-007-0166-0.
[196] S. K. Esser, S. L. Hill, and G. Tononi, ‘Modeling the effects of transcranial magnetic stimulation on cortical circuits’, *J. Neurophysiol.*, vol. 94, no. 1, pp. 622–639, Jul. 2005, doi: 10.1152/jn.01230.2004.
[197] Y. Denoyer, I. Merlet, F. Wendling, and P. Benquet, ‘Modelling acute and lasting effects of tDCS on epileptic activity’, *J. Comput. Neurosci.*, vol. 48, no. 2, pp. 161–176, May 2020, doi: 10.1007/s10827-020-00745-6.
[198] F. Mina, P. Benquet, A. Pasnicu, A. Biraben, and F. Wendling, ‘How deep brain stimulation modulates cortical epileptic dynamics — Insights from computational modeling’, in *2013 6th International IEEE/EMBS Conference on Neural Engineering (NER)*, Nov. 2013, pp. 162–165. doi: 10.1109/NER.2013.6695897.
[199] B. Molaee-Ardekani *et al.*, ‘Effects of transcranial Direct Current Stimulation (tDCS) on cortical activity: a computational modeling study’, *Brain Stimulat.*, vol. 6, no. 1, pp. 25–39, Jan. 2013, doi: 10.1016/j.brs.2011.12.006.
[200] E. Giannakakis *et al.*, ‘Computational modelling of the long-term effects of brain stimulation on the local and global structural connectivity of epileptic patients’, *PLoS ONE*, vol. 15, no. 2, p. e0221380, Feb. 2020, doi: 10.1371/journal.pone.0221380.
[201] M. Bikson, A. Rahman, and A. Datta, ‘Computational models of transcranial direct current stimulation’, *Clin. EEG Neurosci.*, vol. 43, no. 3, pp. 176–183, Jul. 2012, doi: 10.1177/1550059412445138.
[202] M. Bikson, A. Rahman, A. Datta, F. Fregni, and L. Merabet, ‘High-resolution Modeling Assisted Design of Customized and Individualized Transcranial Direct Current Stimulation Protocols’, *Neuromodulation J. Int. Neuromodulation Soc.*, vol. 15, no. 4, pp. 306–315, Jul. 2012, doi: 10.1111/j.1525-1403.2012.00481.x.
[203] P. C. Miranda, M. Lomarev, and M. Hallett, ‘Modeling the current distribution during transcranial direct current stimulation’, *Clin. Neurophysiol. Off. J. Int. Fed. Clin. Neurophysiol.*, vol. 117, no. 7, pp. 1623–1629, Jul. 2006, doi: 10.1016/j.clinph.2006.04.009.
[204] A. Datta, M. Elwassif, F. Battaglia, and M. Bikson, ‘Transcranial current stimulation focality using disc and ring electrode configurations: FEM analysis’, *J. Neural Eng.*, vol. 5, no. 2, pp. 163–174, Jun. 2008, doi: 10.1088/1741-2560/5/2/007.
[205] J. Gomez-Tames, I. Laakso, and A. Hirata, ‘Review on biophysical modelling and simulation studies for transcranial magnetic stimulation’, *Phys. Med. Biol.*, vol. 65, no. 24, p. 24TR03, Dec. 2020, doi: 10.1088/1361-6560/aba40d.
[206] Z. Rezaee and A. Dutta, ‘Lobule-Specific Dosage Considerations for Cerebellar Transcranial Direct Current Stimulation During Healthy Aging: A Computational

Modeling Study Using Age-Specific Magnetic Resonance Imaging Templates', *Neuromodulation J. Int. Neuromodulation Soc.*, vol. 23, no. 3, pp. 341–365, Apr. 2020, doi: 10.1111/ner.13098.

[207] T. Wagner, F. Fregni, S. Fecteau, A. Grodzinsky, M. Zahn, and A. Pascual-Leone, 'Transcranial direct current stimulation: a computer-based human model study', *NeuroImage*, vol. 35, no. 3, pp. 1113–1124, Apr. 2007, doi: 10.1016/j.neuroimage.2007.01.027.

[208] T. F. Oostendorp, Y. A. Hengeveld, C. H. Wolters, J. Stinstra, G. van Elswijk, and D. F. Stegeman, 'Modeling transcranial DC stimulation', *Annu. Int. Conf. IEEE Eng. Med. Biol. Soc. IEEE Eng. Med. Biol. Soc. Annu. Int. Conf.*, vol. 2008, pp. 4226–4229, 2008, doi: 10.1109/IEMBS.2008.4650142.

[209] A. Datta, X. Zhou, Y. Su, L. C. Parra, and M. Bikson, 'Validation of finite element model of transcranial electrical stimulation using scalp potentials: implications for clinical dose', *J. Neural Eng.*, vol. 10, no. 3, p. 036018, May 2013, doi: 10.1088/1741-2560/10/3/036018.

[210] J. D. Bijsterbosch, A. T. Barker, K.-H. Lee, and P. W. R. Woodruff, 'Where does transcranial magnetic stimulation (TMS) stimulate? Modelling of induced field maps for some common cortical and cerebellar targets', *Med. Biol. Eng. Comput.*, vol. 50, no. 7, pp. 671–681, Jul. 2012, doi: 10.1007/s11517-012-0922-8.

[211] N. De Geeter, G. Crevecoeur, A. Leemans, and L. Dupré, 'Effective electric fields along realistic DTI-based neural trajectories for modelling the stimulation mechanisms of TMS', *Phys. Med. Biol.*, vol. 60, no. 2, pp. 453–471, Jan. 2015, doi: 10.1088/0031-9155/60/2/453.

[212] S. M. Rampersad *et al.*, 'Simulating transcranial direct current stimulation with a detailed anisotropic human head model', *IEEE Trans. Neural Syst. Rehabil. Eng. Publ. IEEE Eng. Med. Biol. Soc.*, vol. 22, no. 3, pp. 441–452, May 2014, doi: 10.1109/TNSRE.2014.2308997.

[213] A. Datta, M. Bikson, and F. Fregni, 'Transcranial direct current stimulation in patients with skull defects and skull plates: high-resolution computational FEM study of factors altering cortical current flow', *NeuroImage*, vol. 52, no. 4, pp. 1268–1278, Oct. 2010, doi: 10.1016/j.neuroimage.2010.04.252.

[214] P. Ciechanski, H. L. Carlson, S. S. Yu, and A. Kirton, 'Modeling Transcranial Direct-Current Stimulation-Induced Electric Fields in Children and Adults', *Front. Hum. Neurosci.*, vol. 12, 2018, Accessed: Feb. 01, 2023. [Online]. Available: https://www.frontiersin.org/articles/10.3389/fnhum.2018.00268

[215] A. S. Aberra, B. Wang, W. M. Grill, and A. V. Peterchev, 'Simulation of transcranial magnetic stimulation in head model with morphologically-realistic cortical neurons', *Brain Stimulat.*, vol. 13, no. 1, pp. 175–189, 2020, doi: 10.1016/j.brs.2019.10.002.

[216] B. D. Goodwin and C. R. Butson, 'Subject-Specific Multiscale Modeling to Investigate Effects of Transcranial Magnetic Stimulation', *Neuromodulation J. Int. Neuromodulation Soc.*, vol. 18, no. 8, pp. 694–704, Feb. 2015, doi: 10.1111/ner.12296.

[217] H. Seo, N. Schaworonkow, S. C. Jun, and J. Triesch, 'A multi-scale computational model of the effects of TMS on motor cortex', *F1000Research*, vol. 5, 2017, doi: https://doi.org/10.12688/f1000research.9277.3.

[218] H. Seo and S. C. Jun, 'Relation between the electric field and activation of cortical neurons in transcranial electrical stimulation', *Brain Stimulat.*, vol. 12, no. 2, pp. 275–289, 2019, doi: 10.1016/j.brs.2018.11.004.

[219] N. D. Geeter, L. Dupré, and G. Crevecoeur, ‘Modeling transcranial magnetic stimulation from the induced electric fields to the membrane potentials along tractography-based white matter fiber tracts’, *J. Neural Eng.*, vol. 13, no. 2, p. 026028, Apr. 2016, doi: 10.1088/1741-2560/13/2/026028.
[220] H. Seo, H.-I. Kim, and S. C. Jun, ‘The Effect of a Transcranial Channel as a Skull/Brain Interface in High-Definition Transcranial Direct Current Stimulation-A Computational Study’, *Sci. Rep.*, vol. 7, no. 40612, Jan. 2017, doi: 10.1038/srep40612.
[221] H. Seo, D. Kim, and S. C. Jun, ‘Effect of Anatomically Realistic Full-Head Model on Activation of Cortical Neurons in Subdural Cortical Stimulation-A Computational Study’, *Sci. Rep.*, vol. 6, p. 27353, Jun. 2016, doi: 10.1038/srep27353.
[222] T. Wagner *et al.*, ‘Impact of brain tissue filtering on neurostimulation fields: a modeling study’, *NeuroImage*, vol. 85, no. 3, pp. 1048–1057, Jan. 2014, doi: 10.1016/j.neuroimage.2013.06.079.
[223] H. Chung, C. Im, H. Seo, and S. C. Jun, ‘Key factors in the cortical response to transcranial electrical Stimulations-A multi-scale modeling study’, *Comput. Biol. Med.*, vol. 144, p. 105328, May 2022, doi: 10.1016/j.compbiomed.2022.105328.
[224] H. Seo, D. Kim, and S. C. Jun, ‘Computational Study of Subdural Cortical Stimulation: Effects of Simulating Anisotropic Conductivity on Activation of Cortical Neurons’, *PloS One*, vol. 10, no. 6, p. e0128590, 2015, doi: 10.1371/journal.pone.0128590.
[225] A. Opitz, M. Windhoff, R. M. Heidemann, R. Turner, and A. Thielscher, ‘How the brain tissue shapes the electric field induced by transcranial magnetic stimulation’, *NeuroImage*, vol. 58, no. 3, pp. 849–859, Oct. 2011, doi: 10.1016/j.neuroimage.2011.06.069.
[226] S. S. Shahid, M. Bikson, H. Salman, P. Wen, and T. Ahfock, ‘The value and cost of complexity in predictive modelling: role of tissue anisotropic conductivity and fibre tracts in neuromodulation’, *J. Neural Eng.*, vol. 11, no. 3, p. 036002, Jun. 2014, doi: 10.1088/1741-2560/11/3/036002.
[227] A. Rahman *et al.*, ‘Cellular effects of acute direct current stimulation: somatic and synaptic terminal effects’, *J. Physiol.*, vol. 591, no. 10, pp. 2563–2578, May 2013, doi: 10.1113/jphysiol.2012.247171.
[228] L. Manola, B. H. Roelofsen, J. Holsheimer, E. Marani, and J. Geelen, ‘Modelling motor cortex stimulation for chronic pain control: Electrical potential field, activating functions and responses of simple nerve fibre models’, *Med. Biol. Eng. Comput.*, vol. 43, no. 3, pp. 335–343, Jun. 2005, doi: 10.1007/BF02345810.
[229] D. G. M. Zwartjes *et al.*, ‘Motor cortex stimulation for Parkinson’s disease: a modelling study’, *J. Neural Eng.*, vol. 9, no. 5, p. 056005, Oct. 2012, doi: 10.1088/1741-2560/9/5/056005.
[230] L. Manola, J. Holsheimer, P. Veltink, and J. R. Buitenweg, ‘Anodal vs cathodal stimulation of motor cortex: a modeling study’, *Clin. Neurophysiol. Off. J. Int. Fed. Clin. Neurophysiol.*, vol. 118, no. 2, pp. 464–474, Feb. 2007, doi: 10.1016/j.clinph.2006.09.012.
[231] A. Wongsarnpigoon and W. M. Grill, ‘Computer-based model of epidural motor cortex stimulation: effects of electrode position and geometry on activation of cortical neurons’, *Clin. Neurophysiol. Off. J. Int. Fed. Clin. Neurophysiol.*, vol. 123, no. 1, pp. 160–172, Jan. 2012, doi: 10.1016/j.clinph.2011.06.005.
[232] S. Silva, P. J. Basser, and P. C. Miranda, ‘Elucidating the mechanisms and loci of neuronal excitation by transcranial magnetic stimulation using a finite element

model of a cortical sulcus', *Clin. Neurophysiol. Off. J. Int. Fed. Clin. Neurophysiol.*, vol. 119, no. 10, pp. 2405–2413, Oct. 2008, doi: 10.1016/j.clinph.2008.07.248.
[233] A. Nummenmaa *et al.*, 'Targeting of white matter tracts with transcranial magnetic stimulation', *Brain Stimulat.*, vol. 7, no. 1, pp. 80–84, 2014, doi: 10.1016/j.brs.2013.10.001.
[234] R. Salvador, S. Silva, P. J. Basser, and P. C. Miranda, 'Determining which mechanisms lead to activation in the motor cortex: a modeling study of transcranial magnetic stimulation using realistic stimulus waveforms and sulcal geometry', *Clin. Neurophysiol. Off. J. Int. Fed. Clin. Neurophysiol.*, vol. 122, no. 4, pp. 748–758, Apr. 2011, doi: 10.1016/j.clinph.2010.09.022.
[235] A. L. Hodgkin and A. F. Huxley, 'A quantitative description of membrane current and its application to conduction and excitation in nerve', *J. Physiol.*, vol. 117, no. 4, pp. 500–544, Aug. 1952.
[236] D. Sterratt, B. Graham, Gillies, Andrew, and D. Willshaw, *Principles of Computational Modelling in Neuroscience*. Cambridge University Press, 2011.
[237] W. Gerstner, W. M. Kistler, R. Naud, and L. Paninski, *Neuronal Dynamics: From Single Neurons to Networks and Models of Cognition*. Cambridge: Cambridge University Press, 2014. doi: 10.1017/CBO9781107447615.
[238] E. M. Izhikevich, *Dynamical Systems in Neuroscience*. MIT Press, 2007.
[239] M. W. Barnett and P. M. Larkman, 'The action potential', *Pract. Neurol.*, vol. 7, no. 3, pp. 192–197, Jun. 2007.
[240] CThompson02, *English: Key:(a) Sodium (Na+) ion(b) Potassium (K+) ion(c) Sodium channel(d) Potassium channel(e) Sodium-Potassium Pump*. 2018. Accessed: Feb. 10, 2026. [Online]. Available: https://commons.wikimedia.org/w/index.php?curid=69611670
[241] Efazzari, *English: The open conformation allows the flow of ions (red circles) while the closed conformation does not allow the movement of ions across the cell membrane.* 2016. Accessed: Feb. 10, 2026. [Online]. Available: https://commons.wikimedia.org/w/index.php?curid=47402716
[242] B. A. Reyes, J. S. Pendergast, and S. Yamazaki, 'Mammalian Peripheral Circadian Oscillators Are Temperature Compensated', *J. Biol. Rhythms*, vol. 23, no. 1, pp. 95–98, Feb. 2008, doi: 10.1177/0748730407311855.
[243] B. Hille, *Ion Channels of Excitable Membranes*, Third Edition, Third Edition. Oxford, New York: Oxford University Press, 1992.
[244] B. L. Lichterman, 'Nerve Endings: The Discovery of the Synapse', *BMJ*, vol. 332, no. 7536, p. 308, Feb. 2006.
[245] C. S. Sherrington, *The integrative action of the nervous system*. in The integrative action of the nervous system. New Haven, CT, US: Yale University Press, 1906, pp. xvi, 411. doi: 10.1037/13798-000.
[246] 'File:1225 Chemical Synapse.jpg - Wikimedia Commons'. Accessed: Feb. 10, 2026. [Online]. Available: https://commons.wikimedia.org/w/index.php?curid=30147934
[247] G. B. Saturnino, O. Puonti, J. D. Nielsen, D. Antonenko, K. H. Madsen, and A. Thielscher, 'SimNIBS 2.1: A Comprehensive Pipeline for Individualized Electric Field Modelling for Transcranial Brain Stimulation', in *Brain and Human Body Modeling: Computational Human Modeling at EMBC 2018*, S. Makarov, M. Horner, and G. Noetscher, Eds, Cham (CH): Springer, 2019. Accessed: Aug. 21, 2023. [Online]. Available: http://www.ncbi.nlm.nih.gov/books/NBK549569/

[248] Y. Renard and K. Poulios, ‘GetFEM: Automated FE modeling of multiphysics problems based on a generic weak form language’, Apr. 2020. Accessed: Nov. 14, 2025. [Online]. Available: https://hal.science/hal-02532422
[249] B. Fischl, M. I. Sereno, and A. M. Dale, ‘Cortical Surface-Based Analysis: II: Inflation, Flattening, and a Surface-Based Coordinate System’, *NeuroImage*, vol. 9, no. 2, pp. 195–207, Feb. 1999, doi: 10.1006/nimg.1998.0396.
[250] M. Windhoff, A. Opitz, and A. Thielscher, ‘Electric field calculations in brain stimulation based on finite elements: an optimized processing pipeline for the generation and usage of accurate individual head models’, *Hum. Brain Mapp.*, vol. 34, no. 4, pp. 923–935, Apr. 2013, doi: 10.1002/hbm.21479.
[251] A. Thielscher, A. Antunes, and G. B. Saturnino, ‘Field modeling for transcranial magnetic stimulation: A useful tool to understand the physiological effects of TMS?’, *Annu. Int. Conf. IEEE Eng. Med. Biol. Soc. IEEE Eng. Med. Biol. Soc. Annu. Int. Conf.*, vol. 2015, pp. 222–225, 2015, doi: 10.1109/EMBC.2015.7318340.
[252] ‘Datasets’. Accessed: Nov. 07, 2025. [Online]. Available: https://simnibs.github.io/simnibs/build/html/installation/simnibs_installer.html
[253] M. Drakaki, C. Mathiesen, H. R. Siebner, K. Madsen, and A. Thielscher, ‘Database of 25 validated coil models for electric field simulations for TMS’, *Brain Stimulat.*, vol. 15, no. 3, pp. 697–706, 2022, doi: 10.1016/j.brs.2022.04.017.
[254] T. Nieus, E. Sola, J. Mapelli, E. Saftenku, P. Rossi, and E. D’Angelo, ‘LTP regulates burst initiation and frequency at mossy fiber-granule cell synapses of rat cerebellum: experimental observations and theoretical predictions’, *J. Neurophysiol.*, vol. 95, no. 2, pp. 686–699, Feb. 2006, doi: 10.1152/jn.00696.2005.
[255] K. M. Harris and J. K. Stevens, ‘Dendritic spines of rat cerebellar Purkinje cells: serial electron microscopy with reference to their biophysical characteristics’, *J. Neurosci. Off. J. Soc. Neurosci.*, vol. 8, no. 12, pp. 4455–4469, Dec. 1988.
[256] M. Garwicz and G. Andersson, ‘Spread of synaptic activity along parallel fibres in cat cerebellar anterior lobe’, *Exp. Brain Res.*, vol. 88, no. 3, pp. 615–622, Jan. 1992, doi: 10.1007/BF00228190.
[257] W. a. H. Rushton, ‘A theory of the effects of fibre size in medullated nerve’, *J. Physiol.*, vol. 115, no. 1, pp. 101–122, Sep. 1951, doi: 10.1113/jphysiol.1951.sp004655.
[258] M. Palkovits, P. Magyar, and J. Szenta´gothai, ‘Quantitative histological analysis of the cerebellar cortex in the cat. IV. Mossy fiber-purkinje cell numerical transfer’, *Brain Res.*, vol. 45, no. 1, pp. 15–29, Oct. 1972, doi: 10.1016/0006-8993(72)90213-2.
[259] C. Rosenmund, A. Feltz, and G. L. Westbrook, ‘Synaptic NMDA receptor channels have a low open probability’, *J. Neurosci. Off. J. Soc. Neurosci.*, vol. 15, no. 4, pp. 2788–2795, Apr. 1995, doi: 10.1523/JNEUROSCI.15-04-02788.1995.
[260] P. Rossi *et al.*, ‘NMDA receptor 2 (NR2) C-terminal control of NR open probability regulates synaptic transmission and plasticity at a cerebellar synapse’, *J. Neurosci. Off. J. Soc. Neurosci.*, vol. 22, no. 22, pp. 9687–9697, Nov. 2002, doi: 10.1523/JNEUROSCI.22-22-09687.2002.
[261] M. V. Tsodyks and H. Markram, ‘The neural code between neocortical pyramidal neurons depends on neurotransmitter release probability’, *Proc. Natl. Acad. Sci. U. S. A.*, vol. 94, no. 2, pp. 719–723, Jan. 1997, doi: 10.1073/pnas.94.2.719.

[262] M. Tsodyks, A. Uziel, and H. Markram, ‘Synchrony generation in recurrent networks with frequency-dependent synapses’, *J. Neurosci. Off. J. Soc. Neurosci.*, vol. 20, no. 1, p. RC50, Jan. 2000, doi: 10.1523/JNEUROSCI.20-01-j0003.2000.
[263] D. Gall *et al.*, ‘Intracellular Calcium Regulation by Burst Discharge Determines Bidirectional Long-Term Synaptic Plasticity at the Cerebellum Input Stage’, *J. Neurosci.*, vol. 25, no. 19, pp. 4813–4822, May 2005, doi: 10.1523/JNEUROSCI.0410-05.2005.
[264] T. Radman, R. L. Ramos, J. C. Brumberg, and M. Bikson, ‘Role of cortical cell type and morphology in subthreshold and suprathreshold uniform electric field stimulation in vitro’, *Brain Stimulat.*, vol. 2, no. 4, pp. 215–228, 228.e1–3, Oct. 2009, doi: 10.1016/j.brs.2009.03.007.
[265] A. Destexhe, D. Contreras, T. J. Sejnowski, and M. Steriade, ‘A model of spindle rhythmicity in the isolated thalamic reticular nucleus’, *J. Neurophysiol.*, vol. 72, no. 2, pp. 803–818, Aug. 1994, doi: 10.1152/jn.1994.72.2.803.
[266] Y. Gutfreund, Y. yarom, and I. Segev, ‘Subthreshold oscillations and resonant frequency in guinea-pig cortical neurons: physiology and modelling’, *J. Physiol.*, vol. 483 (Pt 3), no. Pt 3, pp. 621–640, Mar. 1995, doi: 10.1113/jphysiol.1995.sp020611.
[267] A. Roth and M. Häusser, ‘Compartmental models of rat cerebellar Purkinje cells based on simultaneous somatic and dendritic patch-clamp recordings’, *J. Physiol.*, vol. 535, no. Pt 2, pp. 445–472, Sep. 2001, doi: 10.1111/j.1469-7793.2001.00445.x.
[268] H. Schmidt, K. M. Stiefel, P. Racay, B. Schwaller, and J. Eilers, ‘Mutational analysis of dendritic Ca2+ kinetics in rodent Purkinje cells: role of parvalbumin and calbindin D28k’, *J. Physiol.*, vol. 551, no. Pt 1, pp. 13–32, Aug. 2003, doi: 10.1113/jphysiol.2002.035824.
[269] M. Häusser and B. A. Clark, ‘Tonic synaptic inhibition modulates neuronal output pattern and spatiotemporal synaptic integration’, *Neuron*, vol. 19, no. 3, pp. 665–678, Sep. 1997, doi: 10.1016/s0896-6273(00)80379-7.
[270] J. M. Bekkers and M. Häusser, ‘Targeted dendrotomy reveals active and passive contributions of the dendritic tree to synaptic integration and neuronal output’, *Proc. Natl. Acad. Sci. U. S. A.*, vol. 104, no. 27, pp. 11447–11452, Jul. 2007, doi: 10.1073/pnas.0701586104.
[271] M. Bikson, J. Dmochowski, and A. Rahman, ‘The “Quasi-Uniform” Assumption in Animal and Computational Models of Non-Invasive Electrical Stimulation’, *Brain Stimul. Basic Transl. Clin. Res. Neuromodulation*, vol. 6, no. 4, pp. 704–705, Jul. 2013, doi: 10.1016/j.brs.2012.11.005.
[272] ‘Datasets — SimNIBS 4.5.0 documentation’. Accessed: Dec. 30, 2025. [Online]. Available: https://simnibs.github.io/simnibs/build/html/dataset.html#example-dataset
[273] H.-X. Tan *et al.*, ‘The Immediate Effects of Intermittent Theta Burst Stimulation of the Cerebellar Vermis on Cerebral Cortical Excitability During a Balance Task in Healthy Individuals: A Pilot Study’, *Front. Hum. Neurosci.*, vol. 15, p. 748241, 2021, doi: 10.3389/fnhum.2021.748241.
[274] ‘FAQ — SimNIBS 4.5.0 documentation’. Accessed: Dec. 30, 2025. [Online]. Available: https://simnibs.github.io/simnibs/build/html/faq.html#what-is-the-di-dt-in-tms-simulations

[275] D. C. Van Essen, C. J. Donahue, and M. F. Glasser, ‘Development and Evolution of Cerebral and Cerebellar Cortex’, *Brain. Behav. Evol.*, vol. 91, no. 3, pp. 158–169, 2018, doi: 10.1159/000489943.
[276] J. D. T. Engbers, F. R. Fernandez, and R. W. Turner, ‘Bistability in Purkinje neurons: ups and downs in cerebellar research’, *Neural Netw. Off. J. Int. Neural Netw. Soc.*, vol. 47, pp. 18–31, Nov. 2013, doi: 10.1016/j.neunet.2012.09.006.
[277] S. Glasauer, ‘Cerebellar contribution to saccades and gaze holding: a modeling approach’, *Ann. N. Y. Acad. Sci.*, vol. 1004, pp. 206–219, Oct. 2003, doi: 10.1196/annals.1303.018.
[278] U. Rüb, J. C. Jen, H. Braak, and T. Deller, ‘Functional neuroanatomy of the human premotor oculomotor brainstem nuclei: insights from postmortem and advanced in vivo imaging studies’, *Exp. Brain Res.*, vol. 187, no. 2, pp. 167–180, May 2008, doi: 10.1007/s00221-008-1342-8.
[279] S. Marti, D. Straumann, U. Büttner, and S. Glasauer, ‘A model-based theory on the origin of downbeat nystagmus’, *Exp. Brain Res.*, vol. 188, no. 4, pp. 613–631, Jul. 2008, doi: 10.1007/s00221-008-1396-7.
[280] T. Sugimura, T. Miyashita, M. Yamamoto, K. Kobayashi, Y. Yoshimura, and Y. Saito, ‘An Indirect Pathway from the Rat Interstitial Nucleus of Cajal to the Vestibulocerebellum Involved in Vertical Gaze Holding’, *eNeuro*, vol. 11, no. 11, p. ENEURO.0294-24.2024, Nov. 2024, doi: 10.1523/ENEURO.0294-24.2024.

Appendix

Research output

In this appendix I share the abstracts submitted to the 32nd, 33rd, 34th and 35th Annual Computational Neuroscience Meeting. The first abstract presents the cerebellar network. The second abstract presents the vertical oculomotor system model and how I used it to validate the transcranial stimulation model. The third abstract presents a preliminary transcranial stimulation model. The fourth abstract, under review, presents the transcranial magnetic stimulation model and its validation.

A.1 CNS*2023, Leipzig

Below is the abstract accepted in the 32nd Annual Computational Neuroscience Meeting [1].

Development of a biologically realistic cerebellar model to study the effects of non-invasive stimulation

Eleonora Bernasconi [1] , *Nada Yousif* [1], *Volker Steuber* [1]

[1] *Biocomputation Research Group, University of Hertfordshire, Hatfield, United Kingdom*

Email: eleonorabernasconi97@gmail.com

The first use of cerebellar transcranial stimulation to modulate saccades in humans dates back to the 1990s [1]. However, the underlying mechanisms of the action of transcranial stimulation on the cerebellum are still unknown [2,3].

Our goal is to investigate the effect of non-invasive stimulation on neuronal activity in the cerebellar network. To do so we developed a detailed, biologically realistic model of the cerebellar cortex. We will integrate our network with a control theory model of the vertical oculomotor system [4] to predict saccades based on simulated Purkinje cell output. We will test whether the addition of transcranial stimulation to the network model disrupts saccades as seen experimentally [5].

To date we connected a recent Purkinje cell model [6] to a detailed granular layer model [7]. We added one spine per spiny dendrite compartment of the Purkinje cell. The granular layer model was modified to have a network size of 4000 µm × 400 µm along the transversal and sagittal axes. To reduce the computational cost, the thickness of the granular layer was reduced from 200µm to 160µm and the density of the granule cells was reduced to $1.92 * 10^6\, mm^{-3}$ [8]. Figure 1 depicts the network architecture described. All models were implemented in the NEURON simulator

(version 8.1.0) using Python (version 3.10.4) and simulated on a Linux machine (Ubuntu 22.04.1 LTS).

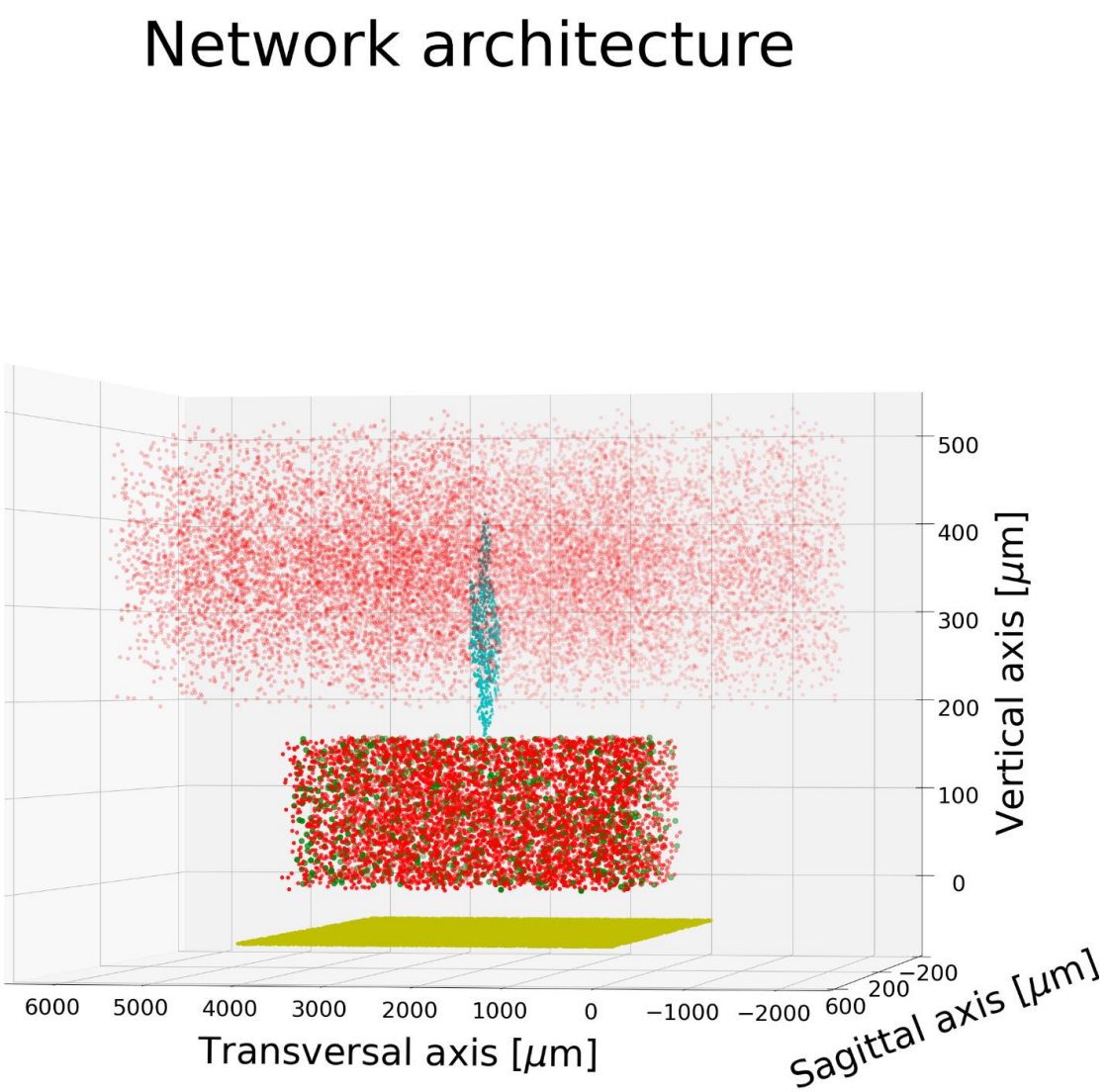


Figure 1 Network architecture of the cerebellar cortex model. The light green plane displays the mossy fibres that excite the granular layer. Dark green dots represent Golgi cells. Blue dots represent the Purkinje cell spines. Red dots represent granule cells. Transparent red dots represent the T-junctions and parallel fibre terminals of the granule cells. Note that for visualisation clarity only 1 out of 100 granule cells is displayed.

We are currently parameter tuning the Purkinje cell to reproduce electrophysiological behaviour as seen *in vivo* [9].

References

1. Hashimoto M, Ohtsuka K. Transcranial magnetic stimulation over the posterior cerebellum during visually guided saccades in man. Brain J Neurol. 1995 Oct;118 (Pt 5):1185–93.

2. Jalali R, Chowdhury A, Wilson M, Miall RC, Galea JM. Neural changes associated with cerebellar tDCS studied using MR spectroscopy. Exp Brain Res. 2018 Apr;236(4):997–1006.

3. Zhang X, Hancock R, Santaniello S. Transcranial direct current stimulation of cerebellum alters spiking precision in cerebellar cortex: A modeling study of cellular responses. PLOS Comput Biol. 2021 Dec 9;17(12):e1009609.

4. Glasauer S, Rössert C. Modelling drug modulation of nystagmus. Prog Brain Res. 2008;171:527–34.

5. Colnaghi S, Ramat S, D'Angelo E, Versino M. Transcranial magnetic stimulation over the cerebellum and eye movements: state of the art. Funct Neurol. 2010;25(3):165–71.

6. Zang Y, Dieudonné S, De Schutter E. Voltage- and Branch-Specific Climbing Fiber Responses in Purkinje Cells. Cell Rep. 2018 Aug 7;24(6):1536–49.

7. Sudhakar SK, Hong S, Raikov I, Publio R, Lang C, Close T, et al. Spatiotemporal network coding of physiological mossy fiber inputs by the cerebellar granular layer. PLOS Comput Biol. 2017 Sep 21;13(9):e1005754.

8. Harvey RJ, Napper RM. Quantitative study of granule and Purkinje cells in the cerebellar cortex of the rat. J Comp Neurol. 1988 Aug 8;274(2):151–7.

9. Goossens J, Daniel H, Rancillac A, van der Steen J, Oberdick J, Crépel F, et al. Expression of protein kinase C inhibitor blocks cerebellar long-term depression without affecting Purkinje cell excitability in alert mice. J Neurosci Off J Soc Neurosci. 2001 Aug 1;21(15):5813–23.

A.2 CNS*2024, Natal

Below is the abstract accepted in the 33rd Annual Computational Neuroscience Meeting [2].

Predicting eye movements with a detailed network model of the cerebellar cortex

Eleonora Bernasconi [1], *Nada Yousif* [1], *Stefan Glasauer*[2], *Volker Steuber* [1]

[1] *University of Hertfordshire, Biocomputation Research Group, Hatfield, United Kingdom*

[2] *Brandenburg University of Technology Cottbus-Senftenberg, Cottbus, Germany*

Email: e.bernasconi@herts.ac.uk

Many models of transcranial stimulation have been developed to study its mechanisms of action. However, one of the main limitations of these models is their lack of validation methods [1], [2]. Our goal is to develop a validation method for non-invasive stimulation models. We connected a detailed model of the cerebellar cortex to a control theory model of the vertical oculomotor system [3]. The output of our cerebellar model predicts a measurable behaviour - gaze holding and smooth pursuit movements.

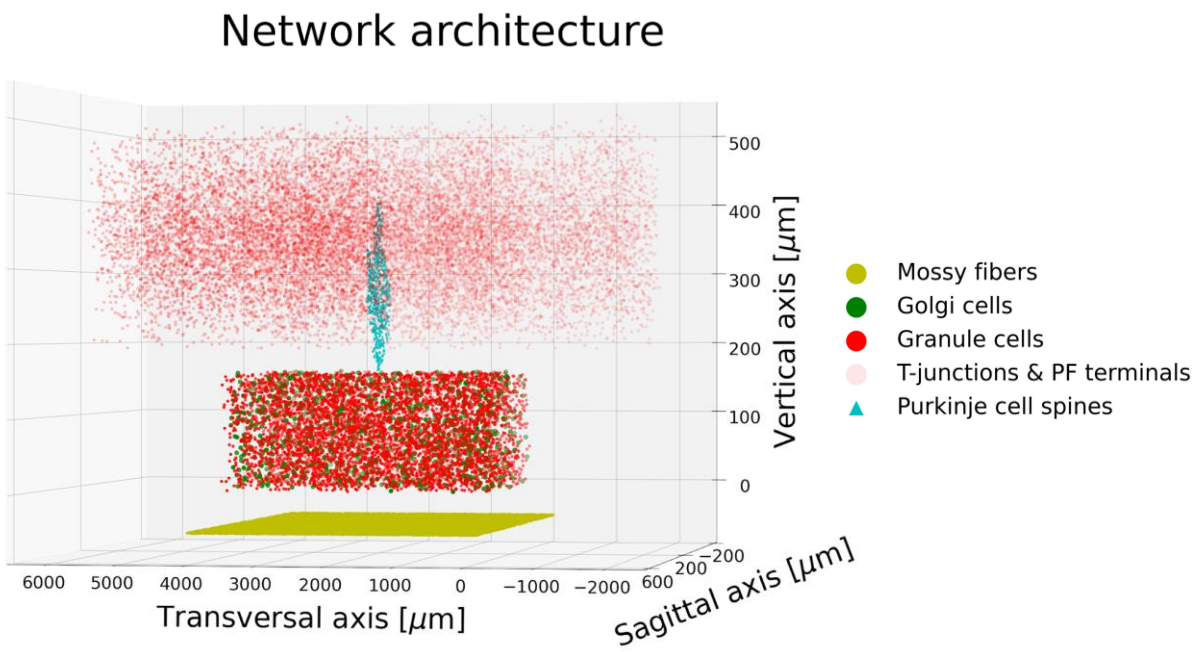


Figure 1 Network architecture of the cerebellar cortex model. The light green plane displays the mossy fibres that excite the granular layer. Dark green dots represent Golgi cells. Blue dots represent the Purkinje cell spines. Red dots represent granule cells. Transparent red dots represent the T-junctions and parallel fibre terminals of the granule cells. Note that for visualisation clarity only 1 out of 100 granule cells is displayed.

To predict eye movements from our cerebellar network, we constructed the activation function used in the oculomotor system model from the population response of 51 simulated Purkinje cells. We ran 94 simulations of the granular layer, with the mossy fibre input increasing from 0 to 186 Hz in 2 Hz steps.

We simulated the population of Purkinje cells by providing the Purkinje cell model with 51 different background inputs (Poisson spike trains with a mean frequency between 0 and 50 Hz in 1 Hz steps) and generated the population response by averaging the mean firing rate of the 51 simulated Purkinje cells. To normalise the population response, we:

1. Fitted the curve with three straight lines;
2. Determined the line with the maximum slope;
3. Normalised the slope of that line to 1 and normalised the slope of the other lines consequently;
4. Normalised the amplitude of the midpoint of the line with slope 1 to 0.5 and shifted the midpoint to zero.

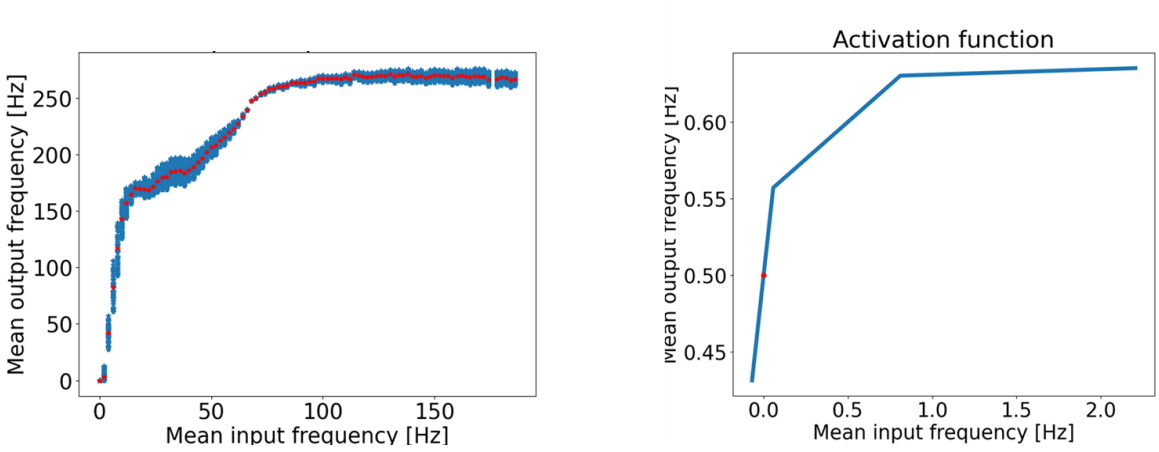


Fig 2 Left: response of 51 Purkinje cells (blue dots). The red dots show the mean firing rate of the population for each input frequency. Right: activation function obtained by normalising the population response.

We replicated the results corresponding to a healthy participant in the original study [3] by simulating the oculomotor system model with our activation function.

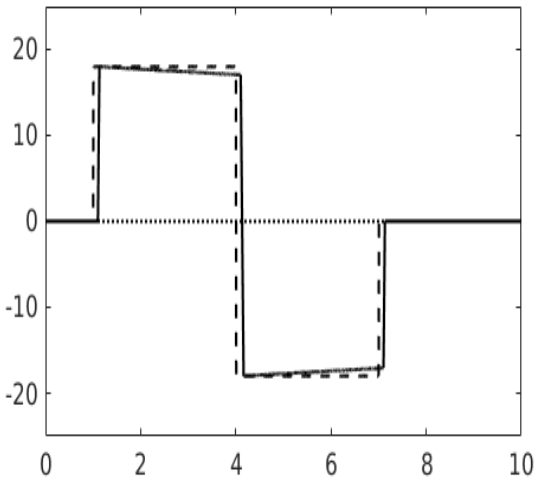


Fig 3 Simulation of vertical saccades and gaze holding using the activation functions shown in Fig. 2. The dashed line is the target position, the solid black line is the eye position.

In conclusion, we connected the output of our cerebellar network to a measurable behaviour. We are currently stimulating our cerebellar network with a simulated electric field estimated by an MRI-generated head model. We will validate the non-invasive stimulation model by comparing the eye movements predicted for a baseline condition with the eye movements predicted from the stimulated network.

References

[1] H. Seo and S. C. Jun, ‘Multi-Scale Computational Models for Electrical Brain Stimulation’, Front Hum Neurosci, vol. 11, p. 515, 2017, doi: 10.3389/fnhum.2017.00515.

[2] S. S. Shahid, M. Bikson, H. Salman, P. Wen, and T. Ahfock, ‘The value and cost of complexity in predictive modelling: role of tissue anisotropic conductivity and fibre tracts in neuromodulation’, J Neural Eng, vol. 11, no. 3, p. 036002, Jun. 2014, doi: 10.1088/1741-2560/11/3/036002.

[3] S. Glasauer and C. Rössert, ‘Modelling drug modulation of nystagmus’, Prog Brain Res, vol. 171, pp. 527–534, 2008, doi: 10.1016/S0079-6123(08)00675-4.

A.3 CNS*2025, Florence

Below is the abstract accepted in the 34th Annual Computational Neuroscience Meeting [3].

Studying the effects of TMS on the cerebellum with a realistic model of the cerebellar cortex

Eleonora Bernasconi *[1], *Nada Yousif* [1], *Volker Steuber* [1]

[1] *Biocomputation Research Group, University of Hertfordshire, Hatfield, United Kingdom*

***Email:** e.bernasconi@herts.ac.uk

Introduction

Transcranial magnetic stimulation (TMS) has been used for over 30 years to modulate cortical excitability and it is currently being applied to other brain regions, such as the cerebellum [1,2]. TMS is a promising technique that could be beneficial for people suffering with dystonia, essential tremor, and Parkinson's disease [1,2]. However, research in this field provides contrasting evidence of the effects of TMS on the cerebellum [1,3]. Our goal is to study the underlying mechanisms of TMS on the cerebellum via a computational approach.

Methods

We stimulated a previously developed model of the cerebellar cortex consisting of granule, Golgi and Purkinje cells [4]. To ensure uniform stimulus application, we replaced the granule cells with a multi-compartmental model by Diwakar et al. [5]. We applied the stimulus as a voltage using the extracellular mechanism in NEURON [6], which requires multi-compartmental models. We stimulated all compartments of all neurons with a sinusoidal waveform, where field decay is only dependent on the distance between the source of the applied electric field (located at the origin) and the

stimulated compartment [7]. We tested 6 stimulus frequencies commonly used in TMS protocols on the cerebellum: 1, 5, 10, 20 and 50 Hz.

Results

For stimulus frequencies up to 20 Hz, the firing rate of the Purkinje cell oscillates in response to the sinusoidal stimulus, as expected (Figure 1A-C). During the positive phase of the stimulus, the cell's soma hyperpolarizes, while during the negative phase, it depolarizes.

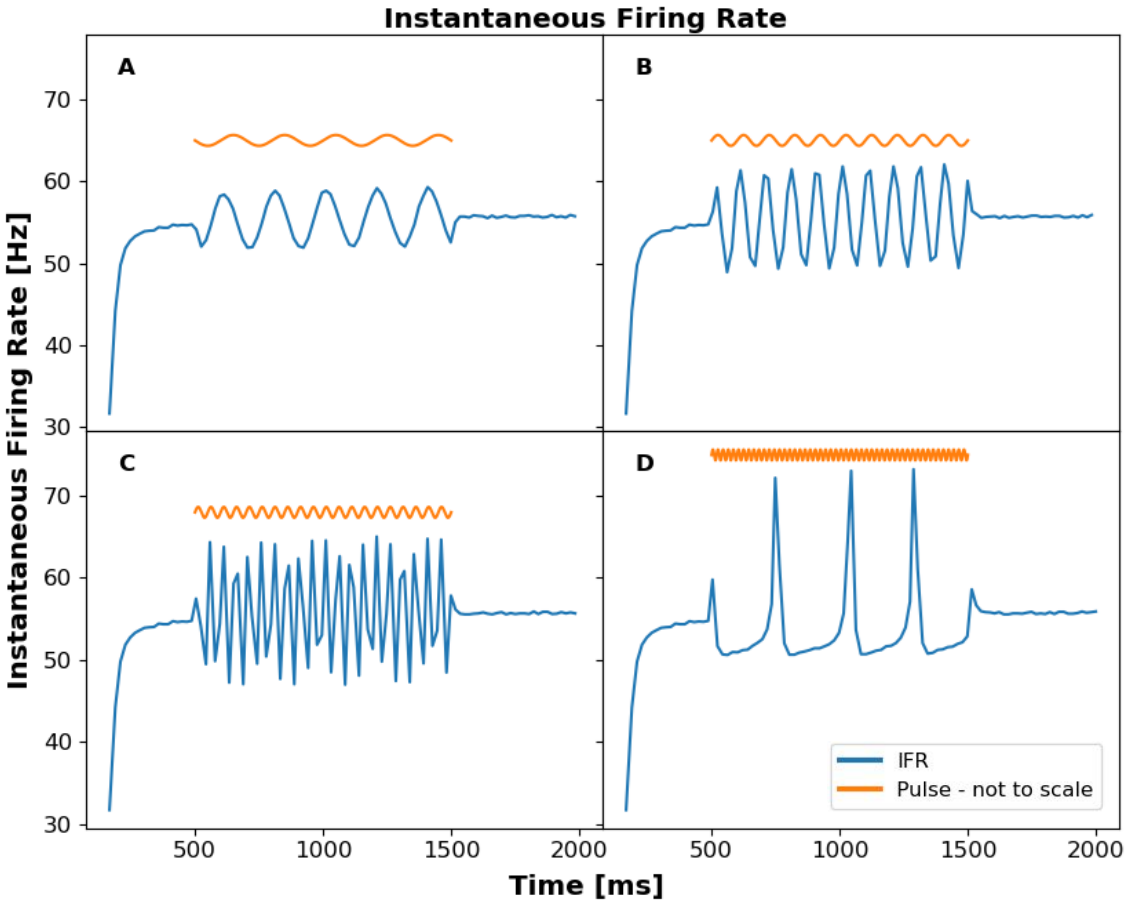


Figure 1: Instantaneous firing rate of the Purkinje cell (in blue) and waveform used to stimulate the cell (in orange). The amplitude of the pulse waveform is not to scale. The stimulus applied has a frequency of 5, 10, 20 and 50 Hz in figures A, B, C and D.

Increasing the stimulus frequency up to 20 Hz amplifies the modulation. The variance of the cell's instantaneous firing rate is 0.4, 5.9, 18.9, 39.0 and 29.6 Hz^2 for stimulus frequencies of 1, 5, 10, 20 and 50 Hz.

At 50 Hz, the cell's instantaneous firing rate no longer follows the stimulus waveform, and instead exhibits a pronounced excitation with weaker inhibition (Figure 1D). This excitation is much stronger than that obtained at lower stimulus frequencies.

Discussion

The behaviour of our Purkinje cell model aligns with the findings of Rattay et al. [8], suggesting that our model can serve as a useful tool to study how TMS influences cerebellar activity.

We show that stimulus frequency can significantly impact the cell's behaviour, highlighting the importance of carefully selecting this parameter in clinical settings. High-frequency stimulation exerts a strong excitatory influence, which may have important implications for therapeutic use.

Future work will extend the simulation model to the granule and Golgi cells. We plan to stimulate the network with a more realistic electric field generated using realistic anatomical head models. We will derive the electric field distribution employing SimNIBS [9].

References

[1] https://doi.org/10.1016/j.brs.2017.11.015

[2] https://doi.org/10.1016/j.neubiorev.2017.10.006

[3] https://doi.org/10.3389/fnagi.2020.578339

[4] https://doi.org/10.1007/s10827-024-00871-5

[5] https://doi.org/10.1017/10.1152/jn.90382.2008

[6] https://doi.org/10.1017/CBO9780511541612

[7] https://doi.org/10.1017/10.1007/978-3-031-08443-0_8

[8] https://doi.org/10.1109/TBME.1986.325670

[9] https://doi.org/10.1007/978-3-030-21293-3_1

A.4 CNS*2026, Halifax

Below is the abstract submitted to the 35th Annual Computational Neuroscience Meeting. This abstract is under review.

Development and Validation of a Multi-Scale Model of Cerebellar Transcranial Magnetic Stimulation

Eleonora Bernasconi*[1], Nada Yousif[1], Volker Steuber[1]

[1]Biocomputation Research Group, Centre for AI and Robotics Research, University of Hertfordshire, United Kingdom

***Email:** eleonorabernasconi97@gmail.com

Introduction

Transcranial magnetic stimulation (TMS) is a promising technique to alleviate symptoms related to cerebellar pathologies. However, the outcomes are variable and it is not understood how neurons are affected by it. Many models, at different scales, have been developed to try to address the open questions on the functioning of TMS. The state of the art are multi-scale models, which integrate MRI generated head models of the electric field induced by TMS and biologically realistic neuron models. A limitation of multi-scale models lies in their validation [1]. In this work we present a framework to model and validate TMS targeting the cerebellum.

Methods

We calculated the mean electric field induced by TMS in the cerebellum vermis using the SimNIBS simulator. We developed a biologically realistic model of the cerebellar cortex [2] and coupled the TMS induced electric field to its neurons using NEURON's extracellular mechanism.

We generated the input-output curve of the cerebellar network, in baseline and in stimulated conditions, by increasing the input mossy fibre frequency from 0 to 150 Hz in 3 Hz steps.

We normalised the input-output curves in the two conditions and utilised them in a vertical oculomotor system model [3] to predict eye movements. We compared predicted eye movements in the baseline and stimulated conditions with experimental data to validate the TMS model.

Results

The maximum mean electric field induced by TMS in the cerebellum vermis is 30.4 V/m. The stimulation does not alter the mean firing rate of the neurons, but it alters the spike timing and the instantaneous firing rate.

We reproduced the eye movements of a healthy subject with the network in baseline conditions. Eye movements in the stimulated condition show a drift during gaze holding. Saccades are not affected by the stimulation.

Experimentally it was found that the application of TMS generated an increase in the amplitude of ipsilateral reflexive saccades and in the acceleration of ipsilateral smooth pursuit movements.

Discussion

The vertical oculomotor system model produces observable differences in predicted eye movements following stimulation. This suggests that the model can serve as a validation framework for transcranial magnetic stimulation models targeting cerebellar circuits involved in saccades and gaze holding.

Predicted eye movements do not accurately reproduce the experimental findings. This may suggest that the employed model is not detailed enough to reproduce experimental results. It may also suggest eye movement changes seen experimentally are not primarily driven by neuronal activity within the targeted cerebellar region, but may arise from activation of more superficial neural structures or neighbouring regions in the cerebral cortex.

References

1. Shahid, S. S., Bikson, M., Salman, H., Wen, P., & Ahfock, T. (2014). The value and cost of complexity in predictive modelling: Role of tissue anisotropic conductivity and fibre tracts in neuromodulation. Journal of Neural Engineering, 11(3), 036002. https://doi.org/10.1088/1741-2560/11/3/036002
2. Bernasconi, E., Yousif, N., & Steuber, V. (2024). 32nd Annual Computational Neuroscience Meeting: CNS*2023 - P194 Development of a biologically realistic cerebellar model to study the effects of non-invasive stimulation. Journal of Computational Neuroscience, 52(1), 3–166. https://doi.org/10.1007/s10827-024-00871-5
3. Glasauer, S., & Rössert, C. (2008). Modelling drug modulation of nystagmus. Progress in Brain Research, 171, 527–534. https://doi.org/10.1016/S0079-6123(08)00675-4

Bibliography

[1] E. Bernasconi, N. Yousif, and V. Steuber, ‘32nd Annual Computational Neuroscience Meeting: CNS*2023 - P194 Development of a biologically realistic cerebellar model to study the effects of non-invasive stimulation’, *J. Comput. Neurosci.*, vol. 52, no. 1, pp. 3–166, Oct. 2024, doi: 10.1007/s10827-024-00871-5.

[2] E. Bernasconi, S. Glasauer, N. Yousif, and V. Steuber, ‘33rd Annual Computational Neuroscience Meeting: CNS*2024 - P015 Predicting eye movements with a detailed network model of the cerebellar cortex’, *J. Comput. Neurosci.*, vol. 53, no. 1, pp. 3–89, Feb. 2025, doi: 10.1007/s10827-024-00889-9.

[3] E. Bernasconi, N. Yousif, and V. Steuber, ‘34th Annual Computational Neuroscience Meeting: CNS*2025 - P021 Studying the effects of TMS on the cerebellum with a realistic model of the cerebellar cortex’, *J. Comput. Neurosci.*, vol. 54, no. 1, pp. 3–395, Feb. 2026, doi: 10.1007/s10827-025-00915-4.